Extended Cosmological Probes of Massive Dark Relics

Von der Fakultät für Mathematik, Informatik und Naturwissenschaften der RWTH Aachen University zur Erlangung des akademischen Grades einer Doktorin der Naturwissenschaften genehmigte Dissertation

vorgelegt von

Deanna C. HOOPER, M.Sc.

aus

Exeter, Vereinigtes Königreich

Berichter: Univ.-Prof. Dr. Julien Lesgourgues
Jun.-Prof. Dr. rer. nat. Felix Kahlhöfer

Tag der mündlichen Prüfung: 9. September 2019

DOCTORAL THESIS

Extended Cosmological Probes of Massive Dark Relics

by

Deanna C. HOOPER

Supervisor

Prof. Dr. Julien LESGOURGUES

This thesis was realised at the

INSTITUTE FOR THEORETICAL PARTICLE PHYSICS AND COSMOLOGY,

RWTH AACHEN UNIVERSITY

Aachen, September 2019

Abstract

Extended Cosmological Probes of Massive Dark Relics

by Deanna C. HOOPER

Despite the incredible progress made in cosmology and particle physics in the last century, there are still many unanswered questions. Specifically, we have robust evidence showing that $\sim 85\,\%$ of the matter content of the universe is invisible and only interacts gravitationally. Furthermore, observations show neutrinos to have a non-zero mass, which is not readily explained with the Standard Model of particle physics. Moreover, as we acquire increasingly precise data on different cosmological scales, we notice that some tensions and mismatches appear within our standard cosmological model. In this work I use both current and future experiments to address these problems, focussing on neutrino masses in cosmology and on the possibility that dark matter has small non-gravitational interactions with other particles.

After a thorough review of the necessary theoretical background, I discuss the main probes at our disposal to observe the universe around us. I detail a new method we have developed to constrain non-cold dark matter models using Lyman-α data, by parametrising the suppression these models induce in the matter power spectrum. Additionally, I discuss the new implementation of spectral distortions in our Boltzmann code, which will allow us to more easily use this probe in combination with other cosmological observables.

Furthermore, I forecast the sensitivity to the sum of neutrino masses of thirty-five different combinations of future Cosmic Microwave Background and Large Scale Structure data sets, showing that future surveys will measure the neutrino mass with high significance, regardless of the underlying cosmological model.

Finally, I discuss the possibility that dark matter has additional interactions, either with baryons or with an additional relativistic dark sector. Using the newly-developed methods, I provide up-to-date constraints on these interactions, and assess their ability to alleviate the tensions among cosmological data sets.

Zusammenfassung

Erweiterte Kosmologische Untersuchungen Massiver Dunkler Relikte

von Deanna C. HOOPER

Trotz des unglaublichen Fortschritts, der während des letzten Jahrhunderts in der Kosmologie und der Teilchenphysik erzielt wurde, bleiben noch immer viele Fragen unbeantwortet. Insbesondere besitzen wir stichhaltige Belege dafür, dass $\sim 85\,\%$ der Materie im Universum unsichtbar ist und nur gravitativ wechselwirkt. Zudem ergeben Beobachtungen, dass Neutrinos eine nicht verschwindende Masse besitzen, was sich im Standardmodell der Teilchenphysik nicht ohne Weiteres erklären lässt. Darüber hinaus zeigen sich, während wir zunehmend präzisere Daten auf unterschiedlichen kosmologischen Skalen erfassen, einige Spannungen und Diskrepanzen innerhalb unseres kosmologischen Standardmodells. In dieser Arbeit nutze ich sowohl gegenwärtige als auch zukünftige Experimente, um diese Probleme zu behandeln. Der Fokus liegt dabei auf Neutrinomassen in der Kosmologie sowie auf der Möglichkeit, dass dunkle Materie schwache nicht-gravitative Wechselwirkungen mit anderen Teilchen aufweist.

Nach einer gründlichen Betrachtung des notwendigen theoretischen Hintergrunds diskutiere ich die wichtigsten Untersuchungen, die uns zur Beobachtung des Universums um uns herum zur Verfügung stehen. Ich beschreibe detailliert eine neue Methode, die wir entwickelt haben, um Modelle nicht-kalter dunkler Materie mithilfe von Lyman-α-Daten einzuschränken, indem wir die Unterdrückung parametrisieren, die diese Modelle im Materie-Leistungsspektrums herbeiführen. Zusätzlich diskutiere ich die neue Implementation von spektralen Verzerrungen in unserem Boltzmann-Code, die es uns erlauben wird, diese leichter in Kombination mit anderen kosmologischen Observablen zu nutzen.

Des Weiteren sage ich die Sensitivität von fünfunddreißig Kombinationen zukünftiger Kosmischer-Mikrowellen-Hintergrund- und Großstruktur-Experimente in Bezug auf die Summe der Neutrinomassen vorher. Dadurch zeige ich, dass zukünftige Untersuchungen die Neutrinomasse, unabhängig von dem zugrundeliegenden kosmologischen Modell, mit hoher Signifikanz messen werden.

Schließlich diskutiere ich die Möglichkeit, dass dunkle Materie weitere Wechselwirkungen aufweist, entweder mit Baryonen oder mit einem zusätzlichen relativistischen dunklen Sektor. Unter Benutzung der neu entwickelten Methoden gebe ich aktuelle Grenzwerte für diese Wechselwirkungen an und beurteile ihr Potential, die Spannungen zwischen kosmologischen Datensätzen zu lindern.

Acknowledgements

First and foremost, I would like to thank my supervisor, Prof. Julien Lesgourgues for giving me the opportunity to work in his group, and for his continued advice and guidance over the last few years. Julien has a contagious passion and dedication to his work, and I have learnt a lot working with him. He has helped me grow into an independent researcher, and has motivated me to continue looking for new challenges.

A special thank you also goes to Prof. Felix Kahlhöfer for agreeing to be my second examiner at a very busy time. I am especially grateful for all the fun and informative discussions that have helped me remember there are many different ways to approach the dark matter problem.

My time at the TTK has been incredible, and it has been made more enjoyable by my colleagues, both former and present. I would like to thank all the members of the group that have helped me grow, both academically and as a person, over the last few years. I especially want to thank everyone who brought food to the office, the constant supply of baked goods has greatly reduced stress levels in the last few months. Of course life at the office would not be the same without my office colleague Nils Schöneberg, who has helped me with so many different topics over the last year and a half. I will certainly miss our intense discussions about work, life, feminism, academia, politics, and everything in between.

I would also like to thank all of my proofreaders: Cristian, Elias, Fatih, Matteo, Nils, Parth, Thejs, and Saniya. Their comments and suggestions, some more critical than others, helped improve this thesis, and helped ground me in the places where I was getting lost in details in my explanations. Furthermore, I am grateful for the invaluable contributions from Elias and Fatih to the German translation of my abstract.

I would not be where I am today without the continued love and support from my family. My Mum, my Dad, and my brother, Stef, have been a constant source of encouragement, from a young age when I was taught that I could be anything I wanted to be. My family have always been there to keep me pushing for what I want, and to help me up whenever I fall. I will always be grateful for their continued support.

Finally, and most importantly, I want to thank my partner Max, for the unconditional support since we met. The last couple of years have seen many ups and downs, and through it all he has always given me a reason to smile and to keep pushing forward. In the last few months of thesis writing, his continued company, love, and support have kept me going. The bond we have goes deeper than words can describe.

Declaration of Authorship

I, *Deanna C. Hooper*, declare that this thesis and the work presented in it are my own and have been generated by me as the result of my own original research. I do solemnly swear that to the best of my knowledge:

1. This work was done wholly or mainly while in candidature for the doctoral degree at this faculty and university;
2. No part of this thesis has previously been submitted for a degree or any other qualification at this university or any other institution;
3. Where I have consulted the published work of others or myself, this is always clearly attributed;
4. Where I have quoted from the work of others or myself, the source is always given. This thesis is entirely my own work, with the exception of such quotations;
5. I have acknowledged all major sources of assistance;
6. Where the thesis is based on work done by myself jointly with others, I have made clear exactly what was done by others and what I have contributed myself;
7. The research carried out during this thesis and described in this work has led to several scientific publications, listed on the following page.

Date Signature

List of Publications

This thesis is based on some of the research I carried out during my doctoral studies at the Institute for Theoretical Particle Physics and Cosmology at the RWTH Aachen University. This research led to several scientific publications, which are referred to by their Roman numerals in the text:

I Planck Collaboration: Akrami, Y. et al. *"Planck 2018 results. X. Constraints on inflation"*, **Accepted by A&A (2019)**, arXiv:1807.06211, [1] (See Appendix A)

II T. Brinckmann, D.C. Hooper, M. Archidiacono, J. Lesgourgues, T. Sprenger *"The promising future of a robust cosmological neutrino mass measurement"*, JCAP **1901** (2019) 059, arXiv:1808.05955, [2] (See section 6.3.)

III M. Archidiacono, D.C. Hooper, R. Murgia, S. Bohr, J. Lesgourgues, M. Viel *"Constraining Dark Matter - Dark Radiation interactions with CMB, BAO, and Lyman-α"*, **Submitted to JCAP (2019)**, arXiv:1907.01496, [3] (See sections 4.3 and 7.1.)

IV D.C. Hooper, M. Archidiacono, J. Lesgourgues, R. Murgia, N. Schöneberg, M. Viel *"Novel constraints on Dark Matter - baryon scattering from Lyman-α data"*, **In Prep (2019)**, arXiv:1911.XXXXX (See sections 4.3 and 7.2.)

V M. Lucca, N. Schöneberg, D.C. Hooper, J. Lesgourgues, J. Chluba *"The synergy between CMB spectral distortions and anisotropies"*, **In Prep (2019)**, arXiv:1909.XXXXX (See section 4.4.)

Not discussed in this thesis:

- N. Schöneberg, J. Lesgourgues, D.C. Hooper *"The BAO+BBN take on the Hubble tension"*, **Submitted to JCAP (2019)**, arXiv:1907.11594, [4]

Contents

Abstract iii

Zusammenfassung v

Acknowledgements vii

Declaration of Authorship ix

List of Publications x

General Overview 1

I Introduction to Particle Cosmology 3

1 Standard Models in Cosmology and Particle Physics 5
1.1 Cosmological Principle . . . 5
1.2 Expansion . . . 6
1.3 Einstein Field Equations . . . 8
1.4 Friedmann-Lemaître-Robertson-Walker Metric . . . 10
1.5 Dynamics of the Expanding Universe . . . 13
1.6 Components of the Universe . . . 16
1.7 Standard Model of Particle Physics . . . 19
1.8 Thermal History . . . 21
1.8.1 Phase-space Distribution and Equilibrium . . . 21
1.8.2 Freeze-out and Decoupling . . . 23
1.8.3 Brief History of The Universe . . . 25
1.9 A Closer Look at Cold Dark Matter . . . 27
1.9.1 Evidence for Dark Matter . . . 27
1.9.2 Standard Properties of Dark Matter . . . 31

2 Inflation 35
2.1 Motivations . . . 35
2.1.1 Horizon Problem . . . 36
2.1.2 Flatness Problem . . . 37
2.1.3 Monopole Problem . . . 38
2.1.4 Origin of CMB Fluctuations . . . 39
2.2 Scalar Field Inflation . . . 40
2.3 Slow-Roll Inflation . . . 42
2.4 Cosmological Parameters Obtained with Slow-Roll Inflation . . . 43

3 Perturbed Cosmology 47
3.1 Linear Perturbation Theory . . . 47
3.2 Boltzmann Equations . . . 51

3.3 Initial Conditions from Inflation . . . 56
3.4 Power Spectra and Transfer Functions . . . 58
3.5 From Perturbations to Temperature Anisotropies . . . 59

II Observing the Universe **67**

4 Cosmological Observables **69**
4.1 Cosmic Microwave Background . . . 69
4.2 Matter Power Spectrum . . . 73
4.3 Lyman-α Forest . . . 77
4.4 Spectral Distortions . . . 82

5 Problems in Cosmology **89**
5.1 Small Scale Crisis . . . 89
5.2 Hubble Constant Tension . . . 94
5.3 σ_8 Tension . . . 98

III Massive Relics in the Universe **101**

6 Neutrino Mass Constraints **103**
6.1 Neutrinos in Particle Physics . . . 103
6.2 Cosmological Implications of Massive Neutrinos . . . 106
6.3 Neutrino Mass Forecast . . . 109
6.3.1 Pipeline . . . 110
6.3.2 Results . . . 115
6.3.3 Conclusions . . . 119

7 Dark Matter Paradigm Revisited **121**
7.1 Dark Matter Interacting with Dark Radiation . . . 121
7.1.1 Formalism . . . 122
7.1.2 Effects on Observables . . . 125
7.1.3 Methodology . . . 129
7.1.4 Results . . . 130
7.1.5 Conclusions . . . 145
7.2 Dark Matter Interacting with Baryons . . . 147
7.2.1 Formalism . . . 148
7.2.2 Effects on Observables . . . 150
7.2.3 Methodology . . . 155
7.2.4 Results . . . 156
7.2.5 Conclusions . . . 157

General Conclusions **159**

A Inflation Potential Reconstruction **161**

Bibliography **169**

Dedicated to all the sanity I lost along the way.

General Overview

So here I am, at the beginning. Staring at a blank document, wondering how to write a thesis. How can I describe cosmology? How can I do justice to such a vast and incredible topic? How do I describe everything I have done these last three years? Where do I start? I guess I will start at the beginning...

Humans are a curious species. Humankind has always been driven to know more about the world around us. To understand more. Throughout our history, one of the biggest questions, perhaps the oldest question, that has driven humankind is "What is out there?". Answering this question is not easy, and yet, in its essence, this is what cosmology tries to do.

Cosmology is the discipline of theoretical physics and astronomy that studies the current content and behaviour of the universe, what has led to this state, and what we can expect to happen to it in the future. But cosmology is not an independent science: it calls on particle physics, astrophysics, astronomy, and many other physical disciplines to be able to explain the different phenomena taking place around us.

The history of cosmology is very rich, with the oldest recorded cosmological ideas dating back to $\sim 3000\,\mathrm{BC}$. Since then there have been countless great contributors to cosmology (with varying levels of recognition) like Aristarchus first proposing the heliocentric model, Galileo perfecting the telescope, Newton first describing gravity, Einstein shaping the way we understand the geometry of the universe, and Hubble measuring the expansion of the universe. All of them with dreams of understanding the universe we live in.

In the last century cosmology has made significant progress, both theoretically and technologically, and we are now closer than ever to turning that dream into a reality. We now have an unprecedented level of understanding of the universe; we are the first generation of humans to know with percent-precision the composition, geometry, and structure of the universe. Cosmology has come a long way in the last few decades; we stand on the shoulders of giants to see further than those before us, yet we are still laying the foundation for those to come.

As is often the case, the more we learn, the more we realise we have yet to understand. We now know the composition of our universe, and we know that we only understand $5\,\%$ of it. We know that there was an asymmetry between matter and antimatter in the early universe, but we do not know what caused it. We know that neutrinos have mass, and yet we have not been able to measure their mass. We know that we can understand the observational data better if we include a species of matter that only interacts gravitationally, but we have not yet been able to find this dark matter in any of our searches.

One problem with cosmology is that we only have one universe, which is statistically inconvenient. We are not able to repeat the experiment to see if the universe turns out the same way. But the universe contains phenomena across many different scales: from particle interactions keeping different components in equilibrium, to the formation and evolution of clusters of galaxies. We need to be able to extract as much information as possible from all these data sets. We might only have one universe, but we have a lot of different ways of observing it.

In this thesis I focus on two main topics: measuring neutrino mass with cosmology and studying possible interactions between dark matter and other species. To see which combination of missions we need to measure the neutrino mass, I perform forecasts for future cosmic microwave background (CMB) and large scale structure experiments. To study dark matter interactions, I combine existing data from the CMB and from structure formation, using a newly-developed technique to take advantage of the full Lyman-α Forest. Additionally, I present a new method that shows the synergy between spectral distortion missions and other cosmological probes, which will help us constrain these interactions even more in the future.

This thesis is composed of three main parts: in the first part I will introduce the current state of theoretical cosmology, in the second part I will discuss how we can observe the universe, and in the third part I will present new constraints on massive relics in the universe. In chapter 1 I will introduce the standard models of both cosmology and particle physics, while in chapter 2 I will discuss the early phase of inflation. In chapter 3 I will delve into perturbation theory, which will allow us to understand structures in the universe. In chapter 4 I will discuss current observables of the universe, as well presenting techniques developed in the course of this research to extract more information from the Lyman-α Forest and from spectral distortions of the CMB. In chapter 5 I will show the main problems in our current cosmological model, and thus justify the need to look beyond. In chapter 6 I will discuss neutrinos, and show how feasible it is going to be to measure the sum of neutrino masses in the next decade. Finally, in chapter 7 I will revisit the dark matter paradigm, introducing two interacting dark matter models, and using several different probes to derive state-of-the-art constraints on these possible interactions.

Remarks on Notations

Throughout this thesis, unless stated otherwise, I will work in natural units: with $\hbar = c = 1$. Furthermore, when discussing general relativity I will use the metric signature $(- + ++)$, as well as using the Einstein summation convention, where repeated indices are automatically summed over. Regarding derivatives, primes will denote time derivatives, $x' = \frac{dx}{dt}$, while over-dots will denote derivatives with respect to conformal time, $\dot{x} = \frac{dx}{d\tau}$. Other derivatives will be explicitly stated. Finally, vector quantities will be indicated with bold font: $\boldsymbol{x}$.

Footnotes

The footnotes in this thesis do not follow the same level of formality as the rest of the manuscript. Some of the footnotes contain useful or informative remarks. Most of them, though, are more a reflection of my thought process while writing. They are not meant to be taken too seriously.

Part I

Introduction to Particle Cosmology

1 Standard Models in Cosmology and Particle Physics

A good cosmological model should be able to explain all the observational data we have detailing the current state of the universe as well as its history and evolution leading to this point. We have data spanning many scales and epochs of the universe: from the Cosmic Microwave Background (CMB) temperature anisotropies produced in the early universe, to the current large scale distribution of galaxies around us. The great challenge for any cosmological model is to be able to accommodate all of this.

The current paradigm that can best accomplish this is the Hot Big Bang model (HBB), in which the universe is homogeneous, isotropic, flat, and expanding. Within this framework, we can explain the evolution of the universe with the Friedmann equations, which can be derived from Einstein's General Relativity (GR). Furthermore, the current components of the universe are well-described by the ΛCDM model: the universe is mainly dominated by dark energy (Λ) and Cold Dark Matter (CDM). Together with an early period of Inflation (explained in chapter 2), the HBB model is able to describe the universe around us to incredible precision, and is thus the current Standard Cosmological Model.

In this chapter I will discuss the elements of this model and how they all fit together. Additionally, the Standard Model of Particle Physics will be introduced, as well as its connections to cosmology. This recap is based on references [5]–[8] and references therein.

1.1 Cosmological Principle

One of the cornerstones of modern cosmology is the cosmological principle, which states that when viewed on sufficiently large scales, the properties of the universe are the same for all observers. This assumption, initially proposed in 1930 by Milne, has several implications. On the one hand it implies that the observer does not occupy a privileged position in the universe: our observable universe is not special and should represent a fair sampling[1]. On the other hand, the cosmological principle leads to two properties of the universe: on large scales the universe is *homogeneous* and *isotropic*, which means that the universe should look the same in every direction from wherever you look.

[1] To be precise, the *observable universe* denotes the maximum part of the *universe* we would theoretically be able to see given infinite precision. However, as that is indeed the only part of the universe we can talk about, from here onwards the two terms will be used interchangeably.

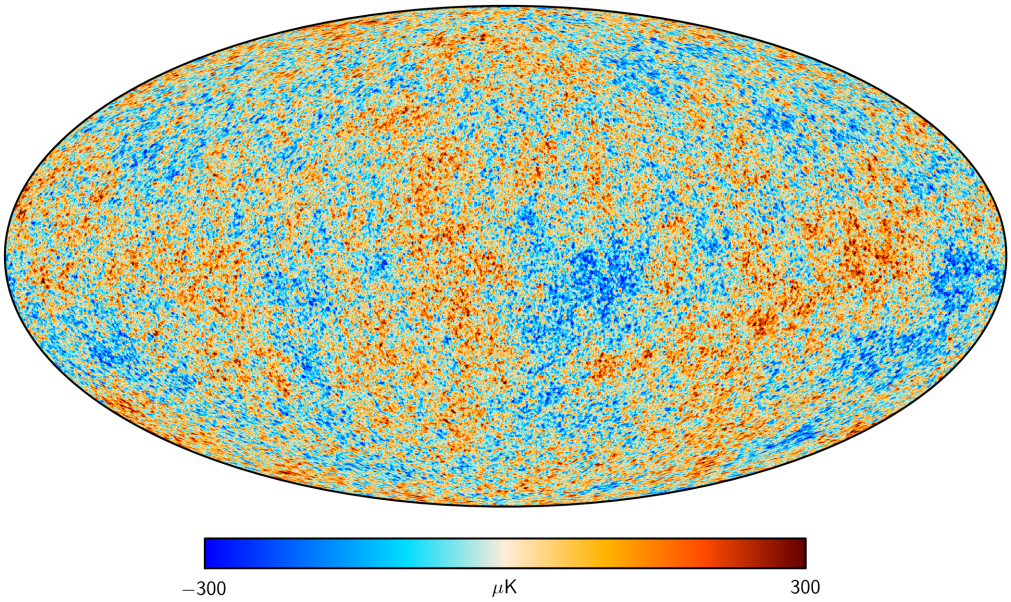

FIGURE 1.1: CMB anisotropies as measured by the ESA satellite Planck in 2015. Image taken from the ESA website: https://www.cosmos.esa.int.

The isotropy of the universe is well supported by observational evidence, for example of the CMB [9]–[11], which only shows temperature anisotropies on the level of $\Delta T/T \sim 10^{-5}$, as seen in Fig. 1.1. The homogeneity of the universe is obviously not true on small scales, as a clustering of galaxies is very different to a cosmic void. Indeed, the homogeneity comes about only after smoothing over some characteristic scale. However, when viewed on larger scales, the homogeneity is supported by the overall distribution of galaxies in the universe, as seen in Fig. 1.2, and indeed from the CMB itself, as discussed in section 4.1.

Given the overall homogeneity of the universe, for the remainder of this chapter I will focus on homogeneous cosmology. Nonetheless, to understand the origin of both the CMB anisotropies, however small, and the density fluctuations seeding the formation and clustering of galaxies, we will need to move beyond homogeneity into perturbed cosmology, which will be the subject of chapter 3.

1.2 Expansion

While the universe is homogeneous and isotropic in space, it is not so in time, and in fact it has experienced several different epochs throughout its history, described in section 1.8. However, the universe has always been expanding: spacetime is stretching and thus the distance between all objects (except those that are gravitationally bound) is increasing.

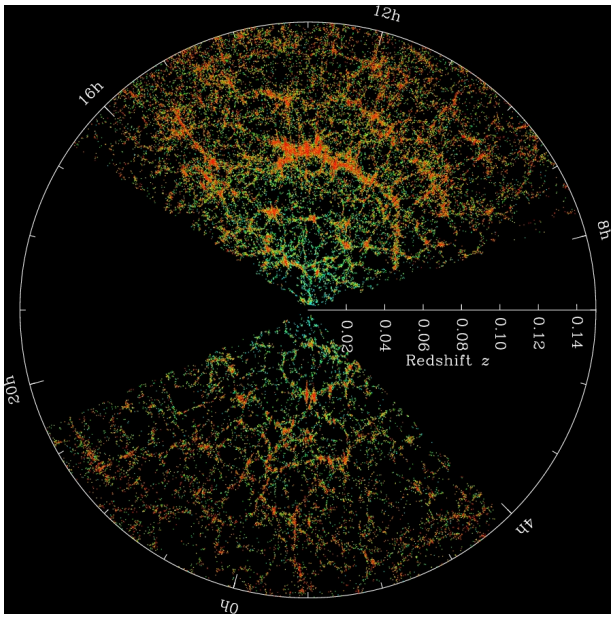

FIGURE 1.2: Distribution of galaxies in the local neighbourhood as seen by SDSS. Each dot represents a galaxy, with the colour bar showing the local density. Image taken from the SDSS website: http://www.sdss.org.

Since the nineteenth century it has been known that objects in motion appear redshifted to observers due to a Doppler shift. This redshift is described by:

$$z \equiv \frac{\Delta\lambda}{\lambda} = \frac{v_r}{c}\,, \tag{1.1}$$

where v_r is the the projection of star velocities along the line-of-sight and c is the speed of light.

In 1920 Leavitt and Sharpley pioneered the measurement of stellar distances with the period-luminosity relationship for Cepheid-type stars [12], and in 1923 Hubble was able to make the first observations of individual stars in distance galaxies [13]. Together with the observation that most of the galaxies Hubble could observe were redshifted, this provided the first indication that the universe is expanding.

However, the expansion of the universe was in apparent contradiction with the Cosmological Principle: in order to maintain homogeneity, the velocity of galaxies along a line-of-sight, and therefore their redshift, should be proportional to their distance:

$$\vec{v} = H\boldsymbol{r}\,, \tag{1.2}$$

where $\boldsymbol{v}$ is the velocity of an object at position $\boldsymbol{r}$, and H is a proportionality constant. In 1929 Hubble was able to confirm this relation experimentally [14], and found that the universe is undergoing homogeneous expansion. The proportionality constant is now known as the Hubble constant.

Since this time, we have been able to get increasingly more precise observations of receding

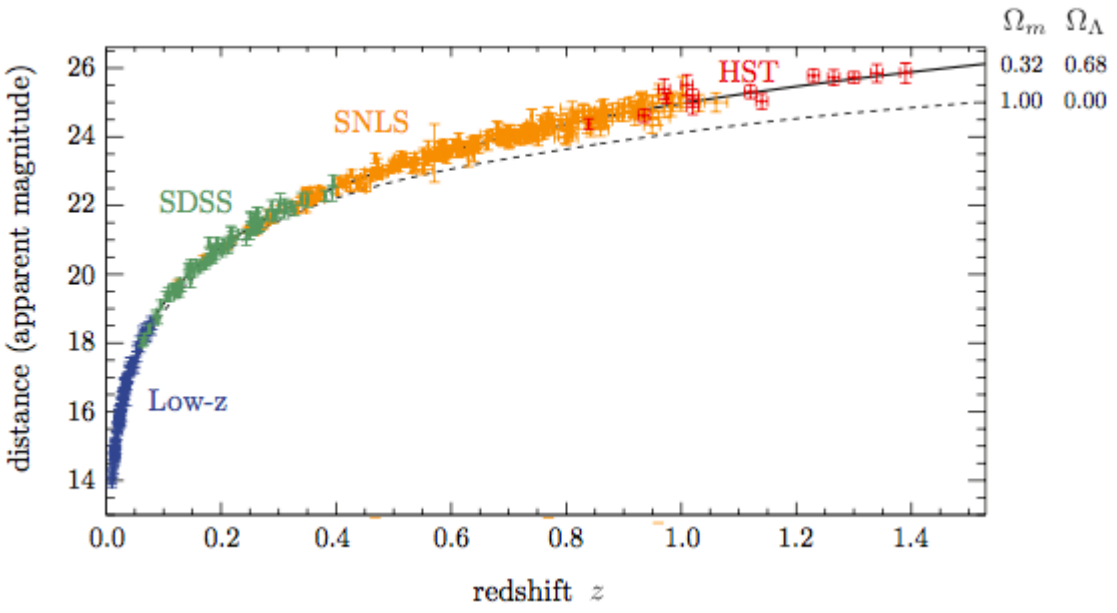

FIGURE 1.3: Hubble Diagram showing the apparent luminosity as a function of redshift of standard candles in local galaxies. Image taken from [15].

galaxies using supernovae, Cepheids, and other standard candles[2]. Fig. 1.3 shows the current Hubble Diagram, with data coming from several different experiments. While the proportionality is clear, the value of the Hubble constant today[3], denoted by H_0, is a matter of ongoing debate and is the topic of section 5.2. The Hubble constant is often parametrised by

$$h = \frac{H_0}{100 \text{ km/s Mpc}^{-1}} \,. \tag{1.3}$$

In recent decades it has been shown that the expansion of the universe is accelerating. This was first measured in 1989 by two independent groups using supernovae Type Ia [16], [17], a discovery which would go on to receive the Nobel Prize in Physics in 2011, and has since been supported by other measurements such as Baryon Acoustic Oscillations and galaxy clustering (described in chapter 4.2). This also leads to the relation defined in equation 1.2 only being valid for small redshifts; the Hubble Law breaks down for $z \gtrsim 1$. For galaxies close by, however, it remains a valid description.

1.3 Einstein Field Equations

In 1915 Albert Einstein revolutionised the way we look at the universe with General Relativity [18], a theory in which gravity is described as a geometric property of spacetime. Gravity is no longer treated as a conventional force, but rather caused by the curvature of spacetime,

[2] A standard candle is any object whose absolute magnitude can be calculated without knowing their distance.
[3] Despite the name, the Hubble constant is only constant in space, not in time.

which is directly related to the energy and momentum of the contained matter. This is often elegantly phrased as "mass tells spacetime how to curve, and spacetime tells mass how to move". The relation between the matter-energy content at a given point $x^\mu = (ct, x^i)$ and the resulting curvature of spacetime at the same point is given by the Einstein Equations, but to understand them we need some basic notions of GR.

An invariant spacetime interval ds^2 can be related to the coordinate dx^μ via the metric tensor $g_{\mu\nu}$ [4]

$$ds^2 = g_{\mu\nu} dx^\mu dx^\nu \,, \tag{1.4}$$

where repeated indices are summed over. To locally recover Lorentz invariance and special relativity, this metric must have a negative signature, for which the $(-+++)$ sign convention will be used[5].

The metric and its derivatives allow us to define the Christoffel symbols

$$\Gamma^\alpha_{\mu\nu} = \frac{1}{2} g^{\alpha\beta} \left(g_{\mu\beta,\nu} + g_{\beta\nu,\mu} - g_{\mu\nu,\beta} \right) \,, \tag{1.5}$$

where the commas represent derivatives with respect to the following index, $g_{\mu\nu,\alpha} = \partial_\alpha g_{\mu\nu}$.

With the Christoffel symbols we can introduce the *Ricci tensor*, which will be used to determine the degree to which matter will tend to converge (or diverge) in time. It is defined as

$$R_{\mu\nu} = \Gamma^\alpha_{\mu\nu,\alpha} - \Gamma^\alpha_{\mu\alpha,\nu} + \Gamma^\alpha_{\beta\alpha}\Gamma^\beta_{\mu\nu} - \Gamma^\alpha_{\beta\nu}\Gamma^\beta_{\mu\alpha} \,, \tag{1.6}$$

which is often contracted with the metric to lead to the *Ricci scalar*: $\mathcal{R} \equiv g^{\mu\nu} R_{\mu\nu}$.

Finally, we can relate the curvature of spacetime to the energy-matter content, parametrised by the *stress-energy tensor* $T_{\mu\nu}$, by using the ten coupled differential equations known as the Einstein Field Equations:

$$R_{\mu\nu} - \frac{1}{2}\mathcal{R} g_{\mu\nu} + \Lambda g_{\mu\nu} = \frac{8\pi G T_{\mu\nu}}{c^4} \,. \tag{1.7}$$

Here I introduced the cosmological constant, Λ, which will be discussed in depth in section 1.5.

Equation 1.7 can be written more succinctly by introducing the Einstein Tensor $G_{\mu\nu}$ and by using the standard convention of $c = \hbar = 1$, which leads to

$$G_{\mu\nu} + \Lambda g_{\mu\nu} = 8\pi G T_{\mu\nu} \,. \tag{1.8}$$

The stress-energy tensor will be revisited in section 1.5, together with the implications of the Einstein Equations on the dynamics of the universe.

[4] Throughout this thesis, Greek indices will take values 0, 1, 2, 3, and will indicate time and space components, while Latin indices will take values 1, 2, 3, and will indicate space coordinates only.

[5] This is a matter of preference, one could equally use a $(+---)$ convention, but I like the convention with more positives.

1.4 Friedmann-Lemaître-Robertson-Walker Metric

Under the assumption of a homogeneous and isotropic universe, the most general solution to equations 1.8 is the Friedmann-Lemaître-Robertson-Walker metric (FLRW). To derive the FLRW metric, we start with the general form of the spacetime metric, with the same sign convention as in the previous section

$$ds^2 = -c^2dt^2 + g_{ij}dx^i dx^j \,. \tag{1.9}$$

To preserve homogeneity and isotropy, the curvature of the universe should be the same everywhere. The only three-dimensional spaces with constant curvature are flat Euclidean space, a 3-sphere, or a 3-hyporboid. The most general spatial line element in these spaces can be written in polar coordinates as

$$dl^2 = \left[\frac{dr^2}{1-kr^2} + r^2\left(d\theta^2 + \sin^2\theta d\phi\right)\right] , \tag{1.10}$$

where k is a constant related to the spatial curvature: a flat Euclidean universe will have $k = 0$; a positively curved and closed universe will have $k > 0$; and a negatively curved and open universe is given by $k < 0$.

Inserting the line element, equation 1.10, into the metric in equation 1.9 gives us

$$ds^2 = -c^2dt^2 + \left[\frac{dr^2}{1-kr^2} + r^2\left(d\theta^2 + \sin^2\theta d\phi\right)\right] , \tag{1.11}$$

which describes an isotropic and *static* universe. However, as we want the universe to be homogeneous and isotropic at any time, we introduce the *scale factor* $a(t)$, which leads to the FLRW metric

$$ds^2 = -c^2dt^2 + a^2(t)\left[\frac{dr^2}{1-kr^2} + r^2\left(d\theta^2 + \sin^2\theta d\phi\right)\right] . \tag{1.12}$$

With the newly-introduced scale factor, we can revisit our definition of redshift: the wavelength of a photon emitted by a moving object is also going to be subject to the expansion of spacetime. As such, in an FLRW universe, we can write the redshift due to the expansion as

$$z = \frac{\Delta\lambda}{\lambda} = \frac{\lambda_r - \lambda_e}{\lambda_e} = \frac{a(t_r)}{a(t_e)} - 1 \,. \tag{1.13}$$

Therefore, if we observe an object today at time t_0, the redshift on its absorption lines will be

$$z = \frac{a(t_0)}{a(t_e)} - 1 \,, \tag{1.14}$$

where, by convention, we normalise the scale factor today such that $a(t_0) = 1$.

Similarly, we can use the scale factor to define the time-dependent Hubble parameter introduced in equation 1.2 as

$$H(t) = \frac{a'(t)}{a(t)}\,, \tag{1.15}$$

where the prime denotes the derivative with respect to the proper time t.

Finally, we can introduce the *conformal time*, which will be significant when defining distances in the universe, as

$$\tau = \int \frac{dt}{a(t)}\,. \tag{1.16}$$

Derivatives with respect to conformal time will be denoted with an overdot. The introduction of conformal time allows us to rewrite the FLRW metric in its most usual form as

$$ds^2 = a^2(\tau)\left(-c^2 d\tau^2 + \left[\frac{dr^2}{1-kr^2} + r^2\left(d\theta^2 + \sin^2\theta d\phi\right)\right]\right)\,. \tag{1.17}$$

Having derived the metric of our universe, the next important step is to discuss the distance to moving objects: in an expanding universe, the notion of distance is not as clearly-defined as we are used to. The first distance we will discuss is the *comoving distance*. Assuming that we are located at the origin of spherical coordinates at time t_0, and we observe photons coming from a comoving object located at $(t_e, r_e, \theta_e, \phi_e)$, the comoving distance travelled by the photons, which will remain constant in an expanding universe, will be

$$\chi(r) \equiv \int_0^{r_e} \frac{dr}{\sqrt{1-kr^2}}\,, \tag{1.18}$$

which integrates to

$$\chi(r) = \begin{cases} \sin^{-1}(r) & \text{if } k = 1\,, \\ r & \text{if } k = 0\,, \\ \sinh^{-1}(r) & \text{if } k = -1\,. \end{cases} \tag{1.19}$$

Photons in a vacuum will have $dl = cdt$, and thus $ds^2 = 0$, which we can use together with the definition of comoving distance, equation 1.18, to find

$$\chi(t) = \int_{t_e}^{t_0} \frac{dt}{a(t)}\,. \tag{1.20}$$

This allows us to give a deeper meaning to conformal time: the conformal time is equal to the comoving distance travelled by a light signal divided by c, which for $c = a(t_0) = 1$ can be expressed in physical units. Furthermore, we can expand equation 1.20 to find the useful relation

$$\chi(t) = \int_{t_e}^{t_0} \frac{dt}{a(t)} = \int_{a(t_0)}^{a(t_e)} \frac{da}{a^2 H(a)} = \int_0^{z(t_e)} \frac{dz}{H(z)}\,. \tag{1.21}$$

In the following section we will relate the evolution of the Hubble parameter with respect to redshift, $H(z)$, to the matter content of the universe, which will be very useful when discussing the value of the H_0 in section 5.2.

The second important distance to discuss is the *angular diameter distance*. There are some objects in the universe, known as standard rulers, whose size can either be computed from first principles or from the physical properties of the object. An example of this is the typical size of the CMB fluctuations, known as the sound horizon at decoupling, which will be explored in section 3.5. Given an object of size D, its angular diameter distance is

$$d_A \equiv \frac{D}{\delta\theta}\,, \tag{1.22}$$

with the assumption that the angular size $\delta\theta$ fulfils the condition $\delta\theta \ll 1$. The angular diameter distance can be related to the comoving distance with

$$d_A = a(t_e)r_e = a(t_0)\frac{r_e}{1+z_e} = \frac{\chi(z)}{(1+z)}\,. \tag{1.23}$$

Finally, we can introduce the third cosmological distance: the *luminosity distance*. In section 1.2 I already introduced standard candles: objects for which the total flux of energy emitted over time (the absolute luminosity) can be calculated by knowing some physical properties of the object, independently of its distance or apparent luminosity. The apparent luminosity l of an object can be related to its absolute luminosity L by

$$l = \frac{L}{4\pi d^2}\,, \tag{1.24}$$

and as such, we can define the luminosity distance as

$$d_L \equiv \sqrt{\frac{L}{4\pi l}}\,. \tag{1.25}$$

We can relate the the luminosity distance to the comoving distance with

$$d_L = a(t_0)r_e(1+z_e) = \chi(z)(1+z)\,, \tag{1.26}$$

and finally we can use equations 1.23 and 1.26 to find the relation between the angular distance and the luminosity distance

$$d_L = (1+z_e)^2 d_A\,. \tag{1.27}$$

The Hubble diagram in Fig. 1.3 shows the luminosity distance as a function of redshift for many nearby standard candles.

1.5 Dynamics of the Expanding Universe

In order to describe the dynamics of particles in the universe, we first need to know how these particles move. Any free-falling particle in an FLRW universe will follow a trajectory parametrised by $x^\mu(\lambda)$, which is given by the geodesic equation

$$\frac{d^2x^\alpha}{d\lambda^2} + \Gamma^\alpha_{\mu\nu}\frac{dx^\mu}{d\lambda}\frac{dx^\nu}{d\lambda} = 0\,, \tag{1.28}$$

where λ is a parameter that increases monotonically along the trajectory. We can now introduce the momentum 4-vector as

$$P^\mu = m\frac{dx^\mu}{d\lambda}\,, \tag{1.29}$$

where λ is normalised in a way to satisfy everywhere the on-shell condition

$$g_{\mu\nu}P^\mu P^\nu = -m^2\,. \tag{1.30}$$

Combined with the geodesic equation, this leads us to the physical energy and physical momentum measured by comoving observers:

$$E = P^0 \qquad p^i = aP^i\,, \tag{1.31}$$

which allow us to say that in an FLRW universe, the physical momentum scales like a^{-1}, and the on-shell condition gives us $E = \sqrt{m^2 + p^2}$.

In the previous sections we discussed the metric contributions to the Einstein Equations (equation 1.8), so now we can shift our focus to the right-hand side: the energy-momentum tensor[6]. In a homogeneous and isotropic universe, the most general stress-energy tensor takes the form

$$T^\mu_\nu = \begin{pmatrix} -\rho & 0 & 0 & 0 \\ 0 & p & 0 & 0 \\ 0 & 0 & p & 0 \\ 0 & 0 & 0 & p \end{pmatrix}\,, \tag{1.32}$$

where ρ is the energy density and p the pressure of the cosmological fluid.

If we consider now the (00) component of equation 1.8, on the left-hand side we have

$$G_{00} = 3\left[\frac{k}{a^2} + \left(\frac{a'}{a}\right)^2\right]\,, \tag{1.33}$$

where for now I am ignoring the contribution coming from the cosmological constant, and I have introduced the shorthand notation $a(t) = a$.

[6]This is also called the stress-energy tensor. I will use both terms interchangeably depending on my own stress levels.

Combining equations 1.32 and 1.33, we find

$$3\left[\frac{k}{a^2}+\left(\frac{a'}{a}\right)^2\right]=8\pi G\rho\,, \tag{1.34}$$

which is often expressed as

$$H^2=\left(\frac{a'}{a}\right)^2=\frac{8\pi G}{3}\rho-\frac{k}{a^2}\,. \tag{1.35}$$

The above equation is known as the First Friedmann Equation, or Friedmann Law.

Before coming to the Second Friedmann Equation, we need to review energy conservation in an expanding universe. The Einstein Equations seen in equation 1.8 necessarily imply Bianchi identities, such that

$$G^{\nu}_{\mu;\nu}=T^{\nu}_{\mu;\nu}=0\,, \tag{1.36}$$

where ; indicates the contravariant derivative. The first Bianchi identity ($T^{\nu}_{0;\nu}=0$) is an energy conservation equation. Using the energy-momentum tensor in an FLRW universe, this becomes

$$\rho'=-3\frac{a'}{a}(\rho+p)\,. \tag{1.37}$$

The above expression implies that the dilution of the energy ρ due to the expansion of the universe depends on the pressure of the system, and as such, on the equation of state. Assuming a perfect cosmological fluid, our equation of state becomes

$$p=w\rho\,, \tag{1.38}$$

where w is a constant dependent on the properties of the individual fluid. By combining the equation of state with equation 1.37, we find

$$\rho\propto a^{-3(1+w)}\,. \tag{1.39}$$

In the case of relativistic matter (often called radiation), such as photons or neutrinos in the early universe, $w=1/3$ and equation 1.38 becomes $p=\frac{1}{3}\rho$, leading to

$$\rho'=-3\frac{a'}{a}(1+\frac{q}{3})\rho=-4\frac{a'}{a}\rho\quad\Rightarrow\quad\rho\propto a^{-4}\,. \tag{1.40}$$

On the other hand, non-relativistic matter such as baryons and cold dark matter (often simply called matter) have negligible pressure, leading to $w=0$ and

$$\rho'=-3\frac{a'}{a}\rho\quad\Rightarrow\quad\rho\propto a^{-3}\,, \tag{1.41}$$

implying that non-relativistic matter dilutes slower than relativistic matter in the universe.

Considering now the (ii) components of equation 1.8, on the left-hand side we have

$$G_{ii} = \left[2\frac{a''}{a} + \left(\frac{a'}{a}\right)^2 + \frac{k}{a^2} \right] , \tag{1.42}$$

where I have once again ignored the contribution from the cosmological constant. Combining with the (ii) components of the stress-energy tensor (equation 1.32) leads to

$$2\frac{a''}{a} + \left(\frac{a'}{a}\right)^2 + \frac{k}{a^2} = -8\pi G p \, . \tag{1.43}$$

Finally, we can use the Friedmann Law in equation 1.35, together with the energy conservation equation 1.37, to rewrite the above expression as

$$\frac{a''}{a} = -\frac{4\pi G}{3} \left(\rho + 3p\right) , \tag{1.44}$$

which is the second Friedmann equation.

Until now I have ignored the cosmological constant Λ, but it plays a very important role in the current evolution of the universe. When Einstein initially proposed his now-famous equations, the expansion of the universe was not known. As such, a geometrical term $\Lambda g_{\mu\nu}$ was added to the left-hand side of equation 1.8. The parameter Λ should be a time-independent constant, and negative to account for a static universe.

Once the expansion of the universe had been found, the cosmological constant was removed from the equation. However, upon discovering the *accelerated expansion* of the universe this term was re-added. The cosmological constant is mathematically equivalent to a homogeneous fluid described by the stress-energy tensor

$$\tilde{T}^{\mu}_{\nu} = -\frac{\Lambda}{8\pi G} g^{\mu}_{\nu} = \begin{pmatrix} -\frac{\Lambda}{8\pi G} & 0 & 0 & 0 \\ 0 & -\frac{\Lambda}{8\pi G} & 0 & 0 \\ 0 & 0 & -\frac{\Lambda}{8\pi G} & 0 \\ 0 & 0 & 0 & -\frac{\Lambda}{8\pi G} \end{pmatrix} . \tag{1.45}$$

By comparing the above stress-energy tensor to the one of an ideal fluid presented in equation 1.32, we can see that the cosmological constant fluid behaves as an energy with $\rho = -p = \frac{\Lambda}{8\pi G}$, which naturally implies the time independence of Λ, and thus $\rho' = 0$.

Historically, this was interpreted as the vacuum energy, as predicted by quantum field theory. However, the vacuum energy density is off by about 120 orders of magnitude, and as such, is now considered a different type of energy. Today we refer to this as *dark energy*, and its true nature is one of the biggest unsolved mysteries in the field. Once we consider dark energy, the first Friedmann equation becomes

$$H^2 = \left(\frac{a'}{a}\right)^2 = \frac{8\pi G}{3}\rho - \frac{k}{a^2} + \frac{\Lambda}{3} , \tag{1.46}$$

and the second Friedmann equation is

$$\frac{a''}{a} = -\frac{4\pi G}{3}(\rho + 3p) + \frac{\Lambda}{3}\,. \tag{1.47}$$

Having derived the Friedmann equations, we are now ready to discuss the ingredients needed to build a universe that behaves like ours.

1.6 Components of the Universe

In the previous section, we already saw that matter (M) and radiation (R) behave differently in the universe: they have different pressure components, as well as a different scale factor dependence. As such, it is natural to separate them. Let us now rewrite the Friedmann law (equation 1.46) with all the contributions to the cosmological fluid:

$$H^2 = \left(\frac{a'}{a}\right)^2 = \frac{8\pi G}{3}\rho_R + \frac{8\pi G}{3}\rho_M - \frac{k}{a^2} + \frac{\Lambda}{3}\,. \tag{1.48}$$

We can now study how the universe would behave if only one of these contributions were present. In the case of radiation domination, we can use equation 1.40 to find

$$\left(\frac{a'}{a}\right)^2 \propto a^{-4}\,, \quad a(t) \propto t^{1/2}\,, \quad H(t) = \frac{1}{2t}\,. \tag{1.49}$$

Likewise for matter domination, we can use equation 1.41 to find

$$\left(\frac{a'}{a}\right)^2 \propto a^{-3}\,, \quad a(t) \propto t^{2/3}\,, \quad H(t) = \frac{2}{3t}\,. \tag{1.50}$$

In the case of curvature, we would find

$$\left(\frac{a'}{a}\right)^2 \propto a^{-2}\,, \quad a(t) \propto t\,, \quad H(t) = \frac{1}{t}\,, \tag{1.51}$$

where to fully understand the behaviour of such a universe we would further need to precise if we have positive or negative curvature.

Finally, in the case of a dark energy domination, we have

$$\left(\frac{a'}{a}\right)^2 \to \text{ constant}\,, \quad a(t) \propto e^{Ht}\,, \quad H = \sqrt{\frac{\Lambda}{3}}\,. \tag{1.52}$$

In all cases, we see that if we look further back in time, there is a point where $a \to 0$. This is known as the Big Bang[7]: the initial singularity, which can not be described by the same

[7]Despite what the name would have you believe, it was neither big nor a bang.

equations we use to describe the rest of the evolution of the universe. For times smaller than the Planck time, we would need a theory of quantum gravity, which is beyond the scope of this work.

We now see that the ordering of the terms in equation 1.48 was not arbitrary; the terms evolve with the scale factor as a^{-4}, a^{-3}, a^{-2}, and a^0. Therefore, if all terms contribute and the scale factor keeps growing throughout the history of the universe, they would dominate the expansion of the universe one after another.

Now that we have seen how the universe would evolve based on different components, we are interested in the behaviour of the universe today. We can evaluate the Friedmann equation 1.48 today to find

$$1 = \frac{8\pi G}{3H_0^2}\rho_{R_0} + \frac{8\pi G}{3H_0^2}\rho_{M_0} - \frac{k}{a_0^2 H_0^2} + \frac{\Lambda}{3H_0^2}\,, \tag{1.53}$$

where I have divided everything by H_0^2. By construction, these terms represent all contributions to the present composition of the universe. We can express the individual terms as

$$\begin{aligned} \Omega_{rad} &= \frac{8\pi G}{3H_0}\rho_{rad_0}\,, & \Omega_M &= \frac{8\pi G}{3H_0}\rho_{M_0}\,, \\ \Omega_{curv} &= -\frac{k}{a_0^2 H_0^2}\,, & \Omega_{rad} &= \frac{\Lambda}{3H_0^2}\,, \end{aligned} \tag{1.54}$$

which leads us to the *budget equation*

$$\Omega_R + \Omega_M + \Omega_k + \Omega_\Lambda = 1\,. \tag{1.55}$$

Furthermore, we can introduce the *critical density*, which is the density needed for a flat universe ($k = 0$),

$$\rho_c(t) = \frac{3H^2(t)}{8\pi G}\,, \tag{1.56}$$

which allows us to rewrite the budget equation today, in the case of a flat universe, as

$$\Omega_0 \equiv \Omega_R + \Omega_M + \Omega_\Lambda\,. \tag{1.57}$$

Finally, we can use the above expressions to find the Hubble parameter as a function of the components of the universe,

$$H^2(a) = H_0^2\left[\Omega_R a^{-4} + \Omega_M a^{-3} + \Omega_k a^{-2} + \Omega_\Lambda\right]\,, \tag{1.58}$$

or equivalently

$$H^2(z) = H_0^2\left[\Omega_R(1+z)^4 + \Omega_M(1+z)^3 + \Omega_k(1+z)^2 + \Omega_\Lambda\right]\,. \tag{1.59}$$

While Ω_x represents the relative abundance of a species x today, it is often more useful to express the physical density of each species as

$$\omega_x \equiv \Omega_x h^2 \,, \tag{1.60}$$

where h is the one first introduced in equation 1.3.

Based on current observations and the history of the universe, which will be discussed in the following section, we know that Ω_R has two main contributions: photons γ and neutrinos ν. In the ΛCDM model, Ω_M also has two main contributions: baryons and cold dark matter (CDM), which will be discussed in more details in section 1.9. Current measurements show [19]

$$\begin{aligned} \Omega_\Lambda &= 0.6889 \pm 0.0056 \,, & \Omega_M &= 0.31110 \pm 0.00561 \,, \\ \Omega_b &= 0.04897 \pm 0.00064 \,, & \Omega_{CDM} &= 0.2607 \pm 0.0035 \,, \\ \Omega_\gamma &\leq 5.38 \cdot 10^{-5} \,, & \Omega_\nu &\leq 0.016 \,, \\ \Omega_k &\leq 0.0026 \,, \end{aligned} \tag{1.61}$$

where we can see that the two main components are dark energy and cold dark matter. The curvature of the universe, on the other hand, is negligible, leading to a flat universe, see section 2.1.2 for further details.

Given the Friedmann equations and the budget equations, we do not need to measure all of the above parameters independently. In fact, we only need three of these, often chosen to be ω_b, ω_m, and Ω_Λ. These are three of the six parameters needed to fully define the ΛCDM universe. The missing parameters are τ_{reio} (discussed in section 1.8.3), and A_s and n_s (discussed in section 2.4).

Finally, as we know that the relative abundances of the species has changed with time, we can discuss two important times in the history of the universe: matter-radiation equality (z_{eq}), and matter-Λ equality (z_Λ). Matter-radiation equality took place at

$$\Omega_R h^2 a_{eq}^{-4} = \Omega_M h^2 a_{eq}^{-3} \Leftrightarrow a_{eq}^{-1} = \frac{\Omega_M}{\Omega_R} \Leftrightarrow 1 + z_{eq} \simeq 3440 \,, \tag{1.62}$$

and matter-Λ equality occurred around

$$\Omega_M h^2 a_\Lambda^{-3} = \Omega_\Lambda h^2 \Leftrightarrow a_\Lambda^{-1} = \left(\frac{\Omega_\Lambda}{\Omega_M}\right)^{1/3} \Leftrightarrow 1 + z_\Lambda \simeq 1.3 \,. \tag{1.63}$$

This allows us to define three main stages in the history of the universe: for early times with $z > z_{eq}$ the universe was in radiation domination, for $z_{eq} > z > z_\Lambda$ the universe was in matter domination, and at late times with $z < z_\Lambda$ the universe is in Λ domination. With this in mind, we are almost ready to discuss the thermal history of the universe, but first we need to review the behaviour of particles within the Standard Model of particle physics.

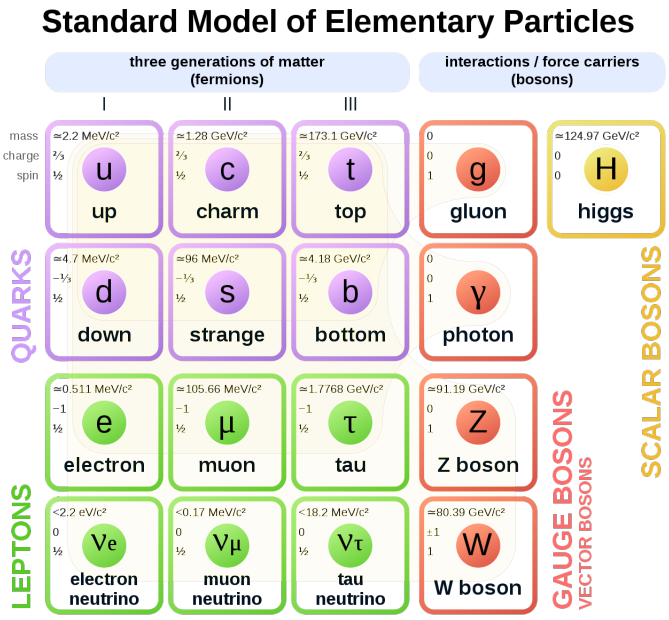

FIGURE 1.4: Sketch of the Standard Model of Particle Physics, showing the division into families and generations, as well as the main properties of each particle, such as the mass, spin, and charge.

1.7 Standard Model of Particle Physics

The Standard Model of Particle Physics is the current best description we have of the fundamental constituents and interactions of normal matter. It is a local (no instantaneous action at a distance) quantum field theory (the basic objects are quantum fields). The Standard Model describes several different fundamental particles and their interactions, summarised in Fig. 1.4. In this section I will very briefly review the main components needed to understand this model.

In a nutshell, the Standard Model describes fermions (matter particles), divided into *quarks* and *leptons*; and bosons, which will serve as mediators of gauge interactions (strong, weak, and electromagnetic interactions). Mathematically, the action of the Standard Model is built via a Lagrangian density $\mathcal{L}_{SM}$, with the requirement that the theory has to be renormalisable (predictive up to arbitrarily high energies). In its most simple form, the Standard Model Lagrangian is written as

$$\mathcal{L}_{\rm SM} = -\frac{1}{4}F_{\mu\nu}F^{\mu\nu} + i\bar{\Psi}\gamma^{\mu}D_{\mu}\Psi + (D_{\mu}\Phi)^{\dagger}D^{\mu}\Phi - V(\Phi) - (Y^{ij}\bar{\Psi}_i\Phi\Psi_j + h.c.)\,. \tag{1.64}$$

The first term of this Lagrangian represents the kinetic terms for the gauge fields, given by their field-strengths $F_{\mu\nu}$. The second term describes the fermions, denoted by Ψ. The third and fourth term are both related to the *Higgs boson*: the third term is the kinetic term for the *Higgs doublet* Φ, which includes its interactions with the gauge bosons, while the fourth

denotes the *Higgs potential*. Finally, the last term represents the Yukawa interactions. These different terms are discussed more in detail below.

The Standard Model is described by the non-abelian symmetry gauge group $G_{SM} = SU(3)_c \otimes SU(2)_L \otimes U(1)_Y$ (where C, L, and Y denote colour, left-handed chirality, and weak hypercharge). The six quark species, also known as flavours, are the only fermions that interact via strong interactions (mediated by the gluon g), so they transform non-trivially under $SU(3)_c$. Electromagnetism and weak interactions are described by the group $SU(2)_L \otimes U(1)_Y$ and their respective gauge couplings. Furthermore, empirical observations show that parity is violated in weak interactions, meaning that all known fermions are chiral fields, with the left-handed partners arranged in doublets (meaning they are charged under $SU(2)_L$), while their right-handed partners are only charged under $U(1)_Y$.

The Yukawa interaction term in equation 1.64 couples the left-handed fermion doublets with the right-handed fermion singlets through the Higgs doublet. At the electroweak scale the symmetry group $SU(2)_L \otimes U(1)_Y$ is spontaneously broken down to the $U(1)_{em}$ subgroup. This symmetry breaking will lead to a massless vector boson (the photon γ) and three massive vector bosons (W^+, W^-, and Z). As such, three out of the four degrees of freedom of the complex Higgs doublet are absorbed to create the massive bosons, with the final degree of freedom being the Higgs boson itself. This is known as the Higgs mechanism and it would require a lot more details to do it full justice; however, I will not go more into detail here.

We can also classify species in terms of electric charge, where leptons (the fermions not charged under $SU(3)_c$) can be charged (electron, muon, tau) or neutral (neutrinos). Additionally, upon electroweak symmetry breaking, the Yukawa interaction term gives mass to the charged leptons and quarks. Importantly, neutrinos have no right-handed component within the Standard Model, and as such, they can not gain mass with the same mechanism as other leptons. Therefore, in the Standard Model neutrinos are massless particles that only interact via weak interactions, making them profoundly difficult to detect. This will be revisited in section 6.1.

Additionally, we can arrange all of the matter content of the Standard Model in three families (or generations), each containing a quark doublet, a lepton doublet, two quark singlets and one lepton singlet. These families are mainly distinguished from one another by their mass. Finally, every particle described here has an antiparticle of the same mass and opposite quantum numbers[8].

To summarise, the Standard Model of particle physics describes the following particles:

1. Electrically charged leptons (electron e, muon μ, and tau τ), which can interact via the electromagnetic and weak forces.
2. Neutral, massless leptons (electron neutrino ν_e, muon neutrino ν_μ, and tau neutrino ν_τ), which can interact via the weak force.
3. Quarks (up u, down d, strange s, charm c, bottom b, and top t), which interact via strong, weak, and electromagnetic forces.

[8]The topic of neutrino antiparticles will also be revisited in section 6.1.

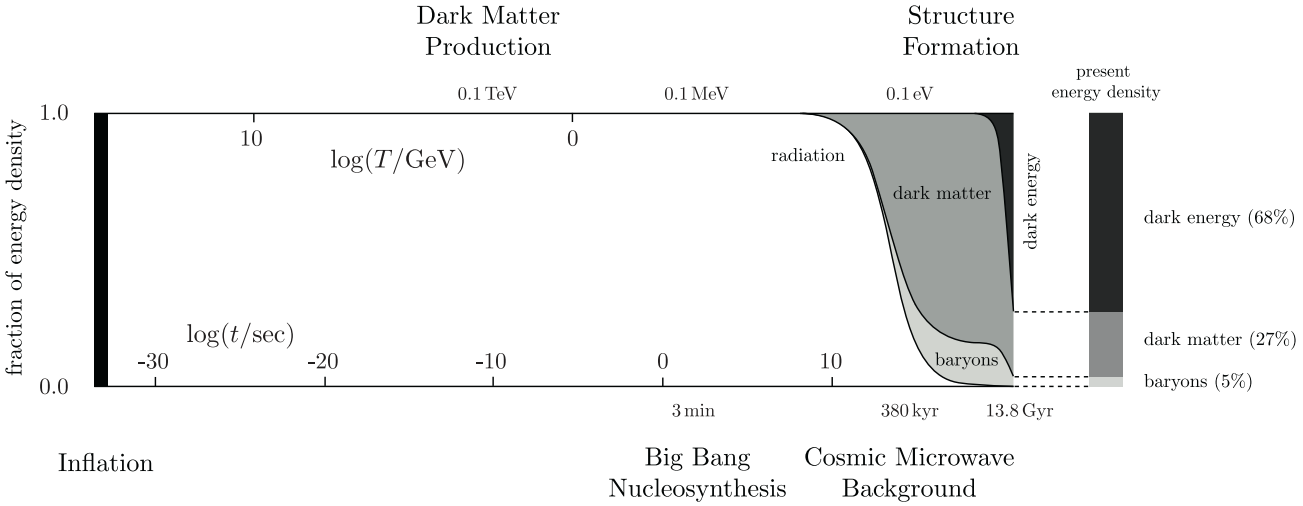

FIGURE 1.5: Sketch of the history of the universe from the time of the Big Bang until today. Image taken from [7].

4. Massless gauge bosons, which mediate the electromagnetic force (photon γ) and strong force (gluon g).
5. Massive vector bosons ($W^{\pm}$ and Z boson), which mediate the weak interaction.
6. Higgs boson h. The Higgs boson interacts with all massive particles, including itself.

Now that we have seen the overall behaviour of the building blocks of *normal matter*[9], we are ready to discuss the thermal history of the universe.

1.8 Thermal History

In this section I will review how the thermodynamical properties, as well as the particle content of the universe, have evolved over time. To properly understand the thermal history of the universe, several concepts need to be introduced first[10]. However, for a general overview of the main stages involved, see Fig. 1.5.

1.8.1 Phase-space Distribution and Equilibrium

To properly understand the behaviour of particles in the early universe, we can describe each species χ in the universe with a phase-space distribution function $f_\chi(x^\mu, P^\nu)$. The arguments of this function can be reduced by using that homogeneity implies that f_χ should not depend on x^i. Additionally, isotropy allows us to take out a dependence on the direction of the physical momentum p^i; however, the dependence on the modulus p remains. Finally, we can use

[9] As a reminder, this only accounts for $\sim 5\,\%$ of the energy content of the observable universe. And yet we call it normal matter.
[10] We are almost there, I promise.

equation 1.31 to see that P^0 is not an additional independent parameter. Thus, the phase-space distribution becomes only $f_\chi(t,p)$. To study the evolution of the phase-space distribution we would need a Boltzmann equation: we will come back to this in section 3.2.

The phase-space distribution allows us to additionally describe the number density, energy density, and pressure of each species as

$$n_\chi(t) = \frac{g}{(2\pi)^3}\int d^3p f_\chi(t,p)\,, \tag{1.65}$$

$$\rho_\chi(t) = \frac{g}{(2\pi)^3}\int d^3p E_\chi f_\chi(t,p)\,, \tag{1.66}$$

$$P_\chi(t) = \frac{g}{(2\pi)^3}\int d^3p \frac{p^2}{3E} f_\chi(t,p)\,, \tag{1.67}$$

where g is the number of spin states of a species (number of quantum degrees of freedom).

With this in mind, we can now discuss particles in the very early universe. Just after the Big Bang the temperature in the universe is very high, and there are constant collisions between particles. With each of these collisions, they exchange momentum in a random way and reach a kinetic equilibrium known as *thermal equilibrium*. Together, all of the species in thermal equilibrium form a thermal bath, with all Standard Model particles following Boltzmann distributions with the coherent temperature T.

The thermal distribution of particles at temperature T and chemical potential μ is given by

$$f_\pm = \frac{1}{e^{(E-\mu)/T}\pm 1}\,, \tag{1.68}$$

where the $(+)$ corresponds to a Fermi-Dirac distribution (fermions), and the $(-)$ corresponds to a Bose-Einstein (bosons) one.

We can now solve the integrals in equations 1.65-1.67 in thermal equilibrium for two different limits. In the relativistic case, with negligible chemical potential, the temperature will be much larger than the particle mass ($T \gg m$) and we obtain

$$n_\chi = \frac{\zeta(3)}{\pi^2} g_\chi T^3 \quad \left(\times\frac{3}{4}\right) \quad \text{(for fermions)}\,, \tag{1.69}$$

$$\rho_\chi = \frac{\pi^2}{30} g_\chi T^4 \quad \left(\times\frac{7}{8}\right) \quad \text{(for fermions)}\,, \tag{1.70}$$

$$P_\chi = \frac{1}{3}\rho_\chi\,, \tag{1.71}$$

where $\zeta(x)$ is the Riemann zeta function.

Conversely, for non-relativistic particles (with $T \ll m$) we would have

$$n_\chi = g_\chi \left(\frac{m_\chi T}{2\pi}\right)^{3/2} e^{-m/T}\,, \tag{1.72}$$

$$\rho_\chi = m_\chi n_\chi\,, \tag{1.73}$$

$$P_\chi = T n_\chi\,. \tag{1.74}$$

We see that in the non-relativistic case the particle distributions are suppressed by a factor $\exp(-m/T)$; this means that particles and antiparticles can annihilate but the thermal bath does not have enough energy to reproduce them.

1.8.2 Freeze-out and Decoupling

In order to see if a species is in thermal equilibrium, we can compare the *interaction rate* Γ with the expansion rate H. If

$$\Gamma \gg H \quad \text{or equivalently} \quad \left\{\tau_\Gamma \equiv \Gamma^{-1}\right\} \ll \left\{\tau_H \equiv H^{-1}\right\}\,, \tag{1.75}$$

thermal equilibrium is reached before the effect of the expansion becomes relevant. Once the rate of interactions decreases faster than the expansion rate, due to the universe cooling down we would reach $\tau_\Gamma \sim \tau_H$, at which point the species will decouple from the thermal bath.

If we focus now on $2 \to 2$ Standard Model processes (as described in 1.7), we can write the generic particle interaction rate as

$$\Gamma = n\langle\sigma v\rangle\,, \tag{1.76}$$

where σ is the interaction cross section, v is the average velocity of the particles, and n is still the number density. At high enough temperatures, $T \gtrsim 100\,\text{GeV}$, all known particles are relativistic ($v \sim 1$) and we can ignore their masses. Interactions are mediated by a boson A[11], and we can calculate the cross section for the strong and electroweak forces to be

$$\sigma \sim \frac{\alpha^2}{T^2}\,, \tag{1.77}$$

where $\alpha \equiv g_A^2/4\pi$ is the coupling constant associated to the boson A. In this regime, we can recall the Hubble rate to be $H \sim \sqrt{\rho}/M_{Pl}$, and using equations 1.70 and 1.77 we find

$$H \sim \frac{T^2}{M_{Pl}} \quad \& \quad \Gamma = n\langle\sigma v\rangle \sim \alpha^2 T\,. \tag{1.78}$$

[11] Massless bosons for now, as at these temperatures we are above the scale of electroweak symmetry breaking.

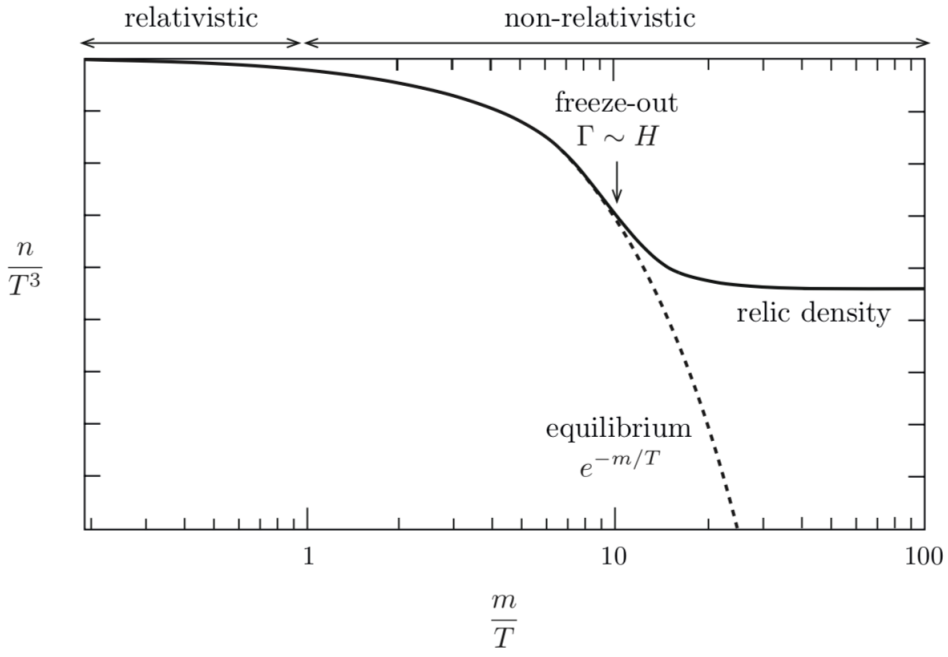

FIGURE 1.6: Schematic illustration of particle freeze-out. When the particle is ultra-relativistic, the abundance will follow the equilibrium value. At low temperatures the particles freeze out and their density is no longer exponentially suppressed. Image taken from [7].

If we insert this into the condition 1.75 and take the numerical value $\alpha \sim 0.01$ (which is the value for electroweak interactions), we find

$$\frac{\Gamma}{H} \sim \frac{\alpha^2 M_{Pl}}{T} \sim \frac{10^{16}\,\text{GeV}}{T}\,, \tag{1.79}$$

so for $10^{16}\,\text{GeV} \gtrsim T \gtrsim 100\,\text{GeV}$ all known particles will be in thermal equilibrium.

This equilibrium could not have persisted today, though, as that would lead to a universe dominated by photons. When the interaction rate of a massive particle drops below the Hubble expansion rate, equilibrium is broken and the particles decouple and their density will *freeze out*. The exact freeze-out time will depend on the interaction type the particle experiences. Fig. 1.6 shows a schematic representation of freeze-out.

After the electroweak symmetry breaking, $T \sim 100\,\text{GeV}$, the three massive vector bosons of the weak interaction ($W^{\pm}$ and Z) come in to play, with masses $M_W \sim M_Z$, and the cross section of the weak interaction becomes

$$\sigma \sim \left(\frac{\alpha}{M_W^2}\right)^2 T^2\,, \tag{1.80}$$

with $\frac{\alpha}{M_W^2} \sim 1.17 \cdot 10^{-5}\,\text{GeV}^{-2}$, which leads us to

$$\frac{\Gamma}{H} \sim \frac{\alpha^2 M_{Pl} T^3}{M_W^4} \sim \left(\frac{T}{1\,\text{MeV}}\right)^3 . \tag{1.81}$$

Therefore, we can see that particles that interact only via the weak interaction with the primordial plasma will decouple at a temperature of $T \sim 1\,\text{MeV}$. This will become very significant in section 1.9.

1.8.3 Brief History of The Universe

Now that we have seen the key elements involved in the discussion of the history of the universe, we can review the main stages of evolution. Of course, when compacting 13.8 billion years of evolution into a few pages, many details will be omitted; this chapter is meant as a general overview. For a more in-depth discussion, see for example [20]. The main phases of the universe can be summarised as

- **Inflation**. This was the early period of exponential expansion, and is the topic of chapter 2. Inflation erases the memory of anything that might have come beforehand, and as such it is the earliest time we can reasonably talk about.
- **Baryogenesis**. This is the process by which the first baryons and antibaryons were formed. From relativistic quantum field theory, we know that matter and antimatter should be produced in equal parts. However, given that particles and antiparticles annihilate through processes such as $e^+ + e^- \to \gamma\gamma$, we would expect to be in a universe completely dominated by radiation, which is obviously not what we observe. Indeed, we observe an over-abundance of matter over antimatter in the universe today. Although many different models try to explain this initial difference between matter and antimatter production, the nature of baryogenesis remains a mystery.
- **Electroweak Phase Transition**. When the universe drops below a temperature of about $100\,\text{GeV}$ ($z \sim 10^{15}$) the gauge bosons gain mass via the Higgs mechanism, leading to the first main phase shift in the universe.
- **QCD Phase Transition**. As the universe cools down to $\sim 150\,\text{MeV}$ ($z \sim 10^{12}$), the strong interaction becomes more important, and quarks and gluons form bound three-quark systems (baryons) and quark-antiquark pairs (mesons).
- **Dark Matter Freeze-out**. Due to its dependence on the dark matter mass M_χ (see section 1.9.2 for more details), the exact time of dark matter decoupling is not known; however, this process can be shown to take place at a T_d such that $M_\chi/T_d \approx 10 - 25$.
- **Neutrino Decoupling**. As neutrinos only interact weakly with the rest of the primordial plasma, they will also decouple at early times, when the temperature is around $1\,\text{MeV}$ ($z \sim 10^{10}$). This process is extremely significant for the history of the universe, as it

will lead to a *Cosmic Neutrino Background* (similar to the CMB). We will see in section 4.1 that the temperature of the CMB is known, and from that we can calculate the temperature of the neutrino background to be $T_{C\nu B} = 1.945\,\mathrm{K}$. Furthermore, once electrons and positrons have annihilated (see below), the relativistic degrees of freedom populating the universe are only photons and neutrinos. Thus we can write the corresponding energy density as

$$\rho_R = \rho_\gamma \left(1 + \frac{7}{8}\left(\frac{4}{11}\right)^{4/3} N_{\mathrm{eff}}\right) , \tag{1.82}$$

where I have introduced the *effective number of neutrino species* N_{eff}. This will be equal to 3 if the following three conditions are fulfilled: i) there are no other additional relativistic particles besides the three neutrino species (discussed in section 6.1), ii) neutrinos follow a Fermi-Dirac distribution with no chemical potential, and iii) neutrino decoupling is instantaneous. However, we already know that the third condition is not fulfilled, and the standard model prediction is $N_{\mathrm{eff}} = 3.046$. This will be discussed again in section 7.1.

- **Electron-positron annihilation**. Shortly after neutrino decoupling, at around $0.5\,\mathrm{MeV}$ ($z \sim 10^9$), electrons and positrons can annihilate, transferring their energy to the photon bath. As the neutrinos have already decoupled, they will not be affected by this.

- **Big Bang Nucleosynthesis**. About three minutes after inflation, the universe reaches temperatures of $100\,\mathrm{keV}$ ($z \sim 10^8$), protons and neutrons are no longer free in the primordial plasma: nucleons are captured into nuclei. This leads to the formation of light elements, mainly helium-4, but also small amounts of deuterium, helium-3, and lithium-7. Heavier elements are not formed until later on in stellar cores. In regions of the universe untouched by stellar evolution, we can measure the primordial abundance of elements: thus Big Bang Nucleosynthesis is the earliest cosmological probe available. The observations match very closely with predictions from ΛCDM, and thus this is considered one of the pillars of evidence for the standard cosmological model.

- **Recombination**. After nucleosynthesis, the universe contains a thermal plasma of photons, electrons, hydrogen nuclei, and decoupled neutrinos (and dark matter). While weak interactions are inefficient, these particles are kept in equilibrium via electromagnetic scattering, driven by Compton scattering ($e^- + \gamma \to e^- + \gamma$) and Coulomb scattering ($e^- + p \to e^- + p$). At a redshift of $z \sim 1100$ neutral hydrogen is formed via the reaction $e^- + p \to H + \gamma$, once the temperature has become low enough to disfavour the inverse reaction. This will be revisited in section 4.1.

- **Photon Decoupling**. Due to recombination, there is a sharp drop in the free electron density, meaning that Compton scattering becomes inefficient and the photons can decouple. These photons have been mostly free-streaming ever since, and today constitute the CMB (see section 4.1).

- **Reionisation**. After photon decoupling, the thermal history of the universe is mostly uneventful, with the exception of reionisation. Between redshifts $z \sim 6 - 20$ the first stars begin to form, and thus a new population of photons is emitted. These photons

partially reionise hydrogen and other heavier elements, but this is not sufficient to re-couple electrons to photons. Nonetheless, this marks the end of the dark ages: between photon decoupling and stellar formation the universe is dark, with few probes able to explore this time period. It is common to parametrise reionisation with the *optical depth to reionisation* τ_{reio}, which represents the opacity of the universe at the time of reionisation and forms one of the six base ΛCDM parameters, as discussed in section 1.6.

1.9 A Closer Look at Cold Dark Matter

In section 1.6 we saw that $\sim 85\,\%$ of the matter content of the universe is in the form of *dark matter*, which is a type of matter that does not interact with the electromagnetic force. As such, this matter is invisible to us; however, due to its gravitational influence on the observable universe, there is little doubt about its existence[12].

The first discussions of dark matter came in 1922, when Kapteyn released a paper in which he introduced the idea of a new unseen type of matter in order to explain the rotating motions of stars in our galaxy [21]. The first convincing evidence for dark matter was presented soon after in the seminal papers by Zwicky in 1933 and 1939 [22], [23], where he estimated the total mass of the Coma cluster assuming it to be mechanically stable, and thus obeying the virial theorem (relates the time-averaged total internal kinetic energy of the galaxies in a cluster to its self-gravitational potential energy).

The subsequent study of similar clusters, together with other probes across many different scales, such as galactic rotation curves, gravitational lensing, cosmological structure formation, and the CMB (more on this in chapter 4), all contribute to a wealth of evidence for dark matter being the dominant matter component of our universe.

While the existence of this dark component is well supported by the evidence, its general lack of interactions make it very difficult for us to study it. As such, there are many different dark matter models and candidates. In this section I will review the main evidence for this species in the universe, and discuss a few of the most well-motivated models.

1.9.1 Evidence for Dark Matter

As mentioned above, the first discussions about dark matter came about in the early twentieth century, when Kapteyn started to look at the rotation of stars in our galaxy [21], and Zwicky started to look into galaxy clusters [22], [23].

[12] At least in general, some people remain sceptical.

The study of dark matter made significant progress in the 1970s, when Vera Rubin[13] observed a discrepancy between the predicted and observed angular motion of stars in spiral galaxies [25], [26], which became known as the *galaxy rotation problem*. The theoretical prediction is easy to reproduce: let us assume a test body with a stable orbit at a distance r from the galactic centre. We can compute its orbital velocity v using Newtonian gravity:

$$\frac{GmM(r)}{r^2} = m\frac{v^2}{r}\,. \tag{1.83}$$

We can now divide the structure of the galaxy into an inner region (bulge) with radius R_1 and density of visible matter ρ_{v_1}, and an outer extended region (or disk) with radius R_2, visible matter density ρ_{v_2}, and thickness d. Therefore, stars located inside the bulge, with $r \ll R_1$, will have a velocity

$$M(r) \simeq \frac{4\pi}{3}r^3\rho_{v_1} \quad \rightarrow \quad v(r) = \sqrt{G\rho_{v_1}\frac{4}{3}\pi}r\,, \tag{1.84}$$

while stars in the outer disk, $r \gg R_2$, are predicted to have a velocity of

$$M(r) = M_{\rm tot} = \frac{4}{3}\pi R_1^3\rho_{v_1} + \pi R_2^2 d\rho_{v_2} \quad \rightarrow \quad v(r) = \sqrt{\frac{GM_{tot}}{r}}\,. \tag{1.85}$$

As such, we can see that the velocity of stars in the disk should decrease with $v(r) \propto 1/\sqrt{r}$. However, Rubin's observations showed that the velocity of these stars was constant, $v(r) \simeq const$. This shows that $M_{\rm tot}$ needs an additional contribution leading to $M(r) \propto r$. This is illustrated in Fig. 1.7.

This result can be generalised to any galaxy type. Assuming a spherical dark matter halo around the galaxy, which would be typical of the spherical collapse of a distribution of collisionless particles bound gravitationally, we can describe the density as

$$M(r) = 4\pi\int_0^r \rho(r')r'^2dr' \propto r \quad \rightarrow \quad \rho(r) \propto \frac{1}{r^2}\,. \tag{1.86}$$

The full *halo density profile* ρ is a matter of ongoing debate, as there are many different ways one can model this, and all of the models have good and bad aspects. This is explored more in depth in section 5.1.

While rotation curves by themselves are a strong argument in favour of dark matter, they are by no means the only existing evidence. Another pillar of support for dark matter comes in the form of *gravitational lensing*. In section 1.3 I discussed how light travels on geodesics, always taking the shortest path possible in curved spacetime. Any object with enough mass will curve spactime, and thus will affect the trajectory of light as it moves close to this object.

[13] Rubin's work was vital to solidifying dark matter as part of the standard cosmological model. Her contribution was initially ignored by her colleagues and has largely been overlooked, partly due to her being a woman [24]. Many people called for her to receive a Nobel Prize for her work[†]; this unfortunately never happened.

[†] Some people feel like this is not justified, however one could argue that it is as justified as the 2011 Nobel Prize for observing the accelerated expansion of the universe.

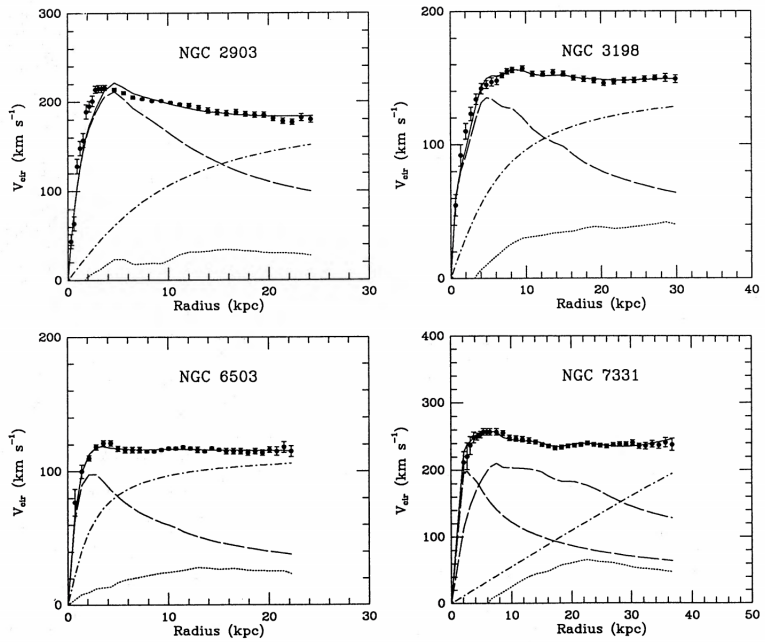

FIGURE 1.7: Rotation curves of spiral galaxies. The long-dashed curves correspond to Newtonian predictions for visible stars, while the dotted curves represent the gas contribution. The dotted-dashed curves show the dark matter halo contribution. The sum of the three components is shown in the solid lines. Image taken from [27].

This bending of light will lead to a deformation of the shape of distant objects such as galaxies. Therefore, by studying this effect we can deduce the spatial distribution of the gravitational potential, which in turn allows us to discuss the mass distribution in the intervening medium.

Depending on the strength of the gravitational lensing, it can lead to different effects and ways of observing it. In the case of *strong gravitational lensing* easily visible distortions appear, such as Einstein rings, arcs, and multiple images of the same object. The study of these distortions allows us to reconstruct the shape of dark matter halos around particular galaxy clusters.

On the other hand, in the case of *weak gravitational lensing* the effect is not visibly apparent, and can only be seen when looking at large numbers of galaxies. As this effect is coherent over many galaxies in a given region, we can average out the random distribution of intrinsic shapes by studying the statistics of the apparent orientation of galaxies in different regions of the sky. This gives us a very good map of the gravitational potential projected along the line-of-sight in each direction around us, and thus allows us to estimate the effects of dark matter. Furthermore, by using lensing information of galaxies located at different redshifts, we can reconstruct the 3D distribution of dark matter, and thus estimate its abundance.

On even larger scales, we can use colliding galaxy clusters to test the dark matter hypothesis. Most of the baryonic matter in clusters is contained in the hot gas, which emits strong X-ray radiation, and thus can be seen with X-ray telescopes. During the collision of two clusters the gas will interact electromagnetically, thus experiencing a drag effect. As such, we have a clear indication as to where the normal matter of the merging clusters should be. We can

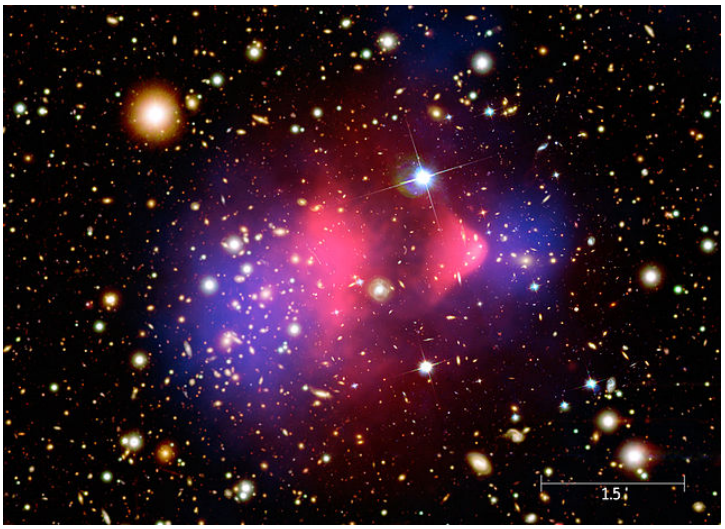

FIGURE 1.8: Composite image of the Bullet Cluster, showing the visible matter, photographed by Hubble Space Telescope. Superimposed are the X-Ray emissions measured by the Chandra X-Ray Observatory, in pink, and the mass distribution obtained by weak lensing observations, in blue. Image taken from the Chandra X-Ray Observatory website: http://chandra.harvard.edu.

additionally measure the distribution of the gravitational potential, and therefore the mass distribution, by using gravitational lensing. If there were no dark matter present, the mass distribution would coincide with the baryonic matter.

One of the clearest examples of merging clusters is the Bullet Cluster, shown in Fig. 1.8. The image is a composite of three images: in the visible spectrum we can see the clusters as photographed by the Hubble Telescope. The ionised gas was imaged by the Chandra telescope in X-rays, and is shown in pink. Finally, the mass distribution obtained from weak lensing experiments is shown in blue. We can see in the image that the regions with more mass do not coincide with the baryonic matter: this implies there is another component in the clusters that did not feel the collision, which is compatible with dark matter that only interacts via the weak and gravitational forces. The results of this analysis were first reported in [28], and this is often considered a smoking gun signal for dark matter.

While all of this together paints a very compelling picture in favour of dark matter, possibly the biggest evidence for this species comes from the observation of the CMB anisotropies (discussed in depth in section 4.1). These anisotropies can not be explained unless the universe contains a species that does not interact with ordinary electromagnetic forces. Furthermore, the CMB reaffirms the idea that this type of matter has to be non-baryonic, not just non-luminous. If we assume that this dark matter component is stable and that its number density is conserved until today, from the CMB we can calculate its density today. We find that it accounts for $\sim 85\,\%$ of the matter content of the universe, and $\sim 25\,\%$ of the overall energy budget, as seen in section 1.6 [14].

[14] While some alternative models to dark matter exist, such as Modified Newtonian Dynamics (MOND), none of these models can simultaneously explain the observed gravitational effects across so many different scales, and none of them can explain the CMB anisotropies.

1.9.2 Standard Properties of Dark Matter

From the observations described above, we can already discuss some of the main properties of dark matter. Firstly, dark matter needs to be stable, or at least have a lifetime larger than the age of the universe: if this were not the case, late time structures (smaller scales) would not be able to form. Secondly, we know dark matter has practically no interactions with photons: it must be electrically neutral. Additionally, from BBN and CMB constraints, we know that dark matter can not be baryonic.

We can look at lower bounds for dark matter particles[15] in a model-independent way. The lowest bounds we can derive come from galaxies: we know dark matter has to be confined in galaxies, which puts a limit on their de Broglie wavelength. For bosonic dark matter, this means that $\lambda = 2\pi/(M_\chi v_\chi)$ has to be smaller than the average dwarf galaxy size of 1 kpc. This limit is pushed higher for fermionic dark matter, due to the Pauli exclusion principle. The resulting bounds are

$$\begin{aligned} M_\chi &\gtrsim 3 \cdot 10^{-22}\,\text{eV} \quad \text{(for bosons)}\,, \\ M_\chi &\gtrsim 25\,\text{eV} \quad \text{(for fermions)}\,. \end{aligned} \tag{1.87}$$

We can also discuss the velocity of dark matter today to see if dark matter is cold, hot, or somewhere in between. We make the natural assumption that dark matter particles χ were in kinetic equilibrium with normal matter in the early universe[16]. In this scenario, at some point the dark matter would depart from equilibrium, and would propagate freely. This leads us to several scenarios: if the decoupling temperature (T_d) is smaller than the dark matter mass M_χ, the dark matter decouples after becoming non-relativistic, leading to *cold dark matter*; conversely if $T_d \gtrsim M_\chi$ we have non-cold dark matter. This latter case can be divided further depending on M_χ: for masses $M_\chi \lesssim 1\,\text{eV}$ the dark matter would remain relativistic at radiation-matter equality, leading to *hot dark matter*; while for masses $M_\chi \gtrsim 1\,\text{eV}$ the dark matter would be non-relativistic before reaching this equality, leading to *warm dark matter*.

In the case of warm and hot dark matter, it would be free-streaming and relativistic while $T_d \gtrsim T \gtrsim M_\chi$, allowing it to fill in under-dense regions of sizes up to current horizon size. This free-streaming would lead to dark matter perturbations of these sizes getting washed out. The horizon size at the time at which free-streaming stops allows us to calculate the present maximum size of suppressed density perturbations: for warm dark matter this would be $l \sim 0.1\,\text{Mpc}$, while for hot dark matter this gives us $l \sim 100\,\text{Mpc}$.

This calculation means that models with hot dark matter predict a suppression of density perturbations on present-day sizes of 100 Mpc, which would lead to the largest structures forming first, and then fragmenting into smaller structures, with galaxies being the last to form. This is in contradiction with observations, which show that structures form hierarchically with smallest structures collapsing first. Thus, dark matter can not be hot. Warm dark matter is

[15] For now, we will treat dark matter as a particle, alternative models will be discussed later.
[16] This assumption is not valid for all models; it is a generalisation.

still allowed, but is strongly constrained: a spatial size of $0.1\,\mathrm{Mpc}$ is typical for perturbations that led to small structures, such as dwarf galaxies. As such, we can use observations of dwarf galaxies to find a constraint on the dark matter mass (assuming it was in thermal equilibrium with normal matter at early times):

$$M_\chi \gtrsim 1\,\mathrm{keV}\,. \tag{1.88}$$

With the above considerations, we can see that no Standard Model particle can explain the observed effects of dark matter. The most logical candidate within the Standard Model would be neutrinos. However, these would be relativistic until very late times, behaving as hot dark matter, and would wash out structures on small scales. With this in mind, we can now discuss dark matter candidates beyond the Standard Model.

The relic density of dark matter today is well measured (see section 1.6), with both the CMB [19] and the Bullet Cluster [28] giving very similar bounds. The current measurement, as described in equation 1.54, is

$$\omega_{CDM} = 0.11933 \pm 0.00091\,. \tag{1.89}$$

Thus, a first step to building a dark matter model is asking ourselves the question of what properties dark matter needs to have to produce the observed relic density today. We have already seen the procedure by which other particles can freeze out in the universe, so it seems reasonable to consider a similar scenario here[17]: we assume a massive, non-relativistic, stable particle χ, that can annihilate with its antiparticle $\bar{\chi}$ into some Standard Model particle f. Thus, we have the process $\chi + \bar{\chi} \leftrightarrow f + \bar{f}$. The evolution of the number density of dark matter is described by the following Boltzmann equation (Boltzmann equations will be explored in depth in section 3.2)

$$\frac{dn_\chi}{dt} = -3Hn_\chi + n_f^2\langle\sigma_{\mathrm{pro}}v\rangle + n_\chi^2\langle\sigma_{\mathrm{ann}}v\rangle\,, \tag{1.90}$$

where $\langle\sigma_{\mathrm{pro}}v\rangle$ is the thermally averaged production cross section multiplied by the velocity, and $\langle\sigma_{\mathrm{ann}}v\rangle$ is the annihilation one. We know that the collisional terms vanish at chemical equilibrium, which leads to

$$\frac{dn_\chi}{dt} = -3Hn_\chi - \langle\sigma v\rangle\left[n_\chi^2 - \left(n_\chi^{eq}\right)^2\right]\,. \tag{1.91}$$

It is now useful to define two new variables. The most interesting physics will take place when $T_\chi \sim m_\chi$, so we define a new time-variable $x \equiv m_\chi/T_\chi$. We will also need the number of these particles for a given entropy density s, given by $Y_\chi = n_\chi/s$. Assuming the particle undergoes freeze-out during radiation domination ($T \propto a^{-1}$), we can write

$$\frac{dY_\chi}{dx} = -\frac{\lambda}{x^2}\left[Y_\chi^2 - \left(Y_\chi^{eq}\right)^2\right] \quad \text{with} \quad \lambda \equiv \frac{2\pi^2}{45}g_\star s\frac{m_\chi^3\langle\sigma v\rangle}{Hx^2}\,. \tag{1.92}$$

[17] A similar procedure can be used if we instead assume freeze-in, as for example in [29].

The above equation can be solved numerically, showing that at high temperature we recover $Y \to Y_{eq}$, while at low temperature the equilibrium abundance is exponentially suppressed as the particles become non-relativistic, $Y \propto e^{-x}$. At some point in between, however, we reach freeze-out at a time x_{fo} and a temperature T_{fo}. By using now $\Gamma(x_{fo}) = \langle\sigma_{ann}v\rangle n_\chi^{fo}$, and setting $\Gamma(x_{fo}) = H(x_{fo})$, we obtain $x_{fo} \sim \mathcal{O}(10)$. Furthermore, we can see from equation 1.92 that a higher $\langle\sigma v\rangle$ leads to later freeze-out[18].

Finally, we can relate the freeze-out abundance for such a dark matter particle to the measured dark matter density today

$$\Omega_{CDM} \equiv \frac{\rho_{\text{cdm},0}}{\rho_{\text{crit},0}} = \frac{m_\chi Y_{\chi,0} s_0}{3M_{Pl}^2 H_0^2}\,, \tag{1.93}$$

which can be solved as

$$\omega_{\text{CDM}} \approx \frac{3\cdot 10^{-27}\text{cm}^3\text{s}^{-1}}{\langle\sigma v\rangle}\,. \tag{1.94}$$

Now that we have calculated the relation between the dark matter annihilation cross section and the relic density today, we can find what type of particles would generate the needed density. In section 1.7, we saw what possible interactions normal particles can have, and we can use that as inspiration to solve the dark matter problem: we consider a *Weakly Interacting Massive Particle* (henceforth WIMP). This massive particle can interact with Standard Model particles in the early universe via the weak force, bringing it into thermal equilibrium with the rest of the primordial particles.

To test if WIMPs can produce the right dark matter density today, we recall that in section 1.8.2 we saw

$$\langle\sigma v\rangle \sim \frac{\alpha_W^2}{m_\chi^2}\,, \tag{1.95}$$

where $\alpha_W \sim 0.01$ is the coupling constant associated to the weak force[19]. If we now assume a mass very close to the electroweak scale, $m_\chi \sim v_{EW} \sim 250\,\text{GeV}$, we can find

$$\langle\sigma v\rangle \sim 10^{-9}\,\text{GeV}^{-2} \sim 10^{-26}\,\text{cm}^3/\text{s}\,. \tag{1.96}$$

We can combine this with equation 1.94 to find $\omega_{\text{CDM}} \sim 0.1$, which is very close to the measured value today. Thus, if we have WIMPs in the early universe, we would naturally obtain the correct relic density of dark matter today. This is known as the *WIMP miracle*, and it has solidified WIMPs as one of the main dark matter models. As such, a lot of effort is being put into detection of WIMPs: at colliders, in indirect searches, and at direct detection experiments. However, so far, these have remained elusive [30].

There are many other models of cold dark matter, and while I will not go into detail here, interesting candidates include

[18] A process known as "survival of the weakest", because we are *very* good at naming things.

[19] This notation is slightly misleading, as the weak force has two couplings g and g', and so the definition of α_W is ambiguous. However, for the order of magnitude calculation I am doing here, this detail is irrelevant.

- Axions. Proposed to solve the strong CP problem in quantum chromodynamics via the Peccei-Quinn mechanism. QCD axions would have a mass in the range $10^{-5} - 10^{-3}$ eV. See [31] for a review.
- Primordial Black Holes. Hypothetical black holes formed during or shortly after inflation. These black holes would be less massive than their stellar counterparts, and could account for a fraction or all of dark matter. See [32] for a review.
- Sterile Neutrinos. An additional fourth neutrino: much heavier than its Standard Model counterparts, right-handed and with no weak interactions. See [33] for a review.

Currently none of these models have been proven, and every day new dark matter models appear in the literature. Until the eventual detection of dark matter[20], dark matter model building will be limited only by the constraints discussed above and the creativity of the model builders.

[20] Not everyone thinks we will find dark matter, but I am an optimist.

2 Inflation

In the previous section we saw that the HBB model provides a very good picture of the history of the universe from early times until today. Despite its remarkable success, there are several problems in the standard cosmological model: the horizon problem, the flatness problem, and the monopole problem. Together, these seem to call for an additional ingredient to describe the very early times in our universe, and thus provide the initial conditions that lead to the universe we observe today. One of the most well-motivated hypothesis to do this is *inflation*, which is the idea that before radiation domination there was a period where the scale factor grew exponentially and the universe was dominated by a slowly varying vacuum energy.

The inflationary paradigm was first proposed by Starobinsky in 1979 [34] and later expanded by Guth in 1981 [35], with them both postulating that an early period of inflation could solve the aforementioned issues. In the first model by Guth, a transition from the false vacuum to the true vacuum was needed. Upon seeing that this was not possible, the model was replaced by Linde [36], and Albrecht and Steinhardt [37] with a new model of inflation, in which the slow evolution of a scalar field rolling down the potential hill resulted in an exponential expansion. This slow roll inflation model is revisited in section 2.3.

In this chapter I will discuss the motivations behind inflation, and how it can solve the initial conditions problems. Furthermore, the underlying physical mechanism of inflation is explored, as well as the implications for the cosmological observables, mainly the impact on the CMB anisotropies. This recap is based mainly on references [38]–[40].

2.1 Motivations

The two biggest problems with the HBB model are the horizon and flatness problem, which both boil down to the question "Why do the initial conditions needed to explain our universe seem so fine-tuned?". Inflation mitigates the fine-tuning issue, instead providing a physical mechanism to generate these conditions. Furthermore, inflation provides a mechanism to generate the CMB anisotropies, which will be discussed in section 3.5. While the nature and physical properties of inflation are still being debated, its experimental success makes it a very attractive model.

2.1.1 Horizon Problem

One of the main outstanding issues with the HBB model is the *horizon problem*, which asks the question as to why the CMB photons have the same temperature across the whole sky: indeed we saw in section 1.1 that the temperature anisotropies are of the order of $10^{-5}\,K$.

To understand the horizon problem we first need to discuss cosmological horizons. The first horizon to consider is the *Hubble Radius*, $R_H \equiv H^{-1} = a/a'$, which defines the limit beyond which particles, due to the expansion of the universe, would appear to move away from us faster than the speed of light. Secondly, we have the *particle horizon* d_H, which gives us the maximum distance between two photons emitted from the same location at a time t. This gives us a limit on the causal patch: the region of spacetime that could have been influenced by these photons in a given time. The particle horizon is equal to the conformal time (seen in equation 1.16) since the emission of the photons multiplied with the speed of the photons.

If we now recover the definition of comoving distance introduced in equation 1.21, we can express the particle horizon as

$$d_H(a_1, a_2) = a_2 = \int_{a(t_1)}^{a(t_2)} \frac{da}{a^2 H(a)}\,, \tag{2.1}$$

and knowing how the Hubble rate changes as a function of the scale factor during both radiation and matter domination, together with the assumption $a_2 \gg a_1$, we can find

$$d_H(a_1, a_2) \backsimeq \frac{1}{H_2} = R_H(t_2)\,. \tag{2.2}$$

Thus, in this picture the Hubble radius and the causal horizon are approximately equivalent. This gives us a causal limit: any process started at t_1 can only affect distances smaller than $d_H(t_1, t_2)$ at time t_2.

Focussing now on CMB photons, before decoupling one would expect a random distribution of temperatures, homogeneous only on scales given by d_H. Therefore, even if we chose our initial time arbitrarily close to the initial singularity, we would expect the CMB temperature to be homogeneous on a region corresponding to $R_H(dec)$, which given the present-day value of H and $z_{dec} \approx 1100$ would correspond to an angular size of $\sim 2°$. This implies that on a CMB map, the homogeneous regions should only encompass a few degrees, and we would expect to find many different causally disconnected temperature regions. The horizon problem can thus be formulated as: *how can photons in regions of the CMB that have never been in causal contact have the same temperature?*

Inflation solves this problem by adding a phase of early accelerated expansion. Indeed, in equation 2.1 we found that the integral was converging with respect to the lower boundary a_1, leading to a causal horizon of the same order of magnitude as the Hubble radius. However, the convergence of this integral depends on the acceleration or deceleration of the expansion:

if a' decreases the integral converges, but if a' increases, as is the case during expansion, the integral would diverge for $a \to 0$.

This means that if a grows exponentially, as is proposed for inflation, the integral diverges, thus allowing us to find a particle horizon much larger than the Hubble radius at decoupling, and thereby solving the horizon problem.

Quantitatively, let us now assume that inflation took place between t_i and t_f, corresponding to a_i and a_f, during which time $a = e^{\alpha t}$. We can calculate the new causal horizon as

$$d_H(a_i, a_f) = a_f \int_{a_i}^{a_f} \frac{da}{a^2 H_i} = \frac{1}{H_i}\left(\frac{a_f}{a_i} - 1\right) \simeq \frac{1}{H_i}\frac{a_f}{a_i}\,. \tag{2.3}$$

Thus, at the end of inflation the causal horizon is larger than the Hubble radius by a factor a_f/a_i. It is now useful to define the *e-fold number*

$$N \equiv \ln a\,, \tag{2.4}$$

from which we can calculate the number of e-folds that take place during inflation to be

$$\Delta N = \ln \frac{a_f}{a_i}\,. \tag{2.5}$$

The condition necessary for the Hubble radius to be smaller than the causal horizon at decoupling, and thus to solve the horizon problem, is that the number of inflationary e-folds should be at least equal to the number of e-folds since inflation took place. Assuming inflation happened at the GUT energy scale ($\sim 10^{16}$ GeV), this corresponds to $\Delta N \sim 60$.

Therefore, if there are sufficient e-folds of inflation, the particle horizon at decoupling would be larger than the Hubble radius, meaning all the observed photons in the CMB would have been in causal contact before decoupling, thus explaining their observed isotropy.

2.1.2 Flatness Problem

The other main issue with FLRW cosmology is the so-called *flatness problem*, which asks the question as to why the universe appears to be flat: indeed we saw in section 1.6 that the curvature density is measured to be $\Omega_k \leq 0.021$.

This becomes a more obvious problem if we rewrite equation 1.54 as

$$\Omega_k \equiv -\frac{k}{a^2 H^2} \quad \to \quad |\Omega_k| = \frac{|k|}{a'(t)^2}\,. \tag{2.6}$$

We can now look at the behaviour of this term in two different stages: radiation domination and matter domination. We have already seen that during matter domination $a(t)$ increases like $t^{2/3}$, so $|k|/a'(t)^2$ also increases as $t^{2/3} \propto T^{-1}$. Using the present day value of the curvature

$\Omega_k < 0.01$, this implies that when the temperature of the universe was $T = 10^4$K, the curvature must have been $|\Omega_k| < 10^{-4}$.

We can apply a similar argument during radiation domination, where the scale factor varies as $t^{1/2}$, thus $|k|/a'(t)^2$ increases as $t \propto T^{-2}$. Therefore, if we take a sample temperature of $T = 10^{10}$K, we would have $|\Omega_k| < 10^{-16}$. We can extrapolate this argument backwards and see that the curvature density has been consistently *growing* with time. This means that in order to have such a low value of the curvature density today, in the past the value had to be significantly lower.

We can find the specific ranges for the Planck time (t_{Pl}), which is the earliest time we can conceive of, and for the Big Bang Nucleosynthesis (t_{BBN}), which is the earliest time for which we have observations:

$$|\Omega_k(t_{Pl})| < 10^{-60} \quad \text{and} \quad |\Omega_k(t_{BBN})| < 10^{-18}\,. \tag{2.7}$$

Therefore, to account for the observed flatness today, we require the curvature to be fine-tuned to within 60 orders of magnitude in the early universe. Even if we adopt the more conservative view of only considering to BBN time, we still require a curvature smaller than 10^{-18}. The flatness problem can thus be formulated as: *why was the flatness of the very early universe negligible enough to lead to a flat universe today?*

A period of exponential expansion in the early universe addresses this issue. During a phase of accelerated expansion the Hubble parameter is constant, and we can see in equation 2.6 that Ω_k would *decrease* as a^{-2}, forcing the universe to become asymptotically flat. Therefore, one does not have to make assumption about the initial state of the universe: if a sufficient amount of inflation precedes radiation domination, this epoch would necessarily have started with negligible curvature.

The amount of inflation required to properly solve the flatness problem can be found (see for example [41]) to be the same amount of expansion that has taken place since inflation, the same as for the horizon problem. Again, assuming inflation took place on the GUT energy scale the flatness problem requires a minimum of 60 e-folds to be solved, similarly to the horizon problem.

2.1.3 Monopole Problem

The final problem with the HBB cosmology is the *monopole problem*, which asks the question as to why we have not found any of the topological defects predicted by many Grand Unified Theories (GUT). In these models, the Standard Model of particle physics arises from phase transitions induced by spontaneous symmetry breakings in the early universe (caused by the expansion and cooling of the universe) and could lead to the formation of topological defects such as domain walls, cosmic strings, and monopoles. The detection of these topological defects would be a smoking gun for GUTs, and has sparked a lot of interest in the past.

The monopole annihilation is predicted to be very slow, which should result in a very high energy density of them today, and thus they should completely dominate the total density of the universe. Furthermore, these defects would be non-relativistic: their energy density would dilute like a^{-3}, which would prevent the domination of normal matter that we see later in the universe. However, no evidence has been found for the existence of these topological defects, calling into question many of the existing GUTs.

Nonetheless, a period of exponential expansion taking place after the creation of these topological defects can save these models. During inflation the leading vacuum energy is nearly constant, which would mean the energy density of the non-relativistic relics would be diluted by a factor $(a_f/a_i)^3$, thus explaining why they have not been found seen in the universe.

2.1.4 Origin of CMB Fluctuations

Solving the above problems is already a very strong motivation for inflation, but it further provides for free a mechanism to explain the tiny anisotropies in the CMB, which will be discussed in more detail in chapter 3. For now, let us assume we have a cosmological perturbation with wavelength $\lambda(t)$. We can expand this in comoving Fourier space as

$$\lambda(t) = \frac{2\pi a(t)}{k}\,. \tag{2.8}$$

In section 1.6 we saw that during radiation domination the Hubble radius varies as $R_H(t) \propto t$, while the scale factor changes as $a(t) \propto t^{1/2}$, which implies that the Hubble radius grew much faster than the wavelength of the perturbations. If the perturbations were generated causally when a wavelength entered the horizon, we would expect them not to be coherent on super-Hubble scales. This would mean the temperature anisotropies on the CMB maps would be smaller than one degree, which is not compatible with observations[1].

We now wish to find a scenario such that all cosmological perturbations observable today were generated *inside* the causal horizon at some earlier time. The largest observable wavelength we can see today is of the order of the Hubble radius, thus we need a mechanism with which this wavelength was already in the causal horizon at an initial time t_i. We can express the ratio between the wavelength and the Hubble radius as

$$\frac{\lambda(t)}{R_H(t)} = \frac{2\pi a(t)}{k} H(t) = \frac{2\pi a'(t)}{k}\,. \tag{2.9}$$

Thus, during decelerated expansion the Hubble radius grows faster than the physical wavelengths, while if the universe is in accelerated expansion the physical wavelengths grow faster than the Hubble radius. Therefore, if between a certain time t_i and t_f the expansion of the universe was accelerating, as is the case during inflation, it is possible to have $\lambda_{max} < R_H, d_H$ at time t_i.

[1] As we already saw in the previous section. Everything is connected.

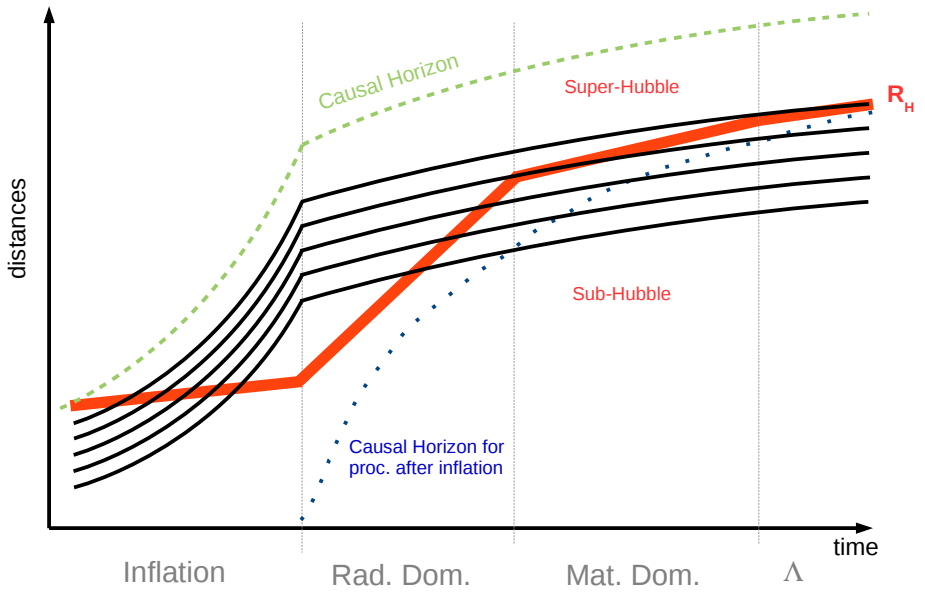

FIGURE 2.1: Wavelength of perturbations (thin lines) compared to the Hubble radius (thick lines). During inflation the Hubble radius grows slower than the wavelengths, allowing these to exit the Hubble radius and re-enter at a later time, thus explaining the observed coherent CMB anisotropies.

This means that perturbations of wavelength λ can be created causally before inflation by quantum fluctuations in the early universe. The perturbations would then exit the Hubble radius during inflation, where they would freeze out until re-entering the Hubble radius today, setting the seeds for CMB anisotropies and structure formation, as will discussed in section 3.3. This is summarised in Fig. 2.1.

2.2 Scalar Field Inflation

We have seen in the previous section that an early stage of accelerated expansion can solve several cosmological problems. In order to see what type of species in the universe can generate this expansion, we can rewrite the Friedmann equation 1.35 as

$$a' = \sqrt{\frac{8\pi G}{3}} a \rho^{1/2} \,. \tag{2.10}$$

If we now take the time derivative of this and insert the energy conservation equation 1.37, we can find

$$a'' = -\sqrt{\frac{8\pi G}{3}} \frac{a'}{2\rho^{1/2}} (\rho + 3p) \,, \tag{2.11}$$

which allows us to directly find the necessary condition for accelerated expansion ($a' > 0$) as

$$a' > 0 \quad \text{iff} \quad \rho + 3p < 0 \,. \tag{2.12}$$

In section 1.6 we saw that the only component that fulfils a negative pressure smaller than $\rho/3$ is a cosmological constant. However, as the cosmological constant never decays, this would lead to infinite inflation. Given that we know that the universe has not been in accelerated expansion throughout its whole history, we require an end to inflation. As such, the mechanism driving the current accelerated expansion does not seem to be the same one that caused inflation in the early universe.

The simplest possibility that could lead to a finite amount of inflation is to consider a *scalar field* ϕ, known as the *inflaton*, slowly rolling down a very flat valley of some potential $V(\phi)$. The rolling attributes an arrow of time, and thus a possible end to inflation, while the overall flatness of the valley means that the field can be seen at any time as being in an instantaneous vacuum state, behaving similar to a cosmological constant. A general example of this slowly-rolling inflaton is shown in Fig. 2.2, and will be discussed more in section 2.3.

Assuming now a scalar field, which is a field of spin zero invariant under Lorentz transformations, the general action in curved spacetime can be written as

$$S = -\int d^4x\sqrt{|g|}\left(\mathcal{L}_g - \mathcal{L}_\phi\right) , \tag{2.13}$$

where $\mathcal{L}_g$ is the gravitation Lagrangian

$$\mathcal{L}_g = \frac{R}{16\pi G} , \tag{2.14}$$

and $\mathcal{L}_\phi$ is the Lagrangian of the scalar field

$$\mathcal{L}_\phi = \frac{1}{2}\partial_\mu\phi\partial^\mu\phi - V(\phi) = \frac{1}{2}g^{\mu\nu}\partial_\mu\phi\partial_\nu\phi - V(\phi) . \tag{2.15}$$

In the above equation we can see $V(\phi)$ is the scalar potential. With the variation of the action with respect to $g_{\mu\nu}$ we can define the stress-energy tensor as

$$T_{\mu\nu} = \partial_\mu\phi\partial_\nu\phi - \mathcal{L}_\phi g_{\mu\nu} . \tag{2.16}$$

Finally, we can look at the variation of the action with respect to ϕ to find the Klein-Gordon equation:

$$\frac{1}{\sqrt{|g|}}\partial_\mu\left[\sqrt{|g|}\partial^\mu\phi\right] + \frac{\partial V}{\partial\phi} = 0 . \tag{2.17}$$

While this idea of scalar field inflation is very well motivated, there are many different models that would lead to such slow-roll inflation, and thus many different possible $V(\phi)$s. Several different ways of reconstructing this potential using the latest Planck 2018 data **[I]** is discussed in Appendix A.

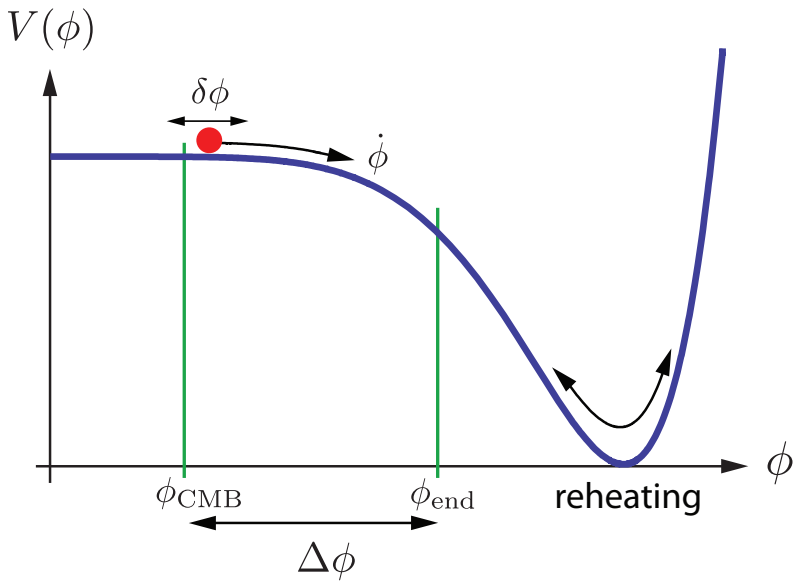

FIGURE 2.2: Example of a slowly-rolling inflaton potential, showing the end of inflation (ϕ_{end}) and when the cosmological fluctuations (ϕ_{CMB}) would be created. Image taken from [39].

2.3 Slow-Roll Inflation

In the previous section we saw the general behaviour of scalar field inflation, now we can now look more in detail at the mechanism of slow-roll inflation. In a flat FLRW universe we can use equation 2.16 to express the energy density and pressure of the inflaton field as

$$\begin{aligned} \rho &= \frac{1}{2}\phi'^2 + V(\phi) \\ p &= \frac{1}{2}\phi'^2 - V(\phi)\,. \end{aligned} \tag{2.18}$$

It is useful to rewrite the Klein-Gordon equation for scalar fields from equation 2.17 as:

$$\phi'' + 3H\phi' + \frac{\partial}{\partial\phi}V(\phi) = 0\,. \tag{2.19}$$

We can now combine equation 2.19 with the Friedmann equation 1.35, expressed as

$$H^2 = \frac{8\pi G\rho}{3} \simeq \frac{8\pi G}{3}V(\phi)\,, \tag{2.20}$$

to find:

$$H' = -4\pi G\phi'^2\,, \tag{2.21}$$

where we see that during scalar field inflation, the Hubble parameter can only decrease with time, as expected.

When discussing scalar field inflation, in equation 2.12 we saw that the equation of state

should have $p < -\rho/3$. Using equations 2.18 we can rewrite this to find the *first slow roll condition*

$$\frac{1}{2}\phi' \ll V(\phi)\,. \tag{2.22}$$

In other words, slow roll inflation requires the potential energy to dominate over the kinetic energy. Furthermore, we want this condition to be fulfilled for a sufficient amount of time, in order to have enough e-folds of inflation to solve the problems discussed in section 2.1. Therefore, we must impose that the time-derivative of the first condition also holds, leading to the *second slow roll condition*

$$|\phi''| \ll \left|\frac{\partial}{\partial\phi}V(\phi)\right|\,. \tag{2.23}$$

When these two conditions hold, the Friedmann equation 2.20 and the Klein-Gordon equation 2.19 become

$$\begin{aligned} 3H^2 &\simeq 8\pi G V(\phi)\,, \\ \phi' &\simeq -\frac{1}{3H}\frac{\partial V}{\partial\phi}(\phi)\,. \end{aligned} \tag{2.24}$$

Thus, the two slow-roll conditions can be expressed as either a condition on the slowness of the variation of $H(t)$, or alternatively a condition on the flatness of the potential $V(\phi)$. This is explored in more detail in Appendix A

The slow-roll conditions are often parametrised with the *slow-roll parameters*, first defined in [42],

$$\epsilon = \frac{M_{Pl}^2}{16\pi}\left(\frac{(\partial V/\partial\phi)}{V}\right)^2 \quad \text{and} \quad \eta = \frac{M_{Pl}^2}{8\pi}\frac{(\partial^2 V/\partial\phi^2)}{V}\,. \tag{2.25}$$

By making use of equation 2.21 and using the relation between the gravitational constant and the Planck mass, $G = M_{Pl}^{-2}$, we can use the slow-roll parameters to express conditions 2.22 and 2.23 as

$$\epsilon \ll 1 \quad \text{and} \quad |\eta| \ll 1\,. \tag{2.26}$$

Therefore, slow-roll inflation can take place provided both conditions are fulfilled.

2.4 Cosmological Parameters Obtained with Slow-Roll Inflation

A complete treatment of scalar field inflation as the origin of cosmological fluctuations (these perturbations will be explored in depth in chapter 3) requires understanding of QFT in curved spacetime, and would thus require an entire chapter or text book. Several very good reviews already exist on the topic, see for example [38]. As such, here I will just review the main stages involved, all summarised in Fig. 2.1,

1. Inflation starts at some time t_i, when the potential energy of ϕ starts to dominate the energy density of the universe. Curvature is rapidly diluted away.

2. At some early time, all the observable cosmological wavelengths are sub-Hubble. For modes deep inside the Hubble radius, we can describe the small quantum fluctuations of the scalar field ($\delta\phi$) and the metric like in a flat spacetime.

3. Starting from the largest wavelength, the modes gradually exit the Hubble radius, and freeze out. This leads to a semi-classical transition of the quantum fluctuations of the scalar field and of the metric: they become indistinguishable from classical stochastic fluctuations. This means that the primordial fluctuations have a random distribution, but their statistics can be well described classically.

4. At some point, the inflaton exits slow-roll and inflation ends. When this happens, the inflaton will decay into Standard Model particles (a phase known as reheating). During this phase the scalar field decays, thus its large wavelength perturbations vanish. However, metric perturbation survive, with those outside of the Hubble radius being impervious to the microphysics of reheating.

5. After the scalar field has decayed, the universe enters radiation domination, dominated by the energy of the particles produced during reheating. The larger wavelength metric perturbations couple gravitationally to radiation and matter perturbations. The subsequent evolution of these perturbations leads to the CMB anisotropies and set the seeds for the later formation of galaxies, and will be discussed in chapter 3.

After the semi-classical transition, the probability distribution of each mode $\delta\phi(\boldsymbol{k})$ can be shown to be a Gaussian dependent only on $\boldsymbol{k}$. As such, at any given time all of the information about the statistics of the field will be contained in the variance

$$\langle|\phi(\boldsymbol{k})|^2\rangle\,. \tag{2.27}$$

The perturbations of the scalar field $\delta\phi$ will couple with the metric perturbations (both the scalar and tensor perturbations), and we can calculate the variance at the end of inflation for observable modes. Furthermore, these larger modes were frozen out and thus unaffected by the later decay of the scalar field during reheating, when radiation particles are formed. These particles will of course be susceptible to the gravitational potential, which will behave as a mediator between the scalar field perturbations during inflation and the radiation perturbations in the radiation dominated universe. Therefore, if we can calculate the variance 2.27 at the end of inflation, we can use this to set the initial conditions for radiation domination (see section 3.3).

Usually, rather than discussing the variance, the most interesting quantity to describe the stochastic variable $A(\boldsymbol{k})$ will be the dimensionless power spectrum, defined as

$$\mathcal{P}_A(k) \equiv \frac{k^3}{2\pi^2}\langle|\phi(\boldsymbol{k})|^2\rangle\,. \tag{2.28}$$

This power spectrum will be given greater physical significance in section 3.4.

Assuming a completely scale-invariant spectrum, which is to say all wavelengths contribute equally, the power spectrum for scalar modes reads as

$$\mathcal{P}_{\mathcal{R}}(k) = \frac{H^4}{4\pi\phi'} = \frac{128\pi V^3}{3M_{Pl}^6 V'^2}\,, \tag{2.29}$$

while the power spectrum for tensor modes is

$$\mathcal{P}_H(k) = \frac{16G}{\pi} = \frac{128V^3}{3M_{Pl}^4}\,. \tag{2.30}$$

To study any deviations from scale-invariance, the power spectra are often approximated as power-laws

$$\mathcal{P}_{\mathcal{R}}(k) = \underbrace{\mathcal{P}_{\mathcal{R}}(k_\star)}_{A_s}\left(\frac{k}{k_\star}\right)^{n_s-1}\,, \tag{2.31}$$

$$\mathcal{P}_h(k) = \underbrace{\mathcal{P}_h(k_\star)}_{A_t}\left(\frac{k}{k_\star}\right)^{n_t}\,, \tag{2.32}$$

where $k_\star$ is an arbitrary reference wavenumber known as the pivot scale. The tilts, which give deviations from scale invariance, are defined as

$$n_s - 1 \equiv \left.\frac{d\ln\mathcal{P}_{\mathcal{R}}}{d\ln k}\right|_{k=k_\star}\,, \tag{2.33}$$

$$n_t \equiv \left.\frac{d\ln\mathcal{P}_h}{d\ln k}\right|_{k=k_\star}\,. \tag{2.34}$$

The two power spectra defined above allow us to define a quantity known as the *tensor-to-scalar ratio*, which is useful when comparing different inflationary models with observations,

$$r \equiv \frac{\mathcal{P}_h(k)}{\mathcal{P}_{\mathcal{R}}(k)}\,. \tag{2.35}$$

We can now find an expression for the tilts, and thus for the tensor-to-scalar ratio, using the slow-roll parameters defined in equation 2.25,

$$\begin{aligned} r &\simeq 16\epsilon_\star\,,\\ n_s - 1 &\simeq -6\epsilon_\star + 2\eta_\star\,,\\ n_t &\simeq -2\epsilon_\star\,, \end{aligned} \tag{2.36}$$

where the subscript $_\star$ indicates that a quantity is evaluated at the pivot scale.

With these expression, given an inflationary model we can trivially calculate the predicted tensor-to-scalar ratio r[2] and scalar tilt n_s. Thus, we can use observational constraints on these

[2]The tensor-to-scalar ratio is always evaluated at a given pivot scale. The most common choices are $k_\star = 0.05$ or $k_\star = 0.002$.

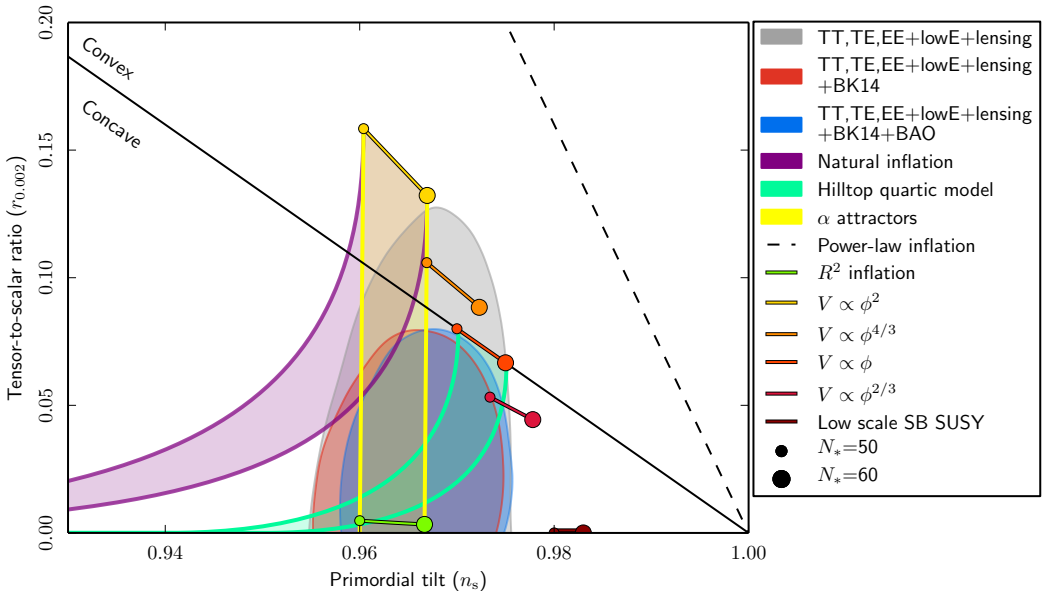

FIGURE 2.3: Latest constraints on the tensor-to-scalar ratio $r_{0.002}$ and the spectral tilt n_s, using data from Planck, Bicep2/Keck Array, and BAO. The predictions for different inflationary models are also shown, computed both for 55 and 60 e-folds. Image taken from **[I]**.

parameters to differentiate between different inflationary models. The latest constraints and model comparisons are shown in Fig. 2.3. Numerically, the current constraints on the most relevant parameters[3] are [19]

$$\begin{aligned} 10^9 A_s &= 2.105 \pm 0.030\,, \\ n_s &= 0.9665 \pm 0.0038\,, \\ r_\star &< 0.058\,, \end{aligned} \tag{2.37}$$

As we can see, n_s is very close to 1, thus justifying our previous assumption of scale-invariance in equation 2.29. Furthermore, given the measurements of Gaussian and adiabatic initial conditions [1] (which will be explored in more detail in section 3.5) it is enough to specify the primordial power spectrum of one quantity to know everything about the system. Thus, the amplitude A_s and tilt n_s of the scalar power spectrum are two of the six parameters needed to fully define the ΛCDM universe. Together with ω_b, ω_m, and Ω_Λ (discussed in section 1.6) and τ_{reio} (discussed in section 1.8.3), we can now fully describe the ΛCDM model.

[3]Tensor modes are known to be very small, if they even exist. As such, constraints on A_t and n_t are not given.

3 Perturbed Cosmology

In chapter 1 we saw how homogeneous cosmology provides a very good description of the history and current status of the universe. However, in section 2.1.4, we also saw how small quantum fluctuations in the very early universe can grow during inflation, leading to inhomogeneities and anisotropies in the universe (typically $\mathcal{O}(10^5)$ times smaller than background quantities). These perturbations lead to the observed CMB anisotropies, as well as setting the seeds for structure formation. Thus, to properly understand the universe around us, we need to be able to study these perturbations, however small. This chapter will provide an overview of *Linear Perturbation Theory* (sticking to first order perturbation theory, and ignoring non-linearities), but for a more in-depth review see for example [43], [44].

Throughout this chapter I will work in Fourier space instead of real space, in order to trade one equation with partial spatial derivatives for a set of equations with k wavenumbers. As we saw in section 2.1.4, a cosmological perturbation with wavelength $\lambda(t)$ can be expanded in comoving Fourier space as

$$\lambda(t) = \frac{2\pi a(t)}{k}\,. \tag{3.1}$$

Furthermore, as shown in Fig. 2.1, perturbations are created causally before inflation by quantum fluctuations in the early universe. These perturbations would then exit the Hubble radius during inflation, where they would freeze out until re-entering the Hubble radius today, with the smaller wavelengths entering earlier than the larger wavelengths modes. This will be important for the rest of this chapter.

3.1 Linear Perturbation Theory

We are interested in small perturbations of the FLWR metric and the stress-energy tensor of the universe. As such, we can decompose these into spatial averages and linear perturbations

$$\begin{aligned} g_{\mu\nu}(t,\boldsymbol{x}) &= \bar{g}_{\mu\nu}(t) + \delta g_{\mu\nu}(t,\boldsymbol{x})\,, \\ T_{\mu\nu}(t,\boldsymbol{x}) &= \bar{T}_{\mu\nu}(t) + \delta T_{\mu\nu}(t,\boldsymbol{x})\,. \end{aligned} \tag{3.2}$$

Due to symmetry reasons, the two perturbed tensors contain only ten degrees of freedom each, describing different gravitational aspects. These can be decomposed into decoupled scalar, vector, and tensor modes. In a perfect vacuum the first two vanish, while the tensor

perturbations can propagate (if they have been excited) and account for gravitational waves[1]. When matter is present, scalars represent the response of the metric to an irrotational distribution of matter, and thus they are the generalisation of Newtonian gravity. Vectors, on the other hand, represent the response of the metric to vorticity (gravitomagnetism), but these decay quickly and can be neglected. Therefore, for the rest of this chapter I will focus only on scalar modes.

The four scalar components of the perturbed metric and stress-energy tensors are given by the (00) term, the trace of the (ij) matrix, the irrotational part of the $(0i)$ vector, and the traceless longitudinal part of the (ij) tensor. For the perturbed metric $\delta g_{\mu\nu}$ these correspond to

(00) term	Generalised gravitational potential ψ ,
(ij) (trace)	The local distortion ϕ of the average scale factor: the local scale factor is given by $(1-\phi)a$,
$(0i)$ term	The potential b such that $\delta g_{0i} = \partial_i b$,
(ij) (traceless)	The potential μ of the metric shear: $\delta g_{ij} = \left(\partial_i\partial_j - \frac{1}{3}\delta_{ij}\Delta\right)\mu$.

For the perturbed stress-energy tensor $\delta T_{\mu\nu}$ these components are

(00) term	The energy density perturbations $\delta\rho$,
(ij) (trace)	The pressure perturbations δp ,
$(0i)$ term	The velocity potential v of the irrotational component of the flux of energy, $\delta T^0_i = \partial_i v$,
(ij) (traceless)	The potential s of the shear stress $\delta T^i_j = \left(\partial_i\partial_j - \frac{1}{3}\delta_{ij}\Delta\right)s$.

The velocity potential is often substituted for the *velocity divergence* θ, defined as

$$\partial_i \delta T^0_i \equiv (\bar{\rho} + \bar{p})\,\theta = \Delta v\,. \tag{3.3}$$

Additionally, the shear is often denoted by the anisotropic stress σ, which is defined as

$$\left(\partial_i\partial_j - \frac{1}{3}\delta_{ij}\Delta\right)\delta T^i_j \equiv (\bar{\rho} + \bar{p})\,\sigma = \Delta\left(\Delta s\right)\,. \tag{3.4}$$

With the above definitions, we see that we can manipulate four degrees of freedom representing the scalar metric perturbations $\{\psi, \phi, \mu, b\}$, and four for the scalar perturbations of the stress-energy components. The latter can be chosen as the density fluctuation, the pressure perturbation, the velocity divergence, and the anisotropic stress $\{\delta, \delta p, \theta, \sigma\}$.

When discussing linear perturbation theory, we encounter an unavoidable problem: this theory is a *gauge* theory, which means we need to choose a reference frame in which to describe

[1] Gravitational waves are a fascinating topic that deserve a whole separate thesis, but they will not be covered here. Maybe if I decide to write a second thesis they will be there.

the perturbations. This will be a gauge choice, a way to slice the spacetime in equal-time hyper-surfaces, as well as a specific spatial coordinate choice on these hyper-surfaces. There are an infinite amount of time slicings compatible with perturbation theory (such that on each slice all quantities remain close to their average value). While physical quantities do not depend on the choice of gauge, intermediate quantities constructed from the perturbations can depend on this choice. This could lead to the equations of motion of perturbed quantities having gauge modes as part of the solution, with no observable consequences.

To deal with this gauge freedom there are two usual approaches: we can work with gauge invariant quantities and gauge invariant equations of motions for these quantities, as was historically done by Bardeen in 1980 [45]; or we can fix the gauge by introducing a condition that completely defines a unique time slicing, and then the number of independent solutions to the equations will be the same as in the gauge invariant formalism. Here I will focus on the second approach, and introduce the two most commonly used gauges: the synchronous gauge and the Newtonian gauge.

The *synchronous gauge*, first introduced by Lifshitz in [46], is defined such that $\delta g_{00} = \delta g_{0i} = 0$ (equivalently, $\phi = b = 0$). Thus, in this gauge there exists a set of comoving observers who experience free fall, or move along a geodesic, without changing their spatial coordinates. This gauge allows a description of scalars, vectors, and tensors simultaneously, but it has the downside that the choice of the initial hyper-surface and its coordinate assignments are arbitrary, and thus this gauge does not eliminate all degrees of freedom.

The *conformal Newtonian gauge*, introduced by Mukhanov in 1992 [47], is defined by $\mu = b = 0$, leading to a diagonal metric tensor $g_{\mu\nu}$. The line element in this gauge is given by

$$ds^2 = a^2(\tau)\{-(1+2\psi)d\tau^2 + (1-2\phi)\, dx^i dx_i\}\,. \tag{3.5}$$

By construction, this gauge can only describe scalar modes: the vector and the tensor degrees of freedom are eliminated from the beginning. This could be generalised to all modes, but we are anyway only interested in scalar modes here. In the weak-field (Newtonian) limit, the perturbation ψ can be interpreted as the gravitational potential, giving the name to the gauge.

As a gauge choice is nothing but a choice of time slicing of spacetime in GR, we can always do a *gauge transformation*, similar to a coordinate transformation. Thus, one can easily move between synchronous and Newtonian gauge, and as mentioned above, the observable quantities do not depend on our choice of gauge. As such, throughout this thesis I will always use the Newtonian gauge.

In section 1.3 we saw how the metric and the matter content of the universe can be related via the Einstein equations. In order to relate the metric perturbations to the matter perturbations, we will solve the linearised Einstein equations in Fourier space k. In the Newtonian gauge the first-order perturbed Einstein equations give

$$(00) \rightarrow \qquad k^2\phi + 3\frac{\dot{a}}{a}\left(\dot{\phi} + \frac{\dot{a}}{a}\psi\right) = -4\pi G a^2 \bar{\rho}\delta\,, \tag{3.6}$$

$$(0i) \rightarrow \qquad k^2\left(\dot{\phi} + \frac{\dot{a}}{a}\psi\right) = 4\pi G a^2(\bar{\rho} + \bar{p})\theta\,, \tag{3.7}$$

$$(ii) \rightarrow \qquad \ddot{\phi} + \frac{\dot{a}}{a}(\dot{\psi} + 2\dot{\phi}) + \left(2\frac{\ddot{a}}{a} - \frac{\dot{a}^2}{a^2}\right)\psi + \frac{k^2}{3}(\phi - \psi) = 4\pi G a^2 \delta p\,, \tag{3.8}$$

$$(ij) \rightarrow \qquad k^2(\phi - \psi) = 12\pi G a^2(\bar{\rho} + \bar{p})\sigma\,. \tag{3.9}$$

Deep in the sub-Hubble regime we have $k \gg (aH)$ and $\sigma \approx 0$, which allows us to rewrite equation 3.6 as

$$k^2\psi = -4\pi G a^2 \delta\rho_{\rm tot}\,, \tag{3.10}$$

which is just the Poisson equation for Newtonian gravity. In addition to the Einstein equations, it is often useful to use the conservation of the stress-energy tensor, which is a direct consequence of these equations. This allows us to find two new equations[2]

$$\text{Continuity equation} \rightarrow \qquad \dot{\delta} = -(1+w)\left(\theta - 3\dot{\phi}\right) - 3\frac{\dot{a}}{a}\left(\frac{\delta p}{\delta\rho} - w\right)\delta\,, \tag{3.11}$$

$$\text{Euler equation} \rightarrow \qquad \dot{\theta} = -\frac{\dot{a}}{a}(1-3w)\theta - \frac{\dot{w}}{1+w}\theta + \frac{\delta p/\delta\rho}{1+w}\,k^2\delta - k^2\sigma + k^2\psi\,, \tag{3.12}$$

where I have recovered the equation of state $w = p/\rho$ from equation 1.38. These equations are valid for a single uncoupled fluid, or for the net δ and θ for all fluids.

Furthermore, we have seen that the perturbations of each species can be described by four variables, and thus generally the Continuity and Euler equations will not be enough to fully define a system. However, in the case of a perfect fluid (denoted by χ), microscopic interactions impose local thermodynamical equilibrium, and the anisotropic shear vanishes, $\sigma_\chi = 0$. In addition, pressure perturbations are given by $\delta p_\chi = c_\chi^2 \delta\rho_\chi$, where c_χ is the adiabatic sound speed inferred from the equation of state of the fluid. Therefore, in these cases the two equations of motion given by the Continuity and Euler equations are enough to compute the evolution of perturbations.

In the case of a decoupled or weakly interacting species, we can not make these simplifications with the shear and pressure. Thus, in general, we will need to use a Boltzmann equation, which will give the full evolution of each phase-space distribution. In the next section I will discuss the Boltzmann equations for individual species, as well as the type of modifications needed to account for interactions between different species.

[2] Somewhat redundant, as they bring no new information, but they are still useful.

3.2 Boltzmann Equations

In the previous section I discussed the linearised Einstein equations, and thus the evolution equations for the global cosmic fluid perturbations. If the universe consisted of uncoupled fluids, we could simply use the above equations summing over every species. However, as discussed in chapter 1, species in the universe are not isolated from each other, and as such they contribute to the evolution of perturbations in different ways.

All species are affected by gravity, and thus all species are coupled to each other through their influence on the metric. Photons and baryons are also strongly coupled together through Compton and Coulomb scattering, while neutrinos are collisionally coupled in the early universe through weak interactions. To properly describe all of these couplings, for each species in the universe we need to make use of a Boltzmann equation

$$\frac{d}{dt} f_\chi = \mathcal{C}\left[f_\chi\right] , \tag{3.13}$$

where the right-hand side is called the collision operator and contains all possible interaction terms.

In section 1.8.1 we saw that the phase-space distribution is a function of 8 parameters, $f(x^\mu, P^\nu)$. However, we can use $P^2 = g_{\mu\nu}P^\mu P^\nu = m^2$, to reduce one of the 4-momentum components. Working in the Newtonian gauge we can write the 4-momentum formula, seen in equation 1.31, in the presence of perturbations as

$$P_\mu = (-E(1+\psi), apn_i(1-\phi)) , \tag{3.14}$$

where n_i indicates the direction, $\boldsymbol{p} = p\hat{n}$ has components $p_i = pn_i$.

In the presence of perturbations, it is also convenient to introduce the relative fluctuation of the phase-space distribution

$$\Psi(x^i, p, n_j, \tau) = \frac{f(x^i, P_j, \tau)}{f_0(p)} - 1 , \tag{3.15}$$

where f_0 is the unperturbed phase-space distribution function. Furthermore, we can express the energy-momentum tensor in terms of the phase-space distribution and the 4-momentum components as

$$T_{\mu\nu} = (-g)^{-1/2} \int \frac{d^3p}{(2\pi)^3} \frac{P_\mu P_\nu}{E} f(x^i, p_j, \tau) , \tag{3.16}$$

where g is the determinant of $g_{\mu\nu}$ and is given by $(-g)^{-1/2} = a^{-4}\left(1 - \psi + 3\phi\right)$; and $d^3p = (1 - 3\phi)p^2 dp d\Omega$, where $d\Omega$ is the solid angle associated with direction n_i. Thus, the full components

of the energy-momentum tensor are given by

$$\begin{aligned} T^0_0 &= -a^{-4}\int p^2 dp\, d\Omega\, \sqrt{p^2+m^2a^2}\, f_0(p)\,(1+\Psi) \\ T^0_i &= a^{-4}\int p^2 dp\, d\Omega\, p\, n_i\, f_0(p)\,\Psi\,, \\ T^i_j &= a^{-4}\int p^2 dp d\Omega\, \frac{p^2 n_i n_j}{\sqrt{p^2+m^2a^2}}\, f_0(q)\,(1+\Psi)\,. \end{aligned} \tag{3.17}$$

We can now write the evolution of the phase-space distribution as

$$\frac{df}{d\tau} = \frac{\partial f}{\partial \tau} + \frac{\partial f}{\partial x^i}\frac{\partial x^i}{\partial \tau} + \frac{\partial f}{\partial p}\frac{\partial p}{\partial \tau} + \frac{\partial f}{\partial n^i}\frac{\partial n^i}{\partial \tau} = \boldsymbol{C}(f(p,t); f_i)\,, \tag{3.18}$$

where the right-hand side defines the *collisional integral*, which is given by the different interactions, and will depend on which species and interactions we are considering.

Finally, keeping only first order terms and making use of the geodesic equation, we can return to k-space, where the Boltzmann equation 3.13 becomes

$$\frac{\partial \Psi}{\partial \tau} + i\,\frac{p}{E}\,(\vec{k}\cdot\hat{n})\,\Psi + \frac{d\ln f_0}{d\ln p}\left[\dot{\phi} - i\,\frac{E}{p}(\vec{k}\cdot\hat{n})\,\psi\right] = \boldsymbol{C}(f(p,t); f_i)\,. \tag{3.19}$$

The Boltzmann equation 3.19 gives the full evolution of each phase-space distribution, and thus allows us to find the equations of motion of a given species in cases when the Euler equation 3.12 and Continuity equation 3.11 are not sufficient. We can now find the evolution equations for the main components of the universe.

Boltzmann Equations for Cold Dark Matter

The easiest species to describe in the universe is cold dark matter, as it only interacts with other particles gravitationally[3]. As such, it can be treated as a perfect, pressureless fluid, and we can describe its evolution without needing to solve the full Boltzmann equation. Making use of the Continuity and Euler equations, we find

$$\begin{aligned} \dot{\delta}_{\rm CDM} &= -\theta_{\rm CDM} + 3\dot{\phi}\,, \\ \dot{\theta}_{\rm CDM} &= -\frac{\dot{a}}{a}\,\theta_{\rm CDM} + k^2\psi\,. \end{aligned} \tag{3.20}$$

Boltzmann Equations for Massless Neutrinos

We already saw in section 1.8.3 that neutrinos decouple early in the universe, and massless neutrinos behave as a relativistic species. As such, $\rho_\nu = 3p_\nu = -T^0_0 = T^i_i$. We can use

[3]For now, in chapter 7 we will make it a more interesting species.

equation 3.17 to find

$$\begin{aligned}
\bar{\rho}_\nu = 3\bar{p}_\nu &= a^{-4}\int p^2 dp d\Omega\, p f_0(q)\,, \\
\delta\rho_\nu = 3\delta p_\nu &= a^{-4}\int p^2 dp d\Omega\, p f_0(q)\Psi\,, \\
\delta T^0_{\nu\, i} &= a^{-4}\int p^2 dp d\Omega\, p n_i\, f_0(p)\Psi\,, \\
T^i_{\nu j} - p_\nu \delta_{ij} &= a^{-4}\int p^2 dp d\Omega\, p(n_i n_j - \frac{1}{3}\delta_{ij})\, f_0(p)\Psi\,.
\end{aligned} \tag{3.21}$$

Furthermore, we can simplify the Boltzmann equation 3.19 by using $E = p$ (valid for massless particles), integrating out the momentum dependence, and expanding the angular dependence of the perturbation in a series of Legendre polynomials $P_\ell(\hat{k}\cdot\hat{n})$, giving us

$$F_\nu(\boldsymbol{k},\hat{n},\tau) \equiv \frac{\int p^2 dp\, p f_0(p)\Psi}{\int p^2 dp\, p f_0(p)} \equiv \sum_{\ell=0}^{\infty}(-i)^\ell(2\ell+1)F_{\nu\,\ell}(\boldsymbol{k},\tau)P_\ell(\hat{k}\cdot\hat{n})\,. \tag{3.22}$$

where the factor $(-i)^\ell(2\ell+1)$ is chosen in order to simplify the expansion of a plane wave: $F_\nu = \exp(-i\boldsymbol{k}\cdot\boldsymbol{x}\,)$ has expansion coefficients $F_{\nu\,\ell} = j_\ell(kr)$, given by spherical Bessel functions.

We can now express the needed perturbations $\delta_\nu, \bar{\rho}_\nu, \theta_\nu$, and σ_ν in terms of the new variable $F_\nu(\boldsymbol{k},\hat{n},\tau)$ as

$$\begin{aligned}
\delta_\nu &= \frac{1}{4\pi}\int d\Omega F_\nu(\boldsymbol{k},\hat{n},\tau) = F_{\nu\,0}\,, \\
\theta_\nu &= \frac{3i}{16\pi}\int d\Omega\,(\boldsymbol{k}\cdot\hat{n})F_\nu(\boldsymbol{k},\hat{n},\tau) = \frac{3}{4}kF_{\nu\,1}\,, \\
\sigma_\nu &= -\frac{3}{16\pi}\int d\Omega\left[(\hat{k}\cdot\hat{n})^2 - \frac{1}{3}\right]F_\nu(\boldsymbol{k},\hat{n},\tau) = \frac{1}{2}F_{\nu\,2}\,.
\end{aligned} \tag{3.23}$$

Finally, we can integrate the Boltzmann equation 3.19 and make use of F_ν to find the equations of motion for massless neutrinos

$$\begin{aligned}
\dot{\delta}_\nu &= -\frac{4}{3}\theta_\nu + 4\dot{\phi}\,, \\
\dot{\theta}_\nu &= k^2\left(\frac{1}{4}\delta_\nu - \sigma_\nu\right) + k^2\psi\,, \\
\dot{F}_{\nu\,\ell} &= \frac{k}{2\ell+1}\left[\ell F_{\nu\,(\ell-1)} - (\ell+1)F_{\nu\,(\ell+1)}\right]\,, \quad \ell \geq 2\,.
\end{aligned} \tag{3.24}$$

We can see that in our final expression, we have transformed the Boltzmann equation into an infinite *hierarchy* of moment equations that must be truncated at some maximum multipole $\ell_{\max}$. The most usual way of doing this is using the truncation scheme proposed in [43], which is based on the solution of these equations in the absence of a gravitational source term and cosmic shear, $\partial_\tau(\phi+\psi) = 0$. In this case, the time dependence of the exact solution is $F_{\nu\,\ell}(k,\tau) \propto j_\ell(k\tau)$ for $\ell > 0$, which allows us to use the recurrence relation for spherical Bessel

functions to find

$$F_{\nu\,(\ell_{\rm max}+1)} \approx \frac{(2\ell_{\rm max}+1)}{k\tau} F_{\nu\,\ell_{\rm max}} - F_{\nu\,(\ell_{\rm max}-1)}\,. \tag{3.25}$$

Boltzmann Equations for Massive Neutrinos

In section 6.1 I will discuss why neutrinos can not be considered massless. As such, we are also interested in the Boltzmann equations for massive neutrinos. The procedure to obtain these equations is similar to that of massless neutrinos, but with a more complicated evolution of the phase-space distribution. Rather than using equation 3.22, we instead expand the perturbation Ψ directly in a series of Legendre polynomials

$$\Psi(\boldsymbol{k}, \hat{n}, p, \tau) = \sum_{\ell=0}^{\infty} (-i)^{\ell}(2\ell+1)\Psi_{\ell}(\boldsymbol{k}, p, \tau)P_{\ell}(\hat{k}\cdot\hat{n})\,. \tag{3.26}$$

which will give us the perturbed energy density, pressure, energy flux, and shear stress in k-space as

$$\begin{aligned}
\delta\rho_{m\nu} &= 4\pi a^{-4}\int p^2 dp\, E f_0(p)\Psi_0\,,\\
\delta p_{m\nu} &= \frac{4\pi}{3}a^{-4}\int p^2 dp\, \frac{p^2}{E} f_0(p)\Psi_0\,,\\
(\bar{\rho}_{m\nu}+\bar{p}_{m\nu})\theta_{m\nu} &= 4\pi k a^{-4}\int p^2 dp\, p f_0(p)\Psi_1\,,\\
(\bar{\rho}_{m\nu}+\bar{p}_{m\nu})\sigma_{m\nu} &= \frac{8\pi}{3}a^{-4}\int p^2 dp\, \frac{p^2}{E} f_0(p)\Psi_2\,.
\end{aligned} \tag{3.27}$$

Following the same procedure as for the massless neutrinos, the Boltzmann equation becomes

$$\begin{aligned}
\dot{\Psi}_0 &= -\frac{pk}{E}\Psi_1 - \dot{\phi}\frac{d\ln f_0}{d\ln p}\,,\\
\dot{\Psi}_1 &= \frac{pk}{3E}(\Psi_0 - 2\Psi_2) - \frac{E\,k}{3p}\psi\frac{d\ln f_0}{d\ln p}\,,\\
\dot{\Psi}_{\ell} &= \frac{pk}{(2\ell+1)E}\left[\ell\Psi_{\ell-1} - (\ell+1)\Psi_{\ell+1}\right]\,, \quad \ell \geq 2\,,
\end{aligned} \tag{3.28}$$

where we see there is an added momentum-dependence, which will mean these equations require much more computing time. The truncation hierarchy for massive neutrinos is easier, as higher multipole moments decay rapidly once the neutrinos become non-relativistic, and so we can usually choose a much smaller $\ell_{\rm max}$.

Boltzmann Equations for Photons

The evolution equations for photons are much more complicated, as photons are coupled with baryons until the time of recombination, as discussed in section 1.8.3. As such, the right-hand side of the Boltzmann equations will no longer be zero, and we will have to take into account collisional terms, while the left-hand side will be the same as for massless neutrinos. The

phase-space distribution of photons can be written as

$$f_\gamma(\tau, x^i, p) = \left[\exp\left(\frac{E(p)}{a\bar{T}\left[1+\Theta(\tau, x^i, \hat{n})\right]}\right)\right]^{-1}, \tag{3.29}$$

where $\Theta \equiv \delta T/\bar{T}$ is an inhomogeneous and anisotropic perturbation to the temperature. Additionally, photons propagating in direction $\hat{n}$ are linearly polarised in the plane perpendicular to $\hat{n}$ due to scattering of electron density perturbations with wavevector $\boldsymbol{k}$. Therefore, we will be interested in keeping track of both the total intensity of the phase-space densities $\Theta_T(\boldsymbol{k}, \hat{n}, \tau)$ and the difference of the phase-space densities $\Theta_P(\boldsymbol{k}, \hat{n}, \tau)$. The former will behave the same as $F_\nu(\boldsymbol{k}, \hat{n}, \tau)$ from equation 3.22, with the same Legendre polynomial expansion leading to an infinite hierarchy.

The linearised collisional operators for the Thomson scattering rate were derived in [48]–[50], and are given by

$$\begin{aligned}
\left(\frac{\partial \Theta_T}{\partial \tau}\right)_C &= a n_e \sigma_T \left[-\Theta_T + \Theta_{T0} + 4\hat{n}\cdot\boldsymbol{v}_e - \frac{1}{2}\left(\Theta_{T2} + \Theta_{P0} + \Theta_{P2}\right) P_2\right], \\
\left(\frac{\partial \Theta_P}{\partial \tau}\right)_C &= a n_e \sigma_T \left[-\Theta_P + \frac{1}{2}\left(\Theta_{T2} + \Theta_{P0} + \Theta_{P2}\right)\left(1 - P_2\right)\right],
\end{aligned} \tag{3.30}$$

where n_e and $\boldsymbol{v}_e$ are the proper mean density and velocity of the electrons, and σ_T is the Thomson scattering rate. Additionally, the P_2 terms come from the polarisation-dependence of the Thomson cross section. Similar to 3.22, we can do the Legendre expansion

$$\Theta(\eta, \vec{k}, \theta) = \sum_\ell (-i)^\ell (2\ell+1)\Theta_\ell(\eta, \vec{k})\mathcal{P}_\ell(\cos\theta), \tag{3.31}$$

which leads us to the equations of motion for photons

$$\begin{aligned}
\dot{\delta}_\gamma &= -\frac{4}{3}\theta_\gamma + 4\dot{\phi}, \\
\dot{\theta}_\gamma &= k^2\left(\frac{1}{4}\delta_\gamma - \sigma_\gamma\right) + k^2\psi + a n_e \sigma_T(\theta_b - \theta_\gamma), \\
\dot{\Theta}_{T2} = 2\dot{\sigma}_\gamma &= \frac{8}{15}\theta_\gamma - \frac{3}{5}k\Theta_{T3} - \frac{9}{5}a n_e\sigma_T\sigma_\gamma + \frac{1}{10}a n_e\sigma_T\left(\Theta_{P0} + \Theta_{P2}\right), \\
\dot{\Theta}_{T\ell} &= \frac{k}{2\ell+1}\left[\ell\Theta_{T(\ell-1)} - (\ell+1)\Theta_{T(\ell+1)}\right] - a n_e\sigma_T\Theta_{T\ell}, \quad \ell \geq 3 \\
\dot{\Theta}_{P\ell} &= \frac{k}{2\ell+1}\left[\ell\Theta_{P(\ell-1)} - (\ell+1)\Theta_{P(\ell+1)}\right] \\
&\quad + a n_e\sigma_T\left[-\Theta_{P\ell} + \frac{1}{2}\left(\Theta_{T2} + \Theta_{P0} + \Theta_{P2}\right)\left(\delta_{\ell 0} + \frac{\delta_{\ell 2}}{5}\right)\right],
\end{aligned} \tag{3.32}$$

where the subscripts γ and b refer to photons and baryons respectively.

The truncation scheme for photons is similar to massless neutrinos, except that we need to add a term for the Thomson opacity

$$\begin{aligned}\dot{\Theta}_{T\,\ell} &= k\Theta_{T\,(\ell-1)} - \frac{\ell+1}{\tau}\Theta_{T\,\ell} - an_e\sigma_T\Theta_{T\,\ell}\,,\\ \dot{\Theta}_{P\,\ell} &= k\Theta_{P\,(\ell-1)} - \frac{\ell+1}{\tau}\Theta_{P\,\ell} - an_e\sigma_T\Theta_{P\,\ell}\,.\end{aligned} \tag{3.33}$$

Additionally, the first few mulitpole moments of Θ_T can be related to the scalar degrees of freedom discussed in section 3.1:

$$\delta_\gamma = 4\Theta_{T,0}\,, \qquad \theta_\gamma = 3k\Theta_{T,1}\,, \qquad \sigma_\gamma = 2\Theta_{T,2}\,. \tag{3.34}$$

Boltzmann Equations for Baryons

The evolution equations for baryons are much easier to compute, as baryons are non-relativistic and have negligible pressure and shear. As such, it is enough to use the Euler and Continuity equations, as for cold dark matter, but with the additional collisional term coming from their scattering with photons. Additionally, we have to keep the the acoustic term as it encodes the effects of the pressure of baryons below their Jeans length. This will be encoded with a sound speed c_s^2, with $\delta p = c_s^2\delta\rho$. With these considerations, the evolution equations for baryons are

$$\begin{aligned}\dot{\delta}_b &= -\theta_b + 3\dot{\phi}\,,\\ \dot{\theta}_b &= -\frac{\dot{a}}{a}\theta_b + c_s^2k^2\delta_b + R_\gamma(\theta_\gamma - \theta_b) + k^2\psi\,.\end{aligned} \tag{3.35}$$

In the above equations, I have introduced the coefficient for baryon-photon coupling

$$R_\gamma = \frac{4\rho_\gamma}{3\rho_b}an_e\sigma_T\,, \tag{3.36}$$

in which ρ_γ is the photon energy density and ρ_b is the baryon energy density. The baryon sound speed is evaluated as

$$c_s^2 \equiv \frac{\dot{p}}{\dot{\rho}} = w + \rho\frac{dw}{d\rho} = \frac{k_\mathrm{B}T_b}{\mu}\left(1 - \frac{1}{3}\frac{d\ln T_b}{d\ln a}\right)\,, \tag{3.37}$$

where μ is the mean molecular weight and T_b is the baryon temperature, which will be revisited in section 7.2.2.

3.3 Initial Conditions from Inflation

In the previous section I introduced the full system of coupled differential equations needed to describe linear perturbations. However, in order to fully describe the system, we are still missing initial conditions. In section 2.1.4 we saw that these perturbations can be related to an early stage of inflation, which will help us to infer the needed initial conditions.

If the universe is composed of N perfect fluids with known sound speed $c_s^2 = \delta p_s/\delta\rho_s$, then there are $2N$ independent initial conditions corresponding to possible initial values of δ_s and $\dot{\delta}_s$. Now let us assume that the universe is perturbed initially by a single degree of freedom, for example a time shift $\delta\tau(\boldsymbol{x})$, as is the case in single-field inflationary cosmology. Densities and pressures are thus described as

$$\begin{aligned} \rho_i(\tau,\boldsymbol{x}) &= \bar{\rho}_i(\tau+\delta\tau(\boldsymbol{x})) \simeq \bar{\rho}_i(\tau) + \dot{\bar{\rho}}_i(\tau)\delta\tau(\boldsymbol{x})\,, \\ p_i(\tau,\boldsymbol{x}) &= \bar{p}_i(\tau+\delta\tau(\boldsymbol{x})) \simeq \bar{p}_i(\tau) + \dot{\bar{p}}_i(\tau)\delta\tau(\boldsymbol{x})\,, \end{aligned} \tag{3.38}$$

where the time shift $\delta\tau(\boldsymbol{x})$ is the same for all species, and is assumed to be of order one in perturbations. This assumption singles out a specific subclass of initial conditions subject to

$$\frac{\delta\rho_i}{\bar{\rho}_i+\bar{p}_i} = \frac{\delta\rho_j}{\bar{\rho}_j+\bar{p}_j}\,, \tag{3.39}$$

for any i,j. This shows that in the presence of such initial conditions, everything is fixed up to a single function of $\boldsymbol{x}$. In section 1.6 we saw that our universe contains mainly dark matter, baryons, photons, and neutrinos. By using that non-relativistic species have $\bar{p}_i \ll \bar{\rho}_i$ and relativistic ones are given by $\bar{p}_i = \bar{\rho}_i/3$, we can show that

$$\delta_b = \delta_{\rm CDM} = \frac{3}{4}\delta_\nu = \frac{3}{4}\delta_\gamma\,. \tag{3.40}$$

Therefore, if one initial function is known, for example $\delta_\gamma(\boldsymbol{x})$, the others can be calculated.

Furthermore, the ansatz in equation 3.38 leads to each species having an *adiabatic* sound speed on super-Hubble scales, given by

$$\frac{\delta p_i(\tau,\boldsymbol{x})}{\delta\rho_i(\tau,\boldsymbol{x})} = \frac{\dot{\bar{p}}_i(\tau)}{\dot{\bar{\rho}}_i(\tau)} \equiv c^2_{\rm adi,i}(\tau)\,, \tag{3.41}$$

and the total perturbations (summed over all species) can also be described by an effective sound speed

$$\delta p = c_s^2(\tau)\delta\rho(\tau,\boldsymbol{x}) \quad \text{with} \quad c_s^2(\tau) \equiv \frac{\Sigma_i \dot{\bar{\rho}}_i(\tau) c^2_{\rm adi,i}(\tau)}{\Sigma_i \dot{\bar{\rho}}_i(\tau)}\,. \tag{3.42}$$

Hence, any set of perturbations satisfying equation 3.38 is such that the fluctuations of the total effective fluid have adiabatic properties, which is why such initial conditions are usually called *adiabatic initial conditions*.

We can also consider cases in which the initial conditions do not satisfy the adiabatic condition 3.38, for example if the perturbations are generated by more than one degree of freedom (as would be the case in multi-field inflation). More general initial conditions can be expanded on different bases, the most common of which is to assume one adiabatic mode, N decaying modes that would be irrelevant, and $N-1$ non-decaying isocurvature modes. The latter have the property that for each of them the total density perturbations vanish in the super-Hubble limit, while two species have opposite density perturbations that compensate each

other. However, current observations from the CMB put strong limits on the amplitude of such isocurvature modes [11], showing a preference for purely adiabatic initial conditions. As such, I will focus only on adiabatic initial conditions for the remainder of this chapter.

For adiabatic initial conditions we saw the relation between different density fluctuations, given in equation 3.39. Furthermore, if we only consider the case of species with no anisotropic stress, we can set $\phi = \psi$ at initial times. Inserting this and equation 3.40 in the Einstein equations, we can find a second-order differential equation for ψ, which can be shown to have two solutions during radiation domination. One of these solutions is constant in time, while the other is decaying and thus not important. The constant solution is related to the density fluctuations through

$$-2\psi = -2\phi = \delta_{\text{tot}} \simeq \delta_\gamma = \text{ constant}\,. \tag{3.43}$$

This means that for adiabatic initial conditions, and assuming that after inflation the universe is dominated by radiation, we have

$$\theta_M = \frac{3}{4}\theta_r \simeq -\frac{3}{2}\psi\,. \tag{3.44}$$

In the next section, we will see how the perturbations described here can be related to the power spectra introduced in section 2.4.

3.4 Power Spectra and Transfer Functions

The theory of cosmological perturbations is a stochastic theory, with the goal of predicting the statistical properties of perturbations at some time τ given the statistical properties at an initial time τ_{ini}. We saw in section 2.1.4 that the perturbations coming from inflation are Gaussian, which means that all fluctuations can be described entirely by their two-point correlation function. For a stochastic Gaussian field, different wavevectors are uncorrelated, and the Fourier two-point correlation function is related to to the Dirac distribution $\delta^{(3)}(\boldsymbol{k}-\boldsymbol{k}')$ via

$$\langle A(\tau,\boldsymbol{k})A^*(\tau,\boldsymbol{k}')\rangle = \delta^{(3)}(\boldsymbol{k}'-\boldsymbol{k})P_A(k)\,, \tag{3.45}$$

where $P_A(k)$ is the power spectrum of the variable A. Due to the isotropy of the universe, this power spectrum can only be a function of the wavenumber k, not of the direction $\hat{k}$. It is common to use the rescaled dimensionless power spectrum

$$\mathcal{P}_A(k) = \frac{k^3}{2\pi}P_A(k)\,, \tag{3.46}$$

as seen in equation 2.28. With this convention, $\mathcal{P}_A(k)$ represents the contribution of each logarithmic interval in wavenumber space to the two-point correlation function in real space.

We have already seen that for adiabatic initial conditions all perturbations are related to each other, and as such we only need to specify the primordial power spectrum of one quantity

to know everything about the system. By convention, it is usual to use the primordial power spectrum of the comoving curvature perturbation $\mathcal{R}$. Unlike ϕ and ψ, which get rescaled when the equation of state of the universe changes, $\mathcal{R}$ is conserved on super-Hubble scales. In the Newtonian gauge this is given by

$$\mathcal{R} = \psi - \frac{1}{3}\frac{\delta\rho_{\rm tot}}{\bar{\rho}_{\rm tot} + \bar{p}_{\rm tot}} \,. \tag{3.47}$$

We can now decompose the power spectrum of a given quantity at time τ into two parts: one accounting for initial conditions and one accounting for the linear evolution with time

$$\langle A(\tau, \boldsymbol{k}) A^*(\tau, \boldsymbol{k}') \rangle = \delta^{(3)}(\boldsymbol{k} - \boldsymbol{k}') \underbrace{\left[\frac{A(\tau, \boldsymbol{k})}{\mathcal{R}(\boldsymbol{k})}\right]^2}_{\text{transfer function}} P_{\mathcal{R}}(k) \,. \tag{3.48}$$

As we have seen that $\mathcal{R}$ is a conserved quantity on super-Horizon scales, $\mathcal{R}(\tau_{\rm ini}, \boldsymbol{k}) = \mathcal{R}(\tau, \boldsymbol{k}) = \mathcal{R}(\boldsymbol{k})$. Additionally, in an isotropic universe the equations of motion do not depend on the direction of the wavevector $\boldsymbol{k}$, and hence the *transfer function*, which accounts for the linear evolution independently of initial conditions, will be a function of k and not of $\boldsymbol{k}$. It is usual to denote the transfer function of A as[4]

$$A(\tau, k) \equiv \frac{A(\tau, \boldsymbol{k})}{\mathcal{R}(\boldsymbol{k})} \,. \tag{3.49}$$

Furthermore, we can define the primordial curvature spectrum $\mathcal{P}_{\mathcal{R}}(k)$, which first appeared in equation 2.29, as

$$\langle \mathcal{R}(\boldsymbol{k}) \mathcal{R}^*(\boldsymbol{k}') \rangle = \frac{2\pi^2}{k^3} \mathcal{P}_{\mathcal{R}}(k) \delta^{(3)}(\boldsymbol{k} - \boldsymbol{k}') \,, \tag{3.50}$$

which will allow us to express all other spectra. For example, this can be used to express the perturbations of the photon temperature as

$$\langle \Theta_{T,\ell}(\tau, \boldsymbol{k}) \Theta^*_{T,\ell}(\tau, \boldsymbol{k}) \rangle = \frac{2\pi^2}{k^3} \mathcal{P}_{\mathcal{R}}(k) \left[\Theta_{T,\ell}(\tau, k)\right]^2 \delta^{(3)}(\boldsymbol{k} - \boldsymbol{k}') \,. \tag{3.51}$$

Having seen how we can use the initial conditions given by inflation to solve the equations of motion of all perturbations, in the next section we will see how to go from perturbations to the temperature anisotropies we can observe in the CMB.

3.5 From Perturbations to Temperature Anisotropies

We now wish to explicitly relate the temperature perturbation equations seen in section 3.2 with a power spectrum, as described in the previous section. The temperature anisotropies

[4] This notation can be a bit confusing, but for some reason it is still the most usual choice in the literature.

on the last scattering surface can be expanded in spherical harmonics as

$$\frac{\delta T}{T}(\hat{n}) = \sum_{\ell m} a_{\ell m} Y_{\ell m}(\hat{n}) \,. \tag{3.52}$$

The temperature anisotropy observed in a direction $\hat{n}$ is a property of photons travelling along the direction $-\hat{n}$. Therefore, $\frac{\delta T}{T}(\hat{n})$ coincides with the function $\Theta_T(\boldsymbol{x}, -\hat{n}, \tau)$ seen in section 3.2, evaluated today ($\tau = \tau_0$). For simplicity, we can choose the origin such that $\boldsymbol{x} = \boldsymbol{o}$. We can then extract each $a_{\ell m}$ from a sky map, giving

$$a_{\ell m} = (-1)^\ell \int d\hat{n} Y^*_{\ell m}(\hat{n}) \Theta_T(\boldsymbol{o}, \hat{n}, \tau_0) \,. \tag{3.53}$$

We can make use of the Legendre expansion seen in equation 3.31 to find

$$a_{\ell m} = (-i)^\ell \int \frac{d^3k}{2\pi^2} Y_{\ell m}(\hat{k}) \Theta_{T,\ell}(\tau_0, \boldsymbol{k}) \,, \tag{3.54}$$

where we can see that there is a linear relation between multipoles $a_{\ell m}$ and Fourier modes $\Theta_{T,\ell}(\tau_0, \boldsymbol{k})$. This leads to several useful realisations. First, if the perturbations are Gaussian, the $a_{\ell m}$s will also be Gaussian distributed, and thus the corresponding two-point correlation function will fully describe their statistics. Furthermore, because the different Fourier modes are uncorrelated, the corresponding multipoles are also uncorrelated. Finally, the isotropic universe implies an isotropic power spectrum in Fourier space, which also implies an isotropic harmonic spectrum which will only depend on ℓ and not on m

$$C_\ell = \langle a_{\ell m} a^*_{\ell m} \rangle \,. \tag{3.55}$$

This harmonic power spectrum is the quantity we want to compute for a given cosmological model, as we can compare it to observations[5]. However, the true harmonic spectrum of our universe can not be extracted from observations, as we only have access to one universe[6], and thus we only observe one realisation of the underlying theory. However, by using an assumption of ergodicity, we can build an estimator of the true power spectrum

$$C^{obs}_\ell = \frac{1}{2\ell + 1} \sum_{-\ell \leq m \leq \ell} |a^{obs}_{\ell m}|^2 \,. \tag{3.56}$$

This estimator is obtained by averaging over $(2\ell + 1)$ independent Gaussian numbers centred at zero, each with variance C_ℓ. As such, it follows a χ^2 distribution with a mean equal to C_ℓ and a variance $\sqrt{2/(2\ell + 1)} C_\ell$. The variance decreases with increasing ℓ, as for higher multipoles we can average over more independent realisations of the same stochastic process. This deviation plays the role of a theoretical error, and is known as *cosmic variance*.

[5] This is basically what cosmologist do all day.
[6] Someone should build another universe.

Now that we have seen how to go from the C_ℓs to the observational quantity, we want to do the opposite process and relate the harmonic power spectrum to the temperature perturbations. We can make use of equation 3.51, together with the definition of $a_{\ell m}$s from equation 3.54 and the harmonic expansion seen in 3.55 to find

$$C_\ell = \frac{1}{2\pi^2} \int \frac{dk}{k} \left[\Theta_{T,\ell}(\tau_0, k)\right]^2 \mathcal{P}_\mathcal{R}(k) \,. \tag{3.57}$$

In order to compute the temperature anisotropy up to some multipole $\ell_{\max}$, a brute-force approach would be to integrate all equations with at least $\ell_{\max}$ multipoles in the Boltzmann hierarchy for the evolution of the photon distribution, between some initial time and today. Of course this is a very time consuming process[7], and it does not provide much knowledge of the underlying physics. Instead of this brute-force approach, it is common to use the *line-of-sight* formalism, first introduced in [51].

We want to integrate the Boltzmann equation for photons, equation 3.19, along the line-of-sight. For now, in order to obtain a more qualitatively understanding of the results, I will stay in real space, and ignore the effects of polarisation. In real space, we can combine the collisional term 3.30 and the evolution of the phase-space distribution of photons, equation 3.29, to find the generalised Boltzmann equation for photons

$$\dot{\Theta}_T + \hat{n} \cdot \boldsymbol{\nabla} \Theta_T - \dot{\phi} + \hat{n} \cdot \boldsymbol{\nabla} \psi = a n_e \sigma_T \left(\Theta_{T,0} - \Theta_T - \hat{n} \cdot \boldsymbol{v}_b\right) \,, \tag{3.58}$$

where $\boldsymbol{v}_b$ is the bulk velocity of baryons and electrons.

Before proceeding, it is useful to remember that the total derivative of a function $\mathcal{F}(\tau, \boldsymbol{x}, \hat{n})$ along the past light cone of a photon coming from direction $\hat{n}$ is given by

$$\frac{d\mathcal{F}}{d\tau} = \dot{\mathcal{F}} + \frac{d\boldsymbol{x}}{d\tau} \cdot \boldsymbol{\nabla} \mathcal{F} = \dot{\mathcal{F}} + \hat{n} \cdot \boldsymbol{\nabla} \mathcal{F} \,, \tag{3.59}$$

where I have used the straight line approximation for the photon geodesics, $d\hat{n}/d\tau = 0$.

Furthermore, it is convenient to introduce the integral of the scattering rate along the line-of-sight

$$\kappa(\tau) \equiv \int_\tau^{\tau_0} d\tau a n_e \sigma_T \tag{3.60}$$

which is known as the *optical depth*[8]. Furthermore, we can use the optical depth to define the visibility function $g(\tau) \equiv -\dot{\kappa}(\tau) e^{-\kappa(\tau)}$, which can be interpreted as the probability of a photon which scattered at a time τ reaching us today.

We can now compute the total derivative of the function $e^{-\kappa}(\Theta_T + \psi)$ along the trajectory between the last scattering surface and us by using equation 3.59, where I have added the

[7] Life is too short for such integrations.
[8] This is not too dissimilar to the reionisation depth discussed in section 1.8.3.

exponential prefactor to make use of the visibility function later on. This will give us

$$\begin{aligned}\frac{d}{d\tau}\left[e^{-\kappa}(\Theta_T+\psi)\right] &= -\kappa e^{-\kappa}(\Theta_T+\psi)+e^{-\kappa}\left[\dot{\Theta}_T+\dot{\psi}+\hat{n}\cdot\boldsymbol{\nabla}(\Theta_T+\psi)\right]\\ &= g(\Theta_{T,0}+\psi+\hat{n}\cdot\boldsymbol{v}_b)+e^{-\kappa}(\dot{\phi}+\dot{\psi})\,,\end{aligned} \tag{3.61}$$

where in the second equality I have used $\dot{\kappa}=-an_e\sigma_T$. We can now integrate this along the line-of-sight between some arbitrary initial time $\tau_{\rm ini}$, well before photon decoupling, and the present τ_0. This yields

$$(\Theta_T+\psi)|_{\rm obs}=\int_{\tau_{\rm ini}}^{\tau_0}d\tau\left[g(\Theta_{T,0}+\psi+\hat{n}\cdot\boldsymbol{v}_b)\right]+e^{-\kappa}(\dot{\phi}+\dot{\psi})\,, \tag{3.62}$$

with the index "obs" indicating a quantity evaluated at the coordinate $(\tau_0,\boldsymbol{o},\hat{n})$. The first term on the left-hand side is the temperature fluctuation of photons coming from a direction $\hat{n}$ observed today. The second term is the metric fluctuation today at the location of the observer. However, this is very small and can not be experimentally distinguished from an overall temperature shift. As such, we can ignore this term.

In order to understand the different physical effects at play, it is useful to make the *instantaneous decoupling approximation*, in which all photons are assumed to decouple precisely at the time $\tau_{\rm dec}$, and the visibility function can be replaced by a Dirac delta. In this limit we can rewrite equation 3.62 as

$$\Theta_T|_{\rm obs}=\underbrace{(\Theta_T+\psi)|_{\rm dec}}_{\rm SW}+\underbrace{\hat{n}\cdot\boldsymbol{v}_b|_{\rm dec}}_{\rm Doppler}+\underbrace{\int_{\tau_{\rm dec}}^{\tau_0}d\tau(\dot{\phi}+\dot{\psi})}_{\rm ISW}\,. \tag{3.63}$$

There are three main physical effects contributing to equation 3.63:

- The first term is the Sachs-Wolfe (SW) term, which includes the intrinsic temperature term $\Theta_{T,0}$ and the gravitational Doppler shift term ψ at one point on the last scattering surface. As expected, the largest contribution to the observed temperature fluctuation in one direction is given by the intrinsic temperature fluctuation on the last scattering surface in the same direction, and so the SW term is the dominant effect for describing large angular patterns on CMB maps. Making use of the result found for adiabatic initial conditions (equation 3.40) and the (00) component of the Einstein equations, we find

$$\begin{aligned}4\Theta_{T,0}=\delta_\gamma=\frac{4}{3}\theta_b=-2\phi=-2\psi \quad &\text{radiation domination}\,,\\ 4\Theta_{T,0}=\delta_\gamma=\frac{4}{3}\theta_b=-\frac{8}{3}\phi=-\frac{8}{3}\psi \quad &\text{matter domination}\,,\end{aligned} \tag{3.64}$$

  At the time of decoupling, the universe is matter dominated. Assuming that the SW term dominates, we have

$$\Theta_T|_{\rm obs}=(\Theta_{T,0}+\psi)|_{\rm dec}=\frac{1}{3}\psi|_{\rm dec}=-\frac{1}{8}\theta_\gamma|_{\rm dec}\,, \tag{3.65}$$

which shows that the gravitational term dominates over the pressure term. This means that an over-density ($\theta_\gamma > 0$) on the last scattering surface leads to a cold spot in the observed CMB map ($\Theta_T < 0$)[9].

- The second term we see is the standard Doppler term. At the time of decoupling, photons are emitted from the tightly coupled baryon-electron fluid with a different peculiar velocity at each point on the last scattering surface. When we do the projection along the line-of-sight, it will introduce a Doppler shift in the photon wavelength.
- The last term is called the Integrated Sachs-Wolfe (ISW) contribution, and contains all non-conservative gravitational effects; along the line-of-sight, photons are constantly redshifted and blueshifted by metric fluctuations. The temperature is shifted by two main effects: gradients in the gravitational potential ψ, which account for the gain or loss of energy of photons feeling gravitational forces; and time variations in the metric fluctuation ϕ, representing a local correction to the average time dilation, responsible for the cosmological redshift in an expanding universe. This can be understood in the following way: a photon entering a potential well will gain energy, and if the value of the potential does not change, it will lose the same amount of energy when exiting the well. However, any changes to the amplitude of the potential well will affect the net photon energy. The ISW effect comes mainly from two time periods: just after photon decoupling and during Λ domination. These are referred to as Early Integrated Sachs-Wolfe (EISW) and Late Integrated Sachs-Wolfe (LISW) respectively.

While expression 3.63 is very informative about the underlying physical mechanisms, it is not directly useful to compute the CMB power spectrum from equation 3.57, as we would instead need it in Fourier space and for each multipole moment ℓ. Following a similar procedure, we find the final result for temperature anisotropies to be

$$\begin{aligned}\Theta_{T,\ell}(\tau_0,k) &= \int_{\tau_{\rm ini}}^{\tau_0} d\tau S_T(\tau,k) j_\ell(k(\tau_0-\tau))\,,\\ S_T &\equiv \underbrace{g(\Theta_0+\psi)}_{\rm SW} + \underbrace{\frac{d}{d\tau}\left(\frac{g}{k^2}\theta_b\right)}_{\rm Doppler} + \underbrace{e^{-\kappa}\left(\dot\phi+\dot\psi\right)}_{\rm ISW} - \underbrace{\left(\frac{3}{4k^2}\frac{d^2}{d\tau^2}\left(\Pi g\right)+\frac{1}{4}\Pi g\right)}_{\rm Polarisation}\,,\end{aligned} \tag{3.66}$$

where I have introduced the shorthand notation

$$\Pi = \frac{1}{4}\left(\Theta_{T,2}+\Theta_{P,2}+\Theta_{P,0}\right)\,. \tag{3.67}$$

Similarly, for the polarisation we find [52]

$$\begin{aligned}\Theta_{P,\ell}(\tau_0,k) &= \sqrt{\frac{(\ell+2)!}{(\ell-2)!}}\int_{\tau_{\rm ini}}^{\tau_0} d\tau S_P(\tau,k) j_\ell(k(\tau_0-\tau))\,,\\ S_P &\equiv \frac{3g\Pi}{4k^2(\tau_0-\tau)^2}\,.\end{aligned} \tag{3.68}$$

[9] Photons in an over-dense region will lose a lot of energy escaping the gravitational well.

In both cases, we see that $\Theta_{T,P}$ is given by the convolution of spherical Bessel functions $j_\ell(x)$ and a source term $S_{T,P}$, which contains the same three terms discussed above. We can once again make use of the instantaneous decoupling approximation to find an expression for $\Theta_{T,\ell}$, which shows that the total C_ℓ can be decomposed into five parts: the power spectra of the SW, Doppler, and ISW terms; a sub-dominant polarisation contribution; and all cross terms (as $\Theta_{T,\ell}$ will be squared in equation 3.57).

For high ℓs the spherical Bessel function $j_\ell(x)$ (and its derivative) is very peaked near $x = \ell$, and so for the SW and Doppler contributions to the spectrum the integral in equation 3.57 will mainly pick up modes with $k = \ell/(\tau_0 - \tau_{\rm dec})$. This result can also be justified geometrically from the definition of the multipole $\ell = \pi/\theta$, where θ is the angle that subtends the physical scale $\theta \times d_A(z_{\rm dec})$ on the last scattering surface, where $d_A(z_{\rm dec})$ is the angular diameter distance defined in equation 1.22. In the case of spherical harmonics, θ is the angle between a maximum and a minimum of the density wave. This leads us to the following relation between k and ℓ

$$\frac{\lambda}{2} = a(\tau_{\rm dec})\frac{\pi}{k} = \theta d_A(z_{\rm dec}) \quad \Rightarrow \quad \frac{a(\tau_{\rm dec})}{k} = \frac{d_A(z_{\rm dec})}{\ell}\,. \tag{3.69}$$

In a flat universe, where we have $d_A(z_{\rm dec}) = a(\tau_{\rm dec})\,(\tau_0 - \tau_{\rm dec})$, we obtain

$$k = \frac{\ell}{\tau_0 - \tau_{\rm dec}}\,. \tag{3.70}$$

This allows us to approximately see how the different terms contribute to the power spectrum in the instantaneous decoupling limit

$$\begin{aligned} C_\ell^{\rm SW} &\sim \langle|\Theta_{T,0} + \psi|^2\rangle \quad \text{at } (\tau_{\rm dec}, k) \simeq (\tau_{\rm dec}, \ell/(\tau_0 - \tau_{\rm dec}))\,, \\ C_\ell^{\rm Doppler} &\sim \langle|\theta_b|^2\rangle \quad \text{at } (\tau_{\rm dec}, k) \simeq (\tau_{\rm dec}, \ell/(\tau_0 - \tau_{\rm dec}))\,, \\ C_\ell^{\rm ISW} &\sim \int_{\tau_{\rm dec}}^{\tau} d\tau(\tau_0 - \tau)\langle|\dot\phi + \dot\psi|^2\rangle \quad \text{for all } (\tau_{\rm dec}, k) \simeq (\tau_{\rm dec}, \ell/(\tau_0 - \tau))\,. \end{aligned} \tag{3.71}$$

While this is good as an approximation, for a completely accurate calculation one needs to use a Boltzmann code, such as CLASS [53] or CAMB [54].

Now that we have seen how to calculate the power spectrum of the temperature anisotropies, we can describe some of its main features, and gain some insight into what causes the acoustic peaks and overall shape. This will allow us to better connect this observable with the underlying cosmological model.

As we saw in section 1.8.3, at early times the baryon and photon fluids are tightly coupled, with $an_e\sigma_T \equiv \Gamma_\gamma \gg H$. At this time, we can combine the Boltzmann equations for photons (equation 3.32) and the ones for baryons (equation 3.35) to find

$$\ddot\Theta_{T,0} + \frac{\dot R}{1+R}\Theta_{T,0} + k^2 c_s^2 \Theta_{T,0} = -\frac{k^2}{3}\psi + \frac{\dot R}{1+R}\dot\phi + \ddot\phi\,, \tag{3.72}$$

where I have introduced the baryon-to-photon ratio $R \equiv 3\rho_b/(4\rho_\gamma)$ and the sound speed at which density waves propagate in the effective photon-baryon fluid, given by

$$c_s^2 = \frac{\delta p_\gamma + \delta p_b}{\delta \rho_\gamma + \delta \rho_b} = \frac{1}{3(1+R)} \,. \tag{3.73}$$

We can see that equation 3.72 corresponds to a damped, driven harmonic oscillator, with a pressure term $k^2 c_s^2 \Theta_{T,0}$, a baryon-induced damping term $\frac{\dot{R}}{1+R}\Theta_{T,0}$, and a gravitational term on the right-hand side. When the universe is completely dominated by radiation ($R \ll 1$) and in the absence of forces, equation 3.72 reduces to

$$\ddot{\Theta}_{T,0} + k^2 c_s^2 \Theta_{T,0} = 0 \quad \Rightarrow \quad \Theta_{T,0} \propto \cos\left(k c_s \tau\right) \,. \tag{3.74}$$

It is now useful to introduce the *comoving sound horizon*

$$r_s \equiv \int_{\tau_{\rm ini}}^{\tau} c_s d\tau \tag{3.75}$$

which represents the comoving distance travelled by a wavefront from some arbitrary time $\tau_{\rm ini}$ deep inside the radiation-dominated regime. At the time of decoupling this reaches its maximum value, and gives the correlation length between density fluctuations (or temperature fluctuations in CMB maps). This quantity can additionally be calculated for a given cosmological model. Thus, as discussed in section 1.4, it is a standard ruler and can be used to measure cosmological distances.

Recovering equation 3.74, we can see from the argument of the cosinusoidal function that if $\lambda = 2\pi a/k \gg a r_s$, the solution will be constant, while for $\lambda < a r_s$ we will have an oscillatory regime corresponding to the propagation of acoustic waves. Thus, modes start to oscillate when their wavelength becomes smaller than the sound horizon. The full evolution of wavelengths as a function of conformal time is sketched in Fig. 3.1 and discussed in detail below.

Modes that are super-Hubble today were frozen at all times in the past, with their value today given by their initial value. Modes in region 1 of Fig. 3.1 experience driven oscillations due to the gravitational terms. This enhances their amplitude and shifts the zero-point of oscillations, due to the metric potential quickly decaying inside the sound horizon. This shifting of the zero-point of oscillations to negative values leads to odd peaks in the power spectrum appearing higher than even peaks.

Modes deep inside the sound horizon during radiation domination correspond to region 2. Here the metric term is negligible and $R \ll 1$, and thus the modes experience acoustic oscillations that are described by equation 3.74.

Modes in region 3 were inside the sound horizon during the stage between matter-radiation equality and photon decoupling, which means that R can no longer be neglected. This leads to damped acoustic oscillations, as the oscillator has a friction term and a decreasing time-varying frequency.

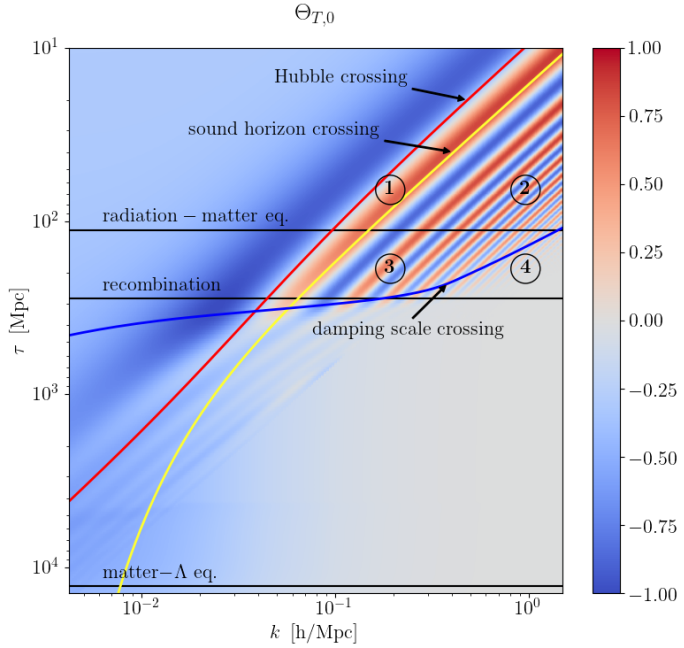

FIGURE 3.1: Evolution of k as a function of conformal time, showing the different regions of interest for the power spectrum. Figure made with CLASS.

Finally, modes in region 4 have smaller wavelength than the diffusion scale in the photon-baryon fluid. Close to recombination the tight-coupling approximation breaks down, and the photons can travel a comoving distance between the early universe and some time τ given by

$$r_d^2(\tau) \sim \int_{\tau_{\rm ini}}^{\tau} d\tau \Gamma_\gamma r_\gamma = \int_{\tau_{\rm ini}}^{\tau} \frac{d\tau}{a n_e \sigma_T} \,, \tag{3.76}$$

where r_γ is the photon mean free path in comoving space. Thus, photon diffusion will erase perturbations with a wavelength smaller than $\lambda_d = a r_d$, corresponding to a wavenumber greater than $k = 2\pi/r_d$. This effect is known as diffusion damping or *Silk damping*.

After photon decoupling, the baryons will start to fall into the dark matter potential wells, and the baryon perturbations will start to grow asymptotically until reaching the dark matter perturbations. This will be revisited in section 4.2.

In this chapter we have seen how to understand the perturbations of the early universe that lead to the complex structures and properties of the universe around us. We have derived the equations needed to describe the evolution of the main species in the universe. Linear perturbation theory allows us to trace a narrative from the fluctuations seeded by inflation to temperature fluctuations we observe in the CMB map. Armed with this knowledge, in the following chapter we will see how cosmological observations allow us to understand the underlying cosmological model.

Part II

Observing the Universe

4 Cosmological Observables

In the previous sections, I gave an introduction to the main pieces needed to understand the universe around us. Furthermore, the current standard model of cosmology was introduced, as well as its predictions for our universe. These predictions need to be tested[1], and the best way to do that is to make observations. Fortunately, the universe provides many different data sets we can use to constrain our models[2].

In this chapter I will introduce several different data sets we can acquire from the universe: the CMB temperature anisotropies; the matter power spectrum (obtained from analysing structures on many different scales); the Lyman-α forest, which comes from the smallest structures possible; and spectral distortions to the thermal blackbody of the CMB. Together, these observations allow us to test our understanding of the universe at many different scales.

4.1 Cosmic Microwave Background

In section 1.8.3 we saw that in the early universe all species were in thermal equilibrium, with each species decoupling from the others as the interactions maintaining this equilibrium became inefficient. The last component to decouple was the photons, which were being kept in thermal equilibrium via electromagnetic scattering, driven by Compton scattering ($e^- + \gamma \rightarrow e^- + \gamma$) and Coulomb scattering ($e^- + p \rightarrow e^- + p$). This last decoupling happened at a redshift of $z \sim 1100$, once neutral hydrogen could form via the reaction $e^- + p \rightarrow H + \gamma$. As a consequence of this reaction, the free electron density dropped off sharply, leading to Compton scattering becoming inefficient. As such, the photons stopped scattering and decoupled (producing the last scattering surface), leading to a background of photons we observe today known as the *Cosmic Microwave Background*.

The CMB was first predicted in 1948 by Gamow [55], and later by Alpher and Herman [56]. However, it did not gain interest in mainstream cosmology until 1964, when Penzias and Wilson found an unexplained background thermal radiation in their radio telescope [57]. Upon closer investigation, it was found that this background signal corresponded to the predicted CMB [58], an accidental discovery that led to Penzias and Wilson winning the Nobel Prize in Physics in 1978[3]. Later observations showed the CMB to have a thermal blackbody spectrum (to first order), as expected within the standard cosmological model. Furthermore, it was predicted in the 1970s that to explain the observed structure of the universe, the early universe

[1] If a model can not make testable observations, it is not a very useful model.
[2] A whole other universe would also be useful, as we saw in the previous chapter.
[3] Accidental discoveries are more Nobel Prize worthy than Rubin finding the first hints of dark matter, it seems.

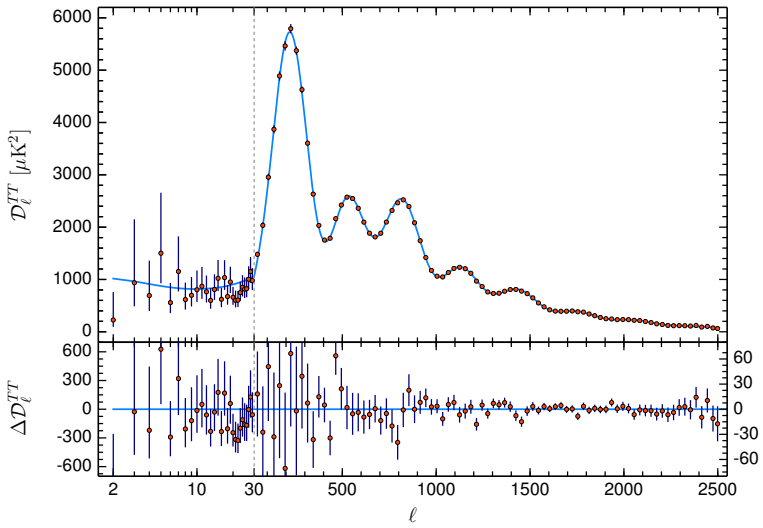

FIGURE 4.1: Temperature power spectrum, normalised with an initial temperature as D_ℓ^{TT}, as measured by Planck 2018. The base ΛCDM theoretical spectrum best-fit is plotted in light blue in the upper panel. Residuals with respect to this model are shown in the lower panel. Image taken from [19].

would need to have small inhomogeneities that would manifest themselves as anisotropies in the CMB [59] (as discussed in section 3.5).

The first experiment to successfully map the CMB was COBE [9] in 1992. The results from COBE showed a largely-homogeneous CMB temperature, with the predicted anisotropies. This experiment was followed by WMAP in 2001 [10], which collected data for nine years. The latest experiment to measure the CMB was the Planck satellite [11], launched in 2009. Planck has provided incredible CMB maps (see Fig. 1.1), as well as giving us percent-precision measurements of the main cosmological parameters, as discussed in 1.6. The latest measurements reveal the CMB to be at an average temperature of $T_{\rm CMB} = 2.7255 \pm 0.0006\,\mathrm{K}$ with anisotropies only on the order of $\Delta T/T \sim 10^{-5}$, as expected [11].

In order to understand how we are able to constrain the ΛCDM parameters from the CMB, we can recover the discussion from section 3.4, where we saw that the anisotropies can be expressed as a power spectrum C_ℓ, which can further be classified as a temperature spectrum C_ℓ^{TT} and a polarisation spectrum C_ℓ^{EE} (plus additional correlation spectra, not discussed here). The latest temperature spectrum from the CMB as measured by Planck is shown in Fig. 4.1, while Fig. 4.2 displays the polarisation power spectrum.

As discussed in the previous section, the shape of the CMB power spectrum can be understood in the following way:

- For $\ell \ll 100$, modes are outside the sound horizon at decoupling, and the spectrum is described by a Sachs-Wolfe plateau given by the primordial spectrum amplitude and tilt. An additional tilting takes place due to the LISW effect.

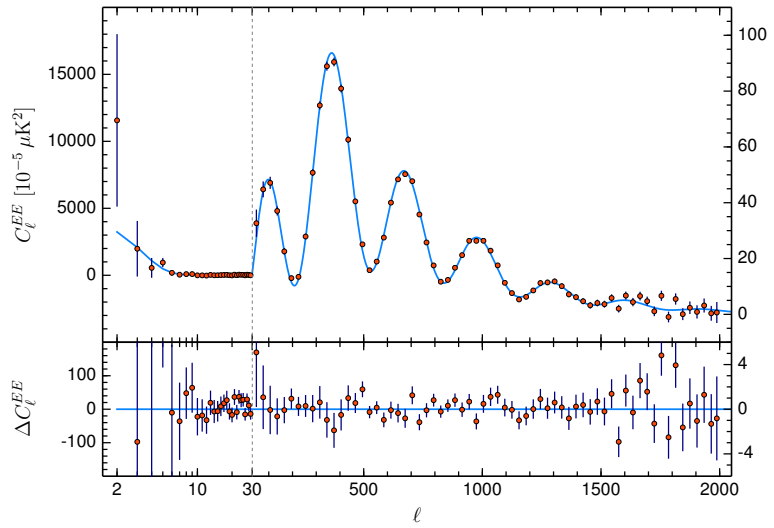

FIGURE 4.2: Polarisation power spectrum C_ℓ^{EE}, as measured by Planck 2018. The base ΛCDM theoretical spectrum best-fit is plotted in light blue in the upper panel. Residuals with respect to this model are shown in the lower panel. Image taken from [19].

- For $l \geq 100$, the spectrum contains a series of acoustic peaks which corresponds to the fundamental modes and harmonic decomposition of the sound horizon at decoupling, modified slightly by the Doppler peaks. Several different effects modify these modes; their amplitude receives an overall suppression during the transition era between equality and decoupling, odd peaks are enhanced with respect to even peaks when the baryon content of the universe increases, the first peak is enhanced by the EISW, and diffusion damping causes an exponential suppression at higher ℓ.
- Reionisation, discussed briefly in section 1.8.3, leads to a scale independent suppression of power accounted for by an exponential factor, affecting all modes that were inside the Hubble horizon at reionisation ($\ell \geq 40$).

To relate the observed CMB to the ΛCDM model, we can recover the six ΛCDM parameters first discussed in section 1.6: the overall amplitude of the primordial power spectrum A_s and the primordial tilt n_s, as described in section 2.4; the baryon density $\omega_b = \Omega_b h^2$; the total non-relativistic matter content, $\omega_M = (\Omega_b + \Omega_{\rm CDM})\, h^2$; the dark energy density fraction Ω_Λ (as we are assuming a flat universe, this will be related to the Hubble parameter via $h = \sqrt{\omega_M/(1-\Omega_\Lambda)}$); and the optical depth to reionisation $\tau_{\rm reio}$, as discussed in section 1.8.3.

The different degrees of freedom controlling the shape of the CMB temperature spectrum are the following:

(C1) **Peak scale**: The peak location depends on the horizon angular scale, given by $\theta_s(z_{\rm dec}) = r_s(z_{\rm dec}) d_A(z_{\rm dec})$. The sound horizon depends on the sound speed and expansion history before decoupling, and is thus affected by ω_b and ω_M. The angular diameter distance, on

the other hand, depends on the expansion era after decoupling, and is thus controlled by Ω_Λ as well.

(C2) **Odd/even ratio**: The ratio of odd/even peaks depends on the balance between gravity and pressure in the tightly coupled photon-baryon fluid before decoupling, thus it depends on (ω_b/ω_γ).

(C3) **Amplitude of peaks**: The overall amplitude of all peaks depends on the amount of expansion between equality and decoupling, due to the damped acoustic oscillations during matter domination. Additionally, the first peak is affected by the EISW effect. The overall amplitude is thus controlled by (ω_M/ω_γ): decreasing ω_M leads to higher peaks, especially the first one.

(C4) **Damping envelope**: The damping envelope at large ℓs is controlled by the diffusion length, and thus by the expansion and decoupling history before recombination. This effect is only significant close to decoupling, and so it mostly depends on ω_b (setting the number of free electrons) and ω_M (setting the expansion rate).

(C5) **Global amplitude**: The global amplitude of the temperature power spectrum is proportional to the amplitude of the primordial power spectrum A_s.

(C6) **Global tilt**: Likewise, the global tilt of the temperature power spectrum depends on the tilt of the primordial power spectrum n_s.

(C7) **Additional plateau tilting**: The slope of the Sachs-Wolfe plateau is affected both by the tilt n_s and by the LISW, which enhances the lower multipoles. The amplitude of the LISW effect depends on the duration of the Λ-domination stage, and is thus dependent on Ω_Λ, with a higher Ω_Λ leading to an enhanced LISW effect.

(C8) **Amplitude for $\ell \geq 40$**: The global amplitude of the spectrum at $\ell \geq 40$ is exponentially suppressed by a factor $\exp(-\tau_{\rm reio})$, due to the amount of photon rescattering after reionisation.

With these effects, we can see that the six ΛCDM parameters can be constrained with a precise measurement of the temperature anisotropies. There is a slight caveat to this, though: cosmic variance on small ℓs is very large, as discussed in section 3.5, and thus the effects that influence the lower multipoles are not easily disentangled ((C7) and a combination of (C5) and (C8)). This leads to a partial degeneracy between A_s and $\tau_{\rm reio}$, which can be solved by using the polarisation angular power spectrum from the CMB. The polarisation spectrum C_ℓ^{EE} is affected by similar, if somewhat simpler, effects as (C1)-(C7), but it receives a significantly bigger correction around reionisation known as the "reionisation bump" (at $\ell \sim 40$).

If the early universe only features Gaussian scalar perturbations on cosmological scales, all the information contained in CMB maps[4] is encoded in the temperature power spectrum C_ℓ^{TT}, the E-mode polarisation spectrum C_ℓ^{EE}, and the cross-correlation spectrum C_ℓ^{TE} (not discussed here). Additionally, if tensor modes are produced in the primordial universe (see section 2.4),

[4] "All" is a bit of an exaggeration, as we will see in section 4.4.

we would have a B-mode polarisation spectrum C_ℓ^{BB} (the cross-correlations of the B-mode vanish due to parity symmetry). Furthermore, there can be secondary effects on the CMB in the form of CMB lensing, caused by large scale structures (similar to the weak lensing discussed in section 1.9.1). This would lead to a $C_\ell^{\phi\phi}$ spectrum, which will not be covered here but is discussed extensively in the literature, for example in [60].

With this in mind, we can see that the CMB provides a wealth of information about the universe, and allows us to obtain very precise measurements of the underlying ΛCDM parameters. It also places constraints on many other models, as any other cosmological model beyond ΛCDM would only be able to impact the CMB very minimally to avoid existing constraints. Given the amount of information contained in the CMB, it is not surprising that it is often referred to as the holy grail of cosmology.

4.2 Matter Power Spectrum

In section 3.5 we saw how to go from the early universe perturbations to the temperature anisotropies, and in the previous section we saw how to actually observe these anisotropies. In addition, we have another very powerful probe to study the universe: the *power spectrum of the matter perturbations*, which allows us to map the growth of structures in the universe.

As we saw in section 1.6, the main contributions to the matter content of the universe are baryons and dark matter. As in the Standard Model of particle physics neutrinos are massless, for now we will ignore their effects (this will be revisited in section 6.2). As such, in the context of large scale structure observables, we can define the matter power spectrum $P(z,k)$ of the non-relativistic matter fluctuation δ_M as

$$\langle \delta_M(z,\boldsymbol{k})\delta_M^*(z,\boldsymbol{k}')\rangle = \delta\left(\boldsymbol{k}-\boldsymbol{k}'\right)P(z,k) \quad \text{with} \quad \delta_M = \frac{\delta\rho_M}{\bar{\rho}_M} = \frac{\delta\rho_b + \delta\rho_{\rm CDM}}{\bar{\rho}_b + \bar{\rho}_{\rm CDM}}\,. \tag{4.1}$$

In section 3.4 we saw that for Gaussian initial conditions, and as long as the perturbations are linear, the power spectrum at a given time can be written as the product of the primordial spectrum and the square of the relevant transfer function. Assuming a power-law primordial spectrum, as seen in equation 2.31, we find

$$P(z,k) = \frac{2\pi^2}{k^3}A_s\left(\frac{k}{k_\star}\right)^{n_s-1}\delta_M^2(z,k)\,, \tag{4.2}$$

where $\delta_M^2(z,k)$ is the matter transfer function.

To properly study this transfer function, I start with the assumption that we only have cold dark matter, and then later I will add the baryon contributions. Working in the Newtonian gauge, we can combine the Continuity equation 3.11 and Euler equation 3.12 from section 3.1 to find

$$\ddot{\delta}_{\rm CDM} + \frac{\dot{a}}{a}\dot{\delta}_{\rm CDM} = -k^2\psi + 3\ddot{\phi} + 3\frac{\dot{a}}{a}\dot{\phi}\,, \tag{4.3}$$

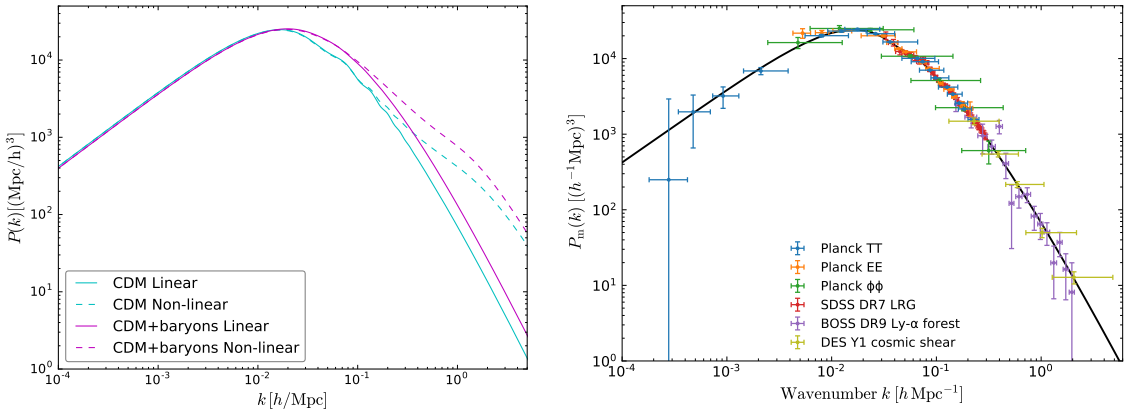

FIGURE 4.3: *Left*: Linear matter power spectrum (solid) at $z = 0$, calculated with CLASS using the best-fit ΛCDM values [19], with cold dark matter with (magenta) and without baryons (cyan). The non-linear matter power spectrum, computed with HALOFIT, is shown for the same models (dashed). *Right*: The linear matter power spectrum at $z = 0$ inferred from different cosmological probes, with the Planck 2018 best-fit shown in black. Right image taken from [11].

where the second term on the left-hand side accounts for the Hubble friction, the first term on the right-hand side represents the gravitational forces, and the last two terms account for dilation effects.

We know that all perturbations are frozen on super-Hubble scales, and thus we are only interested in the evolution of the sub-Hubble modes. As an overview of the evolution of metric perturbations, during radiation domination super-horizon scales are constant, while sub-horizon scales oscillate with a quickly decaying amplitude. During matter domination metric potentials are frozen on all scales, and thus we can safely neglect dilation effects. Furthermore, it is possible to neglect radiation perturbations *regardless* of their size, as they behave as *fast-modes* oscillating rapidly and averaging out to zero. Thus, we can use the Poisson equation to find the *Mészáros equation*, which is roughly valid at all times

$$\ddot{\delta}_{\rm CDM} + \frac{\dot{a}}{a}\dot{\delta}_{\rm CDM} - 4\pi G a^2 \bar{\rho}_{\rm CDM}\delta_{\rm CDM} = 0\,. \tag{4.4}$$

With this expression we can see the behaviour in several different stages of the universe: during radiation domination the growing mode scales like $\delta_{\rm CDM} \propto \log(k\tau)$; during matter domination $\delta_{\rm CDM} \propto \tau^2$; and during Λ domination we would need to use the Friedmann equation with both $\rho_{\rm CDM}$ and ρ_Λ, which would lead to a k-independent growth rate suppression. With this in mind, we can now understand the shape of the matter power spectrum (pending baryon corrections), as shown in Fig. 4.3:

- At initial times, the power spectrum scales like $P(k) \propto k^{-3}k^{n_s-1} = k^{n_s-4}$, with an amplitude given by A_s.
- During radiation domination, modes inside the Hubble radius grow logarithmically,

proportional to $\log(k\tau)$. At equality, super-Hubble modes ($k < k_{eq}$) still maintain their shape from early times, while sub-Hubble modes ($k > k_{eq}$) are enhanced by a factor $[\delta_{\rm CDM}(\tau_{eq}, k)/\delta_{\rm CDM}(\tau_{ini}, k)]^2 \simeq [\log(k\tau_{eq})]^2$. Thus, the $k > k_{eq}$ asymptote is given by $P(k) \propto k^{n_s-4} [\log(k)]^2$

- Before Λ domination begins at τ_Λ, modes inside the horizon will grow $\propto \tau^2$, and the matter power spectrum for these modes will be enhanced by a factor $(\tau_{eq}/\tau_\Lambda)^4$. Modes entering the horizon during matter domination, however, will be more or less enhanced depending on their time of crossing, and thus the power spectrum receives a scale-dependent enhancement $\propto (k\tau_\Lambda)^4$. Therefore, the $k < k_{eq}$ asymptote is given by $P(k) \propto k^{n_s-4}k^4 = k^{n_s}$.

- Finally, during Λ domination the scale-independent reduced growth rate does not change the asymptotic shape of the power spectrum for modes already inside the horizon at τ_Λ.

Now that we have seen the overall behaviour of the matter power spectrum, we can see how it changes when we consider baryons as well. We know that at early times baryons are tightly coupled to the photons and will follow their behaviour. Due to the significantly higher photon fraction compared to baryon fraction, the baryons do not instantaneously stop noticing the effects of the photons at decoupling. Indeed the photons continue to be *dragged* by the baryons until the *baryon drag* time[5], defined as

$$\tau_{\rm dr}(\tau) = \int_\tau^{\tau_0} d\tau' R_\gamma \approx 1\,, \tag{4.5}$$

where I have recovered the baryon-photon coupling coefficient R_γ from equation 3.36. When baryons and photons are coupled this quantity tends to infinity, it is close to 1 at baryon drag time, and it goes to 0 in the decoupled limit when baryons collapse into gravitational wells.

The behaviour of the transfer function $\delta_b(\tau, k)$ before baryon drag time follows from the behaviour of the photon transfer function, as seen in section 3.5: $\delta_b = \frac{3}{4}\delta_\gamma$ (from equation 3.40) is constant on super-sound-horizon scales, experiences stationary oscillations on sub-sound-horizon scales during radiation domination, and undergoes damped oscillations on sub-sound-horizon scales during matter domination. As the baryons will be tightly coupled to photons before baryon drag time they will not affect the dark matter transfer function $\delta_{\rm CDM}(\tau, k)$ and so this will still behave as described above, obeying the Mészáros equation.

After baryon drag time, the baryons collapse into gravitational wells, meaning that δ_b grows, and thus the dark matter will start to feel the gravitational effects of baryons. Eventually, as the two species are collisionless and feel the same gravitational forces, they will equilibrate to $\delta_b = \delta_{\rm CDM}$. Hence, after a quick relaxation period, the power spectra of baryons and dark matter will be equal, and we can envision three different scenarios:

- In the limit $\omega_b \ll \omega_{\rm CDM}$, the matter power spectrum would be fully encompassed by the dark matter only scenario, described above.

[5]Of course the baryon drag time should actually be called "the end of the baryon drag time", but that is too cumbersome.

- In the limit $\omega_b \gg \omega_{\rm CDM}$, the power spectrum would be significantly suppressed with respect to what is described above, with a much more negative slope, and very large oscillations corresponding to photon-baryon acoustic waves before decoupling.
- If $\omega_b < \omega_{\rm CDM}$ (but of the same order of magnitude), the power spectrum will depart slightly from the pure dark matter case, with a smooth step-like suppression and small oscillatory patterns.

The observation in the matter power spectrum of these small oscillatory patterns, known as the Baryon Acoustic Oscillations (BAO), represents clear evidence of baryon-photon acoustic oscillations happening before photon decoupling. As this is an intrinsic behaviour of ΛCDM, this observation helped solidify ΛCDM as the standard cosmological model.

Now that we have described the full shape of the matter power spectrum, we can see how this can be related to the underlying cosmological parameters, as we did for the CMB. We recover all the ΛCDM parameters except $\tau_{\rm reio}$, which has no impact on the matter power spectrum. The different degrees of freedom controlling the shape of the matter power spectrum are the following:

(P1) **Scale of the maximum**: The time of radiation-matter equality determines the scale of k_{eq}, and thus the matter power spectrum peak. As we saw in section 1.6, this time of equality is given by ω_M and Ω_Λ.

(P2) **Large scale slope**: When the ratio of baryon and dark matter densities ($\omega_b/\omega_{\rm CDM}$) increases, the spectrum is more suppressed for $k > k_{eq}$ (larger scales), and the BAO are more pronounced.

(P3) **BAO scale**: The phase of the BAO depends on the sound horizon at the baryon drag epoch $r_s(\tau_{\rm dr})$, while the exponential diffusion dampening depends on the Silk damping scale $r_d(\tau_{\rm dr})$, both of which depend strongly on ω_b.

(P4) **Global amplitude**: The overall amplitude depends both on the primordial amplitude and on the scale independent suppression of the growth-rate during Λ domination, so it is mediated by A_s and Ω_Λ.

(P5) **Global tilt**: The global tilt of the power spectrum depends on the primordial tilt n_s.

With this in mind, we can see how measuring the matter power spectrum can provide important information about the underlying cosmological model. There are many different probes of the large scale structure of the universe, depending on which scales are observed. A summary of current observations of the matter power spectrum at $z = 0$ is shown in the right panel of Fig. 4.3. The matter power spectrum is redshift dependent, and future probes such as Euclid [61] and LSST [62] will be able to measure this at different redshifts, thus allowing us to probe the low-redshift expansion history of the universe.

As a final comment on the matter power spectrum, until now we limited ourselves to *linear* theory, which is good for large scales, but can not describe small scale matter fluctuations at low redshift. When perturbations δ_M become of the same order as $\bar{\rho_M}$, we need to move to

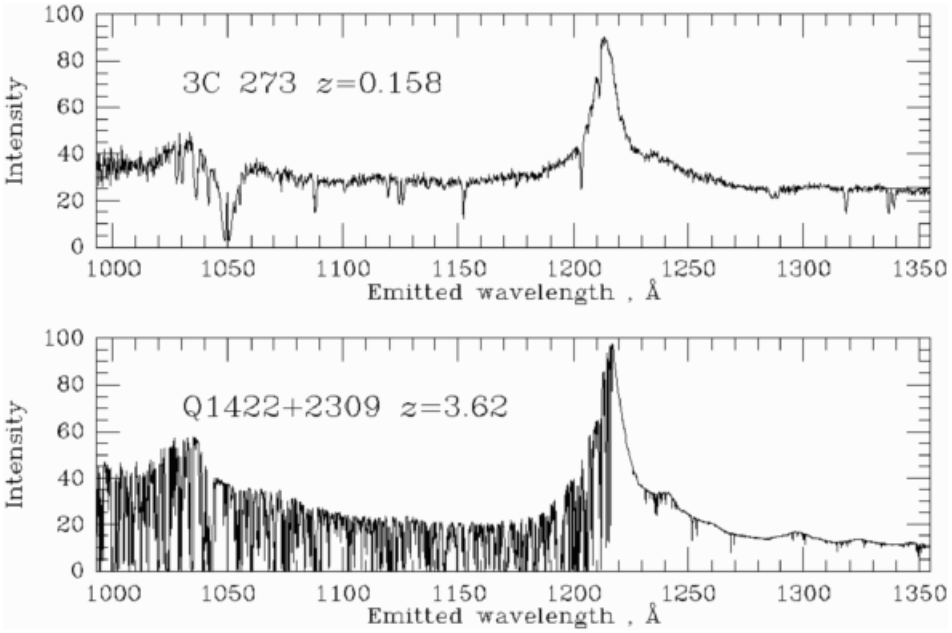

FIGURE 4.4: Sample of two quasar spectra at different redshifts, normalised to the emitted wavelength. The top panel corresponds to Quasar 3C 273 at $z = 0.15$ (from HST), the bottom panel shows Quasar 1422+2309 at $z = 3.62$ (from Keck I HIRES). Image adapted from Bill Keel's website: http://pages.astronomy.ua.edu/keel/agn.

non-linear theory. To describe the non-linear structure formation we need N-body codes, as will be discussed in detail in the next section. The results from N-body codes have allowed approximate methods, such as *halofit* [63] to be added to Boltzmann codes, as shown in the left panel of Fig. 4.3.

4.3 Lyman-α Forest

In the previous section we have seen the importance of the matter power spectrum, and how there are different probes observing this at different scales. One such probe focussing on very small scales is the Lyman-α forest, first discovered in 1970 by Lynds [64], which relies on observations of a type of distant, luminous, active galactic nuclei known as quasars.

The photons emitted by these quasars can interact with hydrogen atoms in the intergalactic medium (IGM) located along the line-of-sight to the quasar, thus leaving an imprint in the resulting quasar spectra. In particular, a fraction of photons is absorbed at the Lyman-α wavelength (corresponding to $\lambda \sim 121\,\text{nm}$), resulting in a depletion of the observed spectrum at a given frequency (which will be redshifted with respect to the absorbed wavelength). As there can be many different hydrogen clouds, which are some of the smallest known structures, along the line-of-sight, we will observe multiple absorption lines, resulting in a *forest*, as shown in Fig. 4.4.

The absorbed fraction of photons in a given point along the trajectory is proportional to the local density of neutral hydrogen, thus in the range of the Lyman-α forest, the frequency dependence of a quasar spectra is a tracer of the spatial fluctuations of the hydrogen density along the line-of-sight. With quasars located at a redshift z, we can Fourier expand each spectrum and take the average of many spectra to obtain a flux power spectrum $P_f(z,k)$. Quasars at higher redshifts have more Lyman-α lines, as there are more hydrogen clouds along the trajectory. However, at redshift of about $z \sim 6$, the forest turns into a Gunn-Peterson trough, signalling the end of reionisation of the universe. Thus, the Lyman-α forest typically probe the range $2 < z < 5$.

If we were dealing with perfectly linear scales, the hydrogen fluctuations would be completely equal to the total baryon fluctuations, which would allow us to probe the total matter fluctuations after the baryon drag epoch. This would mean that the flux power spectrum would be trivially related to the matter power spectrum discussed in section 4.2. However, the flux power spectrum does not probe linear scales[6], but mildly non-linear scales. Thus, in order to relate $P_f(z,k)$ to $P(k)$ it is necessary to perform hydrodynamical N-body simulations, taking into account the complicated thermodynamic evolution of the IGM, as well as a careful modelling of other possible effects on the quasar photons [65]. Once this is done, however, the Lyman-α forest can provide constraints on the matter power spectrum on very small scales, just out of the linear regime, corresponding to $0.5\,\mathrm{h/Mpc} \lesssim k \lesssim 20\,\mathrm{h/Mpc}$. This allows us to study cosmological models that impact these very small scales, such as warm dark matter [66].

As we have seen, in order to relate the Lyman-α flux power spectrum to the matter power spectrum, we need computationally expensive hydrodynamical N-body simulations, which rely on some underlying cosmological model. This means that in order to test different models, we need different simulations. Indeed, even within the same model, for example ΛCDM, any change in the underlying parameters (for example the amount of dark matter or the reionisation depth) would require a new simulation. This makes parameter exploration infeasible: while we can run simulations for individual cases, it is not possible to run simulations for all possible combinations of parameters, thus MCMC type runs are not possible[7].

With this in mind, in [67] a method was devised in order to minimise the amount of simulations needed: instead of simulating an individual model, a specific feature is simulated. In this case, they simulated a suppression of the matter power spectrum, which can then be mapped onto several different underlying models. The focus was on non-cold dark matter (nCDM) models (discussed in detail in chapter 7), which produce a known suppression on small scale structure growth, and are therefore an ideal target for Lyman-α data. The suppression of the matter power spectrum due to the existence of nCDM is usually described by the transfer function

$$T^2(k) = \frac{P(k)_{\mathrm{nCDM}}}{P(k)_{\mathrm{CDM}}}\,. \tag{4.6}$$

[6] Of course not, that would be too easy.
[7] See previous footnote.

This has been well studied for the particular case of thermal warm dark matter [68], and is given by

$$T(k)_{\rm WDM} = \left[1 + (\alpha k)^{2\mu}\right]^{-5/\mu} , \tag{4.7}$$

where $\mu = 1.12$ and α is the only free parameter, which can be related to the dark matter mass. This was generalised to *any nCDM model* in [67] as

$$T(k) = \left[1 + (\alpha k)^{\beta}\right]^{\gamma} , \tag{4.8}$$

by introducing the half-mode scale $k_{1/2}$ as the wavenumber for which $T^2 = 0.5$. The half-mode is thus given by

$$k_{1/2} = \left((0.5)^{1/2\gamma} - 1\right)^{1/\beta} \alpha^{-1} . \tag{4.9}$$

Within this parametrisation, α specifies the scale of the suppression, and is related to the value where the spectrum is suppressed by $50\,\%$ compared to the CDM case ($k_{1/2}$); the shape of the suppression for $k < k_{1/2}$ depends mainly on β, while the shape of the tail ($k > k_{1/2}$) depends on both β and γ.

The advantage of this parametrisation is that models producing the same $\{\alpha, \beta, \gamma\}$ lead to the same matter power spectrum. Thus, instead of performing an N-body simulation for many different nCDM models, simulations can be performed for well-chosen combinations of $\{\alpha, \beta, \gamma\}$.

In [69] 117 well-motivated combinations of $\{\alpha, \beta, \gamma\}$ were chosen, each corresponding to a different nCDM model (shown in the left panel of Fig. 4.5). For each of these, an N-body simulation was ran, with 512^3 particles in a $20\,$Mpc/h box, and with the cosmological parameters fixed to their reference values taken from [70]; $\Omega_m = 0.301$, $\Omega_b = 0.0457$, $n_s = 0.961$, $H_0 = 70.2\,{\rm km\,s^{-1}\,Mpc^{-1}}$, and $\sigma_8 = 0.829$. The resulting flux power spectra were compared to Lyman-α data, coming from the HIRES/MIKE samples of quasar spectra, which was obtained with the HIRES/KECK and the MIKE/Magellan spectrographs, at redshift bins $z = 4.2, 4.6, 5.0, 5.4$, in 10 k-bins in the interval $0.001 - 0.08$ s/km, with spectral resolution of 6.7 and 13.6 km/s, for HIRES and MIKE respectively [71]. This allowed them to obtain constraints on $\{\alpha, \beta, \gamma\}$ coming from Lyman-α data.

In order to apply this method to any nCDM model, provided it can be expressed in terms of the $\{\alpha, \beta, \gamma\}$-parametrisation, together with some of the authors of [67], [69], we have developed a new likelihood, which we call Lyman-$\alpha$$-\alpha\beta\gamma$, interfaced with MONTEPYTHON [72], [73]. This likelihood, and the subsequent extension, was developed and used mainly for **[III]** (discussed in section 7.1) and **[IV]** (discussed in section 7.2), but we intend to make it publicly available, and expect it will be used for many other models.

Our method relies on the large suite of pre-computed hydrodynamical simulations, and on an advanced interpolation method which is able to accurately deal with the sparse, non-regular grid defined by the simulations. The interpolation is done in terms of ratios between the flux power spectra of the nCDM model and the reference ΛCDM one, using the *Ordinary*

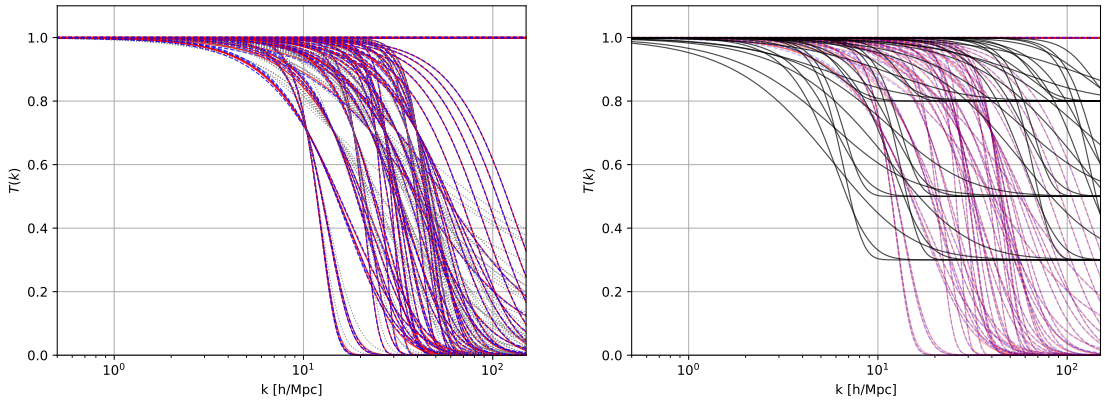

FIGURE 4.5: *Left*: Transfer functions corresponding to the 117 combinations of $\{\alpha, \beta, \gamma\}$ for which we have N-body simulations, used in the Lyman-α−$\alpha\beta\gamma$ likelihood. *Right*: Extended grid of simulations for the Lyman-α−$\alpha\beta\delta$ likelihood. The purple lines show the remapped $\{\alpha, \beta, \gamma\}$ simulations, while the black lines show the new simulations added for $\{\alpha, \beta, \delta\}$.

Kriging method [74]. We do this in several stages: first we interpolate in the astrophysical and cosmological parameter space for the ΛCDM case (corresponding to $\alpha = 0$). We then correct all the $\{\alpha, \beta, \gamma\}$-grid points accordingly, to account for the different ΛCDM parameters. Finally, we interpolate in the $\{\alpha, \beta, \gamma\}$-space. This procedure relies on the assumption that the corrections due to non-reference astrophysical or cosmological parameters are universal. The robustness of such an interpolation was discussed extensively [69]. Thus, our new new likelihood directly translates the limits on α, β, and γ obtained through MIKE/HIRES data into constraints on the fundamental particle physics parameters.

With this in mind, our likelihood scheme is the following:

1. The linear matter power spectrum associated to a given combination of cosmological parameters (six ΛCDM parameters plus additional parameters for the nCDM model) is produced using the Boltzmann solver CLASS[8] [53] up to a maximum wavenumber chosen to be $k_{\rm max} = 200\,h/{\rm Mpc}$. Corresponding values of the derived parameters $(\sigma_8, n_{\rm eff}, z_{\rm reio})$ used to define the N-body simulations are computed, and checked to make sure they lie in the conservative range assumed in the simulations. Otherwise, the model can be safely rejected, given that such models would be ruled out by Planck data anyway.

2. The linear matter power spectrum of the equivalent ΛCDM model is also produced. Depending on the type of nCDM model probed, this will be slightly different: in the case of dark matter interacting with baryons (see section 7.2) the ΛCDM equivalent is computed by switching of the interacting dark matter; for models with dark matter interacting with dark radiation (see section 7.1), we need to re-map the value of the ultra-relativistic relic density, as the simulations assume $N_{\rm eff} = 3.046$. For the latter

[8] Assuming our nCDM model exists in CLASS, of course.

cases, we use the accurate procedure described in [75], which allows to re-map a ΛCDM model with $N_{\rm eff} > 3.046$ to another one sharing the same matter power spectrum up to some scale, but with $N_{\rm eff} = 3.046$: this can be achieved by adjusting the value of other cosmological parameters according to some analytic relations (this is discussed more in detail in section 7.1.1).

3. The transfer function, as described in equation 4.6, is fitted in terms of $\{\alpha, \beta, \gamma\}$ with a simple least squared method. The fitting algorithm only includes points until a finite value $k_{\rm fit}$, which is set by default to $k_{\rm fit} = k_{\rm max} = 200\,h/\text{Mpc}$. In some cases, the transfer function might have oscillations within the range $[0, k_{\rm max}]$. For these models, $k_{\rm fit}$ is reduced to the first zero of the function. The fit is also restricted to values of $\{\alpha, \beta, \gamma\}$ within the region covered by the grid of simulations: $0\,\text{Mpc/h} \leq \alpha \leq 0.17\,\text{Mpc/h}$, $1.5 \leq \beta \leq 10$, and $-10 \leq \gamma \leq -0.15$. Furthermore, we check if the difference between the "exact" transfer function and the fitted one is too large in a region in which the power spectrum is not strongly suppressed. If this is the case, our method can not be considered as accurate and reliable enough, thus these points are removed from the MCMC run.

4. At this point, if the considered model has passed the aforementioned sanity checks (cosmological check, fitting check, equivalent check), its flux power spectrum is produced by performing the interpolation procedure described above. This flux power spectrum can be compared to the Lyman-α forest data, giving a χ^2-value to the corresponding combination of parameters.

5. This procedure is repeated for each step of the MCMC run, providing constraints on $\{\alpha, \beta, \gamma\}$, which are converted into constraints on the nCDM parameters.

While this method is extremely good when dealing with models such as dark matter - dark radiation interactions **[III]**, as discussed in section 7.1, in the left panel of Fig. 4.5 we can see that this parametrisation only covers models that reach a $100\,\%$ suppression. However, many models, such as those with only a fraction of interacting dark matter, do not reach such a high suppression, instead reaching a plateau. In order to extend the validity of this method, we developed a second likelihood, which we call Lyman-$\alpha$$-\alpha\beta\delta$. We parametrise the transfer function as

$$T(k) = (1-\delta)\left[1 + (\alpha k)^{\beta}\right]^{\frac{3\beta}{2}} + \delta\,, \tag{4.10}$$

where the new parameter δ will determine the height of the plateau.

This new formalism offers many more possibilities, but we want to minimise the amount of new N-body simulations we need to run. As most of the simulations do not present a sudden change in the slope at $k_{1/2}$, we can re-map many of the existing $\alpha\beta\gamma$ simulations into corresponding $\alpha\beta\delta$ ones. Furthermore, we have extended our grid of N-body simulations to cover many more cases in which thethere is only a partial suppression. The new set of simulations are shown in the right panel of Fig. 4.5. For everything else, the method is exactly

the same as for the Lyman-α−$\alpha\beta\gamma$ likelihood described above. This extended likelihood can be used for dark matter - baryon interactions **[IV]**, as discussed in section 7.2.

With the methods developed here, we now have an easier way to compare different models that result in a suppression of the matter power spectrum with the high resolution Lyman-α data, without needing new, computationally demanding, N-body simulations. Other similar methods have been developed to exploit the low resolution Lyman-α data, as for example in [76], and could be used in combination with our likelihoods in the future.

4.4 Spectral Distortions

In section 4.1 we saw that the CMB anisotropies provide a wealth of information about the universe. In addition to the anisotropies, the CMB also contains another piece of complimentary information, its energy spectrum. As discussed before, the CMB appears to be an almost perfect blackbody, with FIRAS[9] showing that possible distortions are limited to $\Delta I_\nu/I_\nu \lesssim 5 \times 10^{-5}$ [9]. However, possible deviations from a blackbody[10] could shine a light on many hidden sectors of the universe.

Depending on the time at which a process affects the CMB spectrum, it would lead to a different type of distortion. For $z \geq z_\mu \simeq 2 \times 10^6$ cosmological thermalisation is extremely efficient, so we will only be able to produce temperature shift g-distortions [77]. For processes occurring between $10^5 \lesssim z \lesssim z_\mu$, any energy injection will initially give rise to a Compton y-distortion in the CMB blackbody, which will rapidly evolve into a chemical potential or μ-type distortion, due to efficient redistribution of photons over frequency. Processes taking place at $z \lesssim 10^4$ will maintain the initial shape of a y-distortion. This leads to four different eras, which will be discussed in detail below: a g-era, a μ-era, a mixed y-μ-era, and a y-era, as shown in Fig. 4.6.

The thermalisation of the CMB takes place through various processes, such as Compton scattering, double Compton scattering, and Bremsstrahlung. The CMB will remain as a blackbody while these processes are efficient. Thus, deviations will only appear as these processes become inefficient. To properly model the photon phase-space distribution $f(t, x)$, we can decompose it as

$$f(t, x) = \mathcal{B}(x) + \Delta f(t, x)\,, \tag{4.11}$$

where $\mathcal{B}(x) \equiv 1/(\exp(x) - 1)$ is the phase-space distribution of a blackbody at the temperature T_0. Any contribution to $\Delta f(t, x)$ will be considered as a spectral distortion. With this in mind, we can review the main types of distortions, ordered chronologically. All of the spectral distortions are defined such that relative difference of the photon energy density due to distortions is $\Delta\rho_\gamma/\rho_\gamma = 1$.

Temperature shift g-distortion

The solution for the real radiation temperature T_γ will deviate slightly from T_z (where $T_z =$

[9] Part of the joined COBE/FIRAS experiment already discussed in section 4.1.
[10] Sometimes a lack of perfection can be a benefit.

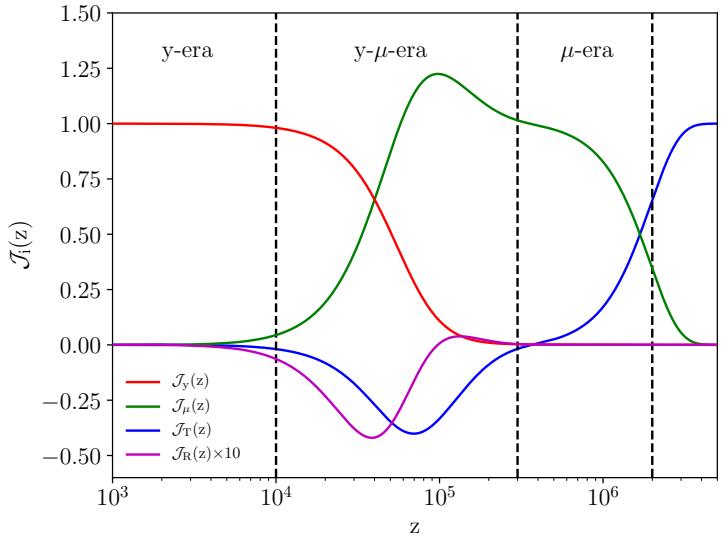

FIGURE 4.6: Branching ratios of the different spectral distortion types, computed using our modified version of CLASS. The different distortion eras are also shown.

$T_0(1+Z)$ is the redshift-dependent temperature) whenever energy is injected, and from the electron temperature T_e when their thermal coupling becomes inefficient. We can write the shift of the phase-space distribution as

$$\Delta f(x) = G(x)\frac{\Delta T}{T_z}\,, \tag{4.12}$$

with $\Delta T = T_\gamma - T_z \ll T_z$, which implies the shape of the temperature shift g-distortion as

$$G(x) = -x\frac{\partial \mathcal{B}(x)}{\partial x} = \frac{xe^x}{(e^x-1)^2}\,. \tag{4.13}$$

Once we have applied the normalisation to maintain $\Delta\rho_\gamma/\rho_\gamma = 1$ and move from phase-space distribution to intensity spectrum, this becomes

$$\mathcal{G}(x) = \frac{1}{4}\mathcal{N}x^3 G(x)\,, \tag{4.14}$$

where $\mathcal{N}x^3 \equiv 2x^3(k_B T_0)^3/(hc)^2$.

Chemical potential μ-distortion

Once double Compton scattering and Bremsstrahlung become inefficient, the chemical potential μ can no longer be considered negligible, and we will find a shift of the phase-space distribution

$$\Delta f(x) = -\mu\frac{G(x)}{x}\,. \tag{4.15}$$

The resulting distortion is a superposition of the μ distortion we are looking for and an additional shift in the blackbody temperature. In order to account for this effect, we simply

subtract the temperature shift away. This leads to the shape of the μ-distortion

$$M(x) = -G(x)\left(\frac{1}{x} - \alpha_\mu\right), \tag{4.16}$$

where $\alpha_\mu \approx 0.4561$.

As before, we apply the normalisation and move to intensity spectrum to find

$$\mathcal{M}(x) = 1.401\mathcal{N}x^3 G(x)\left[\frac{1}{x} - \alpha_\mu\right]. \tag{4.17}$$

Compton y-distortion

Once Compton scattering becomes less efficient, we will depart from equilibrium, but there will still be a distribution of the photons. This leads to a total shift in the phase-space of

$$\Delta f(x) \approx \Delta\tau \frac{T_e - T_z}{m_e} Y(x)\,, \tag{4.18}$$

which then defines the y-distortion shape as

$$Y(x) = G(x)\left[x\frac{e^x+1}{e^x-1} - 4\right]. \tag{4.19}$$

Again, we apply the normalisation and move from phase-space distribution to intensity spectrum to find

$$\mathcal{Y}(x) = \frac{1}{4}\mathcal{N}x^3 G(x)\left[x\frac{e^x+1}{e^x-1} - 4\right]. \tag{4.20}$$

Other distortions

In the region where the redistribution of the y-distortion towards a chemical potential is not yet inefficient but not fully efficient either, we will obtain a mixture of the μ and y distortions. This mixture distortion is usually modelled as a mix of μ, y, and some residual distortion. Essentially, all effects that create distortions that are not covered by the previous three cases are instead captured by the residual distortion shape $R(x)$, which has to be calculated knowing the full thermal history.

We can put all of these different types of spectral distortions together to find the total distortion of the photon intensity spectrum, given by

$$\Delta I_{\rm tot} = \Delta I_y + \Delta I_\mu + \Delta I_{\rm T} + \Delta I_{\rm R}\,, \tag{4.21}$$

where $\Delta I_y = \widetilde{y}\mathcal{Y}(x)$ determines the contribution from y-distortions, $\Delta I_\mu = \widetilde{\mu}\mathcal{M}(x)$ the contribution from μ-distortions, $\Delta I_{\rm T} = \widetilde{g}(1+\widetilde{g}/4)\mathcal{G}(x) + \widetilde{g}^2/8\,\mathcal{Y}(x)$ the contribution from temperature shift g-distortions, and $\Delta I_{\rm R} = R(x)\epsilon$ the contribution from residuals, with $R(x)$ being the residual distortion and ϵ the energy stored within the residual distortion. Additionally, here I

have introduced the useful notation[11]

$$\widetilde{y} = 4y\,, \qquad \widetilde{\mu} = \mu/1.401\,, \qquad \widetilde{g} = 4g\,. \tag{4.22}$$

This decomposition of the total spectral distortion into shapes and amplitudes means that the full knowledge of the distortion is given by a set of four amplitudes (y, μ, g, and ϵ) and one normalised shape $R(x)$. Each of these amplitudes is given by

$$\widetilde{y} = \left.\frac{\Delta\rho_\gamma}{\rho_\gamma}\right|_y, \quad \widetilde{\mu} = \left.\frac{\Delta\rho_\gamma}{\rho_\gamma}\right|_\mu, \quad \widetilde{g} = \left.\frac{\Delta\rho_\gamma}{\rho_\gamma}\right|_g, \quad \epsilon = \left.\frac{\Delta\rho_\gamma}{\rho_\gamma}\right|_R \tag{4.23}$$

where the indices y, μ, and g refer to the corresponding fraction of the total injected energy that generates the given distortion.

We can relate these amplitudes to the relative difference of the photon energy density due to spectral distortions, which is obtained by integrating the Bolztmann equation,

$$\left.\frac{\Delta\rho_\gamma}{\rho_\gamma}\right|_{\rm tot} = \int_z^\infty \frac{Q'}{(1+z)H\rho_\gamma}dz\,, \tag{4.24}$$

where the heating rate Q' corresponds to the energy deposited into the photon fluid in form of heat.

Finally, to see which part of the injected energy generates each of the distortions, we define for each distortion type a the branching ratio of deposited energy into the distortion. We thus find

$$a = \left.\frac{\Delta\rho_\gamma}{\rho_\gamma}\right|_a \equiv \int \frac{dQ/dz}{\rho_\gamma}\cdot \mathcal{J}_a(z)dz \tag{4.25}$$

where the branching ratio $\mathcal{J}_a(z)$ determines the fractional energy release into a given distortion a as a function of redshift. This means that we can effectively split the problem into the *model-dependent* heating function dQ/dz and the *model independent* branching ratios $\mathcal{J}_a(z)$, shown in Fig. 4.6.

These spectral distortions can be produced by many different sources, both within ΛCDM and in more exotic models. Here I provide a non-exhaustive list, but for a full summary see for example [78]:

- Reionisation and structure formation: supernova feedback and the first sources of radiation during reionisation heat up the intergalactic medium at low redshifts ($z \lesssim 10$), leading to a y-type distortion, which could reach $\Delta I_\nu/I_\nu \simeq 10^{-7}$.
- Inflation: the Silk-damping of small scale perturbations (see section 3.5) gives rise to both μ and y-type distortions. Spectral distortions are influenced also by the running of the spectral index (see section 2.4). Furthermore, the overall distortion is also sensitive to

[11] This notation is new from **[V]**, as previous notation in the literature was a bit confusing.

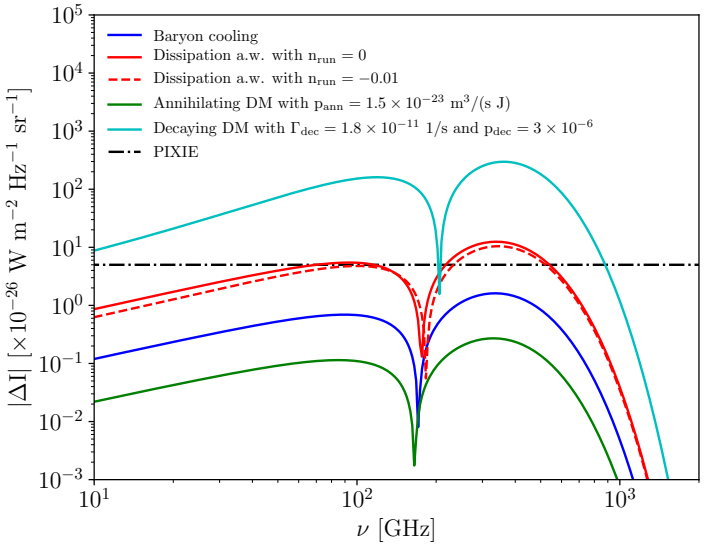

FIGURE 4.7: Predicted total spectral distortion ΔI as a function of frequency for different cosmological scenarios, both for ΛCDM and more exotic models. For reference, the sensitivity of the proposed PIXIE mission is also shown.

the difference between adiabatic and isocurvature perturbations, as well as primordial non-Gaussianities. This is shown by the red lines in Fig. 4.7.

- Cooling of matter: the adiabatic cooling of baryons extracts energy from the CMB photon bath by Compton cooling, leading to both μ and y-type distortions. This is shown by the blue line in Fig. 4.7.
- Cosmological recombination radiation: the recombination process (described in section 1.8.3) introduces distortions of the order $\Delta I_\nu / I_\nu \simeq 10^{-9}$.
- Decaying or annihilating relics: as an example of exotic scenarios, possible dark matter decays or dark matter annihilations (see [79] for an overview) inject energy into the spectrum, shown by the green (annihilation) and cyan (decay) lines in Fig. 4.7.

Given the amount of processes that can lead to different spectral distortions, and the clear predictions from ΛCDM, it is reasonable to assume that any future mission that measures (or fails to measure) spectral distortions would provide vital information. In addition to the mechanisms described above, spectral distortions could help distinguish between different solutions to the small scale crisis [80], [81] (see section 5.1), they could help constrain PBH [82], or even help us to probe possible dark matter - baryon interactions [83] (see section 7.2.2).

With this in mind, in **[V]** we implemented the complete calculation of spectral distortions in CLASS for the following models: all known heating mechanism within ΛCDM, dark matter annihilation, dark matter decay, and evaporation and accretion of primordial black holes. Our framework can easily be extended for any model for which the heating function is known (as the branching ratios do not depend on the model, as seen above), and is currently being expanded to include the possible cooling of baryons by dark matter interactions (see section 7.2

for a discussion on this).

In order to properly study the implications of a possible future spectral distortions mission on cosmological models, in **[V]** I added a new family of likelihoods to the parameter extraction code MONTEPYTHON to deal with *any* spectral distortion mission, making use of the MCMC forecast method detailed in [84]: a future (or current) experiment is encoded as a mock likelihood, providing the probability that the mock data is true given the fiducial model assumed at each step of the MCMC parameter exploration.

Our likelihood computation can be summarised in the following way

1. As a starting point, we choose a fiducial model (for example ΛCDM with cosmological parameters given by the latest Planck measurements [19]).
2. We use our new spectral distortions module in CLASS to compute the total spectral distortions for the fiducial model in each frequency bin of the experiment. This is stored as our *observed* spectral distortion.
3. For each step in the MCMC exploration, we update the parameters of our model, and use CLASS to compute the *predicted* total spectral distortions for our new model in each frequency bin of the experiment.
4. For each step a new χ^2 is computed by comparing the *predicted* model with the *observed* one,
$$\chi^2 = \sum_{\nu_i} \left(\frac{\Delta I_{\rm predicted}(\nu_i) - \Delta I_{\rm observed}(\nu_i)}{\delta I_{\rm noise}(\nu_i)} \right)^2 . \tag{4.26}$$
where δI_{noise} is the overall sensitivity of the experiment to the signal.

With this new family of likelihoods, to define a new detector we simple need to provide either the experimental configuration (minimum probed frequency $\nu_{\rm min}$, maximum probed frequency $\nu_{\rm max}$, bin width $\Delta\nu_c$ or number of bins ν_i, and overall sensitivity δI_{noise}), or the binned frequency array together with the corresponding sensitivity. Additionally, CLASS will make use of this information to perform a more efficient computation of the branching ratios described above.

With this framework we developed likelihoods for two detectors: the existing FIRAS mission [9], and the proposed future mission PIXIE [85]. For FIRAS, we used the binned frequency array results provided in [86]. For PIXIE we use the same assumptions as in [78], [87]: we assume equidistant, independent frequency channels in the range $[30\,\text{GHz} - 1\,\text{THz}]$, with a bin width of $\Delta\nu = 15\,\text{GHz}$. Furthermore, we assume that the measurement is only limited by uncorrelated instrumental noise, and all foregrounds can be removed with higher frequency channels. This gives us an overall constant noise in each frequency bin of $\delta I_{noise} \simeq 5 \times 10^{-26}\,\text{W}\,\text{m}^2\,\text{s}^{-1}\,\text{Hz}^{-1}\,\text{sr}^{-1}$.

With the full computation of spectral distortions now being handled in CLASS , together with the newly developed likelihoods, we can probe the synergy between spectral distortions missions and other data sets, such as information from the CMB anisotropies, or probes of matter

power spectrum, as will be done in our forthcoming paper **[V]**. This means we can not only perform forecasts for future proposed spectral distortions missions, but should one of these receive funding, we have the pipeline ready to analyse the new data in conjunction with other cosmological data.

5 Problems in Cosmology

In the previous chapters we have seen the remarkable successes of ΛCDM cosmology. This model has been tested across many different scales and observables, and to date, it remains the best theory we have to explain the history, evolution, and ingredients of the universe.

Despite its undeniable success, in recent years this model has seen some possible challenges. With increasingly more data becoming available, together with better computing power allowing us to perform extremely precise N-body simulations, tensions have started to rise between the predictions and observations of ΛCDM.

These tensions are arising at different levels: on the smallest scales, such as our galaxy and local neighbourhood, N-body simulations and observations appear to be at a mismatch; meanwhile low redshift probes of the Hubble constant H_0 and σ_8 seem to be in tension with the CMB inferred values. Furthermore, the recent observation by the EDGES team of a 21 cm signal does not align with our expectations for a standard ΛCDM universe.

In this chapter I will discuss these potential issues with our standard model of cosmology.

5.1 Small Scale Crisis

When viewing the universe on large scales, from the horizon scale of $\sim 15000\,\text{Mpc}$ down to the typical spacing between galaxies of $\sim 1\,\text{Mpc}$, all observations are consistent with a universe seeded by nearly scale-invariant fluctuations, as described in chapters 2 and 3. Indeed, this model, in which structures form hierarchically with smallest structures collapsing first, is the cornerstone of our understanding of galaxy formation, and it can accurately describe properties of galaxies such as their count, clustering, morphology, colours, and evolution over time [88], [89].

However, when we observe the universe on scales smaller than $\sim 1\,\text{Mpc}$ and on mass scales smaller than $\sim 10^{11} M_\odot$, we start to notice problems in our theory, known collectively as the *small scale crisis* (see for example [90]–[92] for a review). In the 1990s the increase in computing power allowed N-body simulations to resolve the internal structure of halos for the first time. With this, we are now able to perform very precise simulations, assuming the matter content in our universe is dominated by cold dark matter (as described in section 1.9). When comparing these ΛCDM simulations to observations on small scales, we encounter several discrepancies, known as the *missing satellites problem* [93], [94], the *core-cusp* problem [95], [96], the *too-big-to-fail* problem [97], and the *diversity problem* [98], each described in detail below.

For these discussions, it is useful to introduce some general concepts. In section 3.3, we saw how over-dense regions of the universe form with the initial fluctuations. After these regions become non-linear, they can collapse into virialised dark matter halos with

$$M_{\rm vir} = \frac{4\pi}{3} R_{\rm vir}^3 \Delta \rho_m \,, \tag{5.1}$$

where $R_{\rm vir}$ is used to denote the outer edge of the halo. As there is some ambiguity in this definition, the over-density parameter Δ has been introduced. Here I will follow the convention of [99] and choose Δ to match the over-density predicted for a virialised dark matter region that has undergone a spherical collapse, $\Delta \sim 300$ at redshift $z = 0$. The precise choice of Δ does not significantly affect the discussion, provided one is consistent.

Furthermore, we can make a comment on the internal structure of dark matter halos. In section 1.9.1 I introduced the *halo density profile* (equation 1.86). There are several different profiles we can use to try to describe the internal structure of halos, shown in Fig. 5.1, the most common of which are

- The Burkert profile [100], also known as cored profile, was introduced to fit rotational curves (discussed in section 1.9.1). It is given by

$$\rho(r) = \frac{\rho_s}{\left(1 + \frac{r}{r_s}\right)\left(1 + \left(\frac{r}{r_s}\right)^2\right)} \,, \tag{5.2}$$

  where ρ_s is a constant density core within a radius r_s. However, this profile leads to a diverging total mass M when $r \to \infty$.

- The NFW profile [101], introduced after N-body simulations using cold dark matter showed that profiles are universal, is given by

$$\rho(r) = \frac{\rho_s}{\left(\frac{r}{r_s}\right)\left(1 + \frac{r}{r_s}\right)^2} \,. \tag{5.3}$$

  While this profile can reproduce N-body results fairly accurately, it diverges for small values of r.

- The Einasto profile [102] was introduced to avoid this divergence, and provides a better fit to latest N-body simulations. It is given by

$$\rho(r) = \rho_s \exp\left(-\frac{2}{\alpha}\left[\left(\frac{r}{r_s}\right)^\alpha - 1\right]\right) \,, \tag{5.4}$$

  with $\alpha = 0.17$ for the general Einasto profile, and $\alpha = 0.11$ for the EinastoB, which better describes simulations with added baryons.

A final key concept to understanding the small scale crisis is the *halo mass function*, which gives us the amount of dark matter halos at a given redshift z, per unit mass and unit volume: $n(z, M)$. The mapping between an initial spectrum of density fluctuations at early times, as

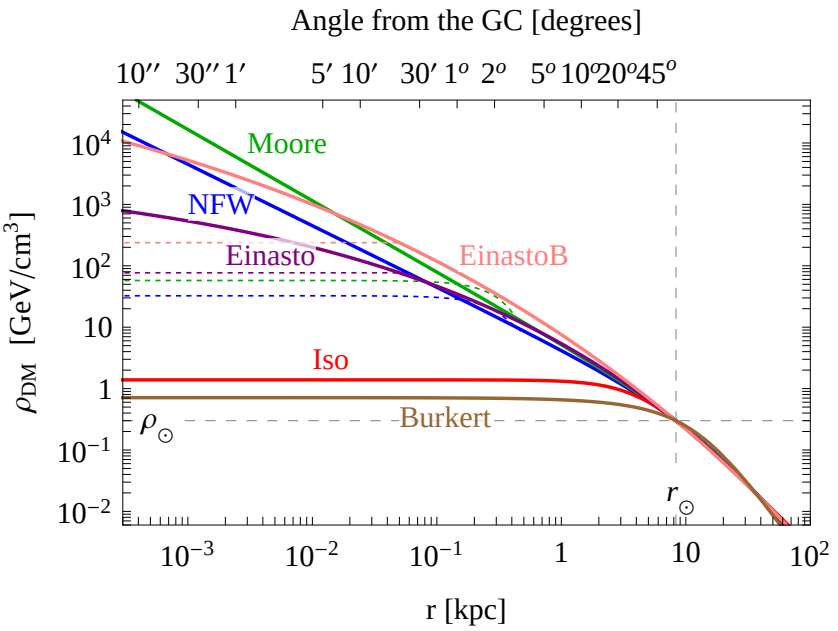

FIGURE 5.1: Different dark matter density profiles. Solid lines represent the full profile, while dashed lines show the profiles modified to remove the Galactic centre divergence. $\rho_\odot$ and $r_\odot$ indicate the local dark matter density and the distance of the Sun to the galactic centre respectively. Image taken from [103].

calculated from an underlying model such as ΛCDM, and the resulting halo mass function at late times appears to be highly non-trivial. However, with certain assumptions the halo mass function can be modelled remarkably well, as proposed for example by Press and Schechter in 1974 [104]. In the Press-Schechter formalism the halo mass function is calculated using the assumption that the fraction of mass in a virialised halo is related to the fraction of volume samples in which the smoothed initial density fluctuations are above some critical density δ_c. A full discussion of this formalism is beyond the scope of this work, but for a good review see for example [105].

Since its conception, the Press-Schechter formalism has been extended in a more rigorously mathematical way, and is known today as the extended Press-Schechter (EPS) theory [106]–[108]. This model can very accurately predict the abundances of dark matter halos, which can be tested with comparisons to large scale N-Body simulations. Both these simulations and the EPS show a universal form for the halo mass function: the comoving number density of dark matter halos is a power-law with log slope of $\alpha \simeq -1.9$, which is exponentially suppressed for masses above the characteristic mass of fluctuations going non-linear at the calculated redshift. Thus, using the EPS formalism, one can make highly accurate predictions for the abundance of dark matter halos given an initial power spectrum of density fluctuations calculated within the ΛCDM universe.

Now that we have seen the main components we can use in N-body simulations to compare our underlying ΛCDM cosmology and the observations, we can discuss the mismatches that appear when doing so.

Missing Satellites

As discussed above, we can use N-Body simulations to predict the number of dark matter halos expected to form in a given mass range in a ΛCDM universe. Simulations show that these dark matter clumps should exist at all resolved masses, with no break in the sub-halo mass function, leading to more smaller halos [109], [110]. Recovering the Press-Schechter formalism from above, we would expect a halo mass function of the form $dn/dM \propto M^{\alpha}$ with $\alpha \simeq -1.9$. However, the observed stellar mass functions of satellite galaxies in the Local Group is much flatter than expected, with $\alpha \simeq -1.5$ [111].

On the more qualitative side, from simulations we would expect as many as ~ 1000 sub-halos that could host galaxies in the Local Group. Nonetheless, we have only found ~ 50 such dwarf satellite galaxies[1] orbiting within the Local Group, and only ~ 10 within the virial radius of the Milky Way [111], [112]. While the simulations do predict the correct amount of normal-sized galaxies, the prediction for sub-halos is very discrepant from observations. This mismatch between the number of predicted and the number of observed dwarf galaxies is known as the missing satellite problem.

Of course one argument against the missing satellite problem is that these galaxies simply have not been observed: if galaxy formation becomes less efficient at smaller halo masses, the smallest dark matter halos would not have been able to form enough stars to be visible to us. This is supported by the discovery of ultra-faint galaxies composed mostly of dark matter [113]. However, while future surveys could detect many more ultra-faint halos, it is not clear if this will be enough to account for the noticeable mismatch in the simulations and predictions.

The missing satellite problem is a matter of ongoing debate in the field, as there are some questions as to how the abundance matching is done, how the halo mass function is calculated, how tidal stripping affects these dwarf galaxies, and the full impact of baryonic effects on such simulations. As such, it remains a controversial topic, but one that persist without a clear solution [93], [114], [115].

Core-Cusp

The second mismatch that we encounter between observations and predictions from simulations that assume cold dark matter comes about when we look at the density profile of dark matter halos. When running N-body simulations, we find that the density profile should rise steeply at small radius, compatible with the NFW (equation 5.3) and the Einasto (equation 5.4) profiles [102], [116]. However, observations seem to show most low-mass dark matter galaxies have a constant central density, more compatible with the Burkert profile (equation 5.2) [117], [118].

More qualitatively, N-body simulations prefer a cuspy distribution of matter, while observations from rotation curves suggest a flat central dark matter profile, thus leading to a cored profile. This is known as the core-cusp problem, and is illustrated in Fig. 5.2.

[1] In this section, I will use the term *dwarf galaxies* for galaxies with stellar mass $M \lesssim 10^9 M_{\odot}$ and $R_{\rm vir} \lesssim 1\,\mathrm{kpc}$.

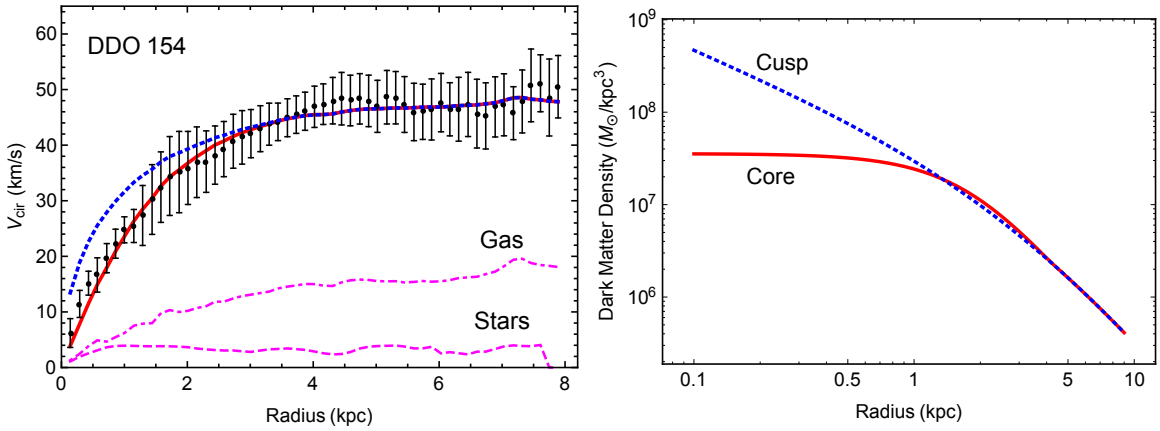

FIGURE 5.2: Example of the core-cusp problem. The left panel shows the observed rotation curve of dwarf galaxy DDO 154 (black data points), compared to an NFW profile (dotted blue) and a cored profile (solid red). The pink lines show the contribution of gas and stars. The right panel shows the corresponding dark matter density profiles. Image taken from [98].

Too-big-to-fail

This problem is tightly connected to the missing satellite problem. Indeed, above I mentioned that one possible way to solve the missing satellite problem is to assume that the satellites are not missing, but rather there is not enough baryonic matter present to make them visible. However, this assumption makes a testable prediction: the central masses of Milky Way satellites should be as massive as the most massive sub-halos seen in simulations [97].

Nonetheless, when comparing observations to simulation results, it was shown that, while there are sub-halos with central masses similar to our local satellites, these were never among the most massive halos [97], [119].

Qualitatively, N-body simulations predict that the most massive satellites should be too big to have failed at forming stars, as the lower-mass satellites we have observed have been capable of doing so. Thus, this is known as the too-big-to-fail problem, and while it was initially found in the Milky Way, it has also been found in Andromeda [120] and the Local Group [121].

Diversity

The final mismatch we encounter between our simulations and observations appears in a similar way to the core-cusp problem. We have already seen that N-body simulations show cuspy profiles, more peaked at the central region of galaxies. Importantly, the N-body simulations show very little scatter in the cuspy density profiles for halos of a given mass. However, observations indicate that galaxies with the same maximal circular velocity have inferred core densities varying by a factor of up to $\mathcal{O}(10)$ [122].

Indeed, we have seen that both the NFW (equation 5.3) and Einasto (equation 5.4) profiles have strongly correlated parameters (ρ_s, r_s), and thus there is not much freedom in specifying a halo. As such, once the maximum velocity $V_{\max}$ is fixed, the halo density profile will be completely determined for all radii. Therefore, our simulations predict very similar density

profiles for similar maximal circular velocity, which is not in agreement with the observation of diverse inner profiles leading to the same velocity at larger radii [123].

As this problem is related to the core-cusp problem, any model proposed to explain why we observe cored profiles, rather than the expected cuspy ones, should also incorporate a mechanism to explain the apparent diversity in inner profiles.

In this section I have introduced the four problems that are commonly referred to as the small scale crisis. There are several proposals to solve these problems, one of which is to improve the already-existing baryonic modelling in the simulations. Indeed, most simulations only include cold dark matter, which seems reasonable given that it accounts for $\sim 85\,\%$ of the matter content of the universe. However, baryonic feedback effects have been shown to mitigate some of the problems [114], [115], but these effects can currently not solve all four problems simultaneously, and often make one problem worse while addressing the other problems.

As such, several models *beyond* ΛCDM have been proposed to address these issues, such as warm dark matter [124], sterile neutrinos [125] or self-interacting dark matter [126]–[130]. Another very interesting class of models to solve the small scale crisis are models in which dark matter can have additional interactions, either within the standard model or within a dark sector. These models are discussed in depth in chapter 7.

5.2 Hubble Constant Tension

In section 1.2 I introduced the Hubble constant, H_0: the proportionality constant between the distance to an object and its receding velocity that gives us the current expansion rate of the universe. This parameter is of vital importance, as we saw in section 1.6, and thus a lot of effort has been invested in measuring the Hubble Constant.

There are several different ways we can measure the Hubble Constant, the two most usual are by using standard candles, such as supernovae, to measure the luminosity distance; and by using standard rulers, such as the BAO scale or the CMB fluctuations, to measure the angular diameter distance. In a consistent cosmological model we would expect these measurements to agree. However, this is not the case[2].

When Hubble first measured the expansion of the universe in 1929, as discussed in section 1.2, he reported a value of $H_0 = 500\,\mathrm{km/(Mpc\ s)}$ [14]. This value has been revised many times since, and in the last 20 years we have been able to get increasingly more precise measurements of this parameter. At the turn of the 21$^{\mathrm{st}}$ century the Hubble Key Project found a value of $H_0 = (72 \pm 8)\,\mathrm{km/(Mpc\ s)}$ [131] using the HST telescope, and a few years later the WMAP team released the first measurement of the Hubble constant using CMB anisotropies: $H_0 = (72 \pm 5)\,\mathrm{km/(Mpc\ s)}$. The locally measured value of H_0 has remained largely unchanged,

[2]Which is fun, the universe would be too boring if everything were consistent.

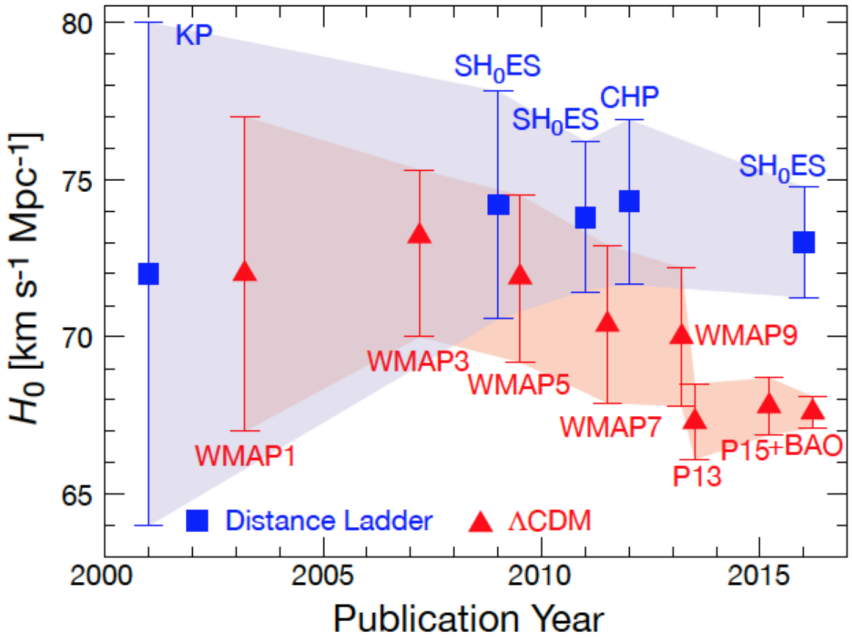

FIGURE 5.3: Recent measurements of the Hubble Constant. Values determined using local measurements based on the Cepheid distance scale are shown in blue, while the values derived from CMB and BAO measurements assuming a base ΛCDM cosmology are shown in red. The discrepancy between these measurements has grown to $\sim 4\sigma$. Image taken from [132].

except for significantly smaller error bars, while the CMB value has yielded a much lower value, also with greatly reduced error bars. The main measurements in the last 20 years are summarised in Fig. 5.3.

The latest measurements of supernovae from the SH0ES collaboration give a value of $H_0 = (73.48 \pm 1.66)$ km/(Mpc s) [133], while the latest Planck data yield $H_0 = (67.36 \pm 0.54)$ km/(Mpc s) [19], which implies the values are at 3.5σ tension which each other. Furthermore, BAO data from SDSS DR12 [134] agree with the predictions from Planck data to high precision, allowing us to combine both measurements, giving a value of $H_0 = (67.66 \pm 0.42)$ km/(Mpc s) [19], increasing the tension between the locally measured value and the early universe measurements to $\sim 4\sigma$. Understanding the source of this tension is one of the biggest challenges in cosmology today. To see what could be the origin of this discrepancy, we should first review how these different measurements are made.

The local measurement of the Hubble Constant has two distinct steps. As a first step, we can use Cepheid-like stars to calibrate stellar luminosities and distances to nearby galaxies, and then we can calibrate brighter objects such as supernovae to obtain distance measurements for more distant galaxies. To reduce errors, Cepheid variables are identified in nearby galaxies that also contain well-observed supernovae, providing the needed calibration. The Cepheid distance scale is anchored to geometric parallax within the Milky Way, thus ensuring its accuracy. For the second step in the process, relative distances to galaxies up to redshifts of $z \sim 0.1$

are measured from the calibrated peak brightness of supernovae. Thus, this measurement is known as the forward distance ladder. Of course this procedure assumes a very good understanding of supernovae brightness, as well as all systematic effects that can alter the apparent luminosity of objects.

To see how we can obtain a measurement of H_0 from Planck data, we first recover the relation between the angular diameter distance and the comoving distance, first introduced in equation 1.23,

$$d_A = \frac{\chi(z)}{(1+z)}\,, \tag{5.5}$$

which we can combine with the definition of comoving distance from equation 1.21 to find

$$d_A = \frac{1}{1+z}\int_0^{z(t_e)} \frac{dz}{H(z)}\,. \tag{5.6}$$

Under the assumption of a ΛCDM universe, in section 1.6 we derived an expression for the Hubble Parameter as a function of redshift, $H(z)$, which we can insert into equation 5.6 to find:

$$d_A = \frac{1}{1+z}\int_0^{z(t_e)} \frac{dz}{H_0\sqrt{[\Omega_R(1+z)^4 + \Omega_M(1+z)^3 + \Omega_k(1+z)^2 + \Omega_\Lambda]}}\,. \tag{5.7}$$

Thus, assuming the universe is described by ΛCDM, if we measure the angular diameter distance of the CMB, as well as the relic densities of the different species Ω_x, we can calculate a value of H_0. Furthermore, we can use measurements of the BAO scale (as discussed in section 4.2) to obtain an inverse distance ladder, which can also give us a measurement of H_0. Fig. 5.4 shows $H(z)$ at low redshift, calculated within ΛCDM, together with several relevant data sets.

Having reviewed how the different measurements are made, we can discuss possible explanations for the $\sim 4\sigma$ tension between the latest measurements:

1. Systematic effects affecting measurements of supernovae luminosity.
2. Systematic effects in the Planck measurements.
3. New physics beyond ΛCDM, leading to a different $H(z)$ in equation 5.6.

These options have all been explored extensively in the literature, and currently no systematic effects big enough to cause this discrepancy have been identified [135]–[141]. Furthermore, measurements of the Hubble constant using strong gravitational lensing are more model dependent, but also give a value of $H_0 = (71.9 \pm 2.4)\,\mathrm{km/(Mpc\ s)}$ [142]. More recently, some arguments have surfaced that perhaps the Gaussian likelihood assumption used when analysing the SH0ES data could lead to an overestimate of the statistical significance of this discrepancy [143].

Given the lack of clear systematic effects, and since the values inferred from early universe data assume ΛCDM cosmology, there has been a surge of interest in models beyond ΛCDM that

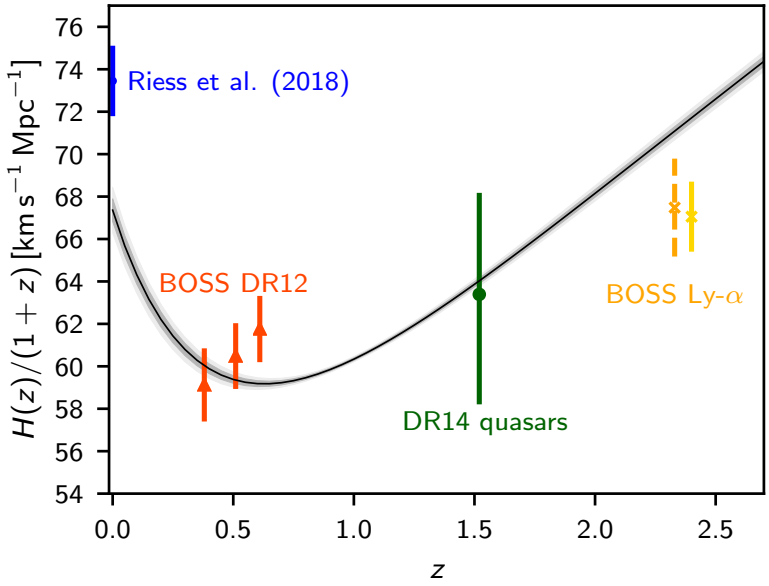

FIGURE 5.4: Comoving Hubble parameter as a function of redshift. The grey bands show the 68 % and 95 % confidence ranges allowed by Planck when assuming a ΛCDM universe. The data points (red, green, yellow) show the result of different measurements using BAO, quasars, and Lyman-α data, all of which agree with the base model. The latest forward distance ladder measurement using supernovae is shown in blue. Image taken from [19].

might be able to solve this tension. However, it is very challenging to find theoretical explanations for this discrepancy while not breaking compatibility with other cosmological data, especially as the angular scale of the acoustic peaks in the CMB power spectrum has been measured very accurately, and it sets the ratio of the sound horizon at decoupling to the distance to the CMB, as discussed in section 4.1. As an example, models with an extra relativistic degree of freedom, $\Delta N_{\text{eff}} = 1$, can lead to an H_0 value closer to the supernovae data, but these are excluded by the CMB angular power spectrum.

There have been many models proposed in the literature recently to address this issue, such as cannibal dark matter [144], early dark energy models [145], and decaying dark matter [146]. Furthermore, models in which there are interactions between dark matter and an additional dark radiation component could alleviate this tension, and are explored in detail in chapter 7. While a clear solution to the H_0 tension remains elusive, the persistence of this discrepancy in the data sets can not be ignored, and indeed is one of the most relevant discussions in modern cosmology.

5.3 σ_8 Tension

In section 4.2 I discussed the importance of the matter power spectrum for cosmology, and how it is related to the growth of fluctuations in the early universe, and thus to the underlying cosmological model. In order to better discuss different models and their impact on the matter power spectrum, I now introduce σ_8, which measures the amplitude of the linear matter power spectrum averaged over the scale of $8\,\mathrm{Mpc/h}$, so it tells us about matter clumpiness[3] on spheres of $8\,\mathrm{Mpc/h}$.

As with H_0, there are several different ways we can measure this value: the primary CMB anisotropies give us a high redshift measurement, placing a constraint on the matter fluctuation amplitude at the time of recombination, which can then be extrapolated to today once a base model is chosen; on the other hand we can use weak lensing and galaxy clustering to obtain a low redshift measurement. When comparing these high and low redshift values, we once again find a discrepancy [147], [148].

The value of σ_8 is correlated with the total matter content of the universe, Ω_m, as the former measures the matter power spectrum on a given scale. Thus, to better compare different measurements, we would need to always give values of σ_8 and Ω_m together. To avoid this, we introduce

$$S_8 \equiv \sigma_8 \sqrt{\frac{\Omega_m}{0.3}}\,. \tag{5.8}$$

The latest measurements from CMB anisotropies measured by Planck yield $S_8 = 0.825 \pm 0.011$ [19], while the most recent cosmic shear surveys give the following values:

- Deep Lens Survey (DLS): $S_8 = 0.940 \pm 0.045$ [149]
- Canada-France-Hawaii Telescope Lensing Survey (CFHTLens): $S_8 = 0.667 \pm 0.070$ [150]
- Dark Energy Survey (DES): $S_8 = 0.783 \pm 0.023$ [151]
- Kilo-Degree Survey (KiDS-450): $S_8 = 0.737 \pm 0.038$ [152]

Therefore, we can see that there is a tension of $\sim 2.5\sigma$ between these different measurements, as shown in Fig. 5.5, with direct measurements preferring a lower value of S_8. Of course, directly comparing the weak lensing experiments is not trivial, as the different surveys differ in the datasets, the shear and photometric redshift estimation algorithms, the theoretical assumptions, and the pipeline used to obtain the final result. Attempts to unify this pipeline have been performed in the literature, and the tension with the Planck measurement is significantly reduced, but not completely solved [153].

As mentioned above, the high redshift measurement obtained from CMB anisotropies is extrapolated to today with a choice of model: usually this is chosen to be ΛCDM. However, given the slight tension with the low redshift values, people are increasingly looking for models *beyond* ΛCDM that could provide better agreement. As an example, one way to reduce

[3] Such a technical word.

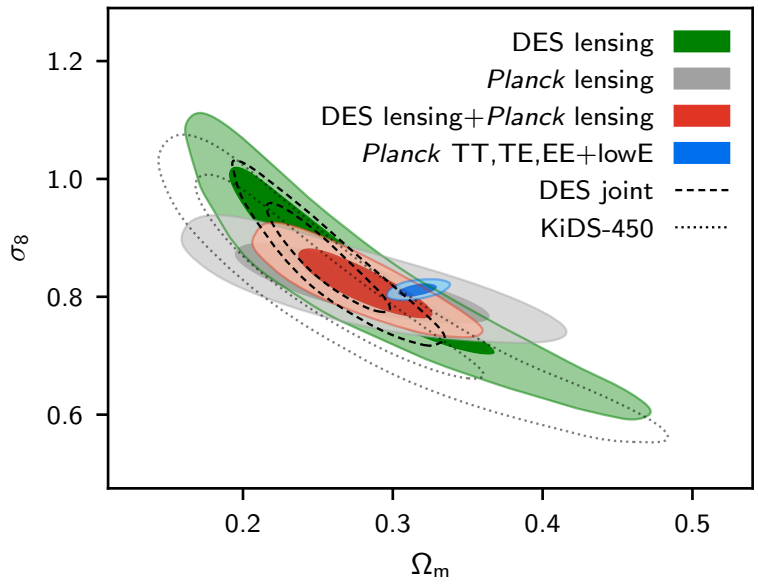

FIGURE 5.5: Joint posterior distribution of the matter-density parameter Ω_m and fluctuation amplitude σ_8, showing the 68 % and 95 % confidence levels, and assuming ΛCDM. Results are shown for DES (green), Planck Lensing (grey), and the joint lensing constraint (red). The DES cosmic shear plus galaxy-clustering joint analysis (dashed line) and the constraint from the original KiDS-450 analysis (dotted) are shown, as well as the independent constraint from the Planck CMB power spectra (blue). Image taken from [19].

the matter clustering rate would be to have a fraction of warm dark matter, which would free-stream and smear out the fluctuations. A clear example of this would be active or sterile neutrinos [148], [154], but of course these models are already very constrained by other cosmological data sets.

Solving the cosmological tensions has the added difficulty that models invoked to solve the σ_8 tension often make the H_0 tension worse, and vice-versa. For example, massive neutrinos would be free-streaming, leading to a small scale matter power suppression and thus a lower S_8, but this would shift the CMB acoustic peaks to lower multipoles, in turn lowering H_0. Similarly, the addition of extra relativistic degrees of freedom, $\Delta N_{\rm eff}$, while maintaining the redshift of matter-radiation equality (discussed in section 1.6) leads to a lower H_0, but introduces a damping of the CMB spectrum at high multipoles, and in turn enhances the matter power spectrum, leading to an increased S_8. The interplay between these two tensions will be revisited in section 7.1.

Given that σ_8 probes the matter power spectrum, it is clear that better measurements of structure formation on all scales are vital to distinguishing between different solutions to this tension. As discussed in section 4.3, Lyman-α data can provide very precise measurements of the small scale matter power spectrum, and thus will be an essential piece of future cosmological measurements, as we will see in more detail in chapter 7.

In this chapter we have seen that there are several challenges to the ΛCDM model, coming from different scales and observations. Taken individually, these problems might not be significant, as they might yet be solved within the ΛCDM paradigm. However, when considered all together, combined with possible issues in the standard model of particle physics, such as the mass of neutrinos (see section 6.1 for a discussion on this), they do raise the question as to whether there is something we are missing with our current description of the universe.

With this motivation, it is very justified to look at models *beyond* ΛCDM, for example models in which dark matter is not cold. Of course, any such extension invoked to solve the problems described here would have to be able to accommodate the existing data without causing new problems. In the remainder of this thesis I will focus on massive relics in the universe (neutrinos and dark matter), and discuss how they can be used to address these problems.

Part III

Massive Relics in the Universe

6 Neutrino Mass Constraints

In 1930, in order to explain the continuous spectrum observed in the beta decay of nuclei, Pauli proposed the existence of a massless, neutral particle with spin $1/2$, known as the neutrino. Since their discovery in the second half of the twentieth century, neutrinos have been a topic of great interest in particle physics, as discussed in section 1.7. The further discovery that neutrinos can oscillate, and therefore can not be massless, cemented neutrinos as one of the most relevant particles for both particle physics and cosmology.

In the following section I will provide an overview of neutrinos from a particle physics perspective, including a discussion on their mass and oscillations. Section 6.2 will discuss the significance of neutrino mass to cosmology, and how cosmology can help us to constrain the sum of neutrino masses. The first two subsections are based on the recent review [155] and the book [156]. Section 6.3 is based on the work carried out by myself together with T. Brinckmann et al. in **[II]**, where we forecast the sensitivity of current and future cosmological experiments to the sum of neutrino masses, finding that future combinations of CMB and large scale structure (LSS) missions are likely to detect the sum of neutrino masses at greater than 5σ.

6.1 Neutrinos in Particle Physics

The idea of neutrinos was first introduced by Pauli in 1930 to save energy conservation in β-decays, leading Pauli to claim *"I have suggested something that can never be verified experimentally"*[1]. However, in 1956 Reines and Cowan [157] first measured electron neutrinos. Muon neutrinos were found in 1962, and tau neutrinos were found in 2000.

In section 1.7 we saw how neutrinos are supposed to behave in the Standard Model of Particle Physics: they are neutral, massless[2] fermions with spin $1/2$. These neutrinos can come in three flavours[3] to accompany leptons within $SU(2)_L$ doublets. Furthermore, they only interact via the weak force, which means they can travel a very long distance without interacting, making them very difficult to detect. Additionally, it is not possible to build a mass term for neutrinos using the process described in section 1.7, and as mass arises from the Higgs mechanism, which couples left-handed and right-handed particles, neutrinos were assumed to have no right-handed partner.

[1] He did not have much faith in future experiments, it seems.
[2] Following our theme of being very good at naming things, "neutrino" means "the small neutral one".
[3] Unfortunately, chocolate is not one of them.

This picture began to change once technology had advanced enough to detect the solar neutrino flux. Electron neutrinos are produced in the core of the Sun as a by-product of hydrogen fusion, and thus the solar neutrino flux provides a good way to study these particles. However, first measurements of solar neutrinos [158] showed a large discrepancy with the predicted flux, with a significant deficit of ν_e. This became known as the Solar Neutrino Problem. Subsequent measurements all found between $1/2$ and $1/3$ of the predicted neutrinos coming from the Sun.

The Solar Neutrino Problem was only properly solved recently, when SuperKamiokande observed elastic scattering of electron neutrinos [159], while the Sudbury Neutrino Observatory (SNO) measured at the same time charged and neutral current, as well as the elastic scattering reaction [160]. By combining these observations, the total neutrino flux ($\nu_e + \nu_\mu + \nu_\tau$) can be compared to the ν_e flux. This comparison showed that the total flux was in agreement with the models, while the electron neutrino flux always showed a deficit, pointing to some type of *flavour changing* process of neutrinos during their propagation between the Sun and the observers. The most plausible explanation for this was *neutrino oscillations*, a discovery which led to a Nobel Prize in Physics in 2015.

The idea of neutrino oscillations was first proposed in the late 1950s by Pontecorvo [161], [162]. These oscillations are a quantum mechanical phenomenon which arises due to neutrinos being produced via charged current interaction as *flavour states*, which are linear superpositions of *mass eigenstates*. Thus, neutrinos are emitted and absorbed in weak interactions in their flavour eigenstates, but they propagate as mass eigenstates.

We now introduce the Pontecorve-Maki-Nakagawa-Sakata (PMNS) matrix U, which is a 3×3 unitary mixing matrix, and allows a particular *ket* state to be written as

$$|\nu_\alpha\rangle = \sum_{k-1}^{3} U^{\star}_{\alpha k} |\nu_k\rangle \quad \text{with} \quad \alpha = \mathrm{e}, \mu, \tau \,, \tag{6.1}$$

where Latin indices indicate mass states and Greek indices label flavour states, and the normalisation $\langle \nu_\alpha | \nu_\beta \rangle = \delta_{\alpha\beta}$ and $\langle \nu_i | \nu_j \rangle = \delta_{ij}$ has been assumed.

Furthermore, we can now introduce the *survival probability*, which is the probability that a given neutrino ν_α is still in the same flavour state at a distance L:

$$P_{\nu_\alpha \to \nu_\alpha}(L) = 1 - 4 \sum_{k>j} |U^2_{\alpha k}| \, |U^2_{\alpha j}| \sin^2 \left(\frac{\Delta m^2_{kj}}{2|\boldsymbol{p}|} \frac{L}{c} \right) \,, \tag{6.2}$$

and conversely we have the *total transition probability* given by $1 - P_{\nu_\alpha \to \nu_\alpha}$. In expression 6.2 we can clearly see that the oscillation probability is dependent on the mass difference term, thus in order for there to be oscillations between two flavours, neutrinos can not be massless.

We can also see from equation 6.2 that experiments located at different distances will be more sensitive to a value of Δm^2 such that $\Delta m^2 L/(2E) \sim 1$. With this, there are two typical regimes of oscillations: a slow one governed by $\nu_1 \leftrightarrow \nu_2$ (the most significant one for solar neutrinos)

and a fast one corresponding to all other oscillations. There are other sources of neutrinos of interest, such as nuclear reactors, which produce ν_e in the MeV range and are classified as short baseline (SBL) with $L \sim 10\,\text{m}$, long baseline (LBL) with $L \sim 1\,\text{km}$, and very long baseline (VLBL) with $L \sim 10^2\,\text{km}$. For neutrinos produced by accelerators in the energy range $1 - 100\,\text{GeV}$ due to the pion, kaon and muon decays, SBL will refer to $L \sim 1\,\text{km}$ and LBL will refer to $L \sim 10^3\,\text{km}$. A final type of neutrino source to be discussed are atmospheric neutrinos, which are produced when cosmic-rays interact with atoms in our atmosphere, producing pions which then decay into neutrinos and muons, which further decay into electrons and create additional neutrinos.

With the different experimental techniques to search for neutrinos, we can express the PMNS matrix in a way that reflects the sensitivity of different experiments to the contributing terms:

$$U = \underbrace{\begin{pmatrix} 1 & 0 & 0 \\ 0 & c_{23} & s_{23} \\ 0 & -s_{23} & c_{23} \end{pmatrix}}_{\text{atm. or LBL}} \underbrace{\begin{pmatrix} c_{13} & 0 & s_{13}e^{-i\delta} \\ 0 & 1 & 0 \\ s_{13}e^{-i\delta} & 0 & c_{13} \end{pmatrix}}_{\text{SBL reactor}} \underbrace{\begin{pmatrix} c_{12} & s_{12} & 0 \\ -s_{12} & c_{23} & 0 \\ 0 & 0 & 1 \end{pmatrix}}_{\text{solar or LBL reactor}} \underbrace{\begin{pmatrix} e^{i\alpha_1} & 0 & 0 \\ 0 & e^{i\alpha_2} & 0 \\ 0 & 0 & 1 \end{pmatrix}}_{\text{neutrinoless double } \beta} \tag{6.3}$$

where I have used the shorthand notation $c_{ij} = \cos(\theta_{ij})$ and $s_{ij} = \sin(\theta_{ij})$, and θ_{ij} is the mixing angle of mass states i and j. Additionally, $\alpha_{1,2}$ are phase factors relevant only if neutrinos are Majorana (meaning they are their own antiparticle). These factors are being probed in neutrinoless double β-decay experiments. Finally, the phase term δ is only non-zero if neutrino oscillations violate CP symmetry (which is yet to be observed experimentally).

A lot of experimental effort is dedicated to measuring the parameters in the PMNS matrix, such as the mixing angles and phases. The masses are much more complicated, though. We can define the mass differences as

$$\delta m^2 = m_2^2 - m_1^2 > 0 \quad \textit{and} \quad \Delta m^2 = m_3^2 - \frac{m_2^2 + m_1^2}{2}\,. \tag{6.4}$$

Solar neutrino studies have been able to deduce the sign of δm^2, showing us that $m_2 > m_1$. However, the sign of Δm^2 is still unknown, which leads us to two possibilities: *normal hierarchy* (NH) if $m_1 < m_2 < m_3$, or *inverted hierarchy* (IH) if $m_3 < m_1 < m_2$. Furthermore, the absolute scale of the neutrino mass is also unknown, but we can set theoretical lower bounds on the sum of neutrino masses $M_\nu = \sum_i m_i$: in NH we can set $m_1 = 0$ and find $M_\nu \gtrsim 0.06\,\text{eV}$, while in IH we can set $m_3 = 0$ and find $M_\nu \gtrsim 0.10\,\text{eV}$. The current experimental bound on the sum of neutrino masses from particle physics is $M_\nu \leq 2.2\,\text{eV}$ [163]. This bound is expected to improve by one order of magnitude with the forthcoming KArlsruhe TRItium Neutrino (KATRIN) experiment [164]. Additionally, current bounds from cosmology are $M_\nu < 0.12\,\text{eV}$ [19], and are explored in more detail in section 6.3.

While we have come a long way since Pauli first proposed unmeasurable neutrinos, there are still important questions about these particles that need addressing, mainly

- The unitarity of the PMNS matrix, as if this is not the case, it would require new physics such as a sterile neutrino.
- The nature of antineutrinos: Majorana or Dirac.
- Possible CP violations in the leptonic sector, which would indicate that neutrinos and antineutrinos oscillate differently.
- The neutrino mass scale and hierarchy.

A lot of experimental effort is being put into solving these questions, both in particle physics and cosmology, and it is likely that the answers will come from many different experiments.

6.2 Cosmological Implications of Massive Neutrinos

Now that we have seen that neutrinos have mass, we can discuss the profound consequences this has on cosmological observables. In this section I will discuss the impact this species has on both the CMB and the matter power spectrum, focussing only on the case of massive neutrinos. In section 7.1.2 I will discuss instead the case of having an extra massless relativistic species.

The overall impact of massive neutrinos on the CMB is shown in the left panel of Fig. 6.1. When discussing the impact of one species on the CMB, we need to be aware of several effects mixing together: we can mitigate the effect of one parameter by tuning other parameters accordingly. Thus, to discuss the impact of massive neutrinos on the CMB, I will divide the effects into

- Background effects: these are encoded in a modified evolution of the scale factor $a(\tau)$. In section 4.1 we saw that the CMB spectrum depends on a small number of effects related to different characteristic scales, characteristic times, to the primordial spectrum, and to density ratios. I will continue to describe these effects as (C1)-(C8), as in section 4.1.
- Perturbation effects: these are more direct than background effects. The presence of a decoupled species can modify the evolution of metric fluctuations, and backreacts on the perturbations of the coupled photon-baryon fluid. When discussing the perturbation effects the background effects will be cancelled out by tuning other parameters.

The effects of massive neutrinos on observables are encoded in two parameters: $N_{\rm eff}$, which will describe the neutrino abundance in the early universe, as seen in equation 1.82; and ω_ν, which gives the total density of neutrinos today and is dominated by the contribution of at least two mass eigenstates, as seen in the previous section. For simplicity, I will assume that all neutrinos have the same mass (as in the degenerate limit of both NH and IH scenarios), and share the same Fermi-Dirac distributions. Furthermore, we can restrict ourselves to the case where neutrinos become non-relativistic after radiation-matter equality, $M_\nu < 1.5\,\text{eV}$, as heavier neutrinos would be in contradiction with current bounds, due to the growth of the comoving free-streaming horizon [165].

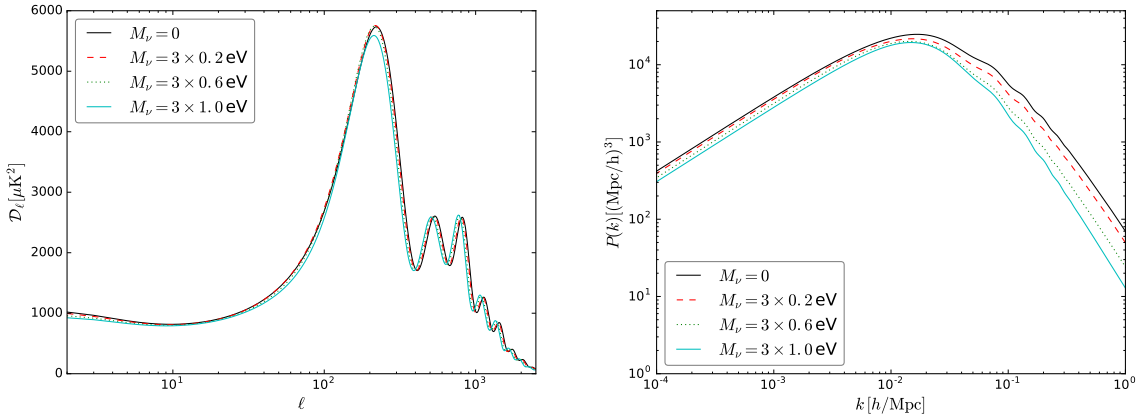

FIGURE 6.1: *Left*: Temperature power spectrum $\mathcal{D}_\ell^{TT}$ for different total neutrino masses, assuming three equal neutrinos and keeping all other ΛCDM parameters fixed to their best-fit value from [19]. *Right*: Same as left for the linear matter power spectrum $P(k)$ evaluated at $z = 0$.

To discuss the background effects, we first need to recover the redshift of radiation-matter equality. In the presence of massive neutrinos this is given by

$$z_{eq} = \frac{\omega_b + \omega_{\rm CDM}}{\omega_\gamma \left[1 + 0.2271 N_{\rm eff}\right]}\,, \tag{6.5}$$

where the neutrinos are counted in the $N_{\rm eff}$ factor (as they were relativistic at the time of this equality). Therefore, when comparing different masses to see how these impact the CMB, we should maintain both ω_b and $\omega_{\rm CDM}$ fixed, thus increasing $\omega_M = \omega_b + \omega_{\rm CDM} + \omega_\nu$ at the same time. Furthermore, by tuning Λ and h we can maintain the same peak and damping scale.

Therefore, if we increase M_ν but maintain the same peak scale and redshift of equality we will only modify two effects: the LISW effect (C7), due to a shift in z_Λ; and the diffusion damping effect (C4), but this latter one will only be for neutrinos with $M_\nu \geq 0.6\,\mathrm{eV}$ (neutrinos that are already non-relativistic at decoupling). Additionally, the added $N_{\rm eff}$ will lead to an overall diffusion damping (this comes from neutrino free-streaming, and will be explored fully in section 7.1.2). Any other differences in the CMB spectra will come from the direct gravitational impact of the massive neutrinos at perturbation level.

On the perturbation level, we will have effects caused by the gravitational driving of the photon-baryon oscillator equation before decoupling, and by the EISW effect. The former will lead to a suppression in the range $30 < \ell < 500$ while the latter will result in a depletion of the spectrum for $20 < \ell < 200$, with the exact location depending on the neutrino mass (as the neutrino becomes non-relativistic and has a clustering component instead of being completely free-streaming). While the depletion of the CMB caused by the EISW effect depends on the time at which neutrinos become non-relativistic, and therefore on the individual masses, this mass-splitting effect is too small to be detectable. Thus, the differences between NH and IH are too small to be seen in the CMB, and so we can not gain information about the individual

masses from this probe, but we can use it to constrain the sum of the neutrino masses.

In addition to the effects described above, there are also some late time effects in the CMB caused by massive neutrinos. Neutrino mass has two opposite effects on the LISW contribution: on the one hand, metric fluctuations are erased slightly on small scales because of the neutrino free-streaming, leading to a suppression of the LISW. On the other hand, ϕ decreases quicker because of neutrino masses, and so in absolute value ϕ' is increased. These competing effects are not discussed here, but are explored fully in [166]. Finally, in the presence of massive neutrinos the CMB lensing power spectrum features a step-like suppression on small scales, due to the enhanced matter fluctuations.

In section 4.2 we saw the overall behaviour of the matter power spectrum, as well as the main effects on its shape, denoted by (P1)-(P5). The impact of extra relativistic degrees of freedom on the matter power spectrum is discussed in depth in section 7.1.2. To summarise, the effects can be classified again into perturbation effects, which will manifest as an impact on the phase and amplitude of the BAO; and background effects, that also depend on which other parameters we fix. If we maintain the baryon-to-dark matter ratio (as well as the redshifts of equality), we will modify effect (P3): higher $N_{\rm eff}$ will shift the BAO peaks to smaller scales. On the other hand, if we instead maintain the baryon density (and the equality redshifts), we modify effect (P2) and the amplitude is enhanced on small scales, while the BAO amplitude receives extra damping.

The impact of adding massive neutrinos is similar to that of adding hot dark matter, and is shown in the right panel of Fig. 6.1. As before, I will restrict the discussion to the case of $M_\nu < 1.5\,\text{eV}$, thus assuming that neutrinos become non-relativistic after radiation-matter equality. The impact of massive neutrinos on the matter power spectrum can be divided into three groups, based on if we are looking at modes close to the non-relativistic transition $k_{\rm nr}$:

- For modes with $k < k_{\rm nr}$, the massive neutrino matter power spectrum is the same as the massless case (assuming the models have the same ω_M).
- For modes with $k \gg k_{\rm nr}$, massive neutrinos free-stream out of high-density regions into low-density regions, leading to a reduction of the growth rate of $\delta_{\rm CDM}$ and $\delta_{b+\rm CDM}$, thus damping out small scale density perturbations
- For modes with k slightly larger than $k_{\rm nr}$, neutrino perturbations are not completely negligible, leading to a smooth transition between the region where the neutrino masses have no effect and where they have maximum effect.

In summary, neutrino masses will produce a smooth step-like suppression of the matter power spectrum on scales $k > k_{\rm nr}$, with heavier neutrinos producing a larger suppression, thus allowing us to constrain the total neutrino mass by studying the matter power spectrum.

With all of these things considered, there are many different cosmological probes we can use to constrain the sum of neutrino masses, the most relevant of which are summarised below.

- CMB temperature and lensing spectra are affected by neutrino mass, as discussed above.

- Precise measurements of the BAO scale and amplitude can also aid us in constraining the relevant parameters.
- Galaxy Clustering: galaxy maps can be smoothed over small scales and Fourier transformed to provide a matter power spectrum. This is non-trivial, as we need to account for a bias (as galaxies are not perfect tracers of dark matter), and it is necessary to convert redshifts into comoving distances, which introduces redshift space distortions. Nonetheless, with increasingly better surveys such as LSST [62] this is a very promising avenue to measuring neutrino properties.
- Galaxy Weak Lensing: As discussed in section 1.9.1, images of observed galaxies are distorted by gravitational lensing effects, caused by density fluctuations along the line-of-sight. One of these effects is cosmic shear: the squeezing of an image in one direction in the sky, and its stretching in the orthogonal direction. This observation will allow us to map the lensing potential, which would allow us to measure the small scale suppression in the matter power spectrum at a specific redshift.
- Lyman-α: As discussed in section 4.3, the Lyman-α forest is very sensitive to the matter power spectrum on small scales, and thus it is able to help us look for a possible suppression in the matter power spectrum induced by neutrino masses, as done for example in [167].
- In addition to Lyman-α, it should be possible to map the hydrogen clouds by directly measuring the photons coming from the hydrogen atoms at a wavelength of $\lambda = 21\,\text{cm}$, as discussed in section 7.2. This would allow us to map the baryonic fluctuations at high redshift, and hence to probe the matter power spectrum deep inside the matter-dominated regime on linear scales. For a review, see [168].

With so many effects on cosmological observables across many different scales, it is not surprising that cosmology is playing a vital role in obtaining increasingly more precise bounds on the sum of neutrino masses.

6.3 Neutrino Mass Forecast

In the previous section we saw the importance of neutrino mass to cosmology, and its effects on cosmological observables. As mentioned in the section 6.1, when assuming a standard ΛCDM universe, the current best bounds from cosmology are [19], [169]

$$\sum M_\nu < 0.12\,\text{eV} \quad (95\,\%\text{C.L., using Planck TT,TE,EE + lowE + lensing + BAO})\,. \tag{6.6}$$

We expect these bounds to become more stringent with increased precision of future cosmological experiments. As such, in **[II]** we performed forecasts for the sensitivity to the sum of

neutrino masses, $\sigma(M_\nu)$, for different combinations of future CMB and LSS missions, with several different underlying cosmological models. This section is based on the aforementioned paper.

6.3.1 Pipeline

Forecasting the sensitivity of future cosmological experiments to the sum of neutrino masses is not new, and indeed many such forecasts have been done in the past in the literature (see for example [170]–[185] and references therein). However, existing forecasts are very difficult to compare to one another, due to big differences in methodology (Fisher formalism with different prescriptions or MCMC forecasts), different underlying cosmological models, and different assumptions relating to the future experimental configurations.

In order to allow for clear comparison between the different experiments, and thus to really see what is needed to, for example, improve the bounds to the point of detecting or excluding inverted hierarchy, in this work we used a *uniform pipeline* with the same assumptions and formalism. With this uniform pipeline we used the parameter extraction code MONTEPYTHON , interfaced with the Boltzmann solver CLASS, to perform a three-dimensional grid of forecasts. The different axes of our grid are explained in detail below, but can be summarised as: four underlying cosmological models, seven CMB experiments (or combination of them when relevant), and five LSS surveys (or a combination of them); leading to a total of 140 different forecasts that can be easily compared.

To carry out our forecasts, we used the MCMC forecast method[4] described in section 4.4, and first proposed in [84]: a future experiment is encoded as a mock likelihood, providing the probability that the mock data is true given the model assumed at each step of the MCMC parameter exploration. We neglected scattering in the mock data: it is directly given by the C_ℓs of the assumed fiducial model. Generating $a_{\ell m}$s as a single random realisation of the fiducial cosmology would change the reconstructed mean values, but not the sensitivities [84]. In the case of mock likelihoods accounting for LSS, we marginalised over nuisance parameters that account for residual systematic effects.

Models

As mentioned above, one of important point to address when doing neutrino mass forecasts is which assumptions we use for the underlying cosmology, as known parameter degeneracies can significantly weaken the obtained constraints. As a first step, however, we needed to decide how we treat the neutrino mass. Cosmological observables are only slightly sensitive to the individual neutrino masses, as described in section 6.2, thus we do not hope to constrain three mass states, but rather the sum of these. Therefore we needed to make some assumptions on the mass splitting.

[4] We chose to use MCMC, rather then Fisher matrix forecasts, as the latter becomes unreliable when the likelihood deviates significantly from a multivariate Gaussian in the model parameters, or when there are strong degeneracies between parameters.

For a completely physically realistic forecast we should float the absolute neutrino mass scale, considering three different masses related to each other by the solar and atmospheric mass square differences, either obeying to the normal or inverted hierarchy [186]. However, it has been shown that the difference between cosmological observables for these realistic neutrino mass hierarchies and a mass-degenerate model with the same total mass M_ν is extremely small (at most $0.1\,\%$ in the matter power spectrum), and therefore below the sensitivity of future experiments [187]–[189]. Thus, for simplicity in our forecasts we assumed a mass-degenerate model, with three massive neutrinos sharing an equal mass of $M_\nu/3$.

With this in mind, we studied the robustness of neutrino mass bounds in four different cosmological models:

- Seven parameter ΛCDM+M_ν: Our baseline model was the minimal ΛCDM parameterised with $\{\omega_{\rm b}, \omega_{\rm cdm}, \theta_s, A_s, n_s, z_{\rm reio}\}$, as discussed in section 1.6, extended to included massive neutrinos. In this model, the neutrino mass has non-trivial correlations and degeneracies with some of the other cosmological parameters, as discussed in [179]. The most significant degeneracy appears between M_ν and the optical depth (or redshift) of reionisation when combining future CMB, BAO, and LSS data sets, although this is absent in the CMB-only forecasts. This degeneracy will be revisited when I discuss the LSS data sets used for our forecast. When producing our mock data for future missions, we need to start from a choice of fiducial cosmological values: we chose values consistent with the Planck measurements, $\omega_{\rm b} = 0.02218$, $\omega_{\rm cdm} = 0.1205$, $\theta_s = 1.04146$, $\ln 10^{10} A_s = 3.056$, $n_s = 0.9619$, $z_{\rm reio} = 8.24$, taken from table 8, column 5 of [190].

- Eight parameter ΛCDM+M_ν + $N_{\rm eff}$: When using older datasets a M_ν–$N_{\rm eff}$ parameter degeneracy often appeared [191]–[195]. However, all post-Planck fits have shown that this degeneracy is now resolved. Nonetheless, we were interested in showing that the neutrino mass measurement will be stable against varying $N_{\rm eff}$. Additionally, $N_{\rm eff}$ is by itself a significant parameter to fit to the data (see section 7.1.2), given the wide range of models with new particle physics assumptions that it covers, and by including it in our forecasts we were also able to see how sensitive future mission will be to this parameter.

- Eight parameter ΛCDM+M_ν + w_0: In principle, dynamical dark energy models can be described by an infinite amount of parameters: even in the sub-class of models with negligible dark energy perturbations the background evolution can be described by a free function $w(z)$. However, in late-time dark energy models, this function only impacts cosmological observables at small redshift, and thus a Chevalier-Polarski-Linder parametrisation [196] $w(z) = w_0 + w_a(1 - a/a_0)$ with two free parameters w_0 and w_a is usually sufficient to catch the main features of a given model and study degeneracies with other parameters. For our first dark energy model we consider only a varying w_0, fixing $w_a = 0$, resulting in an eight-parameter model.

- Nine parameter ΛCDM+M_ν + w_0 + w_a: Similar to the previous case, we consider dark energy models with the CPL parametrisation, extended now to include the cases where $w_a \neq 0$, giving us an additional parameter that can lead to degeneracies. We include

phantom values ($w(z) < -1$) already known to result in weaker bounds on M_ν (see for example [197], [198].

The above choice of models represent only a subset of those that exhibit potential degeneracies with M_ν: there are many other models that could be interesting[5], but the inclusion of these models would have made our already computationally demanding grid too extensive, and were thus ignored. Therefore, apart from the above extensions to ΛCDM, we made the following assumptions about the underlying physics of the universe:

- the universe is spatially flat,
- the motion of particles in the universe is given by GR (as described in section 1.3),
- dark matter behaves as a cold and collisionless particle,
- there are three neutrino species with equal mass, as discussed above,
- neutrinos are non-interacting and have a frozen thermal distribution, and
- inflation leads to power-law spectrum of primordial curvature perturbations and a negligible spectrum of tensor perturbations (as discussed in section 2.4).

CMB Experiments

For our CMB missions, we were interested in four proposed future missions. As these missions are still in the design/proposal phase, the final experimental configuration is not yet known, so we used the current predictions for the instrument sensitivity. We considered the following missions:

- The Planck ESA satellite, used as our baseline, so we can compare future missions to the current state-of-the-art measurements [11].
- The LiteBIRD satellite project of JAXA, optimised for primordial B-modes, with very good sensitivity but modest resolution. Experimental configuration taken from [199], [200] [6].
- The CORE-M5 satellite project, which would have a slightly better sensitivity and significantly better resolution than LiteBIRD, but was unfortunately not selected in the previous ESA M5 call. Experimental configuration taken from [201].
- The CMB Stage Four (CMB-S4) project, a combination of many ground-based detectors, to be deployed over the next decade, with impressive resolution and sensitivity but smaller sky coverage than satellites. Experimental configuration taken from [202], [203].
- The PICO satellite project, which is likely to be submitted to NASA in the future, would improve over the sensitivity of LiteBIRD by a factor of 3 to 4. Experimental configuration taken from [204], [205].

[5] A very interesting case is spatial curvature. As both M_ν and Ω_k affect the CMB peak scale, there is a partial degeneracy between the two. However this can be mitigated by other neutrino mass effects, such as neutrino free-streaming affecting the matter growth factor after the non-relativistic transition.

[6] In the time between publishing **[II]** and writing this thesis, LiteBIRD was approved by JAXA, and construction is set to begin soon.

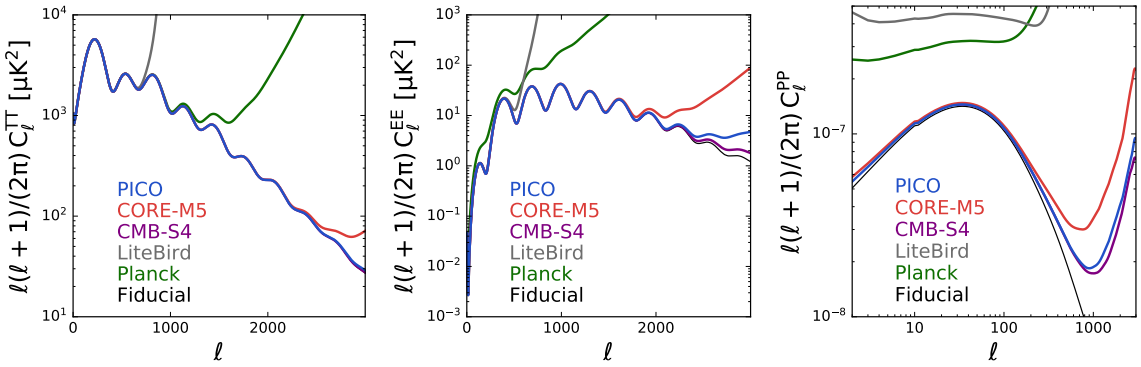

FIGURE 6.2: Noise spectra for each experiment, based on the minimum variance estimator. The fiducial model (black) is compared to the model plus noise spectra, $C_l + N_l$, for each experiment: Planck(green), LiteBIRD (grey), CMB-S4 (purple), CORE-M5 (red), and PICO (blue), for temperature anisotropies (left), E-mode polarisation (middle), and CMB lensing potential (right).

In addition to the experiments listed above, we can exploit the high degree of complementarity between satellite missions (optimised for large angular scales) and ground-based missions (optimised for smaller angular scales) by combining LiteBIRD + CMB-S4 and CORE-M5 + CMB-S4. For these combinations we made the same assumption as in [202]: we neglected regions of overlapping data and considered that the optimal combination will consist in LiteBIRD/CORE-M5 data for $\ell \leq 50$, CMB-S4 data for $\ell > 50$ in the region covered by the experiment ($40\,\%$ of the sky), and additional high-ℓ data from LiteBIRD/CORE-M5 in the region covered by the satellite but not by CMB-S4 ($30\,\%$ of the sky). Once we have incorporated the two combinations, we end up with a total of seven different experimental set-ups.

Finally, in order to have a complete mock likelihood for a future mission, we needed to estimate the noise spectrum for each experiment. The noise spectra of temperature and polarisation can be inferred from the resolution and sensitivity parameters according to standard approximations (see for example equation (2.2) in [84]), and are assumed to be statistically independent, which means that the noise spectrum of the cross-correlation N_ℓ^{TE} is approximated as zero.

To estimate the error that would be performed on the measurement of the lensing potential spectrum we used the fiducial model and noise spectra to run a quadratic estimator [206], done with the FUTURCMB code [84]. These estimators are based on products of four multipoles, each of the T, E, or B type, but for a more conservative forecast we discarded any information coming from the auto-correlation of the B-mode maps, due to the non-Gaussianity of the $a_{\ell m}^B$ multipoles. All quadratic estimators can then be combined in order to minimise the reconstruction noise: this defines the minimum variance estimator [206].

The resulting noise spectra computed using the minimum variance estimator are shown in Fig. 6.2. As expected, LiteBIRD performs very well on large scale polarisation, while not adding significantly to CMB lensing information. CMB-S4 does well on very large scales;

however, as it is a ground-based mission it has a smaller sky fraction, which is not taken into consideration in the noise calculation, and additionally it may be subject to foreground issues. The obtained sensitivity for CORE-M5 is in very good agreement with that presented in the CORE parameters paper [197], with a slight improvement for CMB lensing extraction coming from the use of the minimum variance estimator noise spectra instead of the EB estimator. Finally, once sky coverage is taken into account, the futuristic PICO satellite should out-perform CMB-S4, which covers a much smaller fraction of the sky, while also having the advantage of a large number of channels and full-sky observations for improved foreground removal.

LSS Surveys

As we have seen in section 6.2, neutrino mass has a significant impact on structure formation in the universe. Thus, LSS data will be crucial for constraining the sum of neutrino masses. We considered the following future experiments:

- The Dark Energy Spectroscopic Instrument (DESI), scheduled to start observing in 2019, is set to measure the BAO scale with percent-level precision. While the experiment is designed to measure in the redshift range $0.05 < z < 2.1$, to be more conservative we narrowed this to $0.15 < z < 1.85$. Experimental configuration taken from [207], [208].
- The Euclid satellite, scheduled to be launched in 2021, will perform a highly precise galaxy survey out to $z > 2$, aiming at a $1\,\%$ accuracy on the galaxy clustering and cosmic shear observables. Experimental configuration taken from [61], [209].
- The Square Kilometre Array (SKA) mission, set to be the largest radio telescope in the world, is designed to provide cosmic shear and galaxy clustering information, as well as producing a map of neutral hydrogen through 21 cm intensity mapping, allowing us to trace the LSS distribution up to redshift $z \sim 20$. Experimental configuration taken from [210].

In addition to these missions, we can exploit another parameter degeneracy to improve our bounds on the sum of neutrino masses. In [176], [179], [211], an M_ν–$\tau_{\rm reio}$ degeneracy was shown. Thus, an independent measurement of $\tau_{\rm reio}$ would allow us to gain more information about the neutrino mass. Future 21cm intensity mapping missions, such as HERA or SKA could achieve a measurement accurate up to $\sigma(\tau_{\rm reio}) = 0.001$ [176], [211], if the astrophysical uncertainties are under control. Therefore, we added a fourth LSS data set in the form of a Gaussian prior on $\tau_{\rm reio}$ with such a standard deviation as a final mock likelihood, in order to study the impact on the neutrino mass sum of a possible measurement of this quantity.

Regarding the individual set-ups, for the DESI BAO data we used the same configuration as in [179]. For Euclid and SKA we relied on exactly the same approach and mock likelihoods as in [182]: for galaxy clustering we quantified the information in terms of three dimensional power spectrum, including redshift space distortions [212], fingers of God [213] and Alcock-Paczynski effects, and corrected for the scale-dependent neutrino induced bias [214]–[218], shown to be crucial when measuring massive neutrinos with future surveys like Euclid [219], [220]; for the cosmic shear from Euclid we constructed an angular harmonic power spectrum as our mock dataset, assuming Limber and flat-sky approximations [221], [222].

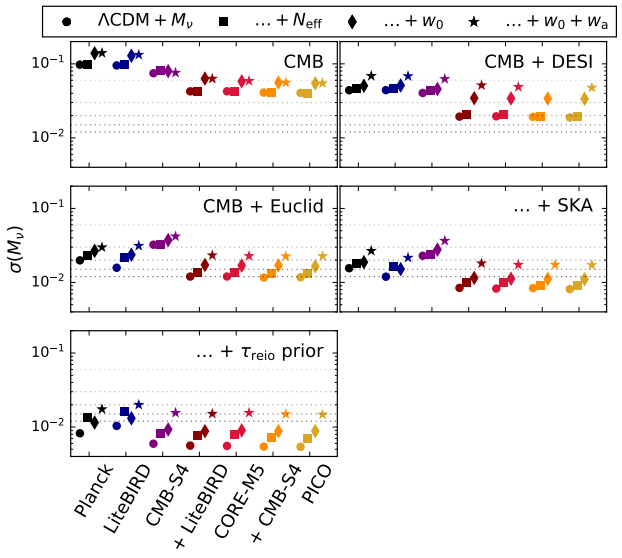

FIGURE 6.3: Neutrino mass sensitivity for each CMB experiment, alone and in combination with DESI, Euclid, Euclid + SKA1 IM, Euclid + SKA1 IM + $\tau_{\rm reio}$ prior. Each subplot corresponds to one CMB set-up plus LSS survey combination (CMB only, CMB + DESI, CMB + Euclid, CMB + Euclid + SKA1 IM, CMB + Euclid + SKA1 IM + $\tau_{\rm reio}$ prior from top left to bottom right). The horizontal dashed lines show the thresholds for a 1 to 5σ detection of $M_\nu = 0.06\,$eV.

In conclusion, in the course of this project, we constructed mock likelihoods for Planck, LiteBIRD, CORE-M5, PICO, CMB-S4, and combinations of these, as well as a DESI BAO likelihood, and a Gaussian $\tau_{\rm reio}$–prior. These were used in combination with the existing Euclid and SKA likelihoods created for [182] to forecast the sensitivity to the sum of neutrino masses for 35 different experimental combinations and for four different underlying cosmological models, leading to 140 total forecasts. The results of these forecasts are discussed in the following section. All of the likelihoods mentioned here were made publicly available in MONTEPYTHON version 3.1.

6.3.2 Results

The objective of **[II]** was to forecast the sensitivity to the neutrino mass $\sigma(M_\nu)$ for a total of 140 different combinations of data sets and underlying model. The detailed results of these forecasts are shown in table 6.1. In the course of this work, we also performed sensitivity forecasts for all other relevant cosmological parameters: $\omega_{\rm cdm}$, ω_b, θ_s, A_s, n_s, $\tau_{\rm reio}$, Ω_m, σ_8, H_0, $N_{\rm eff}$, w_0, and w_a. The figures for all of these parameters were made publicly available online[7].

In order to visualise the results of Table 6.1, Figs. 6.4 and 6.3 provide a more intuitive and graphical summary. Both figures contain the same information; however, in Fig. 6.3 shows the

[7] https://brinckmann.github.io/montepython_public/neutrino_mass_forecasts/.

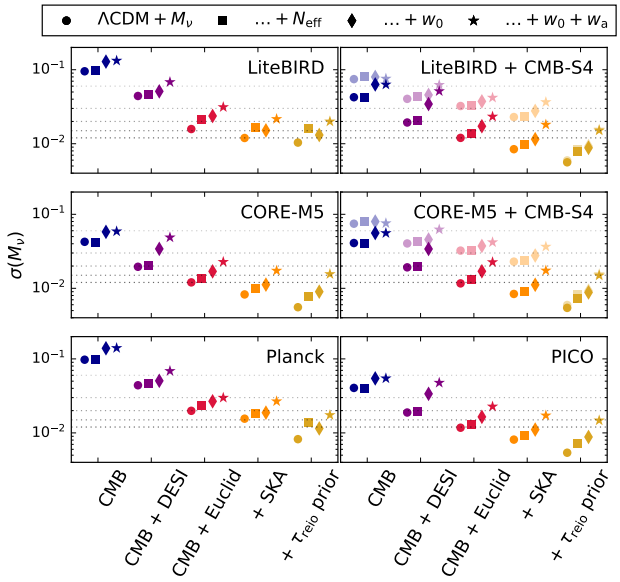

FIGURE 6.4: Neutrino mass sensitivity for each CMB experiment, alone and in combination with DESI, Euclid, Euclid + SKA1 IM, Euclid + SKA1 IM + $\tau_{\rm reio}$ prior. Each subplot corresponds to one CMB set-up (LiteBIRD, LiteBIRD + CMB-S4, CORE-M5, CORE-M5 + CMB-S4, Planck, or PICO from top left to bottom right, where the desaturated symbols indicate the CMB-S4 sensitivity) and relevant combinations with LSS surveys (reported on the x-axis). For each combination the sensitivity is depicted for four cosmological models: the minimal scenario ΛCDM $+M_\nu$, and three extensions $+N_{\rm eff}$, $+w_0$, and $+w_0+w_a$. The horizontal dashed lines show the thresholds for a 1 to 5σ detection of $M_\nu = 0.06$ eV.

importance of using more precise CMB datasets in combination with a given LSS experiment, whereas Fig. 6.4 the results are ordered in a way to highlight the impact of each LSS dataset in combination with a given CMB experiment.

If we focus for now on the minimal ΛCDM+M_ν scenario, our results show that, for a fiducial neutrino mass sum $M_\nu = 0.06$ eV:

- Given the high sensitivity of CORE-M5 and PICO, they would only require additional BAO data from DESI for a 3σ detection.
- Euclid together with the existing Planck data, or with the future LiteBIRD mission, could already achieve a $3-4\sigma$ detection.
- If we further combine LiteBIRD with Euclid and SKA1 intensity mapping, we would reach the 5σ threshold,.
- CORE-M5 or PICO would also achieve a 5σ detection in combination with Euclid only.
- Additionally, CORE-M5 or PICO would even achieve a 7σ detection when SKA1 intensity mapping data is added, and a 10σ one if we have an independent measurement of

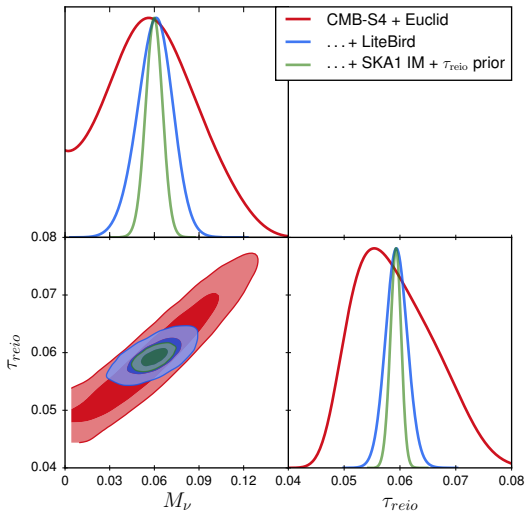

FIGURE 6.5: 95 % and 68 % confidence levels for the posterior distribution of M_ν–$\tau_{\rm reio}$, showing the correlation of these two parameters for the three configurations: CMB-S4 + Euclid (red), CMB-S4 + Euclid + LiteBIRD (blue), CMB-S4 + Euclid + SKA1 IM + $\tau_{\rm reio}$-prior (green) in the minimal 7 parameter ΛCDM+M_ν model.

$\tau_{\rm reio}$, for example from surveys focused on reionisation and the dark ages, thus illustrating the great advantage to neutrino physics this would bring.

- only a $2-3\sigma$ detection could be achieved by LSS experiments like Euclid and SKA when combined only with CMB-S4. It is important to remember that adding information from low-ℓ polarisation data strongly constrains $\tau_{\rm reio}$, which leads to a great improvement on the sensitivity to M_ν, and therefore CMB-S4 provides much better sensitivity once LiteBIRD, CORE-M5, or the $\tau_{\rm reio}$ prior is included (similarly, low-ℓ Planck data would already help in this regard). This effect is illustrated clearly in Fig. 6.5 (for a physical discussion see [179]).

- Finally, combining CMB-S4 with either LiteBIRD or CORE-M5 provides similar results in these forecasts. This is due to our assumption of perfect removal of foregrounds, which for a satellite mission with a large number of channels spanning a wide frequency range is expected to be a reasonable assumption. However, for ground-based missions *without* an accompanying satellite of similar sensitivity and resolution it is less clear if this is still the case. As such, the CMB-S4 + LiteBIRD results should be viewed as *optimistic*: a more realistic result would be obtained if an additional uncertainty due to foreground cleaning was added. In a similar vein, we can view the CMB-S4 + CORE-M5 as *conservative*: the frequency coverage and large number of channels of the satellite mission would lead to increased faith in foreground cleaning; we do not include the high multipoles for lensing $3000 < \ell < 5000$ for CMB-S4, which would likely lead to improved sensitivity of the combinations involving CMB-S4.

		ΛCDM+M_ν	ΛCDM+$M_\nu + N_{\rm eff}$	ΛCDM+$M_\nu + w_0$	ΛCDM+$M_\nu + w_0 + w_a$
	Planck	0.097	0.099	0.14	0.14
	LiteBIRD	0.095	0.098	0.13	0.13
CMB	CORE-M5	0.042	0.041	0.058	0.059
	CMB-S4	0.075	0.081	0.080	0.076
ONLY	CMB-S4 + LiteBIRD	0.042	0.042	0.063	0.063
	CMB-S4 + CORE-M5	0.041	0.041	0.056	0.056
	PICO	0.041	0.040	0.055	0.055
	Planck	0.044	0.047	0.051	0.069
	LiteBIRD	0.044	0.047	0.051	0.068
CMB	CORE-M5	0.020	0.021	0.034	0.049
+	CMB-S4	0.040	0.043	0.046	0.062
DESI	CMB-S4 + LiteBIRD	0.019	0.021	0.034	0.051
	CMB-S4 + CORE-M5	0.019	0.020	0.034	0.035
	PICO	0.019	0.020	0.034	0.048
	Planck	0.020	0.023	0.027	0.030
	LiteBIRD	0.016	0.021	0.024	0.031
CMB	CORE-M5	0.012	0.014	0.017	0.023
+	CMB-S4	0.032	0.033	0.037	0.042
Euclid	CMB-S4 + LiteBIRD	0.012	0.014	0.017	0.023
	CMB-S4 + CORE-M5	0.012	0.013	0.017	0.023
	PICO	0.012	0.013	0.016	0.023
	Planck	0.016	0.018	0.019	0.027
CMB	LiteBIRD	0.012	0.017	0.015	0.022
+	CORE-M5	0.0083	0.0099	0.011	0.017
Euclid	CMB-S4	0.023	0.024	0.028	0.037
+	CMB-S4 + LiteBIRD	0.0084	0.0098	0.012	0.018
SKA	CMB-S4 + CORE-M5	0.0084	0.0092	0.011	0.017
	PICO	0.0081	0.0091	0.011	0.017
CMB	Planck	0.0082	0.014	0.011	0.017
+	LiteBIRD	0.010	0.016	0.013	0.020
Euclid	CORE-M5	0.0056	0.0078	0.0090	0.016
+	CMB-S4	0.0060	0.0082	0.0093	0.016
SKA	CMB-S4 + LiteBIRD	0.0056	0.0078	0.0088	0.015
+	CMB-S4 + CORE-M5	0.0054	0.0072	0.0088	0.015
$\tau_{\rm reio}$-prior	PICO	0.0054	0.0071	0.0088	0.015

TABLE 6.1: Expected 1σ sensitivity for M_ν in eV, for all 140 combinations of data (rows) and model (columns).

When extending the discussion to the more complicated models, we see that the sensitivity to the sum of neutrino masses degrades, as expected. Our main results for these models show:

- When varying the number of extra relativistic degrees of freedom $N_{\rm eff}$, the sensitivity only degrades slightly, as expected as this degeneracy was already broken with Planck. However, when we include the $\tau_{\rm reio}$-prior with a varying $N_{\rm eff}$, the former becomes slightly less helpful in precisely measuring the neutrino mass sum, due to non-trivial

parameter degeneracies.

- Our sensitivity degrades the most when including a time-varying dark energy equation of state: in order to obtain a 3σ level of significance for the detection, CMB plus DESI BAO is never accurate enough, and we need at least the combination of LiteBIRD + CMB-S4 or CORE-M5 or PICO together with Euclid and SKA.
- However, if we succeed in making an independent measurement of $\tau_{\rm reio}$, we would achieve a 4σ neutrino mass detection in *any* of the extended models considered, using CORE-M5 or PICO in combination with Euclid and SKA1 intensity mapping.

6.3.3 Conclusions

In this chapter we have seen the significance of neutrinos both for particle physics and cosmology. Since the discovery of neutrino oscillations, it has been known that neutrinos have mass; however, an exact measurement of this mass remains elusive.

In **[II]** we showed that a detection of a non-zero neutrino mass from cosmology will be possible in the next decade, with upcoming LSS surveys and future CMB experiments set to lead the way. I have discussed here the results of this paper, where we performed forecasts of the sensitivity of an extended array of different CMB experiments in conjunction with LSS surveys, and an additional independent measurement of the optical depth at reionisation.

All of our forecasts were performed using the same methodology and assumptions, thereby making comparison between similar experiments more accessible. The results presented here are consistent with previous works when considering similar combinations of experiments and models: see for example [175], [184], [202], [211], [223]–[225] for CMB-S4; [197] for CORE-M5; [173], [179], [181], [182] for Euclid; [176], [185], [226] for SKA; and for example [227] for DESI. We also demonstrated the extraordinary complementarity of different cosmological probes, the physical effects of which have been studied in detail in the literature [179], [181], [184], [185].

Despite the very encouraging results presented here, we stressed that these forecasts are always performed with a number of assumptions, and thus are not necessarily a completely accurate prediction. For instance, we made the assumption that the noise in the TE cross-correlation channel is negligible, which may prove to be wrong. Additionally, our assumption that CMB foregrounds can be cleaned up to $\ell_{\rm max} = 3000$ for CMB-S4 might turn out to be too optimistic, as for ground-based experiments it will likely prove very challenging to robustly account for foregrounds and systematics with the limitations in sky coverage and number of accessible frequency channels.

On the other hand, the large size of ground-based telescopes allow for resolving very small scales, and thus we stressed that the combination of future high resolution satellite missions and ground-based experiments is crucial to obtain extremely high precision CMB measurements on a wide range of scales.

On the side of underlying model assumptions, we focused on a few representative extensions of the ΛCDM model, but we can not claim fully model-independent results, as we assumed negligible curvature, in addition to assuming GR[8]. Additionally, we ignored possible extensions involving some new physics causing the decay or the annihilation of cosmological neutrinos into lighter or massless particles, in such way that the neutrino mass would remain forever undetectable by cosmological data [228]. While these models can not be excluded, they remain far from reproducing the wealth of datasets as accurately as ΛCDM.

Thus, with our forecasts we can conclude that a neutrino mass detection from cosmology in the next decade is highly likely, provided we use a combination of ground-based and satellite experiments. If this detection does take place, it will solidify neutrino masses as a cornerstone not only of the standard model of cosmology, but also of the Standard Model of particle physics.

[8]Which is, of course, a very valid assumption, as discussed in section 1.3.

7 Dark Matter Paradigm Revisited

In section 1.9.2, I discussed the current paradigm of dark matter, where it is assumed to be cold, collisionless, and only interacting gravitationally. As discussed in section 1.9.1, such a species can explain many observations, ranging from local measurements of stellar velocities, to the observed anisotropies in the CMB. Despite its remarkable success, the standard paradigm faces some challenges, described in chapter 5. Moreover, despite our best efforts, WIMPs - one of the most well-motivated cold dark matter candidates - have so far eluded detection in direct and indirect detection experiments, as well as collider searches. Together with the potential problems on small scales and the apparent mismatch in different cosmological datasets, this has reinvigorated interest in models beyond the standard cold dark matter paradigm.

One of the easiest ways to go beyond the cold dark matter picture is to add additional interactions between dark matter and standard model particles, or even interactions in a *dark sector*: with dark matter interacting either with itself or with a dark relativistic component, known as dark radiation. These potential interactions would have to be very small to not violate existing constraints, such as those from the CMB; however, they could still have a significant impact on alleviating the aforementioned problems.

In the literature one can find plenty of studies on interaction between dark matter and photons (see for example [229]), dark matter and neutrinos (see for example [230]), dark matter and baryons (see for example [231]), self-interacting dark matter (see for example [126]), and dark matter and dark radiation interactions (see for example [232]). One could probably fill a whole book discussing all of these models. In this chapter I will focus on two cases: dark matter - dark radiation interactions, and dark matter - baryon scattering [1].

7.1 Dark Matter Interacting with Dark Radiation

A class of models that have gained a lot of interest in recent years are those where the dark matter can couple to an additional relativistic dark sector, known as dark radiation. Within this class of models, there are several variants depending on the properties of the mediator (scalar or boson, massive or massless), the temperature scaling of the interaction, and whether the dark matter and dark radiation can self-interact. Some variants have been proposed to alleviate the missing satellite problem [233]: the scatterings between this extra dark radiation

[1] As I am moving beyond cold dark matter, the subscript "CDM" will be changed for "DM".

and dark matter can reduce the number of satellites via a small scale matter power suppression. Furthermore, in other models, the additional dark radiation acts like $\Delta N_{\rm eff}$ and can lead to a higher H_0, while the collisional damping between the dark species suppresses growth on small scales, simultaneously leading to a lower σ_8 value, and thus alleviating the cosmological tensions, as proposed in [234]–[236].

Given the potential of these dark radiation interactions to solve the cosmological tensions, in **[III]** we used a generalised formalism to analyse several different realisations of dark matter - dark radiation interactions, using Lyman-α data with the method described in section 4.3. In this section I will first introduce the formalism we used and discuss how it covers several different models. I will then review the effects these interactions have on the observables, thus showing how they might alleviate the aforementioned tensions. In sections 7.1.3-7.1.5 I discuss the results we obtained in **[III]**.

7.1.1 Formalism

Dark matter interacting with dark radiation can significantly alter the formation and evolution of structures; but as discussed above, there are many different particle physics aspects that can greatly influence the actual effect of these models on cosmological observables. As such, it is important to identify which of the particle physics properties have the largest impact on the structure growth in the universe.

To simplify this task, in [237] a generalised framework, known as ETHOS (Effective THeory Of Structure formation), was proposed which aims to provide a mapping between the underlying particle physics dark matter model and its effects on linear structure growth in the universe. With this framework, many dark matter particle models that map to the same observable effects can be constrained simultaneously by comparing a single numerical simulation using ETHOS with observations.

In the ETHOS parametrisation, it is assumed that the single dark matter species (denoted with DM) can interact with a dark relativistic component (denoted with DR), with coupling allowed before matter-radiation equality. It is assumed that the only relevant processes for dark matter are the 2-to-2 scattering $DM + DR \leftrightarrow DM + DR$, and we also allow for dark radiation self-interactions with the process $DR + DR \leftrightarrow DR + DR$. Dark matter self-interactions are not considered within this framework, as the elastic scattering $DM + DM \leftrightarrow DM + DM$ is significant for non-linear structure growth, but would only affect linear perturbations if the dark matter were relativistic.

As a final assumption, the ETHOS parametrisation assumes that the relic abundance of dark matter is fixed at some high temperature via a process such as thermal freeze-out (as described in section 1.8), and thus we do not consider dark matter annihilation or decay. With the above assumptions, and working in the Newtonian gauge, the dark matter Boltzmann equations 3.20

become

$$\begin{aligned}\dot{\delta}_{\rm DM} &= 3\dot{\phi} - \theta_{\rm DM}\,,\\ \dot{\theta}_{\rm DM} &= -\frac{\dot{a}}{a}\theta_{\rm DM} + k^2\psi + k^2 c_{\rm DM}^2\delta_{\rm DM} + \Gamma_{\rm DM-DR}\left(\theta_{\rm DM} - \theta_{\rm DR}\right)\,.\end{aligned} \tag{7.1}$$

Furthermore, the dark radiation Boltzmann hierarchy will be similar to that of massless neutrinos, seen in equation 3.24, with the addition of an interaction term. The equations of motion are thus given by

$$\begin{aligned}\dot{\delta}_{\rm DR} &= 4\dot{\phi} - \frac{4}{3}\theta_{\rm DR}\,,\\ \dot{\theta}_{\rm DR} &= -k^2\left(\sigma_{\rm DR} - \frac{1}{4}\delta_{\rm DR}\right) + k^2\psi + \Gamma_{\rm DR-DM}\left(\theta_{\rm DR} - \theta_{\rm DM}\right)\,,\\ \dot{\pi}_{{\rm DR},\ell} &= -\frac{k}{2\ell+1}\left((\ell+1)\pi_{{\rm DR},\ell+1} - \ell\pi_{{\rm DR},\ell-1}\right)\\ &\quad + \left(\alpha_\ell\Gamma_{\rm DR-DM} + \beta_\ell\Gamma_{\rm DR-DR}\right)\pi_{{\rm DR},\ell} \quad \text{for} \quad \ell \geq 2\,.\end{aligned} \tag{7.2}$$

As discussed in section 3.1, the shear perturbation of the dark radiation $\sigma_{\rm DR}$ is relevant only when dark radiation is free-streaming[2]. Furthermore, I have introduced $\pi_{\rm DR} = 2\sigma_{\rm DR}$, as well as the dark matter sound speed $c_{\rm DM}^2$, given by

$$c_{\rm DM}^2 = \frac{T_{\rm DM}}{m_{\rm DM}}\left(1 - \frac{\dot{T}_{\rm DM}}{3T_{\rm DM}}\right)\,, \tag{7.3}$$

where $m_{\rm DM}$ is the dark matter mass. The dark matter sound speed depends on the heating rate, and is very small in the case of non-relativistic dark matter, and thus will have a minimal contribution in our equations.

The collisional terms that appear in the Boltzmann equations are the key ingredients to the interacting dark matter species, and depend on the underlying particle physics nature. Following [233], if we assume an interaction rate proportional to the temperature with a power-law, our dark radiation - dark matter collisional term becomes

$$\Gamma_{\rm DR-DM} = -\Omega_{\rm DM}h^2 a_{\rm dark}\left(\frac{1+z}{1+z_d}\right)^n\,, \tag{7.4}$$

where $a_{\rm dark}$ will give us the overall interaction strength, n is the power-law dependence of the temperature, and z_d is a normalisation factor related to the time of kinetic decoupling between dark matter and dark radiation, usually taken to be $z = 10^7$ (corresponding to $T_{kd} \sim 1\,{\rm keV}$). The inverse scattering is given by

$$\Gamma_{\rm DM-DR} = \left(\frac{4}{3}\frac{\rho_{\rm DR}}{\rho_{\rm DM}}\right)\Gamma_{\rm DR-DM}\,. \tag{7.5}$$

[2]If the dark radiation behaves as a perfect fluid, it will have no anisotropic stress.

In the simplest case, the coupling between the dark radiation and the mediator is the same as the coupling between the dark matter and the mediator, and thus the dark radiation self-scattering term $\Gamma_{\rm DR-DR}$ is equal to $\Gamma_{\rm DM-DR}$.

Furthermore, the parameters α_ℓ and β_ℓ that appear in the higher order momenta of the dark radiation hierarchy in equation 7.2 are the angular coefficients; the first one is related to the nature of the mediator ($\alpha_\ell = 3/2$ for a vector and $\alpha_\ell = 3/4$ for a scalar), while the latter determines the presence of dark radiation self-interactions ($\beta_\ell = 1$ in the case of interactions, else $\beta_\ell = 0$).

Finally, we can parametrise the dark radiation density from equation 7.5 as

$$\omega_{\rm DR} = f \left(\frac{T_{\rm DR}}{T_\gamma} \right)^4 \omega_\gamma \,, \tag{7.6}$$

where f is a factor related to the nature of the dark radiation ($f = 7/8$ for fermionic dark radiation and $f = 1$ for bosonic dark radiation), and ω_γ and T_γ are the photon density and temperature, respectively. The ratio between the dark radiation temperature and the photon temperature is further parametrised with

$$\xi \equiv \frac{T_{\rm DR}}{T_\gamma} \,. \tag{7.7}$$

We can see with the above expressions that ξ is related to the amount of dark radiation, and thus it can be recast into an increase in the relativistic degrees of freedom $N_{\rm eff}$ as

$$\Delta N_{\rm eff} = \frac{g^*_{\rm DR}}{2} \frac{f}{7/8} \xi^4 \left(\frac{T_\gamma}{T_\nu} \right)^4 \,, \tag{7.8}$$

where $g^*_{\rm DR}$ is the number of internal degrees of freedom of the dark radiation.

With the above considerations, we can see that in addition to the six base ΛCDM parameters, we need the following free parameters to completely define our model in the ETHOS framework:

- the amplitude of the scattering rate $a_{\rm dark}$,
- the amount of dark radiation parametrised with ξ ,
- the dark matter mass $m_{\rm DM}$,
- the temperature dependence of the comoving cross section n ,
- the angular coefficient determining the nature of the mediator α_ℓ , and
- the angular coefficient determining the dark radiation self-interactions, β_ℓ .

Furthermore, for a given model it is important to specify if the dark radiation is free-streaming or behaves as a fluid, as well as specifying if this species is bosonic or fermionic. In addition to

the above parameters, we can include the possibility of only a fraction $f_{\rm DM}$ of dark matter interacting, as there is no reason to assume that all of dark matter would have these scatterings. This would mean we would have two dark matter species: cold dark matter and interacting dark matter.

A very interesting sub-case of dark matter - dark radiation models are those discussed in [234]–[236], like for instance Non-Abelian Dark Matter (NADM), in which the momentum transfer rate from dark matter to dark radiation, related to the ETHOS rate by $\Gamma = -\Gamma_{\rm DM-DR}/a$, scales like a^{-2}. In this case the suppression of the matter power spectrum is smooth, because the temperature dependence of the interaction rate ($n = 0$ in the ETHOS parametrisation) is the same as the temperature dependence of the expansion rate during the radiation dominated epoch. This model is described by the parameters

- $\Delta N_{\rm fluid} \equiv \frac{\rho_{\rm DR}}{\rho_{1\nu}}$, which gives the amount of self-interacting dark radiation, parametrised as the effective number of extra neutrino families, and
- $\Gamma_0 \equiv \Gamma\,(a/a_0)^2$, which gives the momentum transfer rate from dark matter to dark radiation at redshift $z = 0$.

Therefore, the NADM model can be explored using the ETHOS parametrisation provided we use $n = 0$, and describe the dark radiation as behaving like a perfect fluid. With this in mind, in the NADM model the velocity perturbation equations from equations 7.1 and 7.2 become

$$\begin{aligned}\dot{\theta}_{\rm DM} &= -\frac{\dot{a}a}{\theta}_{\rm DM} + k^2\psi + k^2 c^2_{\rm DM}\delta_{\rm DM} - a\Gamma\,(\theta_{\rm DM} - \theta_{\rm DR})\ ,\\ \dot{\theta}_{\rm DR} &= -k^2\left(\sigma_{\rm DR} - \frac{1}{4}\delta_{\rm DR}\right) + k^2\psi - a\Gamma\left(\frac{3\rho_{\rm DM}}{4\rho_{\rm DR}}\right)(\theta_{\rm DR} - \theta_{\rm DM})\ .\end{aligned} \tag{7.9}$$

Finally, we can see that the relation between the ETHOS parameters and the NADM parameters is given by

$$a_0\Gamma_0 = \Gamma_{\rm DM-DR}(z=0) = \frac{4}{3}\omega_{\rm DR}\,a_{\rm dark} = \frac{4}{3}\omega_\gamma\,a_{\rm dark}\xi^4\,. \tag{7.10}$$

7.1.2 Effects on Observables

Dark matter - dark radiation interactions present a rich phenomenology, with several significant impacts both on the matter power spectrum and the CMB anisotropies. To describe these effects properly, first I will discuss the impact of adding a new relativistic species, detailing how the effects change based on the nature of the dark radiation, and then I will look at the effects of turning on the interactions between dark matter and dark radiation.

The impact on cosmological observables coming from increasing the number of relativistic species, $\Delta N_{\rm eff}$ has been well described in the literature (see for example [156], [238]). These effects can be decomposed into background and perturbation effects, as done for neutrinos in section 6.2: for the background effects, the nature of the dark radiation (whether it behaves like a fluid or is free-streaming) has no impact, while it becomes an important detail when looking at the perturbation effects.

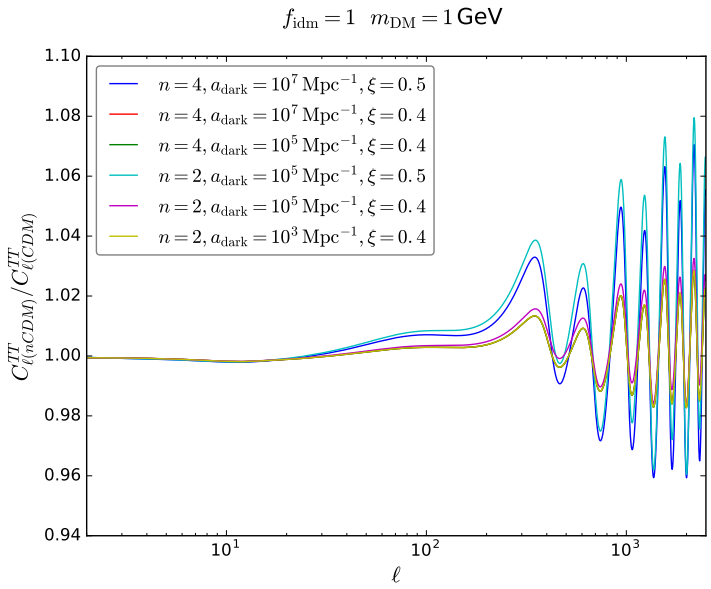

FIGURE 7.1: Effects of dark matter - dark radiation interactions on the CMB. The C_ℓ^{TT} is shown for the interacting model relative to a model with the same ΛCDM parameters but no interactions or additional dark radiation. The different curves illustrate the impact of changing the interaction strength and amount of dark radiation.

To better appreciate the main background effect of increasing $\Delta N_{\rm eff}$, it is necessary to keep the redshift of radiation-matter equality and of matter-Λ equality fixed, otherwise the effects of the new species would be lost in a simple shift of these times. To maintain the redshifts, we can fix ω_b, n_s, A_s, and $\tau_{\rm reio}$, while allowing the remaining two to vary. As we allow ω_m to vary, the critical density today is enhanced (preserving the desired equality redshifts), and therefore H_0 has to increase (see section 1.6 for a detailed description on the interplay between these parameters). With the increase in H_0, the angular diameter distance also increases, as does the sound horizon at decoupling. As a net effect, the amount of Silk damping (as described in section 3.5) is increased.

To discuss the perturbation effects, we need to distinguish between free-streaming dark radiation and self-interacting dark radiation. Extra free-streaming particles would naturally travel at the speed of light, and due to a neutrino drag effect they would pull the CMB peaks towards larger scales, shifting all the acoustic peaks to higher multipoles. Furthermore, the gravitational interaction between the photon perturbations and the free-streaming dark radiation perturbations, taking place before decoupling, reduces the CMB spectrum on scales crossing the sound horizon before decoupling. On the other hand, self-interacting dark radiation has acoustic oscillations propagating at a sound speed of $c^2_{\rm DR} \leq 1/3$, thus mitigating the drag effect. Furthermore, in this latter case, the photon fluid couples with a dark radiation fluid with a comparable fluctuation amplitude, and therefore the overall suppression of the CMB is also reduced.

Having seen the impact of an extra relativistic dark species, we can now discuss what changes

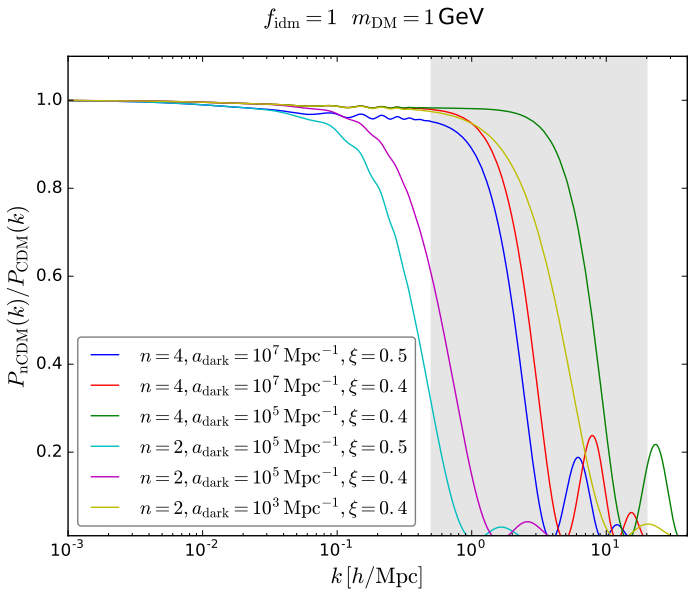

FIGURE 7.2: Effects of dark matter - dark radiation interactions on the matter power spectrum. The $P(k)$ is shown for the interacting model relative to a model with the same ΛCDM parameters but no interactions or additional dark radiation. The different curves illustrate the impact of changing the interaction strength and amount of dark radiation. The grey region corresponds to the scales that can be probed with Lyman-α.

if this species can interact with dark matter. We can discuss several effects caused by these interactions, two of which are very similar to those discussed above. To better illustrate the effects of the interaction itself, we can compare to a base ΛCDM model with an equivalent number of extra neutrinos (ΛCDM+$\Delta N_{\rm eff}$), thus removing the background effects discussed above. The main effects of the interactions on the CMB are shown in Fig. 7.1.

The first effect on the CMB of switching on the interactions is to reduce the amount of suppression induced by the extra dark radiation on small scales. These scales would enter the horizon while the two dark species are still coupled, meaning the dark radiation is not free-streaming. Without the additional anisotropic stress, the gravitational source term of the photon oscillations is not affected by the presence of extra radiation, and the suppression is alleviated. Furthermore, a second effect appears if the onset of dark radiation free-streaming is pushed until after all the scales contributing to the CMB primary anisotropies have crossed the horizon. In this case, the phase shift discussed above for the free-streaming species can not take place. Therefore, one of the main ways the interactions affect the observables is to make the dark radiation behave as a non-free-streaming species at early times.

The third effect introduced by the dark matter - dark radiation interactions comes from the two species forming one single tightly coupled fluid. This coupling leads to the dark matter not being pressureless, and its perturbations can develop a fast mode. This in turn leads to less dark matter clustering, and due to its gravitational effects on the other species, this induces a reduction of the clustering of the baryon-photon fluid, thus the compression peaks (odd

peaks) of the CMB are suppressed.

Finally, while the dark matter is coupled to the dark radiation, the dark matter perturbations can not grow. This leads to an exponential damping of scales entering the horizon before kinetic decoupling, similarly to warm dark matter [239]. This damping will lead to a cut-off in the halo mass function (see section 5.1 for a discussion on this). However, unlike with warm dark matter, the interplay between the dark radiation relativistic pressure and the dark matter gravitational clustering lead to a series of Dark Acoustic Oscillations, with a similar mechanism to the standard BAO described in section 4.2. [240].

To summarise, the effects of dark matter - dark radiation interactions on the CMB, as seen in Fig. 7.1, are the following:

- Due to the coupling with dark matter, dark radiation behaves as non-free-streaming at early times. The lack of additional anisotropic stress means that the dark radiation does not induce the damping and phase-shift of the CMB acoustic peaks that is typically seen in the presence of additional relativistic degrees of freedom.
- The exchange of momentum between the two dark species prevents the dark matter perturbations from growing and forming deep gravitational potentials, thus the odd peaks of the CMB are suppressed.

The effect of the interactions on the matter power spectrum (relevant on small scales) are illustrated in Fig. 7.2, and can be summarised as:

- The dark matter - dark radiation scattering leads to a late kinetic decoupling, which in turn induces a collisional damping of the matter power spectrum on small scales, which translates into a cut-off in the halo mass function. As such, these interactions can alleviate the missing satellite problem.
- The opposing forces of the dark matter gravitational clustering and the dark radiation relativistic pressure induce a series of Dark Acoustic Oscillations, clearly visible in the matter power spectrum.

With the above considerations, we can see why these models can alleviate the missing satellite problem. We can also see precisely how the NADM model, introduced in section 7.1.1, can simultaneously alleviate the H_0 and σ_8 tensions. The dark radiation behaves like $\Delta N_{\rm eff}$, thus in order to maintain the redshift of matter-radiation equality (see section 1.6), H_0 has to increase. Furthermore, the dark matter and dark radiation behave like a coupled fluid at early times, thereby enhancing the acoustic peaks on small scales, which compensates the damping introduced by the new relativistic species.

Additionally, the collisional damping between the two dark species suppresses the dark matter growth, leading to a small scale matter power suppression. This in turn lowers σ_8, however, unlike with massive neutrinos (see section 6.2), the dark radiation is always relativistic, and thus there is no transition to non-relativistic. This means that the late time background history is unaffected (compared to a model with ΛCDM+ $\Delta N_{\rm eff}$). Moreover, the matter power

spectrum behaves like that of ΛCDM up to some suppression feature in k, which means there is no significant impact on the CMB lensing. Therefore, this model can alleviate both tensions, while avoiding the observational constraints that often limit other models designed for this purpose.

7.1.3 Methodology

In the previous section, we saw the importance of dark matter - dark radiation interacting models, and their effect on the cosmological observables. Given the impact these dark sector interactions have on the matter power spectrum, better measurements of this observable on small scales will allow us to greatly constrain dark radiation interactions. With this in mind, in **[III]** we developed the Lyman-α likelihood discussed in section 4.3 and used it to get the most stringent bounds on these models to date.

The ETHOS framework was already implemented in CLASS by Archidiacono et al. in [233]; however, this was done as a set of modifications to the existing cold dark matter equations. For the purpose of this project, and for the subsequent public release of the code, we re-implemented the same set of equations in CLASS, but for a new "interacting dark matter species" coexisting with the plain cold dark matter species. This offers more flexibility in several aspects: we can assume mixed models with only a fraction of dark matter experiencing these interactions, and we can explore the effects of self-interacting dark radiation and the standard collisionless cold dark matter in absence of any interactions among these species. Furthermore, the code was developed in a way to easily accommodating more types of dark matter interactions, such as the dark matter - baryon scattering described in section 7.2.

Our code incorporates the perturbation equations described in section 7.1.1, in both the Newtonian and the Synchronous gauge. Additionally, the background and temperature equations for the interacting dark sector have been implemented following the equations in [237]. With respect to the code in [233], the present version of the code implements the tight-coupling regime between dark matter and dark radiation. By default, CLASS uses a stiff integrator (`ndf15`) [53] for the perturbation equations, which means that rather large values of the interaction rate can be reached while using the default equations and keeping the code fast. However, in order to investigate the very small scales probed by Lyman-α, the tight-coupling is required, which is fully operational in our modified CLASS version. The tightly-coupled equations are switched on automatically whenever the ratio between the conformal interaction rate and Hubble time, $H/\Gamma_{\rm DR-DM}$, falls below a threshold set by default to 0.005, and the ratio between the conformal interaction and acoustic oscillation times, $k/\Gamma_{\rm DR-DM}$, falls below 0.01. These two thresholds can be controlled with new precision parameters.

Following the theoretical framework described in section 7.1.1, our CLASS code incorporates this interacting dark sector, governed by the following list of new input parameters:

- `f_idm_dr`: fraction of cold dark matter that we want to be interacting, between 0 and 1
- `m_dm`: dark matter mass in eV

- `xi_idr`: amount of dark radiation, as seen in equation 7.7
- `stat_f_idr`: statistical factor to differentiate between fermionic and bosonic dark radiation, as seen in equation 7.8
- `idr_nature`: nature of the dark radiation (free-streaming or fluid)
- `nindex_dark`: power of the temperature dependence of the comoving interaction rate
- `a_dark`: strength of the coupling between dark matter and dark radiation in Mpc^{-1}, as seen equation 7.4
- `l_max_idr`: maximum momentum in the Boltzmann hierarchy for dark radiation (between 3 and 17), as discussed in section 3.5
- `alpha_dark`: angular coefficient related to the nature of the mediator
- `beta_dark`: dark radiation self-interaction angular coefficient

Furthermore, our code can also take the NADM parameters Γ_0 and $N_{\rm dg}$ as input instead of the ETHOS a_{dark} and ξ. If these parameters are given, the code will automatically assume the other NADM characteristics ($n = 0$, non-free-streaming dark radiation, and a boson mediator). This allows us to explore all of the relevant cases discussed in section 7.1.1.

In order to constrain these models, we use the Lyman-$\alpha$$-$$\alpha\beta\gamma$ likelihood described in section 4.3. To apply our likelihood to dark matter - dark radiation interactions, the only specification needed in addition to the procedure described in section 4.3 is the calculation of the ΛCDM equivalent. For this step, we need to re-map the value of ξ to $N_{\rm eff}$ using equation 7.8. Then we can use the accurate procedure described in [75], which allows to re-map a ΛCDM model with $N_{\rm eff} > 3.046$ to another one sharing the same matter power spectrum up to some scale, but with $N_{\rm eff} = 3.046$.

In order to show how the pipeline for our likelihood works, in Fig. 7.3 we plot the square of the linear transfer function for several interacting dark matter - dark radiation models, with respect to their ΛCDM equivalent, and their $\{\alpha, \beta, \gamma\}$ fit (left panel), as well as the relative error between them (right panel). By construction, the $\{\alpha, \beta, \gamma\}$ parametrisation does not reproduce the oscillations in $T(k)$ after the first zero (for $k > k_{\rm fit}$); however, the power of the subsequent oscillations is small, and thus can safely be neglected.

7.1.4 Results

As our likelihood is interfaced with MONTEPYTHON, it can be used easily with our modified CLASS code. In **[III]**, with the method implemented above, we used MONTEPYTHON, interfaced with our modified CLASS version, in its default Metropolis Hastings mode, to perform parameter scans on the combination of $\{\omega_{\rm b},\ \omega_{\rm cdm},\ \log(10^{10}A_{\rm s}),\ n_{\rm s},\ \tau_{\rm reio},\ H_0,\ \xi,\ a_{\rm dark}\}$, for the ETHOS models with $n = 4$, $n = 2$, and $n = 0$ (corresponding to different powers of the temperature dependence of the comoving interaction rate $\Gamma \propto T^n$, as seen in equation 7.4). For $n = 4$ and $n = 2$ we assumed dark radiation to be free-streaming and we neglected the impact

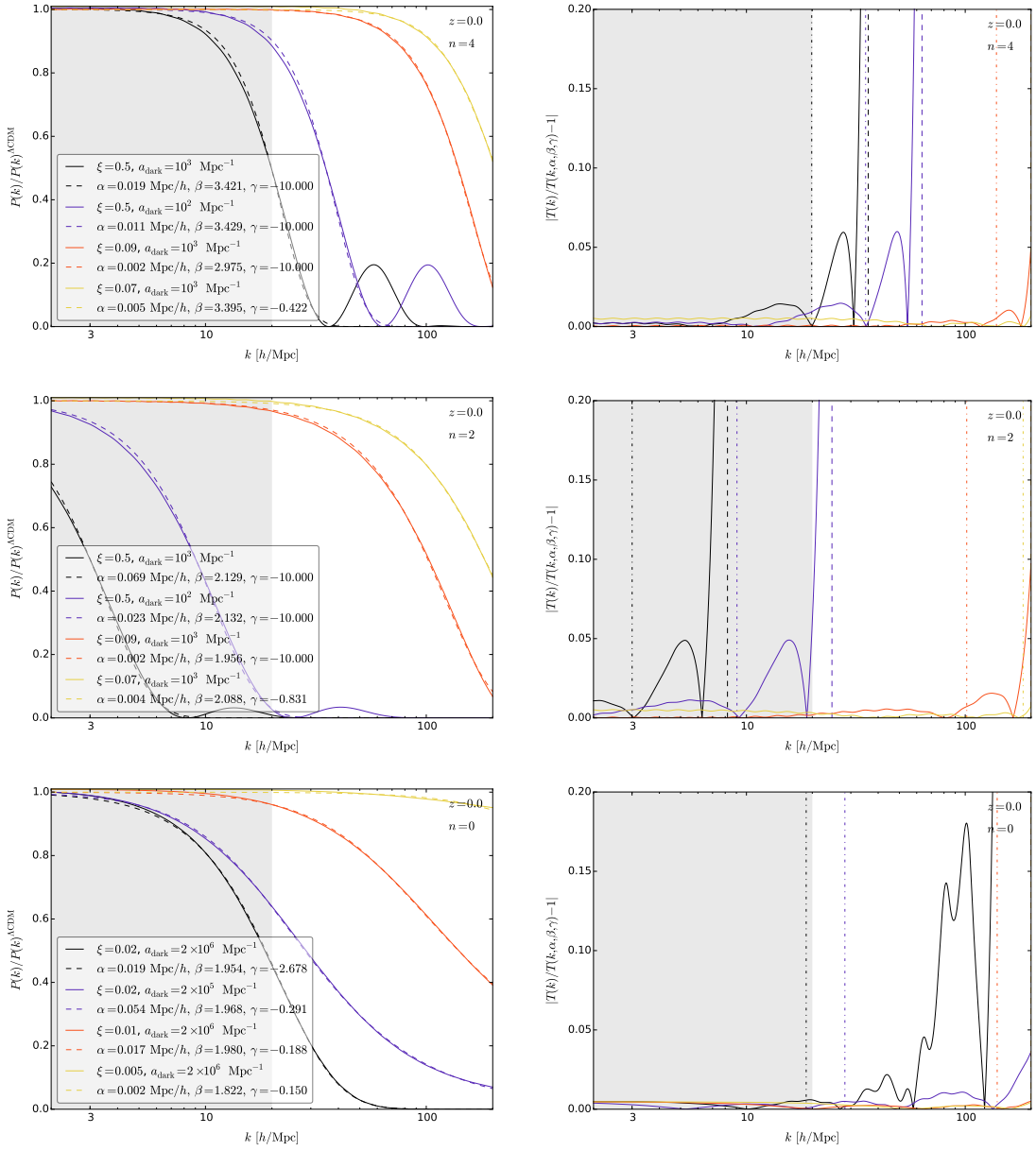

FIGURE 7.3: *Left*: Linear transfer functions $T(k)^2 = P(k)/P(k)^{\Lambda\rm CDM}$ at $z = 0$, for $n = 4$ (top row), $n = 2$ (second row), $n = 0$ (bottom row). The different colours correspond to different values of the amount of dark radiation ξ and of the strength of the interaction $a_{\rm dark}$. Solid lines depict the true $T(k)^2$, while dashed lines of the same color show the corresponding $\{\alpha, \beta, \gamma\}$ fit. *Right*: Relative deviation of the $\{\alpha, \beta, \gamma\}$ fit from the true $T(k)^2$ (solid lines) for the same models (colors) of the left panel. The vertical lines show $k_{1/2}$ (dot-dashed lines) and $k_{\rm fit}$ (dashed lines - for $n = 0$ $k_{\rm fit} = k_{\rm max}$). The gray shaded region approximately represents the k range probed by Lyman-α data.

of dark radiation self-interactions, as [233] showed these to be negligible, while for $n = 0$ we assumed the dark radiation to behave like a fluid. For the latter case, we also investigated the impact of changing our choice of parameters to match the NADM model discussed in [235], [236], thus giving us $\{\omega_{\rm b},\ \omega_{\rm cdm},\ \log(10^{10}A_{\rm s}),\ n_{\rm s},\ \tau_{\rm reio},\ H_0,\ \Delta N_{\rm fluid},\ \Gamma_0\}$.

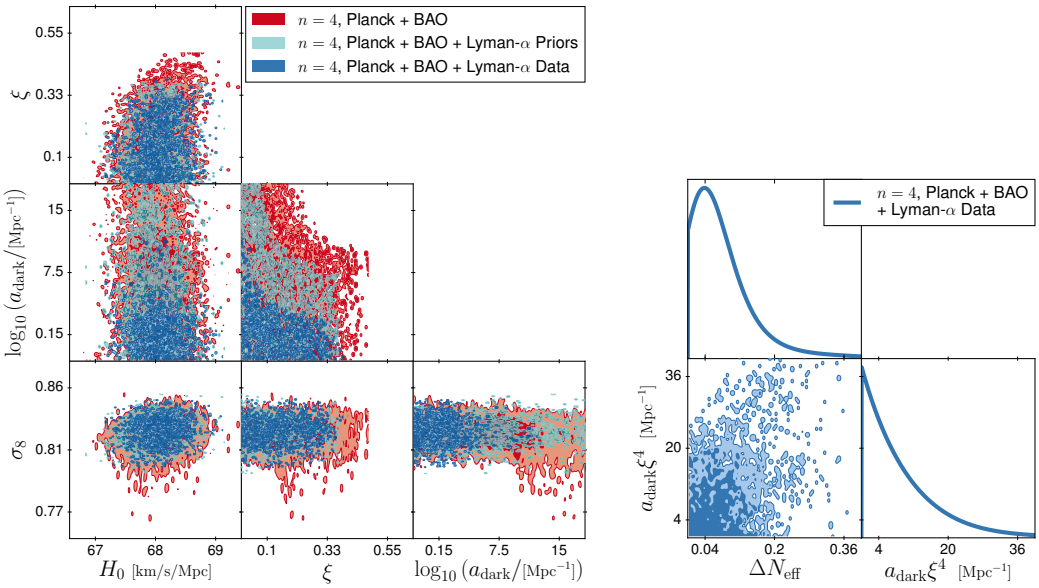

FIGURE 7.4: *Left*: Two-dimensional posterior distributions for all main parameters for the $n = 4$ case, with Planck + BAO (red), Planck + BAO + Lyman-α data (dark blue), and the Lyman-α prior check run explained in the text (light blue), when running with a flat prior on ξ and logarithmic prior on $a_{\rm dark}$. The smoothing was deliberately turned off to show the sharp boundaries of the preferred regions more clearly. *Right*: Posterior distributions when using linear priors on $\Delta N_{\rm eff}$ and the combination $a_{\rm dark}\xi^4$.

For each of the studied ETHOS models, we performed MCMC analysis for two different data combinations:

- **Planck + BAO**: This is the combination of Planck 2015 high-ℓ TT+TE+EE, low-ℓ data [241] and Planck 2015 lensing data [242]. We further added BAO data, using measurements of $D_V/r_{\rm drag}$ by 6dFGS at $z = 0.106$ [243] by SDSS from the MGS galaxy sample at $z = 0.15$ [244], and additionally by BOSS from the CMASS and LOWZ galaxy samples of SDSS-III DR12 at $z = 0.2 - 0.75$ [134].
- **Planck + BAO + Lyman-α**: Same as above, with the additional Lyman-α likelihood described in section 4.3.

The results for the different cases are discussed below.

ETHOS n = 4 model

The underlying particle physics model that leads to the $n = 4$ temperature dependence of the comoving interaction rate is represented by fermionic relativistic particles (for example sterile neutrinos, as discussed in section 1.9.2) interacting with dark matter particles through a new massive boson mediator of a new $U(1)$ broken symmetry. The results of our MCMC runs for this model are shown in Fig. 7.4 and Table 7.1, for both of the dataset combinations mentioned above.

CMB constraints. We expect a clear degeneracy between the amount of dark radiation ξ and the interaction strength $a_{\rm dark}$, as the data should remain compatible with dark matter interacting

parameter	ΛCDM	ETHOS $n = 4$	
	Planck + BAO	Planck + BAO	+ Lyman-α
$100\,\omega_{\rm b}$	$2.219^{+0.013}_{-0.014}$	$2.221^{+0.015}_{-0.015}$	$2.222^{+0.017}_{-0.014}$
$\omega_{\rm cdm}$	$0.1192^{+0.0011}_{-0.0010}$	$0.1195^{+0.0011}_{-0.0014}$	$0.1192^{+0.0011}_{-0.0010}$
$\log(10^{10}A_{\rm s})$	$3.050^{+0.023}_{-0.023}$	$3.053^{+0.025}_{-0.023}$	$3.057^{+0.024}_{-0.024}$
$n_{\rm s}$	$0.9618^{+0.0042}_{-0.0041}$	$0.9622^{+0.0044}_{-0.0045}$	$0.9626^{+0.0044}_{-0.0037}$
$\tau_{\rm reio}$	$0.060^{+0.012}_{-0.012}$	$0.061^{+0.013}_{-0.013}$	$0.063^{+0.013}_{-0.013}$
H_0 / [km/(s Mpc)]	$67.94^{+0.46}_{-0.49}$	$68.06^{+0.52}_{-0.54}$	$68.09^{+0.46}_{-0.48}$
σ_8	$0.8234^{+0.0085}_{-0.0090}$	$0.823^{+0.024}_{-0.013}$	$0.826^{+0.010}_{-0.009}$
$n_{\rm eff}$	$-2.308^{+0.0034}_{-0.0035}$	$-2.9^{+4.3}_{-22.1}$	$-2.307^{+0.0039}_{-0.0035}$
ξ	–	< 0.40	< 0.38
$\log_{10}(a_{\rm dark}$ / $[{\rm Mpc}^{-1}])$	–	n.l.	< 6.8
$\Delta\chi^2$	–	0	-3.62
$\Delta N_{\rm eff}$	–	–	< 0.23
$a_{\rm dark}\xi^4$/ $[{\rm Mpc}^{-1}]$	–	–	< 30

TABLE 7.1: Preferred regions at the 68 % confidence level (C.L.) (or at the 95 % C.L. in the case of upper bounds) for the parameters of the ETHOS $n = 4$ case, both with Planck + BAO and Planck + BAO + Lyman-α. With the first dataset, the interaction parameter is not bounded within the prior range. The $\Delta\chi^2$ is given with respect to ΛCDM with the same datasets. The last two rows show the results obtained with linear priors on $\Delta N_{\rm eff}$ and the combination $a_{\rm dark}\xi^4$ using the second dataset. Entries with "n.l." indicate that there is no upper limit within the prior range, while – means that the parameter is not present.

either strongly with a small amount of dark radiation or barely interacting with a large amount of dark radiation. To capture this behaviour, we chose to use a flat prior on $\log_{10}(a_{\rm dark})$ in the range $[-3, 20]$. Indeed, a linear prior on $a_{\rm dark}$ would only have given weight to the region with a high interaction rate, and thus a tiny dark radiation density. This would have lead to very strong bounds on ξ that would not reflect the fact that the data is perfectly compatible with values up to $\xi \sim 0.40$.

In the middle plot of the left panel of Fig. 7.4 we can see the expected degeneracy between ξ and $\log_{10}(a_{\rm dark})$. The results of MCMC runs are usually plotted as smoothed contour plots; however, in **[III]** we chose instead to plot the non-smoothed density of points in the chains, in order to precisely visualise the edges of the region preferred by the data. The Planck + BAO allowed region has two sharp edges set by the data rather than the priors:

- a vertical line corresponding to the maximum allowed value of ξ (and therefore $\Delta N_{\rm eff}$) in the ETHOS $n = 4$ model. We found $\xi < 0.40$ (95 % C.L.), which is consistent within 1σ with the bound obtained in [233], with our bounds being slightly tighter. This small difference can be attributed to our inclusion of the lensing and BAO likelihoods, which

were not included in the previous study. This can be translated into $\Delta N_{\rm eff} < 0.10$ using equation 7.8, but this result should be taken with a grain of salt because it derives from a flat prior on ξ. The physical interpretation of this boundary is that the CMB data is incompatible with too much dark radiation, even when this is self-interacting. This is caused by various effects, the dominant one being the influence of the amount of extra radiation on the CMB damping tail [245]. Dark radiation has other effects on the scale and amplitude of the acoustic peaks that depend on the rate of dark radiation self-interactions and dark radiation - dark matter interaction, as discussed in section 7.1.2, thus the bound found in this case is specific to the ETHOS $n = 4$ model, and in principle different from what one would obtain in a plain ΛCDM+$N_{\rm eff}$ fit with only free-streaming relativistic relics.

- a roughly hyperbolic boundary, corresponding physically to the limit set by the CMB on the effect of the dark matter - dark radiation interaction. In particular, a too large rate $\Gamma_{\rm DM-DR}$ implies that dark matter develops a fast mode [246], [247] which influences the CMB power spectrum, with a suppression of the clustering of the baryon-photon fluid.

We obtain no upper bound on $\log_{10}(a_{\rm dark})$, since in the limit of small dark radiation density the dark matter - dark radiation and dark radiation - dark matter interaction rates can be arbitrarily high. Thus, the allowed region extends up to our upper prior boundary $\log_{10}(a_{\rm dark}) \leq 20$.

For the other cosmological parameters, the error bars we found are slightly larger than for the ΛCDM model with the same data combination, but smaller than for the ΛCDM+$N_{\rm eff}$ model. This has several causes: our flat prior on ξ gives more weight to small values of $\Delta N_{\rm eff}$; we only allow $N_{\rm eff}$ to increase beyond 3.046, while a run with a flat prior on $N_{\rm eff}$ would return $N_{\rm eff} = 2.98 \pm 0.18$ (68 % C.L.) [70]; and in our model, increasing $\Delta N_{\rm eff}$ comes at the price of introducing dark matter - dark radiation interaction effects not favoured by the data. In any case, we see that the ETHOS $n = 4$ model offers no clear opportunities to accommodate the high value of H_0 or the low value of σ_8 discussed in chapter 5.

Lyman-α constraints. With the addition of the Lyman-α likelihood, we obtain approximately the same bound on $\xi < 0.38$ (95 % C.L.), as the number of additional relativistic degrees of freedom is already well-constrained by CMB data. Instead the upper limit on the interaction rate shrinks by about ten orders of magnitude, due to the suppression of the small scale matter power spectrum induced by these interactions, as discussed in section 7.1.2. This suppression is strongly constrained by Lyman-α data. We checked explicitly that the edge of the allowed region is a curve of constant $a_{\rm dark}\xi^4$, which is what we expected from the $\Gamma_{\rm DM-DR} \propto \rho_{\rm DR}\, \Gamma_{\rm DR-DM} \propto a_{\rm dark}\xi^4$ term in equation 7.10.

This run gives an upper bound $\log_{10}(a_{\rm dark}/{\rm Mpc}^{-1}) < 6.8$ (95 % C.L.), which is strongly prior dependent. Indeed, since $a_{\rm dark}$ is compatible with zero, upper bounds on $\log_{10}(a_{\rm dark})$ are inevitably influenced by the choice of a lower prior boundary on this parameter. Moreover, the data is compatible with arbitrarily large values of $a_{\rm dark}$ for arbitrarily small ξs, such that the bound would entirely disappear if we had chosen a logarithmic prior on ξ.

The analysis with flat priors on ξ and $\log_{10}(a_{\rm dark})$ is particularly useful for identifying the physical mechanisms responsible for the various bounds. It allows us to check that the data is mostly sensitive to the effects of the density of extra radiation, proportional to $\Delta N_{\rm eff}$, and of the dark matter - dark radiation rate $\Gamma_{\rm DM-DR}$, parametrised by $a_{\rm dark}\xi^4$. As such, the most informative and robust way to formulate our final results is to quote bounds on ($\Delta N_{\rm eff}$, $a_{\rm dark}\xi^4$) assuming flat priors on these parameters.

We thus performed another MCMC run with such a choice of priors. The results are shown in the right panel of Fig. 7.4. Our final results for the $n = 4$ ETHOS model are summarised by the 95 % upper bounds $\Delta N_{\rm eff} < 0.23$ and $a_{\rm dark}\xi^4 < 30\,{\rm Mpc}^{-1}$. The upper limit of the Bayesian confidence interval for $\Delta N_{\rm eff}$ is slightly stronger than for a ΛCDM+$N_{\rm eff}$ model with extra free-streaming relativistic relics and Planck + BAO data ($\Delta N_{\rm eff} < 0.28$ 95 % C.L., see [70], [248]), because in our case models with $\Delta N_{\rm eff} > 0$ also come with dark matter - dark radiation interaction effects that are not favoured by the data. Knowing the upper bound on $a_{\rm dark}\xi^4$ is convenient for model building, as a typical particle-physics-motivated model would predict a given value of ξ (related to the physics of the dark sector and to its interactions with the visible sector). In such a case one can immediately conclude that the Lyman-α data imposes a maximum value on the scattering rate $a_{\rm dark}$ given by $30\,\xi^{-4}\,{\rm Mpc}^{-1}$.

It was important to check that our results were actually driven by the Lyman-α data, and not by the restrictions imposed on the small scale matter power spectrum by our likelihood method described in section 4.3). For this purpose, we also performed a run with the Planck + BAO likelihoods combined with a modified version of the Lyman-α likelihood that returns a constant value if the power spectrum passes all of the sanity checks, and a zero likelihood otherwise. Thus, this run relies on the Planck + BAO data and on the Lyman-α likelihood prior, but not on the Lyman-α data, which allows us to derive regions of validity for our implementation. We called it "Planck + BAO + Lyman-α Prior" and its results are also shown in the left panel of Fig. 7.4. If the edge of the allowed region were similar in the Lyman-α Prior and Lyman-α Data runs, we would know that our bounds were driven by the applicability of the method and not by the data. This was not the case, as we can clearly see when comparing the dark blue and light blue regions in Fig. 7.4. As such, we concluded that the sanity checks of our implementation impose no further restriction besides the region that is already excluded by other means.

Furthermore, when adding the Lyman-α likelihood, our error bars on $n_{\rm eff}$, which is the slope of the Lyman-α spectrum, are greatly reduced. This comes mainly from our improved bound on $a_{\rm dark}$; when the interaction strength is allowed to vary over many orders of magnitude, our $P(k)$ is not monotonic, and thus $n_{\rm eff}$ can assume any value, both negative and positive (if the corresponding k value is, for example, just after the first oscillation in $P(k)$).

The inclusion of Lyman-α data tightens the error bars on σ_8, while the mean value is not significantly affected. The mean value and error bars of H_0 are not impacted by the addition of Lyman-α data for this model. The bounds for both parameters are in very close agreement to those obtained for a standard ΛCDM model with the same datasets, once again offering no

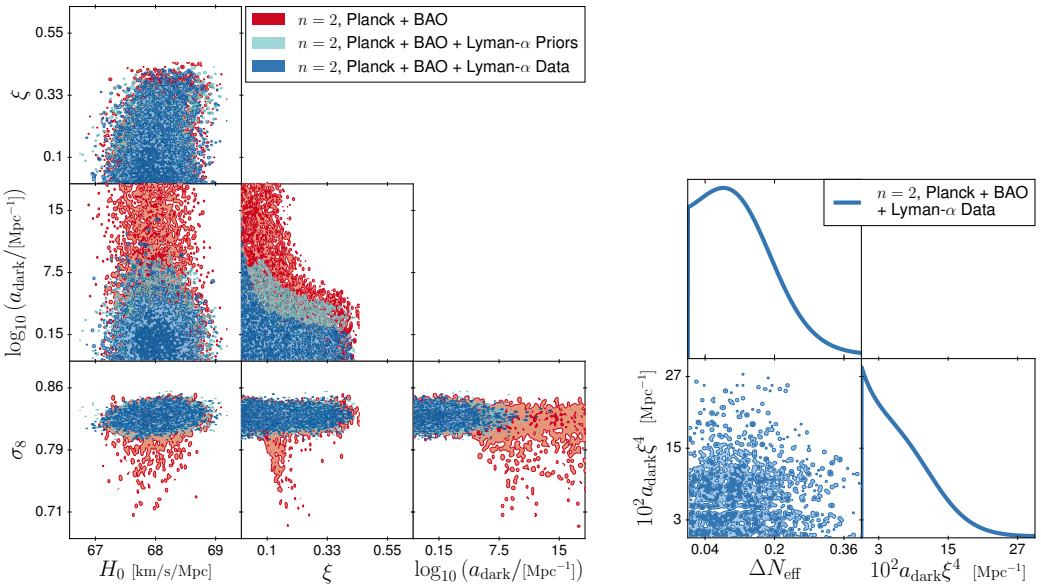

FIGURE 7.5: *Left*: Two-dimensional posterior distributions for all main parameters for the $n = 2$ case, with Planck + BAO (red), Planck + BAO + Lyman-α data (dark blue), and the Lyman-α prior check run explained in the text (light blue), when running with a flat prior on ξ and logarithmic prior on $a_{\rm dark}$. The smoothing was deliberately turned off to show the sharp boundaries of the preferred regions more clearly. *Right*: Posterior distributions when using linear priors on $\Delta N_{\rm eff}$ and the combination $10^2 a_{\rm dark}\xi^4$.

solution to the cosmological tensions. Additionally, the χ^2 obtained in the Planck + BAO case is not any better than for the vanilla ΛCDM model, while the addition of Lyman-α data brings it down by $\Delta\chi^2 = -3.6$. Considering that the model features two additional parameters, we concluded that interacting dark matter - dark radiation models provide a fit of Planck + BAO + Lyman-α as good as the base ΛCDM.

ETHOS n = 2 model

The scenario where the comoving scattering rate of dark radiation off dark matter scales like T^2 can be realised for example with 4-point contact-only interaction. As for $n = 4$, we neglect the sub-dominant contribution of dark radiation self-interactions.

CMB constraints. The results of our MCMC run with Planck + BAO data and for the $n = 2$ case are shown in Fig. 7.5 and Table 7.2. Once more, the middle plot in the left panel of Fig. 7.5 shows that the data imposes two limitations on the ETHOS parameter: an upper bound $\xi < 0.43$ at the 95 % C.L. and a hyperbolic-shaped limit on (ξ, $a_{\rm dark}$).

For other parameters, the preferred intervals only widen moderately with respect to the ΛCDM model, except for σ_8 which is compatible with much smaller values. The contour plot for (ξ, σ_8) shows a degeneracy direction allowing to reach such small values of σ_8 for specific values of ξ and a large interaction rate $a_{\rm dark} > 10^7$. While this region could be potentially interesting to explain the σ_8 tension, we did not investigate it in more detail, as this region is excluded by Lyman-α bounds on the interaction rate. Once this region is ignored, we find that the ETHOS

	ΛCDM	ETHOS $n = 2$	
parameter	Planck+BAO	Planck + BAO	+ Lyman-α
$100\,\omega_{\rm b}$	$2.219^{+0.013}_{-0.014}$	$2.220^{+0.014}_{-0.014}$	$2.220^{+0.014}_{-0.016}$
$\omega_{\rm cdm}$	$0.1192^{+0.0011}_{-0.0010}$	$0.1195^{+0.0011}_{-0.0013}$	$0.1194^{+0.0011}_{-0.0011}$
$\log(10^{10}A_{\rm s})$	$3.050^{+0.023}_{-0.023}$	$3.053^{+0.025}_{-0.025}$	$3.051^{+0.023}_{-0.024}$
$n_{\rm s}$	$0.9618^{+0.0042}_{-0.0041}$	$0.9621^{+0.0044}_{-0.0043}$	$0.9618^{+0.0039}_{-0.0043}$
$\tau_{\rm reio}$	$0.060^{+0.012}_{-0.012}$	$0.061^{+0.013}_{-0.013}$	$0.059^{+0.013}_{-0.013}$
H_0 / [km/(s Mpc)]	$67.94^{+0.46}_{-0.49}$	$68.02^{+0.51}_{-0.51}$	$67.99^{+0.51}_{-0.51}$
σ_8	$0.8234^{+0.0085}_{-0.0090}$	$0.819^{+0.021}_{-0.017}$	$0.8244^{+0.0088}_{-0.0095}$
$n_{\rm eff}$	$-2.308^{+0.0034}_{-0.0035}$	$-2.9^{+7.0}_{-3.5}$	$-2.3080^{+0.0034}_{-0.0037}$
ξ	–	< 0.43	< 0.40
$\log_{10}(a_{\rm dark}\,/\,[{\rm Mpc}^{-1}])$	–	n.l.	< 8.4
$\Delta\chi^2$	–	0	-0.12
$\Delta N_{\rm eff}$	–	–	< 0.29
$10^2 a_{\rm dark}\xi^4/\,[{\rm Mpc}^{-1}]$	–	–	< 18

TABLE 7.2: Preferred regions at the 68 % confidence level (C.L.) (or at the 95 % C.L. in the case of upper bounds) for the parameters of the ETHOS $n = 2$ case, both with Planck + BAO and Planck + BAO + Lyman-α. With the first dataset, the interaction parameter is not bounded within the prior range. The $\Delta\chi^2$ is given with respect to ΛCDM with the same datasets. The last two rows show the results obtained with linear priors on $\Delta N_{\rm eff}$ and the combination $10^2 a_{\rm dark}\xi^4$ using the second dataset.

$n = 2$ model does not offer opportunities to accommodate larger H_0 or lower σ_8 values than ΛCDM.

Lyman-α constraints. Like for $n = 4$, the inclusion of Lyman-α data marginally affects the bound on ξ, but considerably strengthens the upper limit on the interaction rate, which is given once more by a line of constant $a_{\rm dark}\xi^4$. This limit is stronger than in the $n = 4$ case by about two orders of magnitude. This is consistent with the fact that the scales constrained by our Lyman-α data crossed the Hubble scale roughly around $z \simeq 10^6$, and have been suppressed according to the rate $\Gamma_{\rm DM-DR}(z)$ evaluated at that time. From equation 7.5, and with $z_d = 10^7$, we find $\Gamma_{\rm DM-DR}(10^6) \propto 10^{6-n} a_{\rm dark}\xi^4$. As such, it is normal that the Lyman-α data set comparable limits on the combination $(10^{-n} a_{\rm dark}\xi^4)$ for all ns, and that limits on $a_{\rm dark}\xi^4$ become one hundred times stronger when n decreases by two.

Furthermore, we found a bound $\xi < 40$ (95 % C.L.) very similar to that in the $n = 4$ case. As before, the bound $\log_{10}(a_{\rm dark}/[{\rm Mpc}^{-1}]) < 8.4$ (95 % C.L.) should be taken with great care due to its strong dependence on the choice of a linear prior for ξ and on the lower prior edge for $\log_{10}(a_{\rm dark})$. Thus, we switched to linear priors on the parameters directly related to the

physical effects probed by the data, and obtained our final results for the ETHOS $n = 2$ model: $\Delta N_{\rm eff} < 0.29$ and $10^2 a_{\rm dark}\xi^4 < 18\,{\rm Mpc}^{-1}$ (95 % C.L.). The first bound is identical to what is obtained when fitting Planck + BAO with a ΛCDM+$N_{\rm eff}$ model.

We once again performed a "Planck + BAO + Lyman-α Prior" run to check that our bounds do not come from the limitations of the method. In this case, if we compare the $\xi - \log(a_{\rm dark})$ posteriors for the Lyman-α Prior and Lyman-α Data runs in the left panel of Fig. 7.5, we see that for $\xi > 0.05$ our constraints are really derived from the data rather than from the range of validity of our method. However, this is no longer the case in a very small region with $\xi < 0.05$, where the two contours overlap, showing that for these models, the $\alpha - \beta - \gamma$ parametrisation is not accurate. More precisely, for such parameter values the first oscillation in the transfer function does not reach the threshold of 80 % where we stop performing the fit (as discussed in section 4.3), and so the fit is performed on higher oscillations as well. However $\xi < 0.05$ implies a tiny dark radiation density $\Delta N_{\rm eff} < 2 \cdot 10^{-5}$. Nonetheless, this small region is not very interesting for model building, as such tiny values are difficult to motivate theoretically. Furthermore, even if our method was improved in order to correctly deal with this small region of parameter space, there would be no reason for the 95 % C.L. upper bound on (ξ, $a_{\rm dark}$) to be different from $10^2 a_{\rm dark}\xi^4 = 18$, since the shape of this limit can be inferred from simple analytic arguments. Thus, we can safely extrapolate it below $\xi = 0.05$. Finally, we should note that this minor issue is irrelevant when running with a flat prior on $\Delta N_{\rm eff}$, since with such a prior it affects a completely negligible fraction of the preferred region.

As for the $n = 4$ case, we obtained a significantly tighter bound on $n_{\rm eff}$, while the mean value and error bars of H_0 were not impacted by the addition of Lyman-α data. The preferred intervals for H_0 and σ_8 are very close to those of the ΛCDM model. For both data combinations, the difference obtained in the $\Delta\chi^2$ with respect to the base ΛCDM are negligible, and so we once again found no preference for the interacting dark matter - dark radiation models.

ETHOS n = 0 model

The $n = 0$ case is motivated by several particle physics set-ups in which the dark matter - dark radiation momentum transfer rate scales like T^2, meaning that the ETHOS rate $\Gamma_{\rm DR-DM}$ is constant. This occurs, for instance in the Non-Abelian Dark Matter (NADM) scenario described in section 7.1.1. In this model, the dark matter particles are charged under a dark non-abelian symmetry whose dark gluons play the role of dark radiation [234]–[236]). Given that these models tend to predict strong self-interactions in the dark radiation sector, for these models we assumed that dark radiation is a relativistic perfect fluid described by one continuity and one Euler equation (unlike for $n = 4$ and $n = 2$). To make this difference clearer, we denoted the dark radiation density by $\Delta N_{\rm fluid}$ instead of $\Delta N_{\rm eff}$.

For the $n = 0$ model we can use different parametrisations and priors, corresponding to different approaches discussed in the literature: either with the ETHOS general framework, or for specific models like the NADM one. We first looked at the standard ETHOS parametrisation, with the same choice of priors as in previous cases. Then, to compare our results with [235],

	ΛCDM	ETHOS $n = 0$	
parameter	Planck + BAO	Planck + BAO	+ Lyman-α
$100\,\omega_{\rm b}$	$2.219^{+0.013}_{-0.014}$	$2.220^{+0.015}_{-0.015}$	$2.221^{+0.015}_{-0.015}$
$\omega_{\rm cdm}$	$0.1192^{+0.0011}_{-0.0010}$	$0.1195^{+0.0011}_{-0.0014}$	$0.1192^{+0.001}_{-0.001}$
$\log(10^{10} A_{\rm s})$	$3.050^{+0.023}_{-0.023}$	$3.053^{+0.025}_{-0.024}$	$3.054^{+0.025}_{-0.024}$
$n_{\rm s}$	$0.9618^{+0.0042}_{-0.0041}$	$0.9621^{+0.0042}_{-0.0045}$	$0.9624^{+0.0044}_{-0.0041}$
$\tau_{\rm reio}$	$0.060^{+0.012}_{-0.012}$	$0.061^{+0.013}_{-0.012}$	$0.061^{+0.013}_{-0.014}$
H_0 / [km/(s Mpc)]	$67.94^{+0.46}_{-0.49}$	$68.04^{+0.50}_{-0.60}$	$68.03^{+0.47}_{-0.49}$
σ_8	$0.8234^{+0.0085}_{-0.0090}$	$0.815^{+0.044}_{-0.009}$	$0.8237^{+0.0097}_{-0.0093}$
$n_{\rm eff}$	$-2.308^{+0.0034}_{-0.0035}$	$-3.4^{+9.5}_{-4.2}$	$-2.3100^{+0.0071}_{-0.0079}$
ξ	–	< 0.38	< 0.33
$\log_{10}(a_{\rm dark} / [{\rm Mpc}^{-1}])$	–	n.l.	< 3.3
$\Delta\chi^2$	–	0	-0.70
$\Delta N_{\rm fluid}$	–	–	< 0.47
$10^4 a_{\rm dark}\xi^4 / [{\rm Mpc}^{-1}]$	–	–	< 14

TABLE 7.3: Preferred regions at the 68 % confidence level (C.L.) (or at the 95 % C.L. in the case of upper bounds) for the parameters of the ETHOS $n = 0$ case, both with Planck + BAO and Planck + BAO + Lyman-α. With the first dataset, the interaction parameter is not bounded within the prior range. The $\Delta\chi^2$ is given with respect to ΛCDM with the same datasets. The last two rows show the results obtained with linear priors on $\Delta N_{\rm eff}$ and the combination $10^4 a_{\rm dark}\xi^4$ using the second dataset.

[236], we switched to linear priors on the interaction rate, combined with either linear or logarithmic priors on the parameters $\Delta N_{\rm fluid}$, allowing us to see the influence our choice of priors had on the end result.

CMB constraints with ETHOS $n = 0$ parametrisation. Our results for this case when assuming a flat prior on $\xi \geq 0$ and on $-3 \leq \log_{10}(a_{\rm dark}/{\rm Mpc}^{-1}) \leq 20$ are shown in Fig. 7.6 and Table 7.3. In this case, the general behaviour is similar to the previous cases: we obtained an upper bound of ξ and a hyperbolic-shaped upper limit on $(\xi, a_{\rm dark})$. CMB bounds are much stronger in this model than in previous cases, which is consistent with the fact that the rate $\Gamma_{\rm DM-DR}(z)$ evaluated near photon decoupling is much larger for the same value of $a_{\rm dark}\xi^4$ when n decreases. Indeed, we found that for $n = 0$, CMB bounds dominate over Lyman-α bounds at least for some values of ξ, making it necessary to quantify these bounds more precisely. In the space $(\xi, \log_{10}(a_{\rm dark}))$ and within our prior range, the 95 % C.L. preferred region is defined in good approximation by either $\xi < 0.13$, or $\xi < 0.38$ and $10^4 a_{\rm dark}\xi^4 < 14\,{\rm Mpc}^{-1}$. This means that the CMB excludes all ETHOS $n = 0$ models with either a too large dark radiation density ($\xi > 0.38$) or a too large $\Gamma_{\rm DM-DR}$ rate ($10^4 a_{\rm dark}\xi^4 > 14\,{\rm Mpc}^{-1}$), but looses sensitivity to these parameters when the dark radiation density is very small ($\xi < 0.13$).

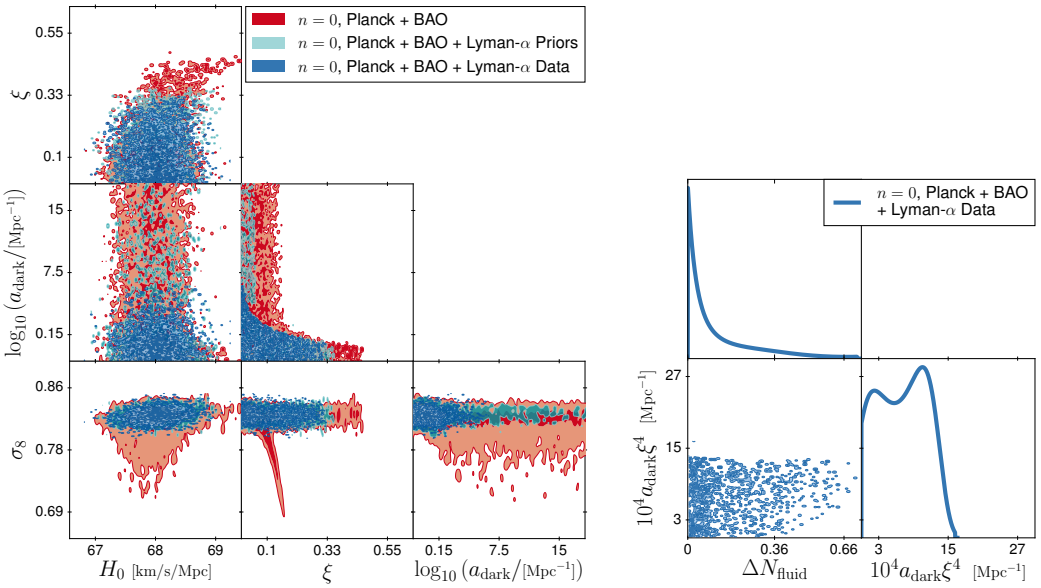

FIGURE 7.6: *Left*: Two-dimensional posterior distributions for all main parameters for the $n = 0$ case, with Planck + BAO (red), Planck + BAO + Lyman-α data (dark blue), and the Lyman-α prior check run explained in the text (light blue), when running with a flat prior on ξ and logarithmic prior on $a_{\rm dark}$. The smoothing was deliberately turned off to show the sharp boundaries of the preferred regions more clearly. *Right*: Posterior distributions when using linear priors on $\Delta N_{\rm eff}$ and the combination $10^4 a_{\rm dark}\xi^4$.

Given the discussion in chapter 5, we are interested in how these models affect H_0 and σ_8. Our results showed that the ETHOS $n = 0$ model allows to reach larger values of H_0 or lower values of σ_8 than the ΛCDM model. By looking at the two-dimensional contour plots in the left panel of Fig. 7.6, we see that:

- high values of H_0 require a large dark radiation density, $\xi > 0.4$ (corresponding $\Delta N_{\rm fluid} > 0.1$): this is a consequence of the well-known $H_0 - N_{\rm fluid}$ degeneracy, which works particularly well in this case because dark radiation is self-interacting, and thus less constrained by CMB observables than extra free-streaming relics [235]. Our 95 % C.L. preferred region reaches values up to $H_0 \simeq 70\,{\rm km\,s^{-1}Mpc^{-1}}$ for $\xi \simeq 0.38$ ($\Delta N_{\rm fluid} \simeq 0.08$). With our choice of priors, this part of the allowed parameter space has little weight, and the 68 % C.L. preferred interval for H_0 is still nearly the same as for ΛCDM.

- a close inspection of the (ξ, σ_8) contour plot of Fig. 7.6 shows that in this plane, the marginalised posterior is bimodal; it ismade of the superposition of two separate categories of models. The first one has $\sigma_8 = 0.823 \pm 0.017$ (95 % C.L.) for any allowed value of the dark radiation density parameter (in the range $0 < \xi < 0.38$). The second one corresponds to a strongly degenerate direction in (ξ, σ_8), as for the ETHOS $n = 2$ model, and requires a large interaction rate $a_{\rm dark} \geq 1$. It stretches down to $\sigma_8 = 0.68$ for $\xi \simeq 0.16$.

Lyman-α constraints with ETHOS $n = 0$ parametrisation. At first sight, the discussion of the Lyman-α constraints seems very similar to that for $n = 2$ or 4. We expect that Lyman-α data will slightly tighten the bound on ξ and put a strong limit on $10^4 a_{\rm dark}\xi^4 < \mathcal{O}(10)$. This is

indeed what happened in our run with a linear prior on ξ and a logarithmic prior on $a_{\rm dark}$: we obtained $\xi < 0.33$ and $10^4 a_{\rm dark}\xi^4 < 14\,{\rm Mpc}^{-1}$ (95 % C.L.). When performing a second run with flat priors on ($\Delta N_{\rm fluid}$, $10^4 a_{\rm dark}\xi^4$), we found $\Delta N_{\rm fluid} < 0.47$ and a confirmation of $10^4 a_{\rm dark}\xi^4 < 14\,{\rm Mpc}^{-1}$ (95 % C.L.).

However, when doing the "Planck + BAO + Lyman-α Prior" run, we found that the previous results must be taken with care. Looking at the middle plot of the left panel of Fig. 7.6 we see:

- the different checks performed inside our Lyman-α likelihood induce a cut at $\xi < 0.33$. Thus, the previous bound on ξ did not come from the Lyman-α data but from our methodology. This comes from the fact that ETHOS $n = 0$ models with $\xi > 0.33$ do not result in a power spectrum that can be accurately represented by the $\alpha - \beta - \gamma$ parametrisation. As such, we should not trust any bound on ξ apart from the one obtained with Planck + BAO alone, namely $\xi < 0.38$.

- for $\xi > 0.13$, the upper bound on $a_{\rm dark}\xi^4$ is nearly the same in the three ETHOS $n = 0$ runs shown in Fig. 7.6, suggesting that CMB data alone provides the strongest bounds, in this case $10^4 a_{\rm dark}\xi^4 < 14\,{\rm Mpc}^{-1}$ (95 % C.L.). Given the impact of this model on CMB and LSS observables this is not a surprise: for parameter values leading to significant effects in the CMB temperature and polarisation spectrum, this model only generates a very smooth and progressive suppression in the small scale matter power spectrum, which is much more difficult to constrain with Lyman-α data than the sharp exponential cut-off observed for $n = 2, 4$.

- for $\xi < 0.02$, the Lyman-α Prior run sets no upper limit on the interaction rate, while the Lyman-α Data run returns $10^4 a_{\rm dark}\xi^4 < 14$ (95 % C.L.), meaning that we can trust this bound as it really comes from the data.

- there is a problematic range $0.02 < \xi < 0.13$ in which the Lyman-α Prior run also sets an upper limit $10^4 a_{\rm dark}\xi^4 < 14\,{\rm Mpc}^{-1}$. The reason is that for $n = 0$ and large amounts of dark radiation $\xi > 0.02$, the $\alpha - \beta - \gamma$ parametric function does not provide an accurate fit of the suppression in the matter power spectrum. This indicates that for this class of models the bounds were driven by the limitations of the method, in particular by the flexibility of the parametric fitting function, and not by the data itself. While we could extend our method or use the Lyman-$\alpha - \alpha - \beta - \delta$ likelihood described in section 4.3, we believed that was not necessary for two reasons. First, $0.02 < \xi < 0.13$ means $6 \cdot 10^{-7} < \Delta N_{\rm fluid} < 10^{-3}$, and the weight of this region would be negligible if we would run with a flat prior on $\Delta N_{\rm fluid}$, so we may simply ignore it. Second, the analytic argument suggesting that the Lyman-α bound on the dark matter - dark radiation interaction takes the form of an upper limit on $a_{\rm dark}\xi^4$ worked very well for $n = 2$ and $n = 4$, and still works very well in the present case for $\xi < 0.02$ and $\xi > 0.13$. As such, there is no reason to believe that this would not be the case in the intermediate range. Therefore, it is very reasonable to expect that a better method would return $10^4 a_{\rm dark}\xi^4 < 14$ (95 % C.L.) throughout the range of allowed values $0 < \xi < 0.38$.

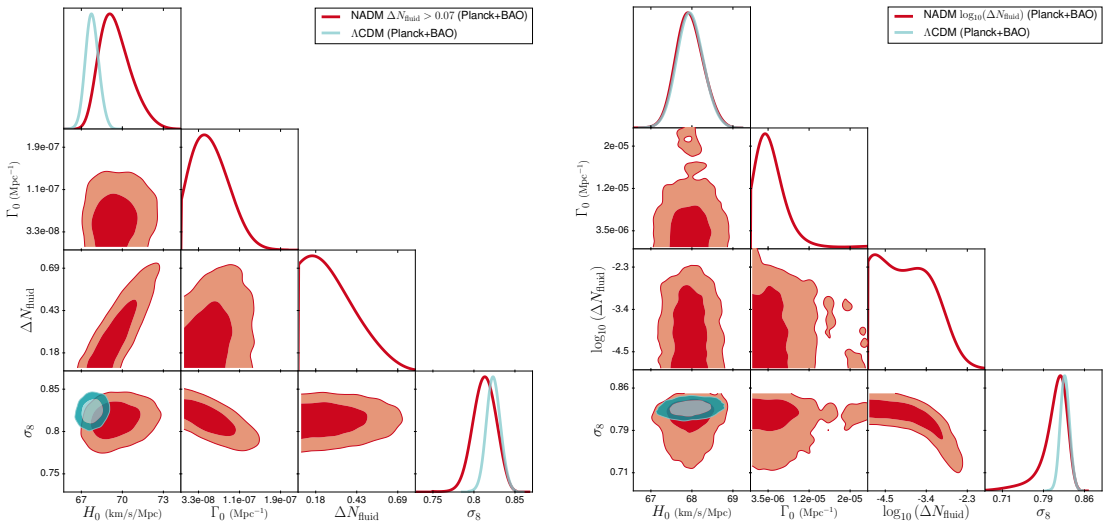

FIGURE 7.7: *Left* Two-dimensional posterior distributions for all main parameters using Planck + BAO, for the NADM case (blue) and for ΛCDM (yellow), with the lower prior $\Delta N_{\rm fluid} > 0.07$. *Right* Same as left but with the log prior $-5 \leq \log_{10}(\Delta N_{\rm fluid}) \leq 0$.

To summarise, we should take away from this analysis that for $\xi > 0.13$, Lyman-α data do not improve over Planck + BAO bounds, which give $10^4 a_{\rm dark}\xi^4 < 14\,{\rm Mpc}^{-1}$ (95 % C.L.). For $0 < \xi < 0.02$, the Lyman-α data gives the same bound, and in the intermediate range a more refined analysis would be needed, but there are some hints that the Lyman-α data would again produce the same bound.

CMB constraints with a particle-physics-motivated flat prior on $\Delta N_{\rm fluid} \geq 0.07$. There are several particle physics models that can be effectively described by the ETHOS $n = 0$ parametrisation, with weakly interacting dark matter - dark radiation, and strongly self-interacting dark radiation. In the NADM model [234], discussed in section 7.1.1, the dark radiation is made up of the dark gluons of a non-abelian gauge symmetry $SU(N)$. Its density is parametrised by $\Delta N_{\rm fluid} = 0.07(N^2 - 1)$ with $N \geq 2$. In [235] a second set-up is presented, leading to approximately the same cosmological signature, in which the dark radiation has two components: the dark photon of a dark $U(1)$ gauge symmetry, plus N_f massless fermions with a dark charge q. For $q \geq 1/3$ the dark radiation density is parametrised by $\Delta N_{\rm fluid} = 0.07(1 + \frac{7}{4}N_f)$, but for smaller charges one gets $\Delta N_{\rm fluid} = 0.07$. As such, these models motivated dedicated runs with a flat prior on $\Delta N_{\rm fluid} \geq 0.07$. To compare our results with previous works, we also adopted a flat prior on the dark matter - dark radiation momentum exchange rate evaluated today, Γ_0, seen in equation 7.10.

The prior $\Delta N_{\rm fluid} \geq 0.07$ translates in the ETHOS parametrisation to $\xi \geq 0.367$. Looking at our previous results, we see that this clearly corresponds to the region in which the CMB bounds are at least as strong as the Lyman-α bounds: thus for this case it was sufficient to run with Planck + BAO data only.

Our results, presented in the left panel of Fig. 7.7 and middle column of Table 7.4, are consistent with those of [235] when using Planck 2015 + BAO 2011 data. However, our bounds are

parameter	ΛCDM	$\Gamma_0 > 0$, $N_{dg} > 0.07$	$\Gamma_0 > 0$, $-5 \leq \log(N_{dg}) \leq 0$
$100\,\omega_{\rm b}$	$2.219^{+0.013}_{-0.014}$	$2.232^{+0.017}_{-0.019}$	$2.219^{+0.014}_{-0.016}$
$\omega_{\rm cdm}$	$0.1192^{+0.0011}_{-0.0010}$	$0.1249^{+0.0023}_{-0.0037}$	$0.1192^{+0.0011}_{-0.0011}$
$ln10^{10}A_{\rm s}$	$3.050^{+0.023}_{-0.023}$	$3.069^{+0.026}_{-0.025}$	$3.054^{+0.025}_{-0.026}$
n_s	$0.9618^{+0.0042}_{-0.0041}$	$0.9653^{+0.0042}_{-0.0045}$	$0.9617^{+0.0042}_{-0.0045}$
$\tau_{\rm reio}$	$0.060^{+0.012}_{-0.012}$	$0.0696^{+0.013}_{-0.013}$	$0.06181^{+0.013}_{-0.014}$
H_0 / [km/(s Mpc)]	$67.94^{+0.46}_{-0.49}$	$69.55^{+0.84}_{-1.3}$	$67.94^{+0.48}_{-0.50}$
σ_8	$0.8234^{+0.0085}_{-0.0090}$	$0.813^{+0.015}_{-0.012}$	$0.806^{+0.029}_{-0.011}$
$n_{\rm eff}$	$-2.308^{+0.0034}_{-0.0035}$	$-2.332^{+0.018}_{-0.011}$	$-3.261^{+0.96}_{-0.36}$
Γ_0 / $\left[\mathrm{Mpc}^{-1}\right]$	–	$< 1.2 \cdot 10^{-7}$	$< 1.5 \cdot 10^{-5}$
$\Delta N_{\rm fluid}$	–	< 0.59	–
$\log_{10}(\Delta N_{\rm fluid})$	–	–	< -2.66
$\Delta\chi^2$	–	1.90	2.34

TABLE 7.4: Parameter 68 % confidence limits (or 95 % upper bound in some cases) for all relevant parameters for the NADM case with two different prior choices, and using Planck + BAO. The $\Delta\chi^2$ is given with respect to ΛCDM with the same datasets.

slightly stronger and more up-to-date, as we included Planck lensing data and more recent BAO data. We did not compare directly our results with those of [236], as the latter always included direct H_0 measurements, as well as Planck data on Sunyaev-Zel'dovitch cluster counts, which were not included in our analyses.

We found $0.07 \leq \Delta N_{\rm fluid} \leq 0.59$ (95 % C.L.), corresponding to $0.367 < \xi < 0.626$ with a non-flat prior on ξ, and $\Gamma_0 < 1.2 \cdot 10^{-7}\mathrm{Mpc}^{-1}$ (95 % C.L.), corresponding to $10^4 a_{\rm dark}\xi^4 < 36$ (95 % C.L.). We see that the lower prior edge on $\Delta N_{\rm fluid}$ and the linear prior on both $\Delta N_{\rm fluid}$ and Γ_0 pushed the MCMC to explore regions that were not reached with our ETHOS $n = 0$ prior: the previous preferred region only stretched up to twice smaller values of ξ and $10^4 a_{\rm dark}\xi^4$. However, the current run is not forced to explore a region in tension with the data, since the best-fit χ^2 only increases marginally (by 1.9) with respect to the best-fit ΛCDM χ^2.

Even though this model is not preferred by the Planck + BAO data, it is a possible way to reconcile CMB + BAO data with the high values of H_0 and low values of σ_8 discussed in chapter 5, and first showed in [235], [236]. In our runs we found that this model can accommodate a large $H_0 = 69.6^{+0.8}_{-1.3}$ (68 % C.L.), reducing the tension with the most recent SH0ES data [249] from 4.1σ to 2.7σ. It also allows for smaller values of the parameter combination $S_8 \equiv \sigma_8\sqrt{\Omega_{\rm m}/0.3} = 0.8129^{+0.015}_{-0.012}$ (68 % C.L.) than the ΛCDM model, which gives $S_8 = 0.8235^{+0.0088}_{-0.0091}$ (68 % C.L.) for the same data set. As such, it increases the compatibility with the KiDS+VIKING-450 measurement [152] from the 2.1σ to 1.8σ level. The physical

explanation is that this model is able to exploit the $H_0 - \Delta N_{\rm fluid}$ degeneracy due to its self-interacting dark radiation component, while at the same time reducing the small scale matter power spectrum amplitude due to the effect of dark radiation dragging dark matter perturbations, as discussed in section 7.2.2.

These results are consistent with those we obtained with the ETHOS $n = 0$ parametrisation (with flat priors on ξ and $\log_{10}(a_{\rm dark})$ and the same data set), although the comparison is not straightforward as the later run explores a different region of parameter space. Our previous results did show the trend to accommodate a larger H_0 when $\Delta N_{\rm fluid}$ increases, which is even clearer in this run that reaches higher values of $\Delta N_{\rm fluid}$. Additionally, our previous results showed that when the interaction rate increases from $\log_{10}(a_{\rm dark}) \simeq -2$ to $\log_{10}(a_{\rm dark}) \simeq 0$, smaller values of σ_8 can be reached. This was confirmed in the run with a flat prior on $\Delta N_{\rm fluid} \geq 0.07$ by the clear correlation between the interaction rate and σ_8 in the left panel of Fig. 7.7.

The comparison between the two runs showed us that the ability of this model to reconcile data sets depends on the priors: the model would appear less effective in this respect with a lower prior edge $\Delta N_{\rm fluid} \geq 0$ (or with logarithmic priors on $\Delta N_{\rm fluid}$ or Γ_0). This prior dependence of the conclusions also applies to most other models attempting to resolve the cosmological tensions, and would only go away if we included the anomalous H_0 and σ_8 data in the analysis: in this case, even with different priors, some non-zero values of $\Delta N_{\rm fluid}$ and Γ_0 would be preferred with a statistical significance of a few sigmas.

CMB constraints with a logarithmic prior on $\Delta N_{\rm fluid}$. In [236], this model was also explored with flat priors on $-5 \leq \log_{10}(N_{dg}) \leq 0$ and on $\Gamma_0 \geq 0$. The motivation for this prior was to provide complementary results to the previous case, exploring very small values of the dark radiation density, which can always be motivated by specific particle physics constructions. As such, we also updated these results with our Planck + BAO data set, but not using Lyman-α data as we have seen that our method can not provide accurate constraints for these models.

The results we obtained for this final case are shown in the right panel of Fig. 7.7 and last column of Table 7.4. We find $-5 \leq \log_{10} \Delta N_{\rm fluid} \leq -2.66$ (95 % C.L.), corresponding to $0.04 < \xi < 0.15$ with a non-flat prior on ξ, and $\Gamma_0 < 1.5 \cdot 10^{-5}{\rm Mpc}^{-1}$ (95 % C.L.), corresponding to $a_{\rm dark}\xi^4 < 0.45$ (95 % C.L.).

With this choice of priors, we no longer allow for larger H_0, as expected from our results for the ETHOS $n = 0$ case. This can be understood in the following way: the flat prior on ξ (and the log prior on N_{dg}) gives less weight to large amounts of dark radiation, and thus the possibility to relax the H_0 tension goes away. Nonetheless, we can still accommodate lower σ_8 values, thanks to a degeneracy between σ_8 and $\log_{10} \Delta N_{\rm fluid}$ that is clearly visible in the right panel of Fig. 7.7. This degeneracy is equivalent to the $\sigma_8 - \xi$ degeneracy previously observed in the ETHOS $n = 0$ results, and could in principle reconcile the Planck + BAO data with values as low as $\sigma_8 \sim 0.7$. This model and prior choice lead to $S_8 = 0.8058^{+0.0088}_{-0.0085}$ (68 % C.L.), which is compatible with KiDS+VIKING-450 [152] (see section 5.3) at the 1.4σ level.

7.1.5 Conclusions

In the first half of this chapter I have discussed the possibility of dark matter interacting with a new relativistic dark species known as dark radiation. In section 7.1.1 I introduced the flexible ETHOS parametrisation used to describe theses models, while in section 7.1.2 I discussed the effects this new species, and its subsequent interactions with dark matter, has on different cosmological observables. In order to study these models properly, in **[III]** we implemented this formalism in CLASS, and developed the Lyman-α likelihood described in section 4.3. With this pipeline, detailed in section 7.1.3, we were able to derive new constraints on the relevant parameters, presented in section 7.1.4.

As seen in section 7.1.2, these dark matter - dark radiation interactions affect the matter power spectrum at small scales, making Lyman-α data an excellent probe to constrain them. The method we developed in **[III]** allows us to do this without needing to re-run computationally expensive hydrodynamical simulations for each set of new cosmological parameters. Furthermore, as discussed in section 4.3, the constraints on dark matter - dark radiation interactions derived with our pipeline are related to the true observable probed by up-to-date Lyman-α data (the flux power spectrum), rather than to the model dependent inferred amplitude, slope, and curvature of the linear matter power spectrum at the scales probed by the forest and used in previous analysis [231], [250].

We applied our method to three different cases, corresponding to three different scaling relations of the comoving dark matter - dark radiation interaction rate with respect to temperature, seen in equation 7.4. For each case we performed MCMC runs using MONTEPYTHON for two dataset combinations (Planck + BAO and adding Lyman-α) and we studied the impact of different prior assumptions on the relevant DM-DR parameters.

For the models with temperature dependent comoving interaction rate ($n = 4$ and $n = 2$), our Planck + BAO constraints in the $\log_{10}(a_{\rm dark}/{\rm Mpc}^{-1})$ - ξ parameter space show a hyperbolic behaviour indicating a degeneracy between small amounts of dark radiation and large interaction strength, and vice-versa. The 2σ upper bounds on the amount of dark radiation ($n = 4 : \ \xi < 0.40$ and $n = 2 : \ \xi < 0.43$) come from the impact on the CMB power spectra of a combination of effects: the presence of dark radiation itself and the induced drag force on dark matter, as seen in section 7.1.2. On the other hand, the combination Planck + BAO does not provide a unique upper bound on $\log_{10}(a_{\rm dark}/{\rm Mpc}^{-1})$, as the aforementioned degeneracy leads to an asymptote in $\log_{10}(a_{\rm dark}/{\rm Mpc}^{-1})$ at small ξ.

When adding our Lyman-α likelihood, first of all we checked that the (α, β, γ) parametric function can successfully reproduce the suppression of the matter power spectrum for most of the relevant parameter space. The only exception we found is a tiny region at $\xi < 0.05$, but as this corresponds to a number of degrees of freedom at dark radiation decoupling a few orders of magnitude larger than the Standard Model expectations, it is not a significant region. While the inclusion of the Lyman-α data only slightly improved the bounds on dark radiation ($n = 4 : \ \xi < 0.38$ and $n = 2 : \ \xi < 0.40$), it proved essential to set upper limits on the

interaction strength ($n = 4 :\ \log_{10}(a_{\rm dark}/{\rm Mpc}^{-1}) < 6.8$ and $n = 2 :\ \log_{10}(a_{\rm dark}/{\rm Mpc}^{-1}) < 8.4$), although these are somewhat prior-dependent.

As the Planck + BAO + Lyman-α limits in the $\log_{10}(a_{\rm dark}/{\rm Mpc}^{-1})$ - ξ plane still show the hyperbolic shape, to further investigate this behaviour we performed new runs with a different parametrisation: ΔN_{eff} and the combination $10^{n-4}(a_{\rm dark}/{\rm Mpc}^{-1})\xi^4$. This choice is motivated by the fact that the front factor of the dark matter dipole moment is proportional to $(a_{\rm dark}/{\rm Mpc}^{-1})\xi^4$ (as seen in equation 7.10), and thus it is the relevant quantity for determining the drag epoch. As expected, with the flat prior on $\Delta N_{\rm eff}$ the bounds on the amount of dark radiation are less constraining than those we found with a flat prior on ξ: $\Delta N_{\rm eff} < 0.23$ for $n = 4$ and $\Delta N_{\rm eff} < 0.29$ for $n = 2$. The limits we obtained on the parameter combination $10^{4-n}(a_{\rm dark}/{\rm Mpc}^{-1})\xi^4$ (< 30 for $n = 4$ and < 18 for $n = 2$) can be translated into constraints on the actual particle physics model, and thus on the impact on the small scale crisis. For instance, we found that in the $n = 4$ case our bound still leaves room for a cut-off mass in the halo mass function that can solve the missing satellite problem.

Regarding the cosmological tensions discussed in chapter 5, the constraints on H_0 and on σ_8 are consistent with ΛCDM, both with and without the Lyman-α data. As such, neither of these models alleviate the discrepancies. Finally, the χ^2 analysis shows that these models are not strongly disfavoured with respect to ΛCDM.

For the models with constant comoving interaction rate, $n = 0$, using the ETHOS parametrisation the results appear to be very similar to those of the previous cases: the shape of the limits in the $\log_{10}(a_{\rm dark}/{\rm Mpc}^{-1})$ - ξ plane is hyperbolic; Planck + BAO constrain only $\xi < 0.38$ at 95% C.L.; the inclusion of Lyman-α slightly improves the constraints on ξ ($\xi < 0.33$) and sets a prior-dependent upper bound $\log_{10}(a_{\rm dark}/{\rm Mpc}^{-1}) < 3.3$; and with different priors, we obtained $\Delta N_{\rm eff} < 0.47$ and $10^4 a_{\rm dark}\xi^4 < 14\,{\rm Mpc}^{-1}$. However, an accurate analysis showed that this case required a dedicated discussion.

Indeed, above a certain threshold at $\xi \gtrsim 0.13$ the dominant constraints come from Planck. This was expected, as for a given value of $a_{\rm dark}$ the impact on the CMB is more pronounced in the $n = 0$ case than in the case of a temperature dependent comoving interaction rate. Furthermore, we noticed that for large values of ξ our Lyman-α likelihood should not be applied, as the (α, β, γ) parametric function does not reproduce the smooth suppression of the matter power spectrum induced by these models.

We further investigated this last case by fitting Planck + BAO using the NADM parametrisation seen in equation 7.9, using $\Delta N_{\rm fluid}$ and Γ_0 as priors. We chose a theoretically motivated flat prior on $\Delta N_{\rm fluid} > 0.07$, which leads to a 2σ range $0.07 < \Delta N_{\rm fluid} < 0.59$ and to an upper bound $\Gamma_0 < 1.2 \cdot 10^{-7}\,{\rm Mpc}^{-1}$. The prior opens up to a larger amount of dark radiation as well as a stronger interaction rate, a combination which induces a reduction of the H_0 tension from 4.1σ to 2.7σ, and a mitigation of the σ_8 tension from 2.1σ to 1.8σ. However, once a flat prior on $-5 \leq \log_{10}(\Delta N_{\rm fluid}) \leq 0$ is assumed, the former tension is restored, while the latter is still mitigated (1.4σ).

Our analysis showed that it is still possible to alleviate the cosmological and astrophysical tensions by means of a modified dark sector with interactions between the non-relativistic dark matter and a new relativistic component, as these models are not disfavoured with respect to ΛCDM. However, before claiming a solution of the H_0 and σ_8 tensions, a careful analysis of the prior dependence of the results must be performed, paying specific attention to the quantities relevant for constraining the interactions, such as the drag force. On the other hand, concerning the astrophysical tensions, our Lyman-α likelihood provides an efficient tool to investigate models featuring a suppression in the matter power spectrum at non-linear scales. In **[III]** we showed that bounds derived with this approach are robust, and thus our pipeline can be applied to other interacting dark matter scenarios.

7.2 Dark Matter Interacting with Baryons

In chapter 5 we already saw several reasons to consider models of dark matter beyond the standard paradigm, and in section 7.1 I introduced one such model. Another type of model that has surged in popularity recently is the idea of dark matter interacting with baryons, which would lead to a drag force between the baryon-photon fluid and the dark matter in the early universe, which in turn would result in a suppression of the growth of dark matter perturbations, and thus an overall suppression of structure formation.

A further motivation for this type of dark matter interactions came about when the Experiment to Detect the Global Epoch of reionisation Signature (EDGES) Collaboration reported recently the first measurement of the 21 cm signal induced by early stars [251]. After stellar formation in the early universe, the high-energy photons from these stars can interact with the primordial hydrogen gas, causing it to jump to a slightly excited state, differing from its ground state. This alteration would cause the gas to absorb photons from the cosmic microwave background at a wavelength of $21\,\mathrm{cm}$, or frequency of $1.4\,\mathrm{GHz}$. This would lead to an absorption profile in the cosmic radio-frequency spectrum at frequencies between $1 - 200\,\mathrm{MHz}$[3].

The EDGES collaboration were able to measure an absorption feature in the profile of the sky-averaged radio spectrum, centred at a frequency of $78\,\mathrm{MHz}$ and with an amplitude of $0.5\,\mathrm{K}$. While this feature is at the expected redshift of stellar formation ($z \sim 17$), the reported amplitude of this signal is significantly higher than expected, at a confidence level of 3.8σ. Although this measurement is pending independent verification, if confirmed it would indicate that either the hydrogen (baryon) gas was much colder than expected during the dark ages (before the first stars formed), or that the temperature of the background radiation was much hotter. One such mechanism to cool the primordial hydrogen would be via interactions with a colder species, such as dark matter [252].

[3]Corresponding to the redshifted frequency of $1.4\,\mathrm{GHz}$.

In my forthcoming paper **[IV]** we study scenarios in which the dark matter interacts with protons via an elastic scattering process, with a cross section σ scaling effectively as a power-law of the dark matter-baryon relative velocity, $\sigma = \sigma_0 v^n$. We make use of Lyman-α data using the extended method described in section 4.3. We also discuss the possibility of using the spectral distortions likelihoods discussed in section 4.4. In section 7.2.1 I will first introduce the formalism we use before reviewing the effects these interactions have on the cosmological observables in 7.2.2, and explain how they could account for the EDGES result. In sections 7.2.3-7.2.5 I discuss the *preliminary* results of **[IV]**.

7.2.1 Formalism

In order to properly characterise the dark matter - baryon interactions, I will follow the formalism first introduced in [231] and extended in [83], [253], where they focus on many different theoretically-motivated models leading to the same type of power-law scaling cross section. I will ignore dark matter - electron scattering (although the formalism could easily be extended to include this case as well), and focus on dark matter - proton elastic scattering, with the cross sections σ scaling effectively as a power-law of the baryon-dark matter relative velocity $\sigma = \sigma_0 v^n$. Some well-motivated values of n include: $n = -4$, corresponding to dark matter with fractional electric charge [254]; $n = -1$, corresponding to a Yukawa potential (a massive-boson exchange) [126], [255]; $n = 0$, with velocity-independent scattering [256]; and $n = \pm 2$, corresponding to dark matter with electric and magnetic dipole moments [257].

Within this formalism, it is assumed that the relative baryon-dark matter bulk velocities are not negligible when compared to the thermal velocities. This leads to the dependence of the drag force on the dark matter-baryon relative velocity being non-linear, with the linear theory breaking down for redshifts smaller than $z \sim 10^4$. Within the formalism presented here, an approximation is made to extend the validity of the linear theory to lower redshifts (however, recently in the literature a more comprehensive approach has been derived [258]). Furthermore, it is assumed that both the dark matter and the baryons are non-relativistic (valid for dark matter masses above the MeV scale), and that in the early universe both species follow a Maxwell velocity distribution (although recently a new formalism was derived in [259] extending this to a Fokker-Planck distribution). With these assumptions, and working in the Newtonian gauge, the dark matter Boltzmann equations 3.20 become

$$\begin{aligned} \dot{\delta}_{\rm DM} &= 3\dot{\phi} - \theta_{\rm DM} \,, \\ \dot{\theta}_{\rm DM} &= -\frac{\dot{a}}{a}\theta_{\rm DM} + k^2\psi + k^2 c_{\rm DM}^2 \delta_{\rm DM} + R_{\rm DM}\left(\theta_b - \theta_{\rm DM}\right) \,. \end{aligned} \tag{7.11}$$

In the presence of these interactions, the Boltzmann equations for the baryons, first seen in equations 3.35, acquire a new interaction term and become

$$\begin{aligned}\dot{\delta}_b &= 3\dot{\phi} - \theta_b\,,\\ \dot{\theta}_b &= -\frac{\dot{a}}{a}\theta_b + k^2\psi + k^2 c_b^2\delta_b + R_\gamma\left(\theta_\gamma - \theta_b\right) + \frac{\rho_{\rm DM}}{\rho_b}R_{\rm DM}\left(\theta_{\rm DM} - \theta_b\right)\,.\end{aligned} \tag{7.12}$$

Here I have recovered the dark matter sound speed $c^2_{\rm DM}$, the baryon sound speed c_b^2, and the coefficient for baryon-photon coupling from section 3.2, given by

$$R_\gamma = \frac{4\rho_\gamma}{3\rho_b}an_e\sigma_T\,, \tag{7.13}$$

where ρ_γ is the photon energy density, ρ_b is the baryon energy density, n_e is the electron number density, and σ_T is the Thomson cross section.

The *dark matter-baryon momentum exchange rate* term in equations 7.11 and 7.12 is given by the deceleration of the dark matter bulk velocity, and at leading order is

$$R_{\rm DM} = \frac{a\rho_b\sigma_0 c_n}{m_{\rm DM}+m_b}\left(\frac{T_b}{m_b} + \frac{T_{\rm DM}}{m_{\rm DM}} + \frac{V^2_{\rm RMS}}{3}\right)^{\frac{n+1}{2}}\mathcal{F}_{He}\,, \tag{7.14}$$

where T_x and m_x represent the temperature and mass of species x. The factor $\mathcal{F}_{He}$ is a corrective factor to account for the helium fraction of the baryons, and will be taken to be $\mathcal{F}_{He} = 1 - Y_{He} \approx 1 - 0.24 \approx 0.76$. The constant c_n is an integration constant depending only on n, given by

$$c_n = \frac{2^{\frac{n+5}{2}}\Gamma\left(3+\frac{n}{2}\right)}{3\sqrt{\pi}}\,, \tag{7.15}$$

and is evaluated to $\{0.27, 0.33, 0.53, 1, 2.1, 5, 13, 35, 102\}$ for $n = \{-4,-3,-2,-1,0,1,2,3,4\}$.

The velocity term appearing in equation 7.14 is significant, as it is the averaged value of the dark matter bulk velocity. This term is added to extend the validity of the formalism into a non-linear regime, as discussed before, and is given by

$$V^2_{\rm RMS} \equiv \langle V^2_{\rm DM}\rangle \simeq \begin{cases} 10^{-8}, & z > 10^3 \\ 10^{-8}\left(\frac{(1+z)}{10^3}\right)^2, & z \leq 10^3 \end{cases}\,. \tag{7.16}$$

Apart from the perturbation equations, we are interested in how the dark matter - baryon interactions affect the temperature evolution of the two species. This will be especially significant when discussing how these interactions are related to the EDGES anomaly. The dark matter and baryon fluid temperatures evolve as

$$\begin{aligned}\dot{T}_{\rm DM} &= -2\frac{\dot{a}}{a}T_{\rm DM} + \frac{2m_{\rm DM}}{m_{\rm DM}+m_b}R^*_{\rm DM}(T_b - T_{\rm DM})\\ \dot{T}_b &= -2\frac{\dot{a}}{a}T_b + \frac{2\mu_b}{m_e}R_\gamma(T_\gamma - T_b) + \frac{2\mu_b}{m_{\rm DM}+m_b}\frac{\rho_{\rm DM}}{\rho_b}R^*_{\rm DM}(T_{\rm DM} - T_b)\,.\end{aligned} \tag{7.17}$$

Here I have introduced the thermalisation rate $R^*_{\rm DM}$ due to dark matter - baryon scattering. Together with the Compton term R_γ, due to photon - baryon coupling, these lead to non-adiabatic terms in the temperature evolution. The thermalisation rate $R^*_{\rm DM}$ is only equal to the momentum exchange rate $R_{\rm DM}$ if there is no scattering between dark matter and helium. As this is a good first-order approach, here I will assume $\sigma_{He} = 0$ and thus $R^*_{\rm DM} = R_{\rm DM}$[4].

The factor μ_b in equation 7.14 is the baryon mean molecular weight, and is given by $\mu_b \simeq m_b(n_H + 4n_{He})/(n_H + n_e + n_{He})$.

To fully solve the coupled equations in expression 7.17 we need to specify initial conditions. In general, for $n > -4$, the dark matter and baryons are coupled in the early universe, until the time at which the scattering rate becomes smaller than the Hubble rate (as discussed in section 1.8.2). Thus, we can calculate the time of decoupling, and choose an earlier time to set the condition $T_{\rm DM} = T_b$. This approach fails for $n = -4$, as the scattering timescales are always longer than the Hubble time. In this case, we can impose the condition that the dark matter gives the observed relic density today, in which case the decoupling redshift will be set by the thermal freeze-out condition seen in section 1.9.2. For the small dark matter masses usually considered, this leads to extremely low initial dark matter temperatures, and thus we can take $T_{\rm DM,ini} = 0$ at very early times.

Additionally, as we saw in section 4.4 the importance of heating functions for the computation of spectral distortions, we can compute the heating rate of dark matter. In the limit of low dark matter peculiar velocity, no helium interactions, and assuming the dark matter fluid behaves as an ideal gas, we can find

$$\frac{dQ_{\rm DM}}{dt} = -\frac{3ac_n m_{\rm DM}\rho_b\sigma_0}{(m_{\rm DM}+m_b)^2}\left(\frac{T_b}{m_b}+\frac{T_{\rm DM}}{m_{\rm DM}}\right)^{\frac{n+1}{2}}(T_{\rm DM}-T_b) \tag{7.18}$$

Finally, to completely follow the evolution of dark matter and baryon perturbations in the presence of interactions between the two species, we would need to describe the behaviour of the two during the photon-baryon tight coupling regime. As the baryons are tightly coupled to photons in this regime, any influence on the baryon perturbations caused by the dark matter will in turn influence the photon perturbations. This results in modifications to the tight coupling equations (as described for example in [253])[5].

7.2.2 Effects on Observables

Interactions between dark matter and baryons have a rich phenomenology, and can affect cosmological probes at many different scales. Dark matter scattering with protons before recombination will modify the evolution of small scale perturbations, affecting the temperature and polarisation anisotropies in the CMB, as well as the matter power spectrum. Additionally,

[4]Note that in the literature it is common to use the notation R' instead of R^*, but this could be confused with a derivative, so I have changed notation.

[5]I do not repeat the equations here for the sake of brevity (the last chapter of a thesis is a good place to remember brevity).

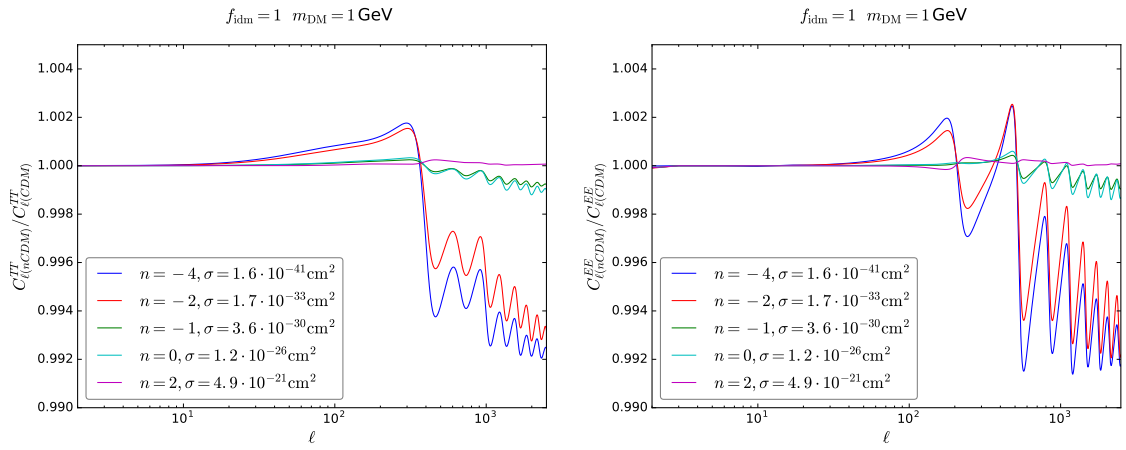

FIGURE 7.8: Effects of dark matter - baryon interactions on the CMB. The temperature (C_ℓ^{TT}, left) and polarisation (C_ℓ^{EE}, right) angular power spectra are shown for the interacting model relative to a model with the same ΛCDM parameters but no interactions. The solid curves illustrate the impact of changing the temperature scaling n.

these interactions can slightly cool or heat normal matter, leading to spectral distortions of the CMB blackbody spectrum, as described in section 4.4. This same temperature effect will play a role at later times as well, by potentially modifying the thermal evolution of the baryonic matter, thus affecting the absorption of 21 cm photons. In this section I will review all of these effects in detail.

In some aspects, dark matter - baryon interaction behave similarly to the dark matter - dark radiation interactions described in section 7.1.2. In the presence of interactions with baryons, the pressure from the photon-baryon fluid will reduce the growth of dark matter overdensities at that time. Thus, the smaller wavelength modes already within the horizon at the time of these interactions will experience a suppression in their growth, while the modes that enter the horizon later, with longer wavelength, will be less affected. As in the case with dark radiation interactions, this affects the CMB anisotropies on small scales.

The effects of these interactions on the CMB are illustrated in Fig. 7.8, where I have chosen cross sections corresponding to the most recent bounds on these interactions [253]. We can see that the main effect on the C_ℓ^{TT} is a phase shift of the peaks, and a suppression of all multipoles above $\ell \sim 350$.

There is also a significant impact on the polarisation of the CMB, as seen in the right panel of Fig. 7.8. This is due to the CMB E-mode polarisation being directly sourced by the velocity of the baryon-photon fluid, as seen in equation 3.68, and thus it is affected by the baryons interacting with dark matter. While the temperature source function is dominated by the temperature monopole (as seen in equation 3.66), the polarisation is dominated by the much smaller temperature quadrupole. Therefore, as the polarisation source depends linearly on the velocity of the photon-baryon fluid, the interactions will result in a significant change to the polarisation source at every k-mode.

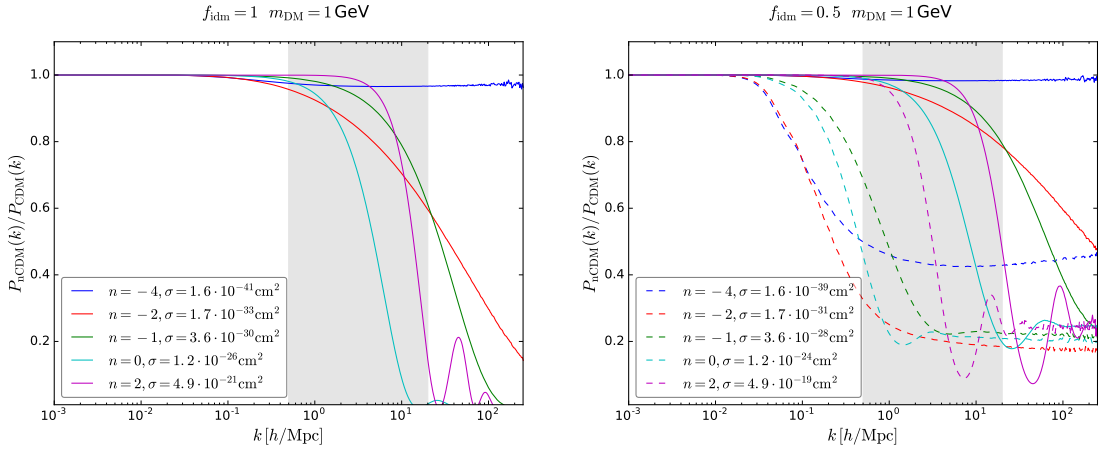

FIGURE 7.9: Effects of dark matter - baryon interactions on the matter power spectrum. The $P(k)$ is shown for the interacting model (left, $100\,\%$ of interacting dark matter) or partially interacting model (right, $50\,\%$ of interacting dark matter) relative to a model with the same ΛCDM parameters but no interactions. The solid curves correspond to the same model in both panels, and show the impact of changing the cross section and the temperature scaling n. The grey region corresponds to the scales that can be probed with Lyman-α.

When it comes to the effects on the matter power spectrum, the behaviour is very similar to the case of dark matter interacting with dark radiation, although in this case we do not see dark acoustic oscillations. The dark matter - baryon scattering leads to a later decoupling time for dark matter, which induces a collisional damping of the matter power spectrum on small scales, shown in Fig. 7.9. For this figure, the solid lines show the same cross sections as in Fig. 7.8, thus corresponding to the most recent bounds on these interactions [253].

In this case we are also interested in having a fraction of dark matter interacting, which is illustrated in the right panel of the Fig. 7.9. When only a fraction of dark matter interacts, the suppression in the matter power spectrum does not reach a $100\,\%$ suppression, instead it reaches a general plateau. As such, these models are perfect to be constrained with the extended Lyman-$\alpha$$-\alpha\beta\delta$ likelihood described in section 4.3.

With the suppression induced on the matter power spectrum, it is reasonable to consider if these models can offer any hope in alleviating the small scale crisis (see section 5.1). This was studied in detail in [231], and they found that, given the existing bounds from the CMB, these interactions can only affect the halo mass function for $M < 10^{12} M_{\odot}$. For smaller masses, significant suppression of structure is still possible, provided $n \geq -3$. This is because models such as $n = -4$ freeze-out at high redshift, when the collisional velocities become large, and freeze-in again at lower redshift when the velocities drop. On the other hand, models with a larger velocity dependence are important at earlier times and then subsequently freeze-out as the universe expands and cools. Therefore, these scatterings are too small to affect the distribution of matter at late times in halos of the size of the Milky Way. As such, these models can not address the missing satellite problem, but it is unclear if they can affect the core-cusp or diversity problems.

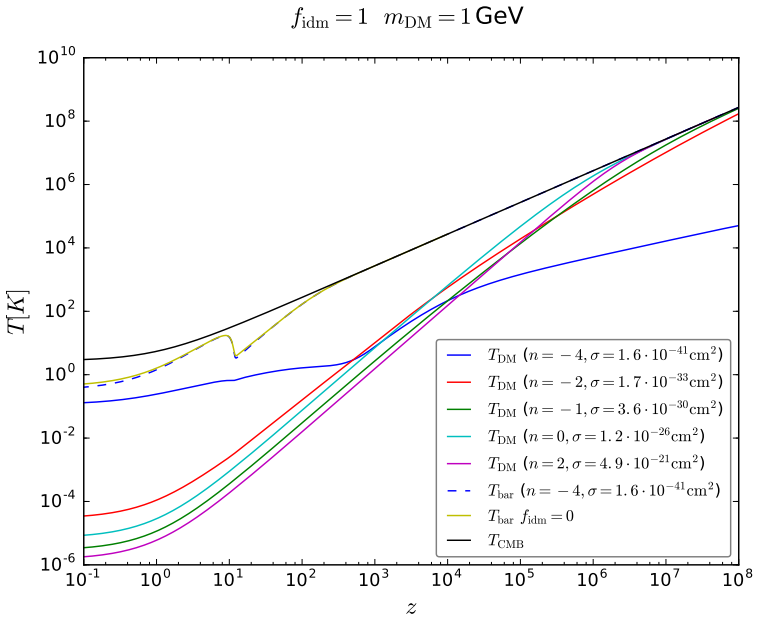

FIGURE 7.10: Temperature of different species as a function of redshift. The evolution of the dark matter temperature is shown for the same five cases as in Fig. 7.8. The dashed blue line shows the baryon temperature in the $n = -4$ case, while the yellow line shows the baryon temperature in the ΛCDM model. The CMB temperature, which is not influenced by the dark matter interactions, is also shown for reference.

A very significant effect of dark matter - baryon interactions is their impact on the temperature of the primordial hydrogen gas, and this has drawn substantial interest since the announcement of the EDGES results, and the apparent mismatch between the ΛCDM predictions and the observations [251].

Once the dark ages end and we enter reionisation (see section 1.8), a very useful measurement is the redshifted hydrogen hyperfine transition at 21 cm wavelength. The overall amplitude of this signal comes from the difference between the hydrogen spin temperature and the CMB temperature: if $T_{\rm CMB} > T_{\rm spin}$, the resulting signal will be an *absorption* profile, whereas if $T_{\rm CMB} < T_{\rm spin}$ we would end up with an *emission* signal. Furthermore, the spin temperature is predicted to be somewhere in between the CMB temperature and the temperature of the hydrogen gas. As the CMB temperature has been measured very accurately (see section 4.1), a measurement of a potential absorption profile would give us an upper limit on the temperature of baryons at the time of reionisation.

As discussed in the beginning of section 7.2, the EDGES collaboration recently reported the first measurement of this absorption feature, but they found its amplitude to be double what was predicted, thus leading to a surge in interest for models that could account for this discrepancy. One way to obtain a deeper absorption signal than predicted by ΛCDM would be to have the hydrogen temperature lower than predicted. As the dark matter is the coldest known species in the universe, it is reasonable to consider dark matter - baryon scatterings as a way to cool the hydrogen gas after the baryons decouple from photons.

In Fig. 7.10 I show the temperature evolution for dark matter, baryons, and the CMB, for different values of the index n. As 21 cm experiments are more sensitive to scatterings that are enhanced at low velocities, the $n = -4$ case is expected to have the biggest impact on the baryon temperature. As such, I only show the baryon temperature for this dark matter model. To better illustrate the impact of the interactions on the hydrogen temperature, the prediction for ΛCDM is also shown. The models correspond to the same ones shown in solid lines in Figs. 7.8 and 7.9, with cross sections chosen to match the results from [253].

After the EDGES results were announced, dark matter - baryon interactions took a central stage, specifically the case of millicharged dark matter ($n = -4$) [252]. However, existing constraints from CMB, BBN, and supernovae already put very stringent bounds on these models. As such, in [260] it was shown that millicharged dark matter can only explain the EDGES result (while avoiding other bounds) if a very small fraction of dark matter interacts. Furthermore, the EDGES result has yet to be verified independently, and there are many other proposals to solve the problem, such as additional radiation backgrounds coming from black holes [261] or alternative dark matter sources [262], [263].

A final effect to consider for dark matter - baryon interactions is their impact on the CMB through spectral distortions to the overall blackbody spectrum, as discussed in [83], [264]. As we already saw in section 4.4, for $z \lesssim 10^6$ photon number changing processes become inefficient, and distortions of the thermal blackbody spectrum can be generated by energy injections into the CMB. For redshifts in the range $5 \cdot 10^4 \lesssim z \lesssim 10^6$ the spectral distortion has the form of a chemical potential, as Compton scattering efficiently redistributes photons, leading to a μ-type distortion, while for lower redshift values we have a y-type distortion caused by the bath of electrons that interacts with the CMB being heated or cooled.

As there are many non-trivial low-redshift backgrounds, such as the thermal Sunyaev-Zeldovich effect, in general we will only be interseted in μ-type distortions. Recovering the definition of fractional spectral distortion from section 4.4, which is the rate at which CMB photons change in energy due to distortions ($\Delta \equiv \Delta\rho_\gamma/\rho_\gamma$), we have

$$\rho_\gamma \frac{d\Delta}{dt} = \frac{3}{2} n_b \frac{2\mu_b}{m_e} R_\gamma \left(T_b - T_\gamma\right) . \tag{7.19}$$

From equation 7.17, we know that T_b is affected by the dark matter - baryon interactions. Using that equation, and assuming $T_b \approx T_\gamma$ (valid for early times), we find

$$\rho_\gamma \frac{d\Delta}{dt} = -\frac{3}{2}\left(n_b + \frac{2\rho_{\rm DM}}{m_{\rm DM} + m_b} \frac{R_{\rm DM}\left(T_b - T_{\rm DM}\right)}{H T_b}\right) H T_\gamma . \tag{7.20}$$

While analytic solutions to this expression exist for some values of n [264], for a more generic description this needs to be evolved using the full temperature equations form 7.17. Given that we know that FIRAS has excluded $\Delta \gtrsim 5 \cdot 10^{-5}$, and we expect PIXIE to push this to $\Delta \sim 10^{-8}$, we can also use spectral distortion missions to constrain these interacting models.

7.2.3 Methodology

In the previous section we saw the importance of models with dark matter - baryon interactions, and their effects on the cosmological observables. With this in mind, for the forthcoming paper **[IV]** I implemented in CLASS the full background, perturbation, and temperature equations describing these interactions, as detailed in section 7.2.1.

These modifications to CLASS were done in a similar manner to the implementation of the dark matter - dark radiation interactions described in section 7.1.3: all perturbation equations are implemented in both the Newtonian and the Synchronous gauge, and the dark matter is in the form of a new "interacting DM species" coexisting with the plain cold dark matter species.

When studying the temperature evolution of both the dark matter and the baryon fluid, as described by equations 7.17, it is often the case in the literature to make use of a *sudden decoupling approximation*, in which the dark matter temperature is only followed after a certain redshift [83], [253]. This is done because computing the full temperature evolution of the two fluids requires a stiff integrator, which is not usually implemented at the temperature level in Boltzmann codes. As described in section 7.1.3, CLASS uses the stiff integrator `ndf15` at the perturbation level. For the sake of this work, we implemented this stiff integrator also for the temperature equations. This allows us to follow the full evolution of the baryon and dark matter temperatures, without needing the sudden decoupling approximation.

In order to choose the initial time for the integration, the modified CLASS code computes the time at which the scattering rate becomes smaller than the Hubble rate (the decoupling time) for a given model. The code then selects an initial redshift $z_{\rm ini} = z_{\rm dec}(1 + \epsilon_z)$ before the decoupling, where ϵ_z can be chosen with a new precision parameter. Additionally, in order to speed up the calculation, the integrator will take logarithmic time steps for very early times (high redshift), switching to linear time steps for late times (low redshift). The redshift at which this switch takes place can also be tweaked with a further precision parameter.

Thus, our modified CLASS code incorporates dark matter - baryon interactions governed by the following main parameters:

- `f_idm_b`: fraction of cold dark matter that we want to be interacting, between 0 and 1
- `m_dm`: dark matter mass in eV
- `cross_idm`: cross section of the interaction, σ_0, in cm^2
- `n_index_idmb`: index giving the velocity-dependence of the cross section $\sigma = \sigma_0 v^n$
- `helium_scattering`: switch to turn on/off helium scattering (turned off by default)
- Additional precision parameters controlling the integrator, as described above

This modified version of CLASS was used to produce Figs. 7.8, 7.9, and 7.10, all of which are in very good agreement with the figures available in the literature (for example in [253]). This code is going to be made publicly available together with the publication of **[IV]**.

In section 7.2.2 I discussed the impact these models have on structure formation, and thus on the matter power spectrum. As such, we would like to constrain these models with Lyman-α data. We can see in the right panel of Fig. 7.9 that the suppression in the transfer function (equation 4.6) does not always reach $100\,\%$, especially in the case of only a fraction of interacting dark matter (as needed to explain the EDGES result). With this in mind, for **[IV]** we developed the extended Lyman-$\alpha-\alpha\beta\delta$ likelihood described in section 4.3.

The procedure of the likelihood is the same as discussed in section 7.1.3: we use our modified CLASS version to compute the linear matter power spectrum for our choice of parameters; we produce the linear matter power spectrum of the equivalent ΛCDM model (by setting $f_{\rm idm} = 0$); $\{\alpha, \beta, \delta\}$ are fitted to the transfer function, as described in equation 4.10, with a simple least squared method; if the model has passed all of the checks, a χ^2-value is assigned to the corresponding combination of parameters; and finally, this is iterated for each step in the MCMC.

As an important remark, in section 7.2.2 we saw that the dark matter - baryon scatterings can affect the halo mass function on small scales, and thus this might need to be considered in the N-body simulations. However, this is a memory effect coming from earlier, linear times: the interactions become less relevant at later times, and thus do not directly influence the physics of the non-linear regime. This means that N-body simulations do not need to account for these scatterings explicitly, rather they can use the linear matter power spectrum at a specific redshift as an input to encode all the effects of the scatterings.

7.2.4 Results

For the upcoming **[IV]**, we are using our new Lyman-$\alpha-\alpha\beta\delta$ likelihood with MONTEPYTHON, interfaced with our modified CLASS version, in its default Metropolis Hastings mode to perform parameter scans on the combination of $\{\omega_{\rm b},\ \omega_{\rm CDM},\ \log(10^{10}A_s),\ n_s,\ \tau_{\rm reio},\ 100\theta_s,\ \sigma_0,\ f_{\rm idm}\}$. We study the physically-motivated models with $n = -4$, $n = -2$, $n = -1$, $n = 0$, and $n = 2$ (as described in section 7.2.1).

For each of the studied models, we will perform MCMC analysis for two different data combinations:

- **Planck**: This is the combination of Planck 2015 high-ℓ TT+TE+EE, low-ℓ data [241] and Planck 2015 lensing data [242].
- **Planck + Lyman-α**: Same as above, with the additional Lyman-$\alpha-\alpha\beta\delta$ likelihood.

Additionally, we will be interested in the impact of varying the fraction of interacting dark matter, and so for each model and data set we will run once with $f_{\rm idm} = 1$, and once more allowing this parameter to take any value between $[0, 1]$.

Most of these cases are ongoing at the time of writing this thesis, but I can already discuss the preliminary results of the Planck only runs, with fully interacting dark matter ($f_{\rm idm} = 1$). These results are summarised in Table 7.5, where I show the $95\,\%$ confidence level limits on

n	σ_0 [cm^2]
-4	1.5×10^{-41}
-2	2.8×10^{-33}
-1	4.1×10^{-30}
0	2.9×10^{-26}
2	1.2×10^{-19}

TABLE 7.5: 95 % confidence level upper bounds on σ_0 in cm^2 from MCMC analyses using Planck data, for each choice of power-law scattering index, with $m_{\rm DM} = 1\,$GeV and $f_{\rm idm} = 1$.

the upper bound values of σ_0, for a fixed $m_{\rm DM} = 1\,$GeV. These bounds can be compared to those presented in Table 1 of [253], where we see our results are in very good agreement, but we obtain slightly tighter constraints. This can be attributed to our inclusion of lensing data from Planck, which was not included in their analysis.

Furthermore, we do not observe any degeneracies between the cross section and the base ΛCDM parameters, as expected. Additionally, our constraints on the ΛCDM parameters are not affected by the presence of dark matter - baryon interactions, in agreement with the literature. For each of the five models studied here, we obtain a $\Delta\chi^2 \sim 3$ when compared to ΛCDM. As we have one additional degree of freedom, this is not significant enough to claim any preference for these models with respect to the standard cosmological model.

The next step needed for our analysis is to see how these bounds change when adding the extended Lyman-$\alpha$$-\alpha\beta\delta$ likelihood, both for fully interacting dark matter, and in cases when we only have a fraction of dark matter interacting. As such we are currently setting up the following analyses:

- Eight parameter model, varying both σ_0 and $f_{\rm idm}$, using Planck only data.
- Seven parameter model, varying only σ_0 and fixing the fraction of interacting dark matter to $f_{\rm idm} = 1$, using Planck + Lyman-$\alpha$$-\alpha\beta\delta$.
- Eight parameter model, varying both σ_0 and $f_{\rm idm}$, using Planck + Lyman-$\alpha$$-\alpha\beta\delta$.

In addition to the data sets mentioned here, once our modified CLASS code has been interfaced with the spectral distortions code and likelihoods developed for **[V]**, and discussed in detail in section 4.4, we will also be able to use the PIXIE likelihood to see how the bounds on the dark matter - baryon cross section could be improved with a future spectral distortions satellite.

7.2.5 Conclusions

In the second half of this chapter I have discussed the possibility of dark matter interacting with baryons, either fully or partially, with a velocity-dependent cross section given by $\sigma = \sigma_0 v^n$. In section 7.2.1 I introduced the modifications to the Boltzmann equations needed to

describe these interactions, as well as the resulting temperature evolution for both species involved.

In section 7.2.2 I reviewed how these interactions affect the cosmological observables. In terms of the CMB, these interactions affect both the temperature and polarisation spectra: the interactions enhance the reionisation bump, induce with a phase shift of the peaks, and result in a suppression of all higher multipoles. In terms of the matter power spectrum, the biggest impact is in the form of a suppression on small scales.

For the forthcoming paper **[IV]** I have implemented the full interacting dark matter - baryon formalism in the Boltzmann code CLASS, described in detail in section 7.2.3. This required adding a new integration method to follow the full temperature evolution of the dark matter, which has not been done before in the literature. Given the impact these interactions have on the matter power spectrum, we have developed an extended Lyman-α likelihood, described in detail in section 4.3. This likelihood is interfaced with MONTEPYTHON, and can thus be used very easily with our modified CLASS code.

In the ongoing work for **[IV]** we are running MCMC analyses to derive bounds on the cross section for dark matter with a mass of $m_{\rm DM} = 1\,\text{GeV}$. We aim at obtaining bounds for four different combinations of models and data: Planck only with fully interacting dark matter, Planck only with a varying fraction of interacting dark matter, and the same two cases with Planck + Lyman-α. In section 7.2.4 I have reviewed the preliminary results of the first combination of data and model.

The bounds on the cross section obtained with Planck data for $m_{\rm DM} = 1\,\text{GeV}$ and $f_{\rm idm}$, shown in Table. 7.5, are compatible with the existing bounds in the literature. Additionally, we do not find any degeneracies between the cross section and the six ΛCDM parameters, nor does the presence of interacting dark matter affect any of our bounds on these parameters, as expected. This serves as a useful cross-check, showing the validity of our modified CLASS code.

In addition to the ongoing work for **[IV]**, which we expect to finish in the coming months, we are preparing the needed framework to be able to constrain these interacting models with the spectral distortions likelihoods developed in **[V]**. Furthermore, our modified CLASS code, which will be made publicly available soon, has the necessary format to be easily integrated with the code we developed for **[III]**, with the aim of having one unified CLASS version that can account for several different dark matter interactions.

General Conclusions

And here we are, at the end. Staring at a long document, wondering how I managed to write a thesis.

The aim of this thesis was to develop and apply new methods to further our understanding of massive relics in the universe. Both neutrinos and dark matter are cornerstones of modern cosmology, but there is still much we do not know about these elusive particles. In this work I have shown that future cosmological probes will help us shed some light on this dark sector, provided we have the necessary tools to use all the data available.

I started by reviewing the standard models of cosmology and particle physics in chapters 1-3, introducing the contents of the universe. I further derived all the necessary equations to describe the behaviour of these different species, both at the homogeneous background level, and at first order in perturbation theory. With the standard model of cosmology we can tell a story from the quantum fluctuations in the very early universe to the formation and evolution of the complex structures we observe today.

In chapter 4 I discussed the main probes we have to observe the universe around us, linking the cosmological fluctuations mentioned above to the CMB and matter power spectrum. Furthermore, I presented a newly-developed method to extract information from the Lyman-α forest seen in the spectra of distant quasars. With this method, used for **[III]** and **[IV]**, rather than running time consuming N-body simulations for each underlying cosmological model, we instead parametrise the effects these models have on the matter power spectrum. We can then interpolate in a pre-existing grid of simulations based on the induced suppression in the matter power spectrum, allowing us to run parameter inference codes on these models. Moreover, in the same chapter I detailed our new implementation in CLASS of spectral distortions of the CMB blackbody, as well as the development of a generic spectral distortions likelihood, which allows us to test the synergy of this probe with other cosmological datasets, as done in **[V]**.

In chapter 5 I discussed three problems in cosmology: the small scale crisis, consisting in a mismatch between simulations and observations on very small scales; the H_0 tension, whereby low redshift and high redshift probes of this measurement show nearly a 4σ tension; and the σ_8 tension, which appears when comparing the clustering of matter in seen in lensing experiments with what we see in the CMB. Combined with the observations of a non-zero neutrino mass, which can not be easily accommodated in the Standard Model of particle physics, these problems provide strong motivation to look beyond the standard ΛCDM paradigm.

With this in mind, in chapter 6 I showed the importance of massive neutrinos to cosmology, and discussed how we can use different cosmological probes to obtain a bound on the sum of neutrino masses. I further discussed the results of **[II]**, where we forecast the sensitivity of

thirty-five different combinations of future Cosmic Microwave Background and Large Scale Structure with a uniform pipeline. We showed that future surveys will measure the total neutrino mass with high significance, for all cosmological models studied.

In chapter 7.1, I introduced interacting dark matter models, focussing on dark matter - dark radiation interactions with a scattering rate scaling like a power-law of the temperature, T^n. After describing the effects these models have on cosmological observables, I presented the results of **[III]**, where we used our newly-developed Lyman-α likelihood in combination with existing CMB and BAO data, to constrain these interactions. We showed that for models with $n = 2, 4$ Lyman-α data strengthen the CMB + BAO bounds on the interaction rate of these species by many orders of magnitude, without excluding models that can solve the missing satellite problem. Furthermore, using a theoretically motivated prior on the minimal density of dark radiation, we found that models with $n = 0$ can reduce the Hubble tension to 2.7σ, while simultaneously accommodating the smaller values of σ_8 hinted at by cosmic shear data.

Finally, in chapter 7.2, I discussed preliminary results of the forthcoming paper **[IV]**, where we will study dark matter - baryon interactions, with the aim of deriving bounds on the interaction strength and fraction of interacting dark matter. We will make use of an extended version of the Lyman-α likelihood, which allows us to probe models that produce only a partial suppression of the matter power spectrum. Furthermore, we are working on a new major public release of the Boltzmann code CLASS, which will include all of the interacting dark matter models described here, as well as the spectral distortions calculation described in **[V]**.

In the work carried out during this thesis, I have extended the Boltzmann code CLASS to include several non-gravitational dark matter interactions, as well as a full treatment and calculation of spectral distortions of the thermal black body. Additionally, I have developed new likelihoods for MONTEPYTHON for many different probes: two new Lyman-α likelihoods applicable to any non-cold dark matter model; mock likelihoods for the future CMB missions LiteBIRD, CMB-S4, and PICO; and mock likelihoods for the spectral distortions missions FIRAS and PIXIE. We have used some of these tools to show that cosmology is highly likely to produce a measurement of the neutrino masses in the next decade. Furthermore, we have derived state-of-the-art bounds on models in which dark matter can interact with dark radiation, and we are ready to do the same for dark matter - baryon interactions.

Despite the incredible progress made in cosmology and particle physics in the last century, there are still many unanswered questions, especially surrounding the elusive massive relics. Of course, in this thesis I have not answered these questions[6], but hopefully I have helped to show that there is a real possibility that we will answer these questions in the coming years. To do so, we are going to need to extract as much information as possible from all available data sets. Until such a time, we will keep looking at the universe, trying to figure out what is out there. We are, after all, a curious species.

[6] Although it would have been a *very* nice thesis if I had.

A Inflation Potential Reconstruction

As discussed in section 2.2, the shape of the inflaton potential can vary a lot, however we can use observational data to try to put constraints on the underlying physical parameters. In this appendix I will discuss the idea of reconstructing the inflaton potential using different Taylor approximations. This work was carried out by myself and J. Lesgourgues for the Planck Collaboration, as part of the *Planck 2018 results. X. Constraints on inflation* paper **[I]**; this appendix is based on our results presented in section 5 of the aforementioned paper. This analysis had already been done in previous Planck Inflation papers [265], however here we include the new case where we expand until the end of inflation, rather than only in the observable window

Taylor expansion of $V(\phi)$ in the observable region

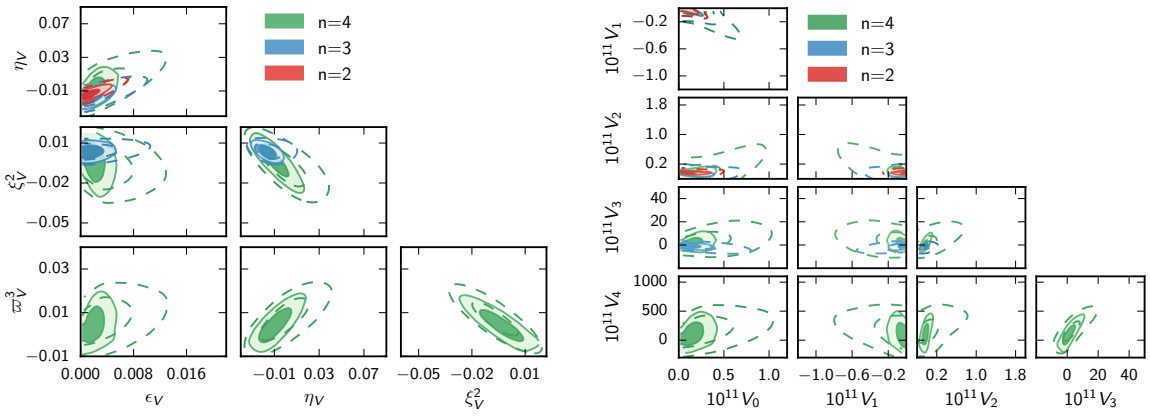

FIGURE A.1: Taylor expansion of $V(\phi)$ at order $n = 2$, 3, and 4 in the observable region, making no assumption about the end of inflation. The left panel shows the parameters that are combinations of Taylor coefficients with flat priors. The right panel shows the parameters that are the Taylor coefficients, obtained here as derived parameters with non-flat priors (in natural units with $\sqrt{8\pi}M_{\rm Pl} = 1$). Dashed contours are *Planck* TT,TE,EE+lowE, while solid contours are *Planck* TT,TE,EE+lowE+lensing+BK15.

First we will try to reconstruct the inflaton potential $V(\phi)$ only in its observable window, making no assumptions about the end of inflation. This is a conservative modelling, motivated by the fact that what happens after the inflaton rolls down beyond this range might not be captured by the simplest descriptions. If we were dealing with more complex inflationary models, such as a waterfall transition involving extra scalar fields, we would require a more complicated treatment. For this analysis we rely on the assumption that the potential is smooth enough inside the observable window to be described by a Taylor expansion up to order four. In the following sections we will also look at the assumption that a Taylor expansion is valid up to the end of inflation.

n	2	3	4
ϵ_V	< 0.0042	< 0.0045	< 0.0048
η_V	$-0.0124^{+0.0033}_{-0.0052}$	$-0.0163^{+0.0057}_{-0.0063}$	$-0.0082^{+0.0096}_{-0.0120}$
ξ^2_V	$\dots$	$0.0036^{+0.0035}_{-0.0037}$	$-0.004^{+0.011}_{-0.009}$
ϖ^3_V	$\dots$	$\dots$	$0.0048^{+0.0052}_{-0.0067}$
τ	$0.0546^{+0.0072}_{-0.0075}$	$0.0559^{+0.0074}_{-0.0080}$	$0.0571^{+0.0077}_{-0.0085}$
n_s	$0.9650^{+0.0042}_{-0.0042}$	$0.9639^{+0.0043}_{-0.0048}$	$0.9623^{+0.0047}_{-0.0050}$
$10^3 \frac{dn_\mathrm{s}}{d\ln k}$	$-0.37^{+0.29}_{-0.19}$	$-7.3^{+7.0}_{-6.7}$	$-1.9^{+9.0}_{-9.2}$
$r_{0.002}$	< 0.060	< 0.063	< 0.069
$\Delta\chi^2_\mathrm{eff}$	$\dots$	$\Delta\chi^2_{3/2} = -0.22$	$\Delta\chi^2_{4/3} = -0.82$

TABLE A.1: Numerical reconstruction of the potential slow-roll parameters *beyond* any slow-roll approximation, when the potential is Taylor-expanded to nth order, using *Planck* TT,TE,EE+lowE+lensing+BK15. We also show the corresponding bounds on some related parameters (here n_s, $dn_\mathrm{s}/d\ln k$, and $r_{0.002}$ are derived from the numerically computed primordial spectra). All error bars are at the 68 % C.L. and all upper bounds at the 95 % C.L.. The effective χ^2 value of model n is given relative to model $n-1$.

We perform the Taylor expansion around the value ϕ_* of the inflaton field, evaluated at the time t_* when the pivot scale $k_* = 0.05\,\mathrm{Mpc}^{-1}$ fulfils the relation $k_* = a(t_*)H(t_*)$. We study three different cases: where the expansion is performed at order $n = 2$, $n = 3$, or $n = 4$. Using the inflationary module of the CLASS code, we compute the primordial spectrum with a full integration of the Fourier mode evolution without assuming slow-roll inflation. However, to speed up convergence of our MCMC chains[1] instead of using the five Taylor coefficients $\{V, V_\phi, \dots, V_{\phi\phi\phi\phi}\}$ we take flat priors on combinations of them matching the definitions of the potential slow-roll parameters $\{\epsilon_V, \eta_V, \xi^2_V, \varpi^3_V\}$. Even when we don't assume the slow-roll approximation, these combinations contribute nearly linearly to the tilt, running, running of the running, etc., of the scalar and tensor spectrum. Thus, they are directly related to observable quantities and well constrained by the data.

The results of this analysis are shown in Fig. A.1 and Table A.1 for $n = 2$, 3, and 4, using two data sets for each: *Planck* TT,TE,EE+lowE alone; or *Planck* TT,TE,EE+lowE+lensing+BK15. We intentionally left lots of white space in the Fig. A.1, as we wanted to compare our results to those presented in the *Planck 2015 results. XX. Constraints on inflation* [265], and so we plotted it over the same parameter ranges as used in that analysis. Compared to previous analysis, we find that error bars on individual parameters have typically been reduced by 30 % thanks to improved polarisation data. Including BK data provides further constraining power, with the error bars on $\{\epsilon_V, \eta_V, \xi^2_V, \varpi^3_V\}$ shrinking by factors of 2 to 4 with respect to the previous paper.

[1] If we were to use flat priors on $\{V, V_\phi, \dots, V_{\phi\phi\phi\phi}\}$, the parameter degeneracies would significantly slow down convergence.

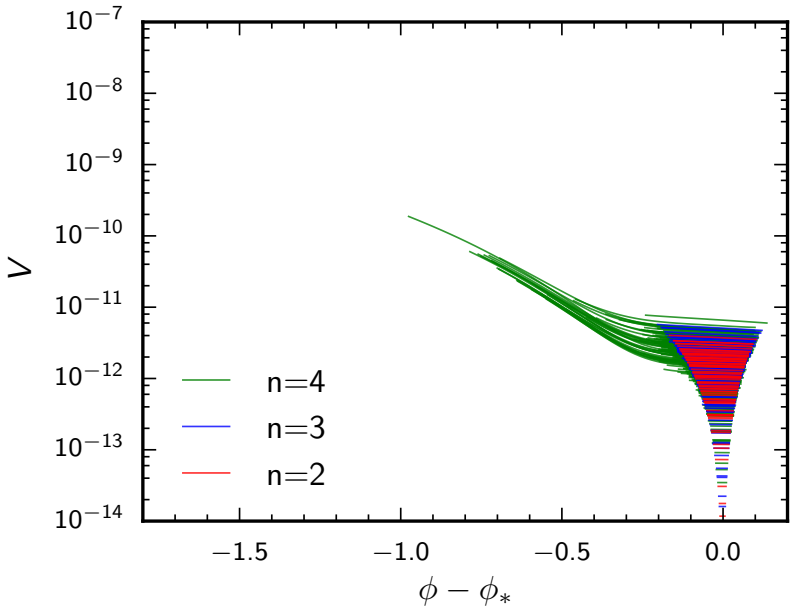

FIGURE A.2: Representative sample of the observable region of inflaton potentials allowed at the 95 % C.L., when the potential is Taylor-expanded at order $n = 2$, 3, and 4 in the observable region, making no assumption about the end of inflation, and using *Planck* TT,TE,EE+lowE+lensing+BK15. We use natural units with $\sqrt{8\pi}M_{\rm Pl} = 1$.

Focussing on the individual parameters, we see that ξ_V^2 and ϖ_V^3 are perfectly compatible with zero, as are $V_{\phi\phi\phi}$ and $V_{\phi\phi\phi\phi}$ (see the contours on the parameters $\{V, V_\phi, \ldots, V_{\phi\phi\phi\phi}\}$ in the right panel of Fig. A.1). As in other sections of the *Planck 2018 results. X. Constraints on inflation* paper, we find no evidence for running or running of the running.

We also observe a decrease of the minimum effective χ^2 when moving from $n = 2$ to $n = 3$, which has decreased with respect to the previous analysis, and is statistically insignificant. This shows that the data do not require anything more complicated than an approximately parabolic shape for the inflaton potential within the observable window. We can check this by looking at the random sample of well-fitting potentials presented in Fig. A.2. We can see in this plot that a few of the plotted potentials for $n = 4$ have a kink and a plateau shape (caused by non-negligible values of $|V_{\phi\phi\phi\phi}|$ still being allowed), however, the lack of improvement in $\chi^2_{\rm eff}$ for $n = 4$ shows that this sub-class of models is by no means preferred over simpler parabolic-like potentials with a negligible $|V_{\phi\phi\phi\phi}|$.

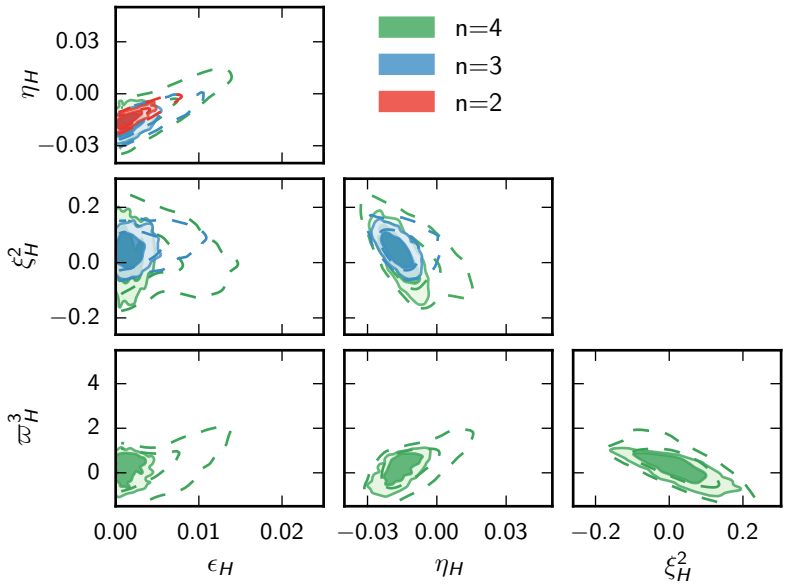

FIGURE A.3: Taylor expansion of $H(\phi)$ at order $n = 2$, 3, and 4 in the observable region, making no assumption about the end of inflation. The parameters are combinations of Taylor coefficients with flat priors. Dashed contours are *Planck* TT,TE,EE+lowE, while solid contours are *Planck* TT,TE,EE+lowE+lensing+BK15.

Taylor expansion of $H(\phi)$ in the observable region

In section 2.3 I discussed that the potential can also be expressed as $H(\phi)$. Thus, to assess the robustness of our method, in this section we repeat the analysis with a Taylor expansion of the Hubble function $H(\phi)$ in the observable window. The difference in this reconstruction with respect to the $V(\phi)$ reconstruction is more than just a choice of priors: for each value of n the new parametrisation covers a slightly different range of potentials, but more significantly it also includes a marginalisation over the uncertainty in the initial value of the derivative $\dot{\phi}$ when the inflaton enters the observable window. In the previous analysis there was the implicit assumption that inflation started well before the observable window, as $\dot{\phi}$ was assumed to have reached the inflaton attractor solution. However, in the analysis based on $H(\phi)$ inflation models with a minimal duration are not excluded by the priors, and thus we cover a broader range of models.

Our results are presented in Table A.2 and Fig. A.3. As in the previous section, we compare our results to [265], where we notice a significant improvement, where bounds on the $n = 4$ parameters are typically 3 to 4 times stronger compared. The main improvements come from the better polarisation data and the inclusion of the BK likelihood.

As before, apart from showing the bounds on individual parameters, we also show a sample of well-fitting potentials in Fig. A.4, where we have a lot of white space as the bounds were deliberately maintained as the ones shown in [265]. In older analysis for $n = 4$ the best-fitting models included many scenarios starting with a fast-roll stage, producing a tail with large $V(\phi)$ before pivot-scale crossing. These models are now excluded by better polarisation data

n	2	3	4
ϵ_H	< 0.0041	< 0.0046	< 0.0041
η_H	$-0.0139^{+0.0026}_{-0.0038}$	$-0.0170^{+0.0044}_{-0.0048}$	$-0.0158^{+0.0057}_{-0.0056}$
ξ^2_H	...	$0.046^{+0.043}_{-0.045}$	$0.021^{+0.071}_{-0.076}$
ϖ^3_H	...	...	$0.16^{+0.64}_{-0.37}$
τ	$0.0548^{+0.0075}_{-0.0074}$	$0.0556^{+0.0076}_{-0.0078}$	$0.0563^{+0.0073}_{-0.0078}$
n_s	$0.9651^{+0.0040}_{-0.0044}$	$0.9637^{+0.0042}_{-0.0046}$	$0.9637^{+0.0042}_{-0.0048}$
$10^3 \frac{dn_\mathrm{s}}{d\ln k}$	$-0.25^{+0.20}_{-0.12}$	$-7.5^{+7.0}_{-6.7}$	$-5.1^{+7.8}_{-8.1}$
$r_{0.002}$	< 0.059	< 0.065	< 0.057
$\Delta\chi^2_\mathrm{eff}$	...	$\Delta\chi^2_{3/2} = -1.60$	$\Delta\chi^2_{4/3} = -2.32$

TABLE A.2: Numerical reconstruction of the Hubble slow-roll parameters *beyond* any slow-roll approximation, using *Planck* TT,TE,EE+lowE+lensing+BK15. We also show the corresponding bounds on some related parameters (here n_s, $dn_\mathrm{s}/d\ln k$, and $r_{0.002}$ are derived from the numerically computed primordial spectra). All error bars are at the 68 % C.L. and all upper bounds at the 95 % C.L.. The effective χ^2 value of model n is given relative to model $n-1$.

and tensor constraints.

We can see in Table A.2 that going beyond the parabolic approximation for $H(\phi)$ does not improve the goodness-of-fit: the $\Delta\chi^2$s between $n = 2$, $n = 3$, and $n = 4$ are negligible. Furthermore, as in the previous section, we see that the parameters ξ^2_H and ϖ^3_H, related to $H_{\phi\phi\phi}$ and $H_{\phi\phi\phi\phi}$, are compatible with zero.

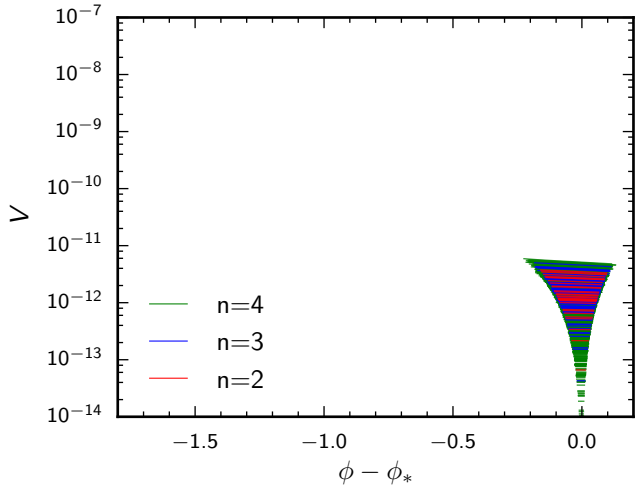

FIGURE A.4: Representative sample of the observable region of inflaton potentials allowed at the 95 % C.L., inferred from $H(\phi)$ when that function is Taylor-expanded at order $n = 2$, 3, and 4 in the observable region, making no assumption about the end of inflation, and using *Planck* TT,TE,EE+lowE+lensing+BK15. We use natural units with $\sqrt{8\pi}M_\mathrm{Pl} = 1$.

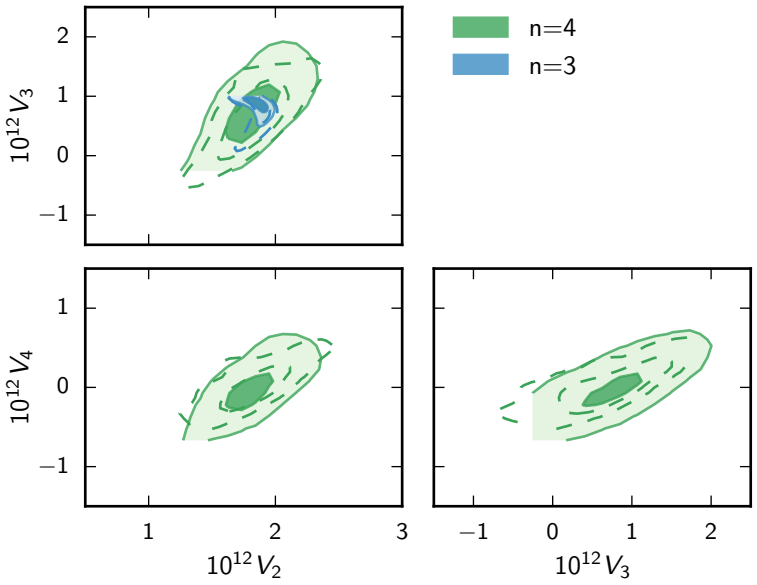

FIGURE A.5: Taylor expansion of the full $V(\phi)$ at order $n = 3$ and 4, trusted until the end of inflation. The parameters are the Taylor coefficients with flat priors. Dashed contours are *Planck* TT,TE,EE+lowE, while solid contours are *Planck* TT,TE,EE+lowE+lensing+BK15. We use natural units with $\sqrt{8\pi}M_{\rm Pl} = 1$.

Taylor expansion of full $V(\phi)$

As a final analysis, we will use less conservative assumptions than in the previous subsections. We switch to the assumption that the inflaton potential is very smooth not only within its observable window, but also until the end of inflation, such that its whole shape can be captured by a Taylor expansion. We make the further assumption that inflation ends when the first slow-roll condition (defined in 2.22 is violated ($\epsilon_V = 1$), without invoking any other field. To completely specify this class of models, we need to fix the number of e-folds between Hubble crossing of the pivot scale and the end of inflation to $N_* = 55$.

The analysis is similar to that performed in the previous sections, except that there is an extra step in the CLASS inflationary module, where it integrates the background equations until the end of inflation, goes backwards in time by 55 e-folds, and imposes that the Hubble crossing for the pivot scale $k_* = 0.05\,\mathrm{Mpc}^{-1}$ matches that time.

By imposing the e-fold condition, these models are much more constrained than those of the previous sections, and thus the constraining power is then sufficient for running the MCMC chains directly with flat priors on $\{V, V_\phi, \ldots, V_{\phi\phi\phi\phi}\}$. Our results are presented in Figs. A.5 and A.6 and in Table A.3.

As we have fixed N_*, the models with a purely quadratic potential have a fixed value of the tilt and tensor-to-scalar ratio, numerically computed as$n_s = 0.963$ and $r_{0.002} = 0.136$. However, such a large r is in tension with the *Planck*+BK data (and even with the *Planck*alone data). Thus, the effective χ^2 is poor in the $n = 2$ case and improves considerably when adding some freedom in going to $n = 3$. Moreover, the presence of an additional cubic term allows us to reach smaller values of the tensor-to-scalar ratio for roughly the same scalar tilt, and

n	2	3	4
$10^{12}V_2$	$1.631^{+0.022}_{-0.022}$	$1.81^{+0.12}_{-0.06}$	$1.86^{+0.25}_{-0.23}$
$10^{12}V_3$	...	$0.89^{+0.10}_{-0.03}$	$0.85^{+0.46}_{-0.64}$
$10^{12}V_4$	...	...	$0.044^{+0.26}_{-0.35}$
τ	$0.0518^{+0.0066}_{-0.0066}$	$0.0501^{+0.0078}_{-0.0069}$	$0.05628^{+0.0075}_{-0.0087}$
n_s	0.963	$0.9599^{+0.0034}_{-0.0018}$	$0.9656^{+0.0035}_{-0.0043}$
$10^3 dn_\mathrm{s}/d\ln k$	$-0.6731^{+0.0005}_{-0.0005}$	$-0.534^{+0.079}_{-0.096}$	$-0.74^{+0.16}_{-0.13}$
$r_{0.002}$	0.136	$0.066^{+0.010}_{-0.016}$	$0.042^{+0.009}_{-0.014}$
$\Delta\chi^2_\mathrm{eff}$	...	$\Delta\chi^2_{3/2} = -13.18$	$\Delta\chi^2_{4/3} = -3.50$

TABLE A.3: Numerical reconstruction of the potential parameters *beyond* any slow-roll approximation, when the potential is Taylor-expanded to nth order, trusted until the end of inflation, and using *Planck* high-ℓ TT,TE,EE+lowE+lensing+BK15. We also show the corresponding bounds on some related parameters (here n_s, $dn_\mathrm{s}/d\ln k$, and $r_{0.002}$ are derived from the numerically computed primordial spectra). All error bars are at the 68 % C.L. and all upper bounds at the 95 % C.L.. The effective χ^2 value of model n is given relative to model $n-1$.

therefore lowers χ^2_eff by more than 13. When we further expand with a quartic term we find no significant improvement in the goodness of fit, and the coefficient of the ϕ^4 term is consistent with zero.

Our findings are consistent with the global picture presented in **[I]**, where it seems that *Planck* data prefer potentials which are concave in the observable window. The blue and green curves in the lower left panel of Fig. A.6 illustrate the preference of the *Planck*+lensing+BK15 data for potentials with an inflection point. The models appear qualitatively similar to scalar field potentials associated with spontaneous symmetry breaking models, hilltop models, new inflation, and natural inflation, to name a few.

In our analysis, the value of the scalar tilt running is always very precisely constrained around a value of $dn_\mathrm{s}/d\ln k \simeq -6\times10^{-4}$. This was to be expected, as these bounds are not imposed directly by the data, but rather by the class of inflationary potentials considered here, with potential parameters fixed by observational bounds on the *amplitude* and *tilt* of the scalar and tensor spectra. This means that the running is not directly measured, instead it is predicted as a function of the scalar/tensor amplitudes and scalar tilt.

This final point shows us that if future combinations of CMB and large-scale structure data with a wide lever arm in wavenumber space could become directly sensitive to such tiny values,we would potentially be able to confirm or rule out a very large class of currently successful inflationary models.

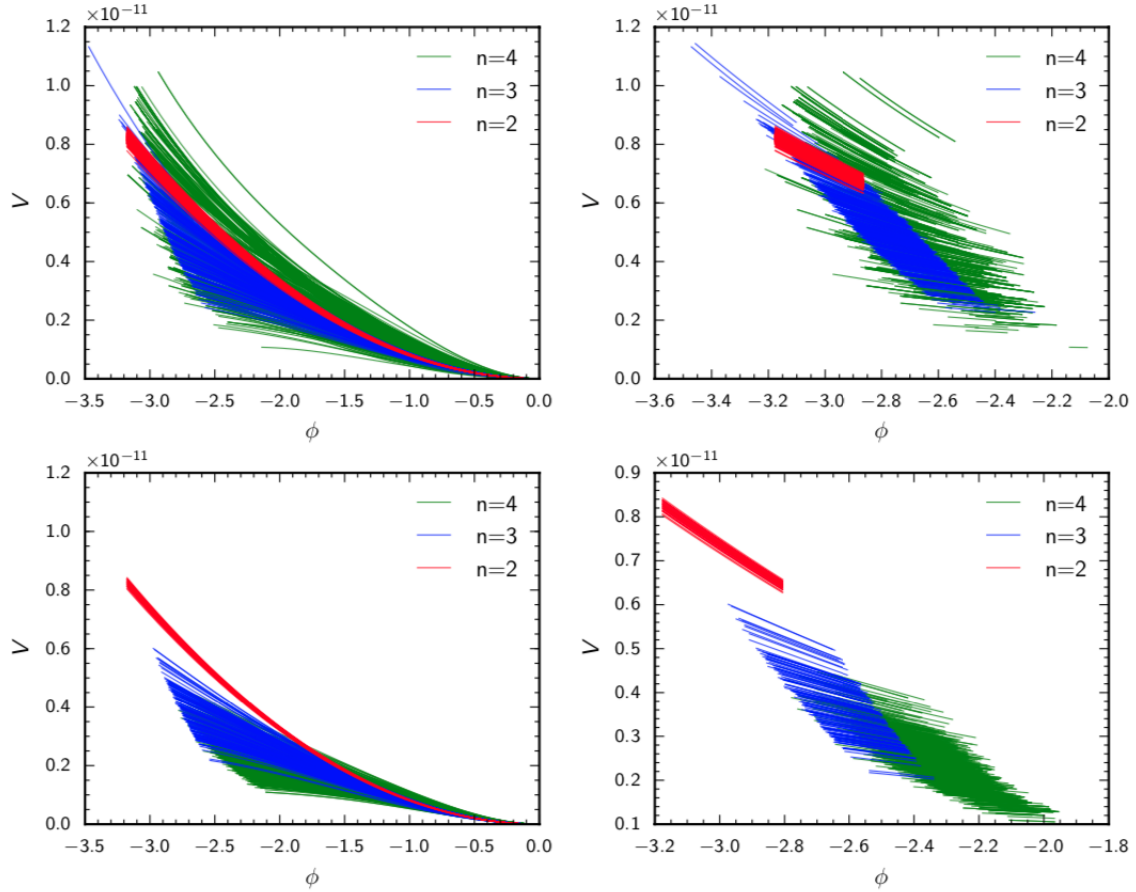

FIGURE A.6: Representative sample of the inflaton potentials allowed at the 95 %C.L., when the potential is Taylor-expanded at order $n = 2$, 3, and 4 and trusted until the end of inflation, and under the assumption of $N_* = 55$ e-folds of inflation between Hubble-radius crossing for the pivot scale and the end of inflation. *Left panels:* Full potential from the beginning of the observable window until the end of inflation. *Right:* Zoom on the observable window directly constrained by inflation. *Top: Planck* TT,TE,EE+lowE. *Bottom: Planck* TT,TE,EE+lowE+lensing+BK15. We use natural units with $\sqrt{8\pi}M_{\rm Pl} = 1$.

Bibliography

[1] Y. Akrami et al. "Planck 2018 results. X. Constraints on inflation". In: (July 17, 2018). arXiv: http://arxiv.org/abs/1807.06211v2 [astro-ph.CO].

[2] Thejs Brinckmann, Deanna C. Hooper, Maria Archidiacono, et al. "The promising future of a robust cosmological neutrino mass measurement". In: *JCAP* 1901 (2019), p. 059. DOI: 10.1088/1475-7516/2019/01/059. arXiv: 1808.05955 [astro-ph.CO].

[3] Maria Archidiacono, Deanna C. Hooper, Riccardo Murgia, et al. "Constraining Dark Matter – Dark Radiation interactions with CMB, BAO, and Lyman-α". In: (2019). arXiv: 1907.01496 [astro-ph.CO].

[4] Nils Schöneberg, Julien Lesgourgues, and Deanna C. Hooper. "The BAO+BBN take on the Hubble tension". In: (2019). arXiv: 1907.11594 [astro-ph.CO].

[5] Dmitry S. Gorbunov and Valery A. Rubakov. *Introduction to the theory of the early universe: Hot big bang theory*. Hackensack: World Scientific, 2011. URL: http://www.DESY.eblib.com/patron/FullRecord.aspx?p=737614.

[6] P. Coles and F. Lucchin. *Cosmology: The Origin and evolution of cosmic structure*. 1995.

[7] Daniel Baumann. "Cosmology: Part III Mathematical Tripos". Lecture Notes. 2013. URL: http://www.damtp.cam.ac.uk/user/db275/Cosmology/Lectures.pdf.

[8] Vivian Poulin. "Gravitative und elektromagnetische Signaturen von massiven Relikten in Kosmologie". Dissertation. Aachen: RWTH Aachen University, L'ecole doctorale de physique de Grenoble, 2017. DOI: 10.18154/RWTH-2018-225652. URL: http://publications.rwth-aachen.de/record/728431.

[9] D. J. Fixsen et al. "Cosmic microwave background dipole spectrum measured by the COBE FIRAS". In: *Astrophys. J.* 420 (1994), p. 445. DOI: 10.1086/173575.

[10] C. L. Bennett et al. "Nine-Year Wilkinson Microwave Anisotropy Probe (WMAP) Observations: Final Maps and Results". In: *Astrophys. J. Suppl.* 208 (2013), p. 20. DOI: 10.1088/0067-0049/208/2/20. arXiv: 1212.5225 [astro-ph.CO].

[11] Y. Akrami et al. "Planck 2018 results. I. Overview and the cosmological legacy of Planck". In: (July 17, 2018). arXiv: 1807.06205 [astro-ph.CO].

[12] Henrietta S. Leavitt and Edward C. Pickering. "Periods of 25 Variable Stars in the Small Magellanic Cloud". In: *Harvard Obs. Circ.* 173 (1912), pp. 1–3.

[13] E. P. Hubble. "Extragalactic nebulae". In: *Astrophys. J.* 64 (1926), pp. 321–369. DOI: 10.1086/143018.

[14] Edwin Hubble. "A relation between distance and radial velocity among extra-galactic nebulae". In: *Proc. Nat. Acad. Sci.* 15 (1929), pp. 168–173. DOI: 10.1073/pnas.15.3.168.

[15] M. Betoule et al. "Improved cosmological constraints from a joint analysis of the SDSS-II and SNLS supernova samples". In: *Astron. Astrophys.* 568 (2014), A22. DOI: 10.1051/0004-6361/201423413. arXiv: 1401.4064 [astro-ph.CO].

[16] Adam G. Riess et al. "Observational evidence from supernovae for an accelerating universe and a cosmological constant". In: *Astron. J.* 116 (1998), pp. 1009–1038. DOI: 10.1086/300499. arXiv: astro-ph/9805201 [astro-ph].

[17] Pierre Astier and Reynald Pain. "Observational Evidence of the Accelerated Expansion of the Universe". In: *Comptes Rendus Physique* 13 (2012), pp. 521–538. DOI: 10.1016/j.crhy.2012.04.009. arXiv: 1204.5493 [astro-ph.CO].

[18] Albert Einstein. "The Foundation of the General Theory of Relativity". In: *Annalen Phys.* 49 (1916). [Annalen Phys.14,517(2005)], pp. 769–822. DOI: 10.1002/andp.200590044,10.1002/andp.19163540702.

[19] N. Aghanim et al. "Planck 2018 results. VI. Cosmological parameters". In: (July 17, 2018). arXiv: 1807.06209 [astro-ph.CO].

[20] Steven Weinberg. *The First Three Minutes. A Modern View of the Origin of the Universe*. 1977. ISBN: 0465024378, 9780465024377. URL: http://www.amazon.com/The-First-Three-Minutes-Universe/dp/0465024378.

[21] J. C. Kapteyn. "First Attempt at a Theory of the Arrangement and Motion of the Sidereal System". In: *Astrophys. J.* 55 (1922), pp. 302–328. DOI: 10.1086/142670.

[22] F. Zwicky. "On the Masses of Nebulae and of Clusters of Nebulae". In: *Astrophys. J.* 86 (1937), pp. 217–246. DOI: 10.1086/143864.

[23] F. Zwicky. "Die Rotverschiebung von extragalaktischen Nebeln". In: *Helv. Phys. Acta* 6 (1933). [Gen. Rel. Grav.41,207(2009)], pp. 110–127. DOI: 10.1007/s10714-008-0707-4.

[24] R. Irion. "VERA RUBIN PROFILE: The Bright Face Behind the Dark Sides of Galaxies". In: *Science* 295.5557 (2002), pp. 960–961. DOI: 10.1126/science.295.5557.960.

[25] Vera C. Rubin, W. Kent Ford Jr., Norbert Thonnard, et al. "Rotational properties of 23 SB galaxies". In: *Astrophys. J.* 261 (1982), p. 439. DOI: 10.1086/160355.

[26] Vera C. Rubin and W. Kent Ford Jr. "Rotation of the Andromeda Nebula from a Spectroscopic Survey of Emission Regions". In: *Astrophys. J.* 159 (1970), pp. 379–403. DOI: 10.1086/150317.

[27] K. G. Begeman, A. H. Broeils, and R. H. Sanders. "Extended rotation curves of spiral galaxies: Dark haloes and modified dynamics". In: *Mon. Not. Roy. Astron. Soc.* 249 (1991), p. 523.

[28] Douglas Clowe, Marusa Bradac, Anthony H. Gonzalez, et al. "A direct empirical proof of the existence of dark matter". In: *Astrophys. J.* 648 (2006), pp. L109–L113. DOI: 10.1086/508162. arXiv: astro-ph/0608407 [astro-ph].

[29] Saniya Heeba, Felix Kahlhoefer, and Patrick Stöcker. "Freeze-in production of decaying dark matter in five steps". In: *JCAP* 1811.11 (2018), p. 048. DOI: 10.1088/1475-7516/2018/11/048. arXiv: 1809.04849 [hep-ph].

[30] Giorgio Arcadi, Maíra Dutra, Pradipta Ghosh, et al. "The waning of the WIMP? A review of models, searches, and constraints". In: *Eur. Phys. J.* C78.3 (2018), p. 203. DOI: 10.1140/epjc/s10052-018-5662-y. arXiv: 1703.07364 [hep-ph].

[31] David J. E. Marsh. "Axions and ALPs: a very short introduction". In: *Proceedings, 13th Patras Workshop on Axions, WIMPs and WISPs, (PATRAS 2017): Thessaloniki, Greece, 15 May 2017 - 19, 2017*. 2018, pp. 59–74. DOI: 10.3204/DESY-PROC-2017-02/marsh_david. arXiv: 1712.03018 [hep-ph].

[32] Misao Sasaki, Teruaki Suyama, Takahiro Tanaka, et al. "Primordial black holes: perspectives in gravitational wave astronomy". In: *Class. Quant. Grav.* 35.6 (2018), p. 063001. DOI: 10.1088/1361-6382/aaa7b4. arXiv: 1801.05235 [astro-ph.CO].

[33] M. Drewes et al. "A White Paper on keV Sterile Neutrino Dark Matter". In: *JCAP* 1701.01 (2017), p. 025. DOI: 10.1088/1475-7516/2017/01/025. arXiv: 1602.04816 [hep-ph].

[34] Alexei A. Starobinsky. "Spectrum of relict gravitational radiation and the early state of the universe". In: *JETP Lett.* 30 (1979). [Pisma Zh. Eksp. Teor. Fiz.30,719(1979)], pp. 682–685.

[35] Alan H. Guth. "The Inflationary Universe: A Possible Solution to the Horizon and Flatness Problems". In: *Phys. Rev.* D23 (1981), pp. 347–356. DOI: 10.1103/PhysRevD.23.347.

[36] Andrei D. Linde. "A New Inflationary Universe Scenario: A Possible Solution of the Horizon, Flatness, Homogeneity, Isotropy and Primordial Monopole Problems". In: *Phys. Lett.* B108 (1982), pp. 389–393. DOI: 10.1016/0370-2693(82)91219-9.

[37] Andreas Albrecht and Paul J. Steinhardt. "Cosmology for Grand Unified Theories with Radiatively Induced Symmetry Breaking". In: *Phys. Rev. Lett.* 48 (1982), pp. 1220–1223. DOI: 10.1103/PhysRevLett.48.1220.

[38] Julien Lesgourgues. "Inflationary Cosmology". In: *Lecture notes of the doctoral school "3ieme cycle de physique de Suisse romande"* (2006).

[39] Daniel Baumann. "Inflation". In: *Physics of the large and the small, TASI 09, proceedings of the Theoretical Advanced Study Institute in Elementary Particle Physics, Boulder, Colorado, USA, 1-26 June 2009*. 2011, pp. 523–686. DOI: 10.1142/9789814327183_0010. arXiv: 0907.5424 [hep-th]. URL: https://inspirehep.net/record/827549/files/arXiv:0907.5424.pdf.

[40] Dmitry S. Gorbunov and Valery A. Rubakov. *Introduction to the theory of the early universe: Cosmological perturbations and inflationary theory*. 2011. DOI: 10.1142/7874. URL: http://www.DESY.eblib.com/patron/FullRecord.aspx?p=737613.

[41] Steven Weinberg. *Cosmology*. 2008. URL: http://www.oup.com/uk/catalogue/?ci=9780198526827.

[42] Andrew R. Liddle, Paul Parsons, and John D. Barrow. "Formalizing the slow roll approximation in inflation". In: *Phys. Rev.* D50 (1994), pp. 7222–7232. DOI: 10.1103/PhysRevD.50.7222. arXiv: astro-ph/9408015 [astro-ph].

[43] Chung-Pei Ma and Edmund Bertschinger. "Cosmological perturbation theory in the synchronous and conformal Newtonian gauges". In: *Astrophys. J.* 455 (1995), pp. 7–25. DOI: 10.1086/176550. arXiv: astro-ph/9506072 [astro-ph].

[44] Julien Lesgourgues. "Cosmological Perturbations". In: *Proceedings, Theoretical Advanced Study Institute in Elementary Particle Physics: Searching for New Physics at Small and Large Scales (TASI 2012): Boulder, Colorado, June 4-29, 2012*. 2013, pp. 29–97. DOI: 10.1142/9789814525220_0002. arXiv: 1302.4640 [astro-ph.CO]. URL: https://inspirehep.net/record/1220222/files/arXiv:1302.4640.pdf.

[45] James M. Bardeen. "Gauge-invariant cosmological perturbations". In: *Physical Review D* 22.8 (1980), pp. 1882–1905. DOI: 10.1103/physrevd.22.1882.

[46] E. Lifshitz. "Republication of: On the gravitational stability of the expanding universe". In: *General Relativity and Gravitation* 49.2 (2017). DOI: 10.1007/s10714-016-2165-8.

[47] V Mukhanov. "Theory of cosmological perturbations". In: *Physics Reports* 215.5-6 (1992), pp. 203–333. DOI: 10.1016/0370-1573(92)90044-z.

[48] J. R. Bond and G. Efstathiou. "Cosmic background radiation anisotropies in universes dominated by nonbaryonic dark matter". In: *The Astrophysical Journal* 285 (1984), p. L45. DOI: 10.1086/184362.

[49] J. R. Bond and G. Efstathiou. "The statistics of cosmic background radiation fluctuations". In: *Monthly Notices of the Royal Astronomical Society* 226.3 (1987), pp. 655–687. DOI: 10.1093/mnras/226.3.655.

[50] Arthur Kosowsky. "Cosmic microwave background polarization". In: *Annals Phys.* 246 (1996), pp. 49–85. DOI: 10.1006/aphy.1996.0020. arXiv: astro-ph/9501045 [astro-ph].

[51] Uros Seljak and Matias Zaldarriaga. "A Line of sight integration approach to cosmic microwave background anisotropies". In: *Astrophys. J.* 469 (1996), pp. 437–444. DOI: 10.1086/177793. arXiv: astro-ph/9603033 [astro-ph].

[52] Matias Zaldarriaga and Uros Seljak. "An all sky analysis of polarization in the microwave background". In: *Phys. Rev.* D55 (1997), pp. 1830–1840. DOI: 10.1103/PhysRevD.55.1830. arXiv: astro-ph/9609170 [astro-ph].

[53] Diego Blas, Julien Lesgourgues, and Thomas Tram. "The Cosmic Linear Anisotropy Solving System (CLASS) II: Approximation schemes". In: *JCAP* 1107 (2011), p. 034. DOI: 10.1088/1475-7516/2011/07/034. arXiv: 1104.2933 [astro-ph.CO].

[54] Antony Lewis, Anthony Challinor, and Anthony Lasenby. "Efficient computation of CMB anisotropies in closed FRW models". In: *Astrophys. J.* 538 (2000), pp. 473–476. DOI: 10.1086/309179. arXiv: astro-ph/9911177 [astro-ph].

[55] G. Gamow. "Expanding universe and the origin of elements". In: *Phys. Rev.* 70 (1946), pp. 572–573. DOI: 10.1103/PhysRev7.0.572.

[56] R. A. Alpher and R. C. Herman. "The origin and abundance distribution of the elements". In: *Ann. Rev. Nucl. Part. Sci.* 2 (1953), pp. 1–40. DOI: 10.1146/annurev.ns.02.120153.000245.

[57] Arno A. Penzias and Robert Woodrow Wilson. "A Measurement of excess antenna temperature at 4080-Mc/s". In: *Astrophys. J.* 142 (1965), pp. 419–421. DOI: 10.1086/148307.

[58] R. H. Dicke, P. J. E. Peebles, P. G. Roll, et al. "Cosmic Black-Body Radiation". In: *Astrophys. J.* 142 (1965), pp. 414–419. DOI: 10.1086/148306.

[59] P. J. E. Peebles and J. T. Yu. "Primeval adiabatic perturbation in an expanding universe". In: *Astrophys. J.* 162 (1970), pp. 815–836. DOI: 10.1086/150713.

[60] Antony Lewis and Anthony Challinor. "Weak gravitational lensing of the cmb". In: *Phys. Rept.* 429 (2006), pp. 1–65. DOI: 10.1016/j.physrep.2006.03.002. arXiv: astro-ph/0601594 [astro-ph].

[61] Luca Amendola et al. "Cosmology and fundamental physics with the Euclid satellite". In: *Living Rev. Rel.* 16 (2013), p. 6. DOI: 10.12942/lrr-2013-6. arXiv: 1206.1225 [astro-ph.CO].

[62] Paul A. Abell et al. "LSST Science Book, Version 2.0". In: (2009). DOI: 10.2172/1156415. arXiv: 0912.0201 [astro-ph.IM].

[63] Ryuichi Takahashi, Masanori Sato, Takahiro Nishimichi, et al. "Revising the Halofit Model for the Nonlinear Matter Power Spectrum". In: *Astrophys. J.* 761 (2012), p. 152. DOI: 10.1088/0004-637X/761/2/152. arXiv: 1208.2701 [astro-ph.CO].

[64] Roger Lynds. "The Absorption-Line Spectrum of 4c 05.34". In: *The Astrophysical Journal* 164 (1971), p. L73. DOI: 10.1086/180695.

[65] David H. Weinberg, Romeel Dave, Neal Katz, et al. "The Lyman - alpha forest as a cosmological tool". In: *AIP Conf. Proc.* 666.1 (2003). [,21(2005)], pp. 157–169. DOI: 10.1063/1.1581786. arXiv: astro-ph/0301186 [astro-ph].

[66] Matteo Viel, Julien Lesgourgues, Martin G. Haehnelt, et al. "Constraining warm dark matter candidates including sterile neutrinos and light gravitinos with WMAP and the Lyman-alpha forest". In: *Phys. Rev.* D71 (2005), p. 063534. DOI: 10.1103/PhysRevD.71.063534. arXiv: astro-ph/0501562 [astro-ph].

[67] Riccardo Murgia, Alexander Merle, Matteo Viel, et al. ""Non-cold" dark matter at small scales: a general approach". In: *JCAP* 1711 (2017), p. 046. DOI: 10.1088/1475-7516/2017/11/046. arXiv: 1704.07838 [astro-ph.CO].

[68] Paul Bode, Jeremiah P. Ostriker, and Neil Turok. "Halo formation in warm dark matter models". In: *Astrophys. J.* 556 (2001), pp. 93–107. DOI: 10.1086/321541. arXiv: astro-ph/0010389 [astro-ph].

[69] Riccardo Murgia, Vid Irsic, and Matteo Viel. "Novel constraints on noncold, nonthermal dark matter from Lyman-α forest data". In: *Phys. Rev.* D98.8 (2018), p. 083540. DOI: 10.1103/PhysRevD.98.083540. arXiv: 1806.08371 [astro-ph.CO].

[70] P. A. R. Ade et al. "Planck 2015 results. XIII. Cosmological parameters". In: *Astron. Astrophys.* 594 (2016), A13. DOI: 10.1051/0004-6361/201525830. arXiv: 1502.01589 [astro-ph.CO].

[71] Matteo Viel, George D. Becker, James S. Bolton, et al. "Warm dark matter as a solution to the small scale crisis: New constraints from high redshift Lyman-α forest data". In: *Phys. Rev.* D88 (2013), p. 043502. DOI: 10.1103/PhysRevD.88.043502. arXiv: 1306.2314 [astro-ph.CO].

[72] Benjamin Audren, Julien Lesgourgues, Karim Benabed, et al. "Conservative Constraints on Early Cosmology: an illustration of the Monte Python cosmological parameter inference code". In: *JCAP* 1302 (2013), p. 001. DOI: 10.1088/1475-7516/2013/02/001. arXiv: 1210.7183 [astro-ph.CO].

[73] Thejs Brinckmann and Julien Lesgourgues. "MontePython 3: boosted MCMC sampler and other features". In: *Physics of the Dark Universe* 24 (Apr. 19, 2018), p. 100260. ISSN: 2212-6864. DOI: 10.1016/j.dark.2018.100260. arXiv: http://arxiv.org/abs/1804.07261v2 [astro-ph.CO].

[74] R. Webster and M.A. Oliver. *Geostatistics for Environmental Scientists*. Statistics in Practice. Wiley, 2007. ISBN: 9780470517260. URL: https://books.google.de/books?id=WBwSyvIvNY8C.

[75] Graziano Rossi, Christophe Yéche, Nathalie Palanque-Delabrouille, et al. "Constraints on dark radiation from cosmological probes". In: *Phys. Rev.* D92.6 (2015), p. 063505. DOI: 10.1103/PhysRevD.92.063505. arXiv: 1412.6763 [astro-ph.CO].

[76] Mathias Garny, Thomas Konstandin, Laura Sagunski, et al. "Lyman-α forest constraints on interacting dark sectors". In: *JCAP* 1809.09 (2018), p. 011. DOI: 10.1088/1475-7516/2018/09/011. arXiv: 1805.12203 [astro-ph.CO].

[77] Ya. B. Zeldovich and R. A. Sunyaev. "The interaction of matter and radiation in a hot-model universe". In: *Astrophysics and Space Science* 4.3 (1969), pp. 301–316. DOI: 10.1007/bf00661821.

[78] Jens Chluba. "Distinguishing different scenarios of early energy release with spectral distortions of the cosmic microwave background". In: *Mon. Not. Roy. Astron. Soc.* 436 (2013), pp. 2232–2243. DOI: 10.1093/mnras/stt1733. arXiv: 1304.6121 [astro-ph.CO].

[79] Vivian Poulin, Pasquale D. Serpico, and Julien Lesgourgues. "A fresh look at linear cosmological constraints on a decaying dark matter component". In: *JCAP* 1608.08 (2016), p. 036. DOI: 10.1088/1475-7516/2016/08/036. arXiv: 1606.02073 [astro-ph.CO].

[80] James A. D. Diacoumis and Yvonne Y. Y. Wong. "Using CMB spectral distortions to distinguish between dark matter solutions to the small-scale crisis". In: *JCAP* 1709.09 (2017), p. 011. DOI: 10.1088/1475-7516/2017/09/011. arXiv: 1707.07050 [astro-ph.CO].

[81] Tomohiro Nakama, Jens Chluba, and Marc Kamionkowski. "Shedding light on the small-scale crisis with CMB spectral distortions". In: *Phys. Rev.* D95.12 (2017), p. 121302. DOI: 10.1103/PhysRevD.95.121302. arXiv: 1703.10559 [astro-ph.CO].

[82] Christian T. Byrnes, Philippa S. Cole, and Subodh P. Patil. "Steepest growth of the power spectrum and primordial black holes". In: *Journal of Cosmology and Astroparticle*

Physics 2018.02 (2018), pp. 019–019. ISSN: 1475-7516. DOI: 10.1088/1475-7516/2018/02/019. arXiv: 1811.11158 [astro-ph.CO].

[83] Tracy R. Slatyer and Chih-Liang Wu. "Early-Universe constraints on dark matter-baryon scattering and their implications for a global 21 cm signal". In: *Phys. Rev.* D98.2 (2018), p. 023013. DOI: 10.1103/PhysRevD.98.023013. arXiv: 1803.09734 [astro-ph.CO].

[84] Laurence Perotto, Julien Lesgourgues, Steen Hannestad, et al. "Probing cosmological parameters with the CMB: Forecasts from full Monte Carlo simulations". In: *JCAP* 0610 (2006), p. 013. DOI: 10.1088/1475-7516/2006/10/013. arXiv: astro-ph/0606227 [astro-ph].

[85] A. Kogut et al. "The Primordial Inflation Explorer (PIXIE): A Nulling Polarimeter for Cosmic Microwave Background Observations". In: *JCAP* 1107 (2011), p. 025. DOI: 10.1088/1475-7516/2011/07/025. arXiv: 1105.2044 [astro-ph.CO].

[86] D. J. Fixsen, E. S. Cheng, J. M. Gales, et al. "The Cosmic Microwave Background Spectrum from the FullCOBEFIRAS Data Set". In: *The Astrophysical Journal* 473.2 (1996), pp. 576–587. DOI: 10.1086/178173.

[87] Jens Chluba and Donghui Jeong. "Teasing bits of information out of the CMB energy spectrum". In: *Mon. Not. Roy. Astron. Soc.* 438.3 (2014), pp. 2065–2082. DOI: 10.1093/mnras/stt2327. arXiv: 1306.5751 [astro-ph.CO].

[88] Mark Vogelsberger, Shy Genel, Volker Springel, et al. "Introducing the Illustris Project: Simulating the coevolution of dark and visible matter in the Universe". In: *Mon. Not. Roy. Astron. Soc.* 444.2 (2014), pp. 1518–1547. DOI: 10.1093/mnras/stu1536. arXiv: 1405.2921 [astro-ph.CO].

[89] Joop Schaye et al. "The EAGLE project: Simulating the evolution and assembly of galaxies and their environments". In: *Mon. Not. Roy. Astron. Soc.* 446 (2015), pp. 521–554. DOI: 10.1093/mnras/stu2058. arXiv: 1407.7040 [astro-ph.GA].

[90] Alyson M. Brooks and Adi Zolotov. "Why Baryons Matter: The Kinematics of Dwarf Spheroidal Satellites". In: *Astrophys. J.* 786 (2014), p. 87. DOI: 10.1088/0004-637X/786/2/87. arXiv: 1207.2468 [astro-ph.CO].

[91] David H. Weinberg, James S. Bullock, Fabio Governato, et al. "Cold dark matter: controversies on small scales". In: *Proc. Nat. Acad. Sci.* 112 (2015), pp. 12249–12255. DOI: 10.1073/pnas.1308716112. arXiv: 1306.0913 [astro-ph.CO].

[92] James S. Bullock and Michael Boylan-Kolchin. "Small-Scale Challenges to the ΛCDM Paradigm". In: *Ann. Rev. Astron. Astrophys.* 55 (2017), pp. 343–387. DOI: 10.1146/annurev-astro-091916-055313. arXiv: 1707.04256 [astro-ph.CO].

[93] Anatoly A. Klypin, Andrey V. Kravtsov, Octavio Valenzuela, et al. "Where are the missing Galactic satellites?" In: *Astrophys. J.* 522 (1999), pp. 82–92. DOI: 10.1086/307643. arXiv: astro-ph/9901240 [astro-ph].

[94] B. Moore, S. Ghigna, F. Governato, et al. "Dark matter substructure within galactic halos". In: *Astrophys. J.* 524 (1999), pp. L19–L22. DOI: 10.1086/312287. arXiv: astro-ph/9907411 [astro-ph].

[95] Ricardo A. Flores and Joel R. Primack. "Observational and theoretical constraints on singular dark matter halos". In: *Astrophys. J.* 427 (1994), pp. L1–4. DOI: 10.1086/187350. arXiv: astro-ph/9402004 [astro-ph].

[96] Ben Moore. "Evidence against dissipation-less dark matter from observations of galaxy haloes". In: *Nature* 370.6491 (1994), p. 629.

[97] Michael Boylan-Kolchin, James S. Bullock, and Manoj Kaplinghat. "Too big to fail? The puzzling darkness of massive Milky Way subhaloes". In: *Mon. Not. Roy. Astron. Soc.* 415 (2011), p. L40. DOI: 10.1111/j.1745-3933.2011.01074.x. arXiv: 1103.0007 [astro-ph.CO].

[98] Sean Tulin and Hai-Bo Yu. "Dark Matter Self-interactions and Small Scale Structure". In: *Phys. Rept.* 730 (2018), pp. 1–57. DOI: 10.1016/j.physrep.2017.11.004. arXiv: 1705.02358 [hep-ph].

[99] G. L. Bryan and M. L. Norman. "Statistical properties of x-ray clusters: Analytic and numerical comparisons". In: *Astrophys. J.* 495 (1998), p. 80. DOI: 10.1086/305262. arXiv: astro-ph/9710107 [astro-ph].

[100] A. Burkert. "The Structure of dark matter halos in dwarf galaxies". In: *IAU Symp.* 171 (1996). [Astrophys. J.447,L25(1995)], p. 175. DOI: 10.1086/309560. arXiv: astro-ph/9504041 [astro-ph].

[101] Julio F. Navarro, Carlos S. Frenk, and Simon D. M. White. "The Structure of cold dark matter halos". In: *Astrophys. J.* 462 (1996), pp. 563–575. DOI: 10.1086/177173. arXiv: astro-ph/9508025 [astro-ph].

[102] Julio F. Navarro, Aaron Ludlow, Volker Springel, et al. "The Diversity and Similarity of Cold Dark Matter Halos". In: *Mon. Not. Roy. Astron. Soc.* 402 (2010), p. 21. DOI: 10.1111/j.1365-2966.2009.15878.x. arXiv: 0810.1522 [astro-ph].

[103] Marco Cirelli, Gennaro Corcella, Andi Hektor, et al. "PPPC 4 DM ID: A Poor Particle Physicist Cookbook for Dark Matter Indirect Detection". In: *JCAP* 1103 (2011). [Erratum: JCAP1210,E01(2012)], p. 051. DOI: 10.1088/1475-7516/2012/10/E01, 10.1088/1475-7516/2011/03/051. arXiv: 1012.4515 [hep-ph].

[104] William H. Press and Paul Schechter. "Formation of galaxies and clusters of galaxies by selfsimilar gravitational condensation". In: *Astrophys. J.* 187 (1974), pp. 425–438. DOI: 10.1086/152650.

[105] Gaelle Giesen, Julien Lesgourgues, Benjamin Audren, et al. "CMB photons shedding light on dark matter". In: *JCAP* 1212 (2012), p. 008. DOI: 10.1088/1475-7516/2012/12/008. arXiv: 1209.0247 [astro-ph.CO].

[106] J. R. Bond, S. Cole, G. Efstathiou, et al. "Excursion set mass functions for hierarchical Gaussian fluctuations". In: *The Astrophysical Journal* 379 (Oct. 1991), pp. 440–460. DOI: 10.1086/170520.

[107] Shaun Cole. "Modeling galaxy formation in evolving dark matter halos". In: *The Astrophysical Journal* 367 (Jan. 1991), p. 45. DOI: 10.1086/169600.

[108] Ravi K. Sheth, H. J. Mo, and Giuseppe Tormen. "Ellipsoidal collapse and an improved model for the number and spatial distribution of dark matter haloes". In: *Mon. Not.*

Roy. Astron. Soc. 323 (2001), p. 1. DOI: 10.1046/j.1365-8711.2001.04006.x. arXiv: astro-ph/9907024 [astro-ph].

[109] Volker Springel, Jie Wang, Mark Vogelsberger, et al. "The Aquarius Project: the subhalos of galactic halos". In: *Mon. Not. Roy. Astron. Soc.* 391 (2008), pp. 1685–1711. DOI: 10.1111/j.1365-2966.2008.14066.x. arXiv: 0809.0898 [astro-ph].

[110] Brendan F. Griffen, Alexander P. Ji, Gregory A. Dooley, et al. "The Caterpillar Project: a Large Suite of Milky way Sized Halos". In: *Astrophys. J.* 818.1 (2016), p. 10. DOI: 10.3847/0004-637X/818/1/10. arXiv: 1509.01255 [astro-ph.GA].

[111] A. Drlica-Wagner et al. "Eight Ultra-faint Galaxy Candidates Discovered in Year Two of the Dark Energy Survey". In: *Astrophys. J.* 813.2 (2015), p. 109. DOI: 10.1088/0004-637X/813/2/109. arXiv: 1508.03622 [astro-ph.GA].

[112] Mario Mateo. "Dwarf galaxies of the Local Group". In: *Ann. Rev. Astron. Astrophys.* 36 (1998), pp. 435–506. DOI: 10.1146/annurev.astro.36.1.435. arXiv: astro-ph/9810070 [astro-ph].

[113] Joshua D. Simon and Marla Geha. "The Kinematics of the Ultra-Faint Milky Way Satellites: Solving the Missing Satellite Problem". In: *Astrophys. J.* 670 (2007), pp. 313–331. DOI: 10.1086/521816. arXiv: 0706.0516 [astro-ph].

[114] Till Sawala et al. "The APOSTLE simulations: solutions to the Local Group's cosmic puzzles". In: *Mon. Not. Roy. Astron. Soc.* 457.2 (2016), pp. 1931–1943. DOI: 10.1093/mnras/stw145. arXiv: 1511.01098 [astro-ph.GA].

[115] Marcel S. Pawlowski, Benoit Famaey, David Merritt, et al. "On the persistence of two small-scale problems in ΛCDM". In: *Astrophys. J.* 815.1 (2015), p. 19. DOI: 10.1088/0004-637X/815/1/19. arXiv: 1510.08060 [astro-ph.GA].

[116] W. J. G. de Blok. "The Core-Cusp Problem". In: *Adv. Astron.* 2010 (2010), p. 789293. DOI: 10.1155/2010/789293. arXiv: 0910.3538 [astro-ph.CO].

[117] Stacy S. McGaugh, Vera C. Rubin, and W. J. G. de Blok. "High - resolution rotation curves of low surface brightness galaxies: Data". In: *Astron. J.* 122 (2001), pp. 2381–2395. DOI: 10.1086/323448. arXiv: astro-ph/0107326 [astro-ph].

[118] Lam Hui. "Unitarity bounds and the cuspy halo problem". In: *Phys. Rev. Lett.* 86 (2001), pp. 3467–3470. DOI: 10.1103/PhysRevLett.86.3467. arXiv: astro-ph/0102349 [astro-ph].

[119] Michael Boylan-Kolchin, James S. Bullock, and Manoj Kaplinghat. "The Milky Way's bright satellites as an apparent failure of LCDM". In: *Mon. Not. Roy. Astron. Soc.* 422 (2012), pp. 1203–1218. DOI: 10.1111/j.1365-2966.2012.20695.x. arXiv: 1111.2048 [astro-ph.CO].

[120] Erik J. Tollerud, Michael Boylan-Kolchin, and James S. Bullock. "M31 Satellite Masses Compared to LCDM Subhaloes". In: *Mon. Not. Roy. Astron. Soc.* 440.4 (2014), pp. 3511–3519. DOI: 10.1093/mnras/stu474. arXiv: 1403.6469 [astro-ph.GA].

[121] Evan N. Kirby, James S. Bullock, Michael Boylan-Kolchin, et al. "The dynamics of isolated Local Group galaxies". In: *Mon. Not. Roy. Astron. Soc.* 439.1 (2014), pp. 1015–1027. DOI: 10.1093/mnras/stu025. arXiv: 1401.1208 [astro-ph.GA].

[122] Kyle A. Oman et al. "The unexpected diversity of dwarf galaxy rotation curves". In: *Mon. Not. Roy. Astron. Soc.* 452.4 (2015), pp. 3650–3665. DOI: 10.1093/mnras/stv1504. arXiv: 1504.01437 [astro-ph.GA].

[123] Rachel Kuzio de Naray, Gregory D. Martinez, James S. Bullock, et al. "The Case Against Warm or Self-Interacting Dark Matter as Explanations for Cores in Low Surface Brightness Galaxies". In: *Astrophys. J.* 710 (2010), p. L161. DOI: 10.1088/2041-8205/710/2/L161. arXiv: 0912.3518 [astro-ph.CO].

[124] Mark R. Lovell, Vincent Eke, Carlos S. Frenk, et al. "The Haloes of Bright Satellite Galaxies in a Warm Dark Matter Universe". In: *Mon. Not. Roy. Astron. Soc.* 420 (2012), pp. 2318–2324. DOI: 10.1111/j.1365-2966.2011.20200.x. arXiv: 1104.2929 [astro-ph.CO].

[125] Shunsaku Horiuchi, Brandon Bozek, Kevork N. Abazajian, et al. "Properties of resonantly produced sterile neutrino dark matter subhaloes". In: *Mon. Not. Roy. Astron. Soc.* 456.4 (2016), pp. 4346–4353. DOI: 10.1093/mnras/stv2922. arXiv: 1512.04548 [astro-ph.CO].

[126] Matthew R. Buckley and Patrick J. Fox. "Dark Matter Self-Interactions and Light Force Carriers". In: *Phys. Rev.* D81 (2010), p. 083522. DOI: 10.1103/PhysRevD.81.083522. arXiv: 0911.3898 [hep-ph].

[127] Sean Tulin, Hai-Bo Yu, and Kathryn M. Zurek. "Beyond Collisionless Dark Matter: Particle Physics Dynamics for Dark Matter Halo Structure". In: *Phys. Rev.* D87.11 (2013), p. 115007. DOI: 10.1103/PhysRevD.87.115007. arXiv: 1302.3898 [hep-ph].

[128] Kimberly K. Boddy, Jonathan L. Feng, Manoj Kaplinghat, et al. "Self-Interacting Dark Matter from a Non-Abelian Hidden Sector". In: *Phys. Rev.* D89.11 (2014), p. 115017. DOI: 10.1103/PhysRevD.89.115017. arXiv: 1402.3629 [hep-ph].

[129] Mark Vogelsberger, Jesus Zavala, Francis-Yan Cyr-Racine, et al. "ETHOS - An Effective Theory of Structure Formation: Dark matter physics as a possible explanation of the small-scale CDM problems". In: *Mon. Not. Roy. Astron. Soc.* 460.2 (2016), pp. 1399–1416. DOI: 10.1093/mnras/stw1076. arXiv: 1512.05349 [astro-ph.CO].

[130] Felix Kahlhoefer, Manoj Kaplinghat, Tracy R. Slatyer, et al. "Diversity in density profiles of self-interacting dark matter satellite halos". In: (Apr. 23, 2019). arXiv: 1904.10539 [astro-ph.GA].

[131] W. L. Freedman et al. "Final results from the Hubble Space Telescope key project to measure the Hubble constant". In: *Astrophys. J.* 553 (2001), pp. 47–72. DOI: 10.1086/320638. arXiv: astro-ph/0012376 [astro-ph].

[132] Wendy L. Freedman. "Cosmology at a Crossroads". In: *Nat. Astron.* 1 (2017), p. 0121. DOI: 10.1038/s41550-017-0121. arXiv: 1706.02739 [astro-ph.CO].

[133] Adam G. Riess et al. "Milky Way Cepheid Standards for Measuring Cosmic Distances and Application to Gaia DR2: Implications for the Hubble Constant". In: *Astrophys. J.* 861.2 (2018), p. 126. DOI: 10.3847/1538-4357/aac82e. arXiv: 1804.10655 [astro-ph.CO].

[134] Shadab Alam et al. "The clustering of galaxies in the completed SDSS-III Baryon Oscillation Spectroscopic Survey: cosmological analysis of the DR12 galaxy sample".

In: *Mon. Not. Roy. Astron. Soc.* 470.3 (2017), pp. 2617–2652. DOI: 10.1093/mnras/stx721. arXiv: 1607.03155 [astro-ph.CO].

[135] David N. Spergel, Raphael Flauger, and Renée Hlozek. "Planck Data Reconsidered". In: *Phys. Rev.* D91.2 (2015), p. 023518. DOI: 10.1103/PhysRevD.91.023518. arXiv: 1312.3313 [astro-ph.CO].

[136] G. E. Addison, Y. Huang, D. J. Watts, et al. "Quantifying discordance in the 2015 Planck CMB spectrum". In: *Astrophys. J.* 818.2 (2016), p. 132. DOI: 10.3847/0004-637X/818/2/132. arXiv: 1511.00055 [astro-ph.CO].

[137] N. Aghanim et al. "Planck intermediate results. LI. Features in the cosmic microwave background temperature power spectrum and shifts in cosmological parameters". In: *Astron. Astrophys.* 607 (2017), A95. DOI: 10.1051/0004-6361/201629504. arXiv: 1608.02487 [astro-ph.CO].

[138] George Efstathiou. "H0 Revisited". In: *Mon. Not. Roy. Astron. Soc.* 440.2 (2014), pp. 1138–1152. DOI: 10.1093/mnras/stu278. arXiv: 1311.3461 [astro-ph.CO].

[139] Wilmar Cardona, Martin Kunz, and Valeria Pettorino. "Determining H_0 with Bayesian hyper-parameters". In: *JCAP* 1703.03 (2017), p. 056. DOI: 10.1088/1475-7516/2017/03/056. arXiv: 1611.06088 [astro-ph.CO].

[140] Bonnie R. Zhang, Michael J. Childress, Tamara M. Davis, et al. "A blinded determination of H_0 from low-redshift Type Ia supernovae, calibrated by Cepheid variables". In: *Mon. Not. Roy. Astron. Soc.* 471.2 (2017), pp. 2254–2285. DOI: 10.1093/mnras/stx1600. arXiv: 1706.07573 [astro-ph.CO].

[141] Brent Follin and Lloyd Knox. "Insensitivity of the distance ladder Hubble constant determination to Cepheid calibration modelling choices". In: *Mon. Not. Roy. Astron. Soc.* 477.4 (2018), pp. 4534–4542. DOI: 10.1093/mnras/sty720. arXiv: 1707.01175 [astro-ph.CO].

[142] V. Bonvin et al. "H0LiCOW ? V. New COSMOGRAIL time delays of HE 0435-1223: H_0 to 3.8 per cent precision from strong lensing in a flat ΛCDM model". In: *Mon. Not. Roy. Astron. Soc.* 465.4 (2017), pp. 4914–4930. DOI: 10.1093/mnras/stw3006. arXiv: 1607.01790 [astro-ph.CO].

[143] Stephen M. Feeney, Hiranya V. Peiris, Andrew R. Williamson, et al. "Prospects for resolving the Hubble constant tension with standard sirens". In: *Phys. Rev. Lett.* 122.6 (2019), p. 061105. DOI: 10.1103/PhysRevLett.122.061105. arXiv: 1802.03404 [astro-ph.CO].

[144] Manuel A. Buen-Abad, Razieh Emami, and Martin Schmaltz. "Cannibal Dark Matter and Large Scale Structure". In: *Phys. Rev.* D98.8 (2018), p. 083517. DOI: 10.1103/PhysRevD.98.083517. arXiv: 1803.08062 [hep-ph].

[145] Vivian Poulin, Tristan L. Smith, Tanvi Karwal, et al. "Early Dark Energy Can Resolve The Hubble Tension". In: *Physical Review Letters* 122.22 (2018). ISSN: 0031-9007. DOI: 10.1103/physrevlett.122.221301. arXiv: 1811.04083 [astro-ph.CO].

[146] Kyriakos Vattis, Savvas M. Koushiappas, and Abraham Loeb. "Late universe decaying dark matter can relieve the H_0 tension". In: *Phys. Rev. D 99, 121302 (2019)*

(Mar. 14, 2019). DOI: 10.1103/PhysRevD.99.121302. arXiv: 1903.06220 [astro-ph.CO].

[147] Richard A. Battye, Tom Charnock, and Adam Moss. "Tension between the power spectrum of density perturbations measured on large and small scales". In: *Phys. Rev.* D91.10 (2015), p. 103508. DOI: 10.1103/PhysRevD.91.103508. arXiv: 1409.2769 [astro-ph.CO].

[148] Niall MacCrann, Joe Zuntz, Sarah Bridle, et al. "Cosmic Discordance: Are Planck CMB and CFHTLenS weak lensing measurements out of tune?" In: *Mon. Not. Roy. Astron. Soc.* 451.3 (2015), pp. 2877–2888. DOI: 10.1093/mnras/stv1154. arXiv: 1408.4742 [astro-ph.CO].

[149] M. James Jee, J. Anthony Tyson, Stefan Hilbert, et al. "Cosmic Shear Results from the Deep Lens Survey - II: Full Cosmological Parameter Constraints from Tomography". In: *Astrophys. J.* 824.2 (2016), p. 77. DOI: 10.3847/0004-637X/824/2/77. arXiv: 1510.03962 [astro-ph.CO].

[150] Shahab Joudaki et al. "CFHTLenS revisited: assessing concordance with Planck including astrophysical systematics". In: *Mon. Not. Roy. Astron. Soc.* 465.2 (2017), pp. 2033–2052. DOI: 10.1093/mnras/stw2665. arXiv: 1601.05786 [astro-ph.CO].

[151] T. M. C. Abbott et al. "Dark Energy Survey year 1 results: Cosmological constraints from galaxy clustering and weak lensing". In: *Phys. Rev.* D98.4 (2018), p. 043526. DOI: 10.1103/PhysRevD.98.043526. arXiv: 1708.01530 [astro-ph.CO].

[152] H. Hildebrandt et al. "KiDS+VIKING-450: Cosmic shear tomography with optical+infrared data". In: (2018). arXiv: 1812.06076 [astro-ph.CO].

[153] Chihway Chang, Michael Wang, Scott Dodelson, et al. "A Unified Analysis of Four Cosmic Shear Surveys". In: *Monthly Notices of the Royal Astronomical Society* 482.3 (Aug. 22, 2018), pp. 3696–3717. DOI: 10.1093/mnras/sty2902. arXiv: 1808.07335 [astro-ph.CO].

[154] Eleonora Di Valentino, Céline Bøehm, Eric Hivon, et al. "Reducing the H_0 and σ_8 tensions with Dark Matter-neutrino interactions". In: *Phys. Rev.* D97.4 (2018), p. 043513. DOI: 10.1103/PhysRevD.97.043513. arXiv: 1710.02559 [astro-ph.CO].

[155] Massimiliano Lattanzi and Martina Gerbino. "Status of neutrino properties and future prospects - Cosmological and astrophysical constraints". In: *Front.in Phys.* 5 (2018), p. 70. DOI: 10.3389/fphy.2017.00070. arXiv: 1712.07109 [astro-ph.CO].

[156] Julien Lesgourgues, Gianpiero Mangano, Gennaro Miele, et al. *Neutrino Cosmology*. Cambridge University Press, 2009. DOI: 10.1017/cbo9781139012874.

[157] C. L. Cowan, F. Reines, F. B. Harrison, et al. "Detection of the free neutrino: A Confirmation". In: *Science* 124 (1956), pp. 103–104. DOI: 10.1126/science.124.3212.103.

[158] R. Davis. "Solar neutrinos. II: Experimental". In: *Phys. Rev. Lett.* 12 (1964). [,107(1964)], pp. 303–305. DOI: 10.1103/PhysRevLett.12.303.

[159] K. Abe et al. "Solar neutrino results in Super-Kamiokande-III". In: *Phys. Rev.* D83 (2011), p. 052010. DOI: 10.1103/PhysRevD.83.052010. arXiv: 1010.0118 [hep-ex].

[160] B. Aharmim et al. "Low Energy Threshold Analysis of the Phase I and Phase II Data Sets of the Sudbury Neutrino Observatory". In: *Phys. Rev.* C81 (2010), p. 055504. DOI: 10.1103/PhysRevC.81.055504. arXiv: 0910.2984 [nucl-ex].

[161] B. Pontecorvo. "Inverse beta processes and nonconservation of lepton charge". In: *Sov. Phys. JETP* 7 (1958). [Zh. Eksp. Teor. Fiz.34,247(1957)], pp. 172–173.

[162] B. Pontecorvo. "Neutrino Experiments and the Problem of Conservation of Leptonic Charge". In: *Sov. Phys. JETP* 26 (1968). [Zh. Eksp. Teor. Fiz.53,1717(1967)], pp. 984–988.

[163] J. Bonn, B. Bornschein, L. Bornschein, et al. "The Mainz neutrino mass experiment". In: *Nuclear Physics B - Proceedings Supplements* 91.1-3 (2001), pp. 273–279. DOI: 10.1016/s0920-5632(00)00951-8.

[164] A. Osipowicz et al. "KATRIN: A Next generation tritium beta decay experiment with sub-eV sensitivity for the electron neutrino mass. Letter of intent". In: (2001). arXiv: hep-ex/0109033 [hep-ex].

[165] Alexey Boyarsky, Julien Lesgourgues, Oleg Ruchayskiy, et al. "Lyman-alpha constraints on warm and on warm-plus-cold dark matter models". In: *JCAP* 0905 (2009), p. 012. DOI: 10.1088/1475-7516/2009/05/012. arXiv: 0812.0010 [astro-ph].

[166] Julien Lesgourgues, Wessel Valkenburg, and Enrique Gaztanaga. "Constraining neutrino masses with the ISW-galaxy correlation function". In: *Phys. Rev.* D77 (2008), p. 063505. DOI: 10.1103/PhysRevD.77.063505. arXiv: 0710.5525 [astro-ph].

[167] Nathalie Palanque-Delabrouille et al. "Neutrino masses and cosmology with Lyman-alpha forest power spectrum". In: *JCAP* 1511.11 (2015), p. 011. DOI: 10.1088/1475-7516/2015/11/011. arXiv: 1506.05976 [astro-ph.CO].

[168] Jonathan R. Pritchard and Abraham Loeb. "21-cm cosmology". In: *Rept. Prog. Phys.* 75 (2012), p. 086901. DOI: 10.1088/0034-4885/75/8/086901. arXiv: 1109.6012 [astro-ph.CO].

[169] Sunny Vagnozzi, Elena Giusarma, Olga Mena, et al. "Unveiling ν secrets with cosmological data: neutrino masses and mass hierarchy". In: *Phys. Rev.* D96.12 (2017), p. 123503. DOI: 10.1103/PhysRevD.96.123503. arXiv: 1701.08172 [astro-ph.CO].

[170] Carmelita Carbone, Licia Verde, Yun Wang, et al. "Neutrino constraints from future nearly all-sky spectroscopic galaxy surveys". In: *JCAP* 1103 (2011), p. 030. DOI: 10.1088/1475-7516/2011/03/030. arXiv: 1012.2868 [astro-ph.CO].

[171] Yoshihiko Oyama, Akie Shimizu, and Kazunori Kohri. "Determination of neutrino mass hierarchy by 21 cm line and CMB B-mode polarization observations". In: *Phys. Lett.* B718 (2013), pp. 1186–1193. DOI: 10.1016/j.physletb.2012.12.053. arXiv: 1205.5223 [astro-ph.CO].

[172] Jan Hamann, Steen Hannestad, and Yvonne Y. Y. Wong. "Measuring neutrino masses with a future galaxy survey". In: *JCAP* 1211 (2012), p. 052. DOI: 10.1088/1475-7516/2012/11/052. arXiv: 1209.1043 [astro-ph.CO].

[173] Benjamin Audren, Julien Lesgourgues, Simeon Bird, et al. "Neutrino masses and cosmological parameters from a Euclid-like survey: Markov Chain Monte Carlo forecasts including theoretical errors". In: *JCAP* 1301 (2013), p. 026. DOI: 10.1088/1475-7516/2013/01/026. arXiv: 1210.2194 [astro-ph.CO].

[174] Ruth Pearson and Oliver Zahn. "Cosmology from cross correlation of CMB lensing and galaxy surveys". In: *Phys. Rev.* D89.4 (2014), p. 043516. DOI: 10.1103/PhysRevD.89.043516. arXiv: 1311.0905 [astro-ph.CO].

[175] R. Allison, P. Caucal, E. Calabrese, et al. "Towards a cosmological neutrino mass detection". In: *Phys. Rev.* D92.12 (2015), p. 123535. DOI: 10.1103/PhysRevD.92.123535. arXiv: 1509.07471 [astro-ph.CO].

[176] Francisco Villaescusa-Navarro, Philip Bull, and Matteo Viel. "Weighing neutrinos with cosmic neutral hydrogen". In: *Astrophys. J.* 814.2 (2015), p. 146. DOI: 10.1088/0004-637X/814/2/146. arXiv: 1507.05102 [astro-ph.CO].

[177] Yoshihiko Oyama, Kazunori Kohri, and Masashi Hazumi. "Constraints on the neutrino parameters by future cosmological 21 cm line and precise CMB polarization observations". In: *JCAP* 1602.02 (2016), p. 008. DOI: 10.1088/1475-7516/2016/02/008. arXiv: 1510.03806 [astro-ph.CO].

[178] Marilena LoVerde. "Neutrino mass without cosmic variance". In: *Phys. Rev.* D93.10 (2016), p. 103526. DOI: 10.1103/PhysRevD.93.103526. arXiv: 1602.08108 [astro-ph.CO].

[179] Maria Archidiacono, Thejs Brinckmann, Julien Lesgourgues, et al. "Physical effects involved in the measurements of neutrino masses with future cosmological data". In: *JCAP* 1702.02 (2017), p. 052. DOI: 10.1088/1475-7516/2017/02/052. arXiv: 1610.09852 [astro-ph.CO].

[180] Marcel Schmittfull and Uros Seljak. "Parameter constraints from cross-correlation of CMB lensing with galaxy clustering". In: *Phys. Rev.* D97.12 (2018), p. 123540. DOI: 10.1103/PhysRevD.97.123540. arXiv: 1710.09465 [astro-ph.CO].

[181] Aoife Boyle and Eiichiro Komatsu. "Deconstructing the neutrino mass constraint from galaxy redshift surveys". In: *JCAP* 1803.03 (2018), p. 035. DOI: 10.1088/1475-7516/2018/03/035. arXiv: 1712.01857 [astro-ph.CO].

[182] Tim Sprenger, Maria Archidiacono, Thejs Brinckmann, et al. "Cosmology in the era of Euclid and the Square Kilometre Array". In: *Journal of Cosmology and Astroparticle Physics* 2019.02 (2018), pp. 047–047. ISSN: 1475-7516. DOI: 10.1088/1475-7516/2019/02/047. arXiv: 1801.08331 [astro-ph.CO].

[183] Dhiraj Kumar Hazra, Daniela Paoletti, Fabio Finelli, et al. "Reionization in the dark and the light from Cosmic Microwave Background". In: *JCAP* 1809.09 (2018), p. 016. DOI: 10.1088/1475-7516/2018/09/016. arXiv: 1807.05435 [astro-ph.CO].

[184] Byeonghee Yu, Robert Z. Knight, Blake D. Sherwin, et al. "Towards Neutrino Mass from Cosmology without Optical Depth Information". In: (Sept. 6, 2018). arXiv: 1809.02120 [astro-ph.CO].

[185] Aoife Boyle. "Understanding the neutrino mass constraints achievable by combining CMB lensing and spectroscopic galaxy surveys". In: *JCAP* 1904.04 (Nov. 19, 2018), p. 038. DOI: 10.1088/1475-7516/2019/04/038. arXiv: 1811.07636 [astro-ph.CO].

[186] S. Gariazzo, M. Archidiacono, P. F. de Salas, et al. "Neutrino masses and their ordering: Global Data, Priors and Models". In: *JCAP* 1803.03 (2018), p. 011. DOI: 10.1088/1475-7516/2018/03/011. arXiv: 1801.04946 [hep-ph].

[187] Julien Lesgourgues, Sergio Pastor, and Laurence Perotto. "Probing neutrino masses with future galaxy redshift surveys". In: *Phys. Rev.* D70 (2004), p. 045016. DOI: 10.1103/PhysRevD.70.045016. arXiv: hep-ph/0403296 [hep-ph].

[188] Julien Lesgourgues and Sergio Pastor. "Massive neutrinos and cosmology". In: *Phys. Rept.* 429 (2006), pp. 307–379. DOI: 10.1016/j.physrep.2006.04.001. arXiv: astro-ph/0603494 [astro-ph].

[189] Julien Lesgourgues, Gianpiero Mangano, Gennaro Miele, et al. *Neutrino cosmology*. Cambridge: Cambridge Univ. Press, 2013. URL: http://cds.cern.ch/record/1519137.

[190] N. Aghanim et al. "Planck intermediate results. XLVI. Reduction of large-scale systematic effects in HFI polarization maps and estimation of the reionization optical depth". In: *Astron. Astrophys.* 596 (2016), A107. DOI: 10.1051/0004-6361/201628890. arXiv: 1605.02985 [astro-ph.CO].

[191] Steen Hannestad. "Neutrino masses and the number of neutrino species from WMAP and 2dFGRS". In: *JCAP* 0305 (2003), p. 004. DOI: 10.1088/1475-7516/2003/05/004. arXiv: astro-ph/0303076 [astro-ph].

[192] Oystein Elgaroy and Ofer Lahav. "Upper limits on neutrino masses from the 2dFGRS and WMAP: the role of priors". In: *JCAP* 0304 (2003), p. 004. DOI: 10.1088/1475-7516/2003/04/004. arXiv: astro-ph/0303089 [astro-ph].

[193] Steen Hannestad and Georg Raffelt. "Cosmological mass limits on neutrinos, axions, and other light particles". In: *JCAP* 0404 (2004), p. 008. DOI: 10.1088/1475-7516/2004/04/008. arXiv: hep-ph/0312154 [hep-ph].

[194] Patrick Crotty, Julien Lesgourgues, and Sergio Pastor. "Current cosmological bounds on neutrino masses and relativistic relics". In: *Phys. Rev.* D69 (2004), p. 123007. DOI: 10.1103/PhysRevD.69.123007. arXiv: hep-ph/0402049 [hep-ph].

[195] Maria Archidiacono, Elena Giusarma, Alessandro Melchiorri, et al. "Neutrino and dark radiation properties in light of recent CMB observations". In: *Phys. Rev.* D87.10 (2013), p. 103519. DOI: 10.1103/PhysRevD.87.103519. arXiv: 1303.0143 [astro-ph.CO].

[196] Michel Chevallier and David Polarski. "Accelerating universes with scaling dark matter". In: *Int. J. Mod. Phys.* D10 (2001), pp. 213–224. DOI: 10.1142/S0218271801000822. arXiv: gr-qc/0009008 [gr-qc].

[197] Eleonora Di Valentino et al. "Exploring cosmic origins with CORE: Cosmological parameters". In: *JCAP* 1804 (2018), p. 017. DOI: 10.1088/1475-7516/2018/04/017. arXiv: 1612.00021 [astro-ph.CO].

[198] Sunny Vagnozzi, Suhail Dhawan, Martina Gerbino, et al. "Constraints on the sum of the neutrino masses in dynamical dark energy models with $w(z) \geq -1$ are tighter than those obtained in ΛCDM". In: *Phys. Rev.* D98.8 (2018), p. 083501. DOI: 10.1103/PhysRevD.98.083501. arXiv: 1801.08553 [astro-ph.CO].

[199] T. Matsumura et al. "Mission design of LiteBIRD". In: *Journal of Low Temperature Physics September 2014, Volume 176, Issue 5-6, pp 733-740* (Nov. 12, 2013). [J. Low. Temp. Phys.176,733(2014)]. DOI: 10.1007/s10909-013-0996-1. arXiv: 1311.2847 [astro-ph.IM].

[200] A. Suzuki et al. "The LiteBIRD Satellite Mission - Sub-Kelvin Instrument". In: *17th International Workshop on Low Temperature Detectors (LTD 17) Kurume City, Japan, July 17-21, 2017*. 2018. arXiv: 1801.06987 [astro-ph.IM]. URL: https://inspirehep.net/record/1649560/files/arXiv:1801.06987.pdf.

[201] J. Delabrouille et al. "Exploring cosmic origins with CORE: Survey requirements and mission design". In: *JCAP* 1804.04 (2018), p. 014. DOI: 10.1088/1475-7516/2018/04/014. arXiv: 1706.04516 [astro-ph.IM].

[202] Kevork N. Abazajian et al. "CMB-S4 Science Book, First Edition". In: (Oct. 10, 2016). arXiv: 1610.02743 [astro-ph.CO].

[203] Maximilian H. Abitbol et al. "CMB-S4 Technology Book, First Edition". In: (June 8, 2017). arXiv: 1706.02464 [astro-ph.IM].

[204] Brian M. Sutin et al. "PICO - the probe of inflation and cosmic origins". In: *Proc. SPIE Int. Soc. Opt. Eng.* 10698 (2018), 106984F. DOI: 10.1117/12.2311326. arXiv: 1808.01368 [astro-ph.IM].

[205] Karl Young et al. "Optical Design of PICO, a Concept for a Space Mission to Probe Inflation and Cosmic Origins". In: *Proceedings, SPIE Astronomical Telescopes + Instrumentation 2018: Modeling, Systems Engineering, and Project Management for Astronomy VIII: Austin, USA, June 10-15, 2018*. 2018. arXiv: 1808.01369 [astro-ph.IM].

[206] Takemi Okamoto and Wayne Hu. "CMB lensing reconstruction on the full sky". In: *Phys. Rev.* D67 (2003), p. 083002. DOI: 10.1103/PhysRevD.67.083002. arXiv: astro-ph/0301031 [astro-ph].

[207] Michael Levi et al. "The DESI Experiment, a whitepaper for Snowmass 2013". In: (Aug. 4, 2013). arXiv: 1308.0847 [astro-ph.CO].

[208] "The DESI Experiment Part I: Science,Targeting, and Survey Design". In: (Oct. 31, 2016). arXiv: 1611.00036 [astro-ph.IM].

[209] Luca Amendola et al. "Cosmology and fundamental physics with the Euclid satellite". In: *Living Rev. Rel.* 21.1 (2018), p. 2. DOI: 10.1007/s41114-017-0010-3. arXiv: 1606.00180 [astro-ph.CO].

[210] Mario G. Santos et al. "Cosmology with a SKA HI intensity mapping survey". In: *PoS AASKA14 (2015) 019* (Jan. 16, 2015). arXiv: 1501.03989 [astro-ph.CO].

[211] Adrian Liu, Jonathan R. Pritchard, Rupert Allison, et al. "Eliminating the optical depth nuisance from the CMB with 21 cm cosmology". In: *Phys. Rev.* D93.4 (2016), p. 043013. DOI: 10.1103/PhysRevD.93.043013. arXiv: 1509.08463 [astro-ph.CO].

[212] N. Kaiser. "Clustering in real space and in redshift space". In: *Mon. Not. Roy. Astron. Soc.* 227 (1987), pp. 1–27.

[213] Philip Bull, Pedro G. Ferreira, Prina Patel, et al. "Late-time cosmology with 21cm intensity mapping experiments". In: *Astrophys. J.* 803.1 (2015), p. 21. DOI: 10.1088/0004-637X/803/1/21. arXiv: 1405.1452 [astro-ph.CO].

[214] Francisco Villaescusa-Navarro, Federico Marulli, Matteo Viel, et al. "Cosmology with massive neutrinos I: towards a realistic modeling of the relation between matter, haloes and galaxies". In: *JCAP* 1403 (2014), p. 011. DOI: 10.1088/1475-7516/2014/03/011. arXiv: 1311.0866 [astro-ph.CO].

[215] Emanuele Castorina, Emiliano Sefusatti, Ravi K. Sheth, et al. "Cosmology with massive neutrinos II: on the universality of the halo mass function and bias". In: *JCAP* 1402 (2014), p. 049. DOI: 10.1088/1475-7516/2014/02/049. arXiv: 1311.1212 [astro-ph.CO].

[216] Matteo Costanzi, Francisco Villaescusa-Navarro, Matteo Viel, et al. "Cosmology with massive neutrinos III: the halo mass function andan application to galaxy clusters". In: *JCAP* 1312 (2013), p. 012. DOI: 10.1088/1475-7516/2013/12/012. arXiv: 1311.1514 [astro-ph.CO].

[217] Matteo Biagetti, Vincent Desjacques, Alex Kehagias, et al. "Nonlocal halo bias with and without massive neutrinos". In: *Phys. Rev.* D90.4 (2014), p. 045022. DOI: 10.1103/PhysRevD.90.045022. arXiv: 1405.1435 [astro-ph.CO].

[218] Emanuele Castorina, Carmelita Carbone, Julien Bel, et al. "DEMNUni: The clustering of large-scale structures in the presence of massive neutrinos". In: *JCAP* 1507.07 (2015), p. 043. DOI: 10.1088/1475-7516/2015/07/043. arXiv: 1505.07148 [astro-ph.CO].

[219] Alvise Raccanelli, Licia Verde, and Francisco Villaescusa-Navarro. "Biases from neutrino bias: to worry or not to worry?" In: *Mon. Not. Roy. Astron. Soc.* 483.1 (2019), pp. 734–743. DOI: 10.1093/mnras/sty2162. arXiv: 1704.07837 [astro-ph.CO].

[220] Sunny Vagnozzi, Thejs Brinckmann, Maria Archidiacono, et al. "Bias due to neutrinos must not uncorrect'd go". In: *JCAP 1809 (2018) 001* (July 12, 2018). DOI: 10.1088/1475-7516/2018/09/001. arXiv: 1807.04672 [astro-ph.CO].

[221] Pablo Lemos, Anthony Challinor, and George Efstathiou. "The effect of Limber and flat-sky approximations on galaxy weak lensing". In: *JCAP* 1705.05 (2017), p. 014. DOI: 10.1088/1475-7516/2017/05/014. arXiv: 1704.01054 [astro-ph.CO].

[222] Marika Asgari, Andy Taylor, Benjamin Joachimi, et al. "Flat-Sky Pseudo-Cls Analysis for Weak Gravitational Lensing". In: *Mon. Not. Roy. Astron. Soc.* 479.1 (2018), pp. 454–477. DOI: 10.1093/mnras/sty1412. arXiv: 1612.04664 [astro-ph.CO].

[223] Erminia Calabrese, David Alonso, and Jo Dunkley. "Complementing the ground-based CMB-S4 experiment on large scales with the PIXIE satellite". In: *Phys. Rev.* D95.6 (2017), p. 063504. DOI: 10.1103/PhysRevD.95.063504. arXiv: 1611.10269 [astro-ph.CO].

[224] Christiane S. Lorenz, David Alonso, and Pedro G. Ferreira. "Impact of relativistic effects on cosmological parameter estimation". In: *Phys. Rev.* D97.2 (2018), p. 023537. DOI: 10.1103/PhysRevD.97.023537. arXiv: 1710.02477 [astro-ph.CO].

[225] Siddharth Mishra-Sharma, David Alonso, and Joanna Dunkley. "Neutrino masses and beyond- ΛCDM cosmology with LSST and future CMB experiments". In: *Phys. Rev.* D97.12 (2018), p. 123544. DOI: 10.1103/PhysRevD.97.123544. arXiv: 1803.07561 [astro-ph.CO].

[226] Andrej Obuljen, Emanuele Castorina, Francisco Villaescusa-Navarro, et al. "High-redshift post-reionization cosmology with 21cm intensity mapping". In: *JCAP* 1805.05 (2018), p. 004. DOI: 10.1088/1475-7516/2018/05/004. arXiv: 1709.07893 [astro-ph.CO].

[227] Andreu Font-Ribera, Patrick McDonald, Nick Mostek, et al. "DESI and other dark energy experiments in the era of neutrino mass measurements". In: *JCAP* 1405 (2014), p. 023. DOI: 10.1088/1475-7516/2014/05/023. arXiv: 1308.4164 [astro-ph.CO].

[228] John F. Beacom, Nicole F. Bell, and Scott Dodelson. "Neutrinoless universe". In: *Phys. Rev. Lett.* 93 (2004), p. 121302. DOI: 10.1103/PhysRevLett.93.121302. arXiv: astro-ph/0404585 [astro-ph].

[229] Ryan J. Wilkinson, Julien Lesgourgues, and Céline Boehm. "Using the CMB angular power spectrum to study Dark Matter-photon interactions". In: *JCAP* 1404 (2014), p. 026. DOI: 10.1088/1475-7516/2014/04/026. arXiv: 1309.7588 [astro-ph.CO].

[230] Ryan J. Wilkinson, Celine Boehm, and Julien Lesgourgues. "Constraining Dark Matter-Neutrino Interactions using the CMB and Large-Scale Structure". In: *JCAP* 1405 (2014), p. 011. DOI: 10.1088/1475-7516/2014/05/011. arXiv: 1401.7597 [astro-ph.CO].

[231] Cora Dvorkin, Kfir Blum, and Marc Kamionkowski. "Constraining Dark Matter-Baryon Scattering with Linear Cosmology". In: *Phys. Rev.* D89.2 (2014), p. 023519. DOI: 10.1103/PhysRevD.89.023519. arXiv: 1311.2937 [astro-ph.CO].

[232] Maria Archidiacono, Erminia Calabrese, and Alessandro Melchiorri. "The Case for Dark Radiation". In: *Phys. Rev.* D84 (2011), p. 123008. DOI: 10.1103/PhysRevD.84.123008. arXiv: 1109.2767 [astro-ph.CO].

[233] Maria Archidiacono, Sebastian Bohr, Steen Hannestad, et al. "Linear scale bounds on dark matter–dark radiation interactions and connection with the small scale crisis of cold dark matter". In: *JCAP* 1711.11 (2017), p. 010. DOI: 10.1088/1475-7516/2017/11/010. arXiv: 1706.06870 [astro-ph.CO].

[234] Manuel A. Buen-Abad, Gustavo Marques-Tavares, and Martin Schmaltz. "Non-Abelian dark matter and dark radiation". In: *Phys. Rev.* D92.2 (2015), p. 023531. DOI: 10.1103/PhysRevD.92.023531. arXiv: 1505.03542 [hep-ph].

[235] Julien Lesgourgues, Gustavo Marques-Tavares, and Martin Schmaltz. "Evidence for dark matter interactions in cosmological precision data?" In: *JCAP* 1602.02 (2016), p. 037. DOI: 10.1088/1475-7516/2016/02/037. arXiv: 1507.04351 [astro-ph.CO].

[236] Manuel A. Buen-Abad, Martin Schmaltz, Julien Lesgourgues, et al. "Interacting Dark Sector and Precision Cosmology". In: *JCAP* 1801.01 (2018), p. 008. DOI: 10.1088/1475-7516/2018/01/008. arXiv: 1708.09406 [astro-ph.CO].

[237] Francis-Yan Cyr-Racine, Kris Sigurdson, Jesus Zavala, et al. "ETHOS—an effective theory of structure formation: From dark particle physics to the matter distribution of the Universe". In: *Phys. Rev.* D93.12 (2016), p. 123527. DOI: 10.1103/PhysRevD.93.123527. arXiv: 1512.05344 [astro-ph.CO].

[238] Benjamin Audren et al. "Robustness of cosmic neutrino background detection in the cosmic microwave background". In: *JCAP* 1503 (2015), p. 036. DOI: 10.1088/1475-7516/2015/03/036. arXiv: 1412.5948 [astro-ph.CO].

[239] Laura Lopez-Honorez, Olga Mena, Sergio Palomares-Ruiz, et al. "Constraints on warm dark matter from the ionization history of the Universe". In: *Phys. Rev. D 96, 103539 (2017)* (Mar. 7, 2017). DOI: 10.1103/PhysRevD.96.103539. arXiv: 1703.02302 [astro-ph.CO].

[240] Francis-Yan Cyr-Racine, Roland de Putter, Alvise Raccanelli, et al. "Constraints on Large-Scale Dark Acoustic Oscillations from Cosmology". In: *Phys. Rev.* D89.6 (2014), p. 063517. DOI: 10.1103/PhysRevD.89.063517. arXiv: 1310.3278 [astro-ph.CO].

[241] N. Aghanim et al. "Planck 2015 results. XI. CMB power spectra, likelihoods, and robustness of parameters". In: *Astron. Astrophys.* 594 (2016), A11. DOI: 10.1051/0004-6361/201526926. arXiv: 1507.02704 [astro-ph.CO].

[242] P. A. R. Ade et al. "Planck 2015 results. XV. Gravitational lensing". In: *Astron. Astrophys.* 594 (2016), A15. DOI: 10.1051/0004-6361/201525941. arXiv: 1502.01591 [astro-ph.CO].

[243] Florian Beutler, Chris Blake, Matthew Colless, et al. "The 6dF Galaxy Survey: Baryon Acoustic Oscillations and the Local Hubble Constant". In: *Mon. Not. Roy. Astron. Soc.* 416 (2011), pp. 3017–3032. DOI: 10.1111/j.1365-2966.2011.19250.x. arXiv: 1106.3366 [astro-ph.CO].

[244] Ashley J. Ross, Lado Samushia, Cullan Howlett, et al. "The clustering of the SDSS DR7 main Galaxy sample ? I. A 4 per cent distance measure at $z = 0.15$". In: *Mon. Not. Roy. Astron. Soc.* 449.1 (2015), pp. 835–847. DOI: 10.1093/mnras/stv154. arXiv: 1409.3242 [astro-ph.CO].

[245] Zhen Hou, Ryan Keisler, Lloyd Knox, et al. "How Massless Neutrinos Affect the Cosmic Microwave Background Damping Tail". In: *Phys. Rev.* D87 (2013), p. 083008. DOI: 10.1103/PhysRevD.87.083008. arXiv: 1104.2333 [astro-ph.CO].

[246] Steven Weinberg. "Cosmological fluctuations of short wavelength". In: *Astrophys. J.* 581 (2002), pp. 810–816. DOI: 10.1086/344441. arXiv: astro-ph/0207375 [astro-ph].

[247] Luc Voruz, Julien Lesgourgues, and Thomas Tram. "The effective gravitational decoupling between dark matter and the CMB". In: *JCAP* 1403 (2014), p. 004. DOI: 10.1088/1475-7516/2014/03/004. arXiv: 1312.5301 [astro-ph.CO].

[248] R. Adam et al. "Planck 2015 results. I. Overview of products and scientific results". In: *Astron. Astrophys.* 594 (Feb. 5, 2015), A1. DOI: 10.1051/0004-6361/201527101. arXiv: 1502.01582 [astro-ph.CO].

[249] Adam G. Riess, Stefano Casertano, Wenlong Yuan, et al. "Large Magellanic Cloud Cepheid Standards Provide a 1% Foundation for the Determination of the Hubble Constant and Stronger Evidence for Physics Beyond LambdaCDM". In: *Astrophys. J.* 876.1 (Mar. 18, 2019), p. 85. DOI: 10.3847/1538-4357/ab1422. arXiv: 1903.07603 [astro-ph.CO].

[250] Rebecca Krall, Francis-Yan Cyr-Racine, and Cora Dvorkin. "Wandering in the Lyman-alpha Forest: A Study of Dark Matter-Dark Radiation Interactions". In: *JCAP* 1709.09 (2017), p. 003. DOI: 10.1088/1475-7516/2017/09/003. arXiv: 1705.08894 [astro-ph.CO].

[251] Judd D. Bowman, Alan E. E. Rogers, Raul A. Monsalve, et al. "An absorption profile centred at 78 megahertz in the sky-averaged spectrum". In: *Nature, Volume 555, Issue 7694, pp. 67-70, 2018* (Oct. 13, 2018). DOI: 10.1038/nature25792. arXiv: http://arxiv.org/abs/1810.05912v1 [astro-ph.CO].

[252] Rennan Barkana. "Possible interaction between baryons and dark-matter particles revealed by the first stars". In: *Nature* 555.7694 (2018), pp. 71–74. DOI: 10.1038/nature25791. arXiv: 1803.06698 [astro-ph.CO].

[253] Weishuang Linda Xu, Cora Dvorkin, and Andrew Chael. "Probing sub-GeV Dark Matter-Baryon Scattering with Cosmological Observables". In: *Phys. Rev.* D97.10 (2018), p. 103530. DOI: 10.1103/PhysRevD.97.103530. arXiv: 1802.06788 [astro-ph.CO].

[254] Alessandro Melchiorri, Antonello Polosa, and Alessandro Strumia. "New bounds on millicharged particles from cosmology". In: *Phys. Lett.* B650 (2007), pp. 416–420. DOI: 10.1016/j.physletb.2007.05.042. arXiv: hep-ph/0703144 [hep-ph].

[255] Nima Arkani-Hamed, Douglas P. Finkbeiner, Tracy R. Slatyer, et al. "A Theory of Dark Matter". In: *Phys. Rev.* D79 (2009), p. 015014. DOI: 10.1103/PhysRevD.79.015014. arXiv: 0810.0713 [hep-ph].

[256] Xue-lei Chen, Steen Hannestad, and Robert J. Scherrer. "Cosmic microwave background and large scale structure limits on the interaction between dark matter and baryons". In: *Phys. Rev.* D65 (2002), p. 123515. DOI: 10.1103/PhysRevD.65.123515. arXiv: astro-ph/0202496 [astro-ph].

[257] Kris Sigurdson, Michael Doran, Andriy Kurylov, et al. "Dark-matter electric and magnetic dipole moments". In: *Phys. Rev.* D70 (2004). [Erratum: Phys. Rev.D73,089903(2006)], p. 083501. DOI: 10.1103/PhysRevD.70.083501, 10.1103/PhysRevD.73.089903. arXiv: astro-ph/0406355 [astro-ph].

[258] Kimberly K. Boddy, Vera Gluscevic, Vivian Poulin, et al. "Critical assessment of CMB limits on dark matter-baryon scattering: New treatment of the relative bulk velocity". In: *Phys. Rev.* D98.12 (2018), p. 123506. DOI: 10.1103/PhysRevD.98.123506. arXiv: 1808.00001 [astro-ph.CO].

[259] Yacine Ali-Haïmoud. "Boltzmann-Fokker-Planck formalism for dark-matter–baryon scattering". In: *Phys. Rev.* D99.2 (2019), p. 023523. DOI: 10.1103/PhysRevD.99.023523. arXiv: 1811.09903 [astro-ph.CO].

[260] Asher Berlin, Dan Hooper, Gordan Krnjaic, et al. "Severely Constraining Dark Matter Interpretations of the 21-cm Anomaly". In: *Phys. Rev. Lett.* 121.1 (2018), p. 011102. DOI: 10.1103/PhysRevLett.121.011102. arXiv: 1803.02804 [hep-ph].

[261] José Luis Bernal, Alvise Raccanelli, Licia Verde, et al. "Signatures of primordial black holes as seeds of supermassive black holes". In: *JCAP* 1805.05 (2018), p. 017. DOI: 10.1088/1475-7516/2018/05/017. arXiv: 1712.01311 [astro-ph.CO].

[262] Josef Pradler. "Dark radiation: 21cm signals and laboratory tests". In: *PoS* NOW2018 (2018), p. 085. DOI: 10.22323/1.337.0085. arXiv: 1812.09122 [hep-ph].

[263] Maxim Pospelov, Josef Pradler, Joshua T. Ruderman, et al. "Room for New Physics in the Rayleigh-Jeans Tail of the Cosmic Microwave Background". In: *Phys. Rev. Lett.* 121.3 (2018), p. 031103. DOI: 10.1103/PhysRevLett.121.031103. arXiv: 1803.07048 [hep-ph].

[264] Yacine Ali-Haïmoud, Jens Chluba, and Marc Kamionkowski. "Constraints on Dark Matter Interactions with Standard Model Particles from Cosmic Microwave Background Spectral Distortions". In: *Phys. Rev. Lett.* 115.7 (2015), p. 071304. DOI: 10.1103/PhysRevLett.115.071304. arXiv: 1506.04745 [astro-ph.CO].

[265] P. A. R. Ade et al. "Planck 2015 results. XX. Constraints on inflation". In: *Astron. Astrophys.* 594 (2015), A20. DOI: 10.1051/0004-6361/201525898. arXiv: 1502.02114 [astro-ph.CO].